The University Of Sheffield.

High Force Density Linear Electromagnetic Actuators for Active Suspension

By

Zhengmeng Liu

A thesis submitted for the degree of Doctor of Philosophy

Department of Electronic and Electrical Engineering

Faulty of Engineering

The University of Sheffield

May 2021

Abstract

Active suspension is key to improve ride comfort while maintaining good stability of the vehicle under various road conditions. However, active suspensions which employ linear electromagnetic actuators that directly generate thrust force are generally heavy and bulky due to low power density of the current state-of-art linear electromagnetic actuator technologies. This thesis is concerned with research, development and optimisation of high thrust force density linear electromagnetic actuators for active suspensions, as well as with construction and testing of a selected magnetic screw based high force density linear actuator.

A number of high force density linear electromagnetic actuator technologies have been investigated. First, two tubular permanent magnet (PM) vernier motors and three dual-stator PM vernier linear motors have been proposed and globally optimised against the target performance and constraints for an active suspension system. The equivalent thermal model and demagnetization assessment are also described and discussed. The outcome is compared with a reference motor under the same volumetric and thermal constraints. It is shown that the advantage of the PM vernier motor is not obvious but the dual-stator PM vernier linear motor exhibit significantly higher force capability with comparable power factor than that of the reference motor.

Subsequently, a linear actuator with an integrated magnetic screw and rotary motor is proposed and optimally designed based on the principle of torque-force transmission and magnetic screw thrust force characteristic. The saturation level in the back iron of the rotor is evaluated and the heat transfer due to the losses in the rotary motor to the magnetic screw is also assessed. Further, 3D FE analysis is used to predict magnetic screw based linear actuator (MSLA) performance. It has been shown that the designed MSLA exhibits extremely high thrust force density while meeting the design specifications.

The characteristics of unbalanced magnetic force (UMF) in a magnetic screw under static eccentricity have been investigated analytically and by a full 3-D FE model with high-quality meshes. It is shown that the impact of UMF on the mechanical design and the resultant increase in bearing friction are not significant.

Finally, the optimised MSLA and dedicated test rig are mechanical designed and constructed. All key mechanical components of the actuator including the motor housing

are described in detail. A practical means of employing discrete parallel magnetised magnet array to form helical magnetisation pattern is discussed and measured B-H characteristics of magnets are represented in the FE model. The back EMF, torque characteristic, static thrust force and transient load characteristics are measured and compared with predictions. The test results demonstrate that the linear actuator with the integrated magnetic screw exhibits significantly high force capability than that of traditional linear electromagnetic actuators.

Acknowledgement

First of all, I would like to offer my most sincere respect and heartfelt thanks to my supervisors: First supervisor Professor Jiabin Wang and second supervisor Dr. Antonio Griffo. The rigorous academic attitudes, profound technical attainments, and diligent professionalism of the two supervisors have set me to learn from throughout my life. From the topic selection of the thesis, the grasp of the research plan and implementation results, as well as the writing of the thesis, all the sweat and effort of Professor Wang have been devoted. In terms of scientific research, Professor Wang has been careful to guide me, and when I am confused, he will give me guidance. And I am deeply inspired and benefited by expanding my thinking. In terms of life, he also gives me meticulous care.

Thanks to Dr Liang Chen, Dr Xiao Chen,who gave me guidance on the Python code and FLUX modelling during my research process. And Thanks to the colleagues in office F26, I happily spent my PhD years. Thanks to Dr Bo Wang, Dr Rongguang Hu, Dr Tianfu Sun, Dr Chaohui Liu, Dr Shangjian Dai, Hao Chen and all my fellows from the Electrical Machine and Drives Group of the University of Sheffield.

Thank my parents for their selfless dedication, support, encouragement and love. And accompanying me on the Ph.D. study for so many years, and inspiring me to continue to study in the future.

Finally, thank everyone who supported and helped me.

Table of Contents

NOMENCLATURES

Symbol	Meaning	Unit
A	Electrical load	I/mm
B_{PM}	Flux density of the PM field in air gap	T
$B\delta$	Amplitude of the PM flux density	T
B_{rem}	Remanence of the magnet	T
B_i	Stator back iron thickness	mm
D_1	Inner diameter of the stator	mm
D_2	Stator inner bore diameter	mm
e_A	No-load back EMF of the phase A winding	V
E_{ph}	No-load back EMF rms	V
E_0	Back EMF	V
F_t	Magnetic screw thrust force	N
G	Magnetic gear ratio	
$G_1, G_2, G_3, G_4, G_5, G_6$	Inverses of $R_1, R_2, R_3, R_4, R_5, R_6$	
g_{ax}	Axial air-gap width	mm
$g0$	Air gap length without eccentricity	mm
h_c	Thermal convection coefficient at the ambient temperature	$W/m^2/C$
I_{ph}	Rms of the phase current	A
Jc	Equivalent current density of the magnet	A/mm^2

K_w	Equivalent thermal conductivity of stator winding	W/m/C
K_{line}	Thermal conductivity of the slot line	W/m/C
K_g	Thermal conductivity of air gap	W/m/C
K_{Fe}	Equivalent thermal conductivity of the stator core	W/m/C
k_{dp1}	Fundamental winding factor of the stator winding	
l_{stk}	Length of the laminate	mm
L_2	Length of armature	mm
L_q	q-axis inductance	mH
N_{ph}	Number of turns in series per phase	
n_f	The number of magnetic modulating rings	
n_s	Number of cogging slots	
$R_1, R_2, R_3, R_4, R_5, R_6, R_7, R_8, R_9, R_{10}, R_{11}, R_{12}, R_{13}$	Thermal resistances of simplified thermal model	C/W
Rb_3	Mover core height	mm
Rb_4	Stator back iron thickness	mm
Rb_5	Stator outer radius	mm
Rb_6	Rotor outer radius	mm
$R_{s1}, R_{s2}, R_{s3}, R_{s4}, R_{s5}, R_{s6}, R_{s7}, R_{s8}$	Thermal resistances in air gap	C/W

$R_{F1,}R_{F2,}R_{F3,}R_{F4,}R_{F5,}$ $R_{F6,}R_{F7}$	Thermal resistances in core	C/W
$R_{W1,}R_{W2,}R_{W3,}R_{W4}$	Thermal resistances in copper	C/W
$R_{c,}R_{c1,}R_{c2}$	Thermal resistance representing the heat convection on the stator surface	C/W
R_w	Mover core width	mm
R_l	Mover core height	mm
R_m	Mover radius	mm
T_1, T_2, $T_{3,}T_4$	Temperature rises	^oC
Tp	Pole pitch	mm
T_w	Stator teeth width	mm
T_{TW}	Teeth tips width	mm
T_{TH}	Teeth tips height	mm
T_n	Magnetic screw torque	N/m
T_e	Three-phase VPM electromagnetic torque	N/m
P_N	Output power	W
P_r	Rotational power	W
P_t	Linear motion power	W
$P_{Cu,}P_{Cu1,}P_{Cu2}$	Copper loss of the motor	W
$P_{Fe,}P_{Fe1,}P_{Fe2}$	Iron loss of the motor	W
p_s	Armature magnetic field pole pairs	
p_r	PM pole pairs	

v	Actuator linear speed	m/s
X_q	Inductive reactance	Ω
z_d	Mover linear displacement	mm
μ_0	Permeability of the airspace region	H/mm
ω	Rotor angular speed	rad/s
Ψ_{ph}	Flux linkage of each phase	Wb
Ψ_{PM}	PM fundamental flux linkage	Wb
δ_s	Slot line thickness	mm
θ_r	Rotor rotates angle	rad

ABBREVIATION

DTVPM	Double-sided, tubular, Vernier permanent magnet
EMF	Electromotive force
FE	Finite element
LCM	Least common multiple
MGM	Magnetic geared motor
MSLA	Magnetic screw based linear actuator
PM	Permanent magnet
PMSM	Permanent magnet synchronous motor
SPM	Surface permanent magnet
UMF	Unbalanced magnetic force
VPM	Vernier permanent magnet

CHAPTER 1
Introduction to Vehicle Active Suspension and High Force Density Linear Actuator

1.1 General Vehicle Suspension Topologies

Since 1886, when the German Bentz designed and manufactured the world's first three-wheeled vehicles equipped with a gasoline internal combustion engine, vehicles have begun to change human life and change the traditional concept of human transportation. After World War II, the automobile industry has experienced unprecedented rapid development, a large number of technological innovations have been made. However, with the rapid development of the automobile industry, the comfort of passengers and the safety performance of vehicles on the road has gradually become the two most important performance indicators [1-2]. The vehicle suspension system has the greatest impact on these two performance indicators.

Broadly speaking, the vehicle suspension topologies includes all the connections and damping devices between the body and the wheels. Its basic components are the spring and the damping system (the active suspension system has an additional actuator). When the vehicle is driving, the various vibrations caused by uneven road surface are attenuated and isolated by the suspension system to ensure the comfort of passengers, while at the same time, increasing the adhesion of the wheels to the ground [3-5]. So a well-designed suspension will undoubtedly greatly improve the overall performance of the vehicle.

1.1.1 Passive Suspension and Semi-Active Suspension

According to different control forms, suspension systems can be roughly divided into three categories [6-7], namely passive suspension systems (fixed springs, damping structures), semi-active suspension systems (springs, variable damping structures) and active suspensions system (spring, damping, actuator structure). Fig. 1-1 shows the passive suspension systems and semi-active suspension systems.

At present, most of the suspension systems installed on vehicles are passive suspensions. Among the three suspension systems, it has the simplest structure, lower design complexity and low price. When the traditional passive suspension system has external excitation, its spring and damping characteristics can respond passively and act on the body and wheels to achieve the purpose of buffering and reducing vibration. Olley

first developed the K^2 device for testing ride comfort, and studied the effect of suspension system stiffness and damping on suspension dynamics [8]. The design of the suspension system needs to be coordinated and selected in terms of the ride comfort, the dynamic deflection of the suspension and the dynamic load requirements of the tires [9-11].

In order to obtain better driving performance, the researchers used asymmetric damping elements, nonlinear elastic parts and automatic height adjustment structure. Semi-active suspension was first proposed by D.A.Crosby and D.C.Kamopp in 1973 [12-13]. Unlike passive suspension, semi-active suspension requires a small amount of energy input. The semi-active suspension system replaces the invariable damping element with a variable damping shock absorber on the basis of the passive suspension system. The variable damping shock absorber can be controlled and planned through a certain control input to adjust the damping state of the shock absorber, so that the semi-active suspension system can have a certain adaptability to changing road conditions [14-17]. The performance of semi-active suspension systems is usually between passive suspension and active suspension.

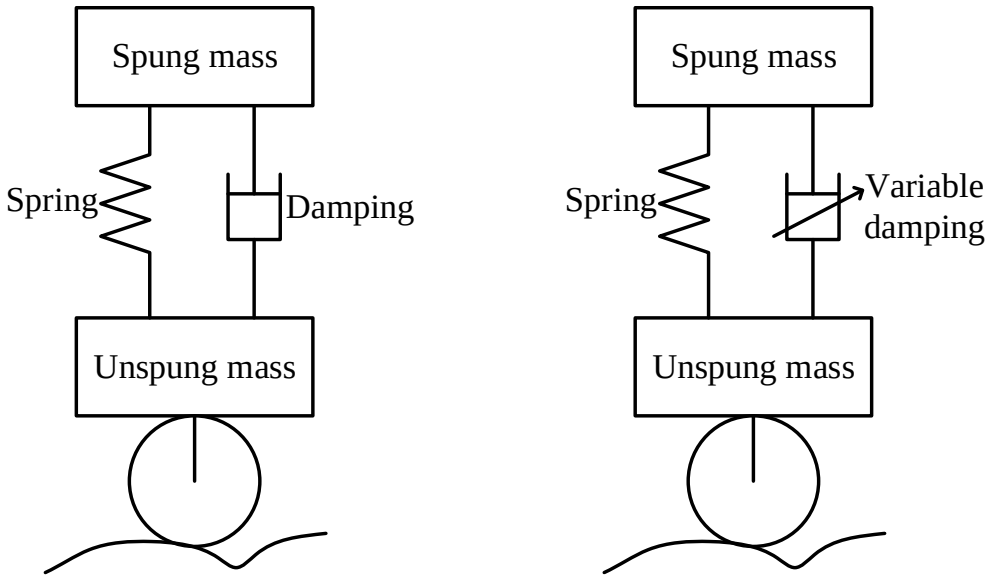

(a) (b)

Fig. 1-1 Passive suspension systems and semi-active suspension systems (a) Passive suspension (b) Semi-active suspension.

1.1.2 Active Suspension

If an active force generating device is added to the passive suspension, and the actuator is driven to assist the suspension system through appropriate control laws to achieve the desired performance, the so-called active suspension system is formed.

Compared with passive suspension system and semi-active suspension system, the active suspension can adjust the damping and stiffness of the suspension in real time according to the impact of the road, the acceleration and speed of the wheel and the vehicle body, and ensure the smoothness and stability of the vehicle under various road conditions [18-21]. The adjustment is provided by actuators supplied with external energy. Compared with the passive suspension with fixed damping and stiffness, the damping and stiffness of an active suspension is automatically adjusted through control of the force of the suspension device based on the measurement of vehicle and tyre movements.

There are two basic forms of active suspension; one is the parallel active suspension, as shown in Fig. 1-2(a). It is based on a passive suspension with the addition of a drive which only needs to provide part of the adjustment. Such a system is of low energy consumption. When the active suspension part is faulty, it can be operated in a passive mode. The other is a separate suspension which is driven by an actuator as shown in Fig. 1-2 (b). The structure is simple but the system is energy-consuming. At present, this concept is realised by electro-hydraulic servo system. The higher the required control bandwidth, the more difficult to achieve with such a system while the cost and size will increase, and so does the energy consumption. If a conventional spring and shock absorber is incorporated into an active suspension to withstand static loads and provide conventional damping, the system's energy consumption and the size of the actuator as well as the hydraulic pressure will decrease. But this approach is not well integrated. In general, from the perspective of reducing energy consumption, active suspensions have retained a traditional spring in parallel with the actuator. The design rules of the two active suspensions are basically the same. At present, active suspension systems mainly employ active air suspension, active hydraulic suspension and electromagnetic suspension as shown in Table 1-1.

Among them, active hydraulic suspension systems generally have shortcomings such as slow response, large energy consumption, and complex structure. Active air suspension have disadvantages such as low accuracy and low reliability. Electromagnetic suspensions are based on the principle of electromagnetic induction and have compact and the advantages of fast response time, high precision and good controllability, and good energy recovery. They have great potential in improving vehicle driving comfort while reducing energy consumption.

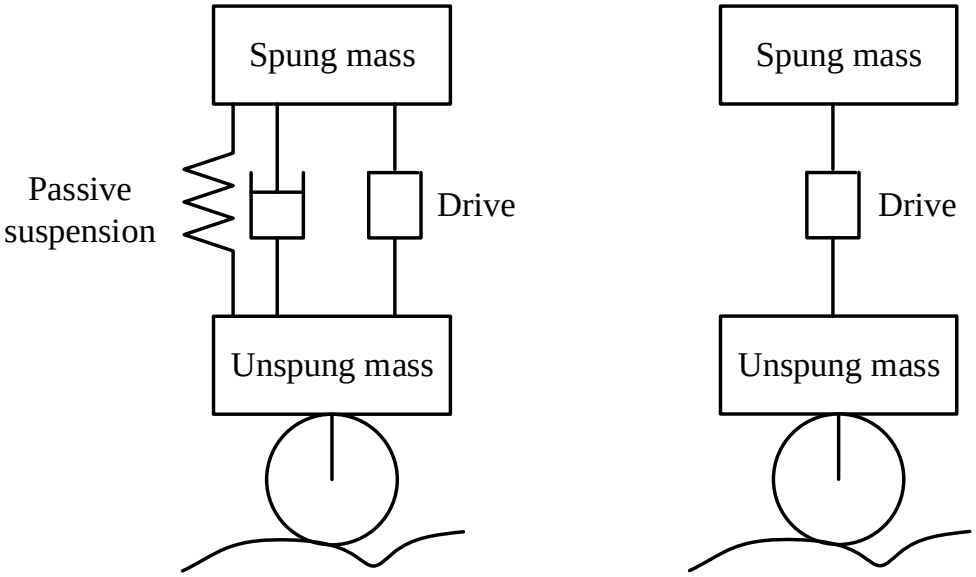

Fig. 1-2 Parallel active suspension systems and separate suspension systems (a) Parallel active suspension (b) Separate suspension.

Table 1-1 Performance comparison of various suspension actuators

Actuator classification	Working principle	Application
Active air suspension	Pneumatic transmission	Aviation, vehicle
Active hydraulic suspension	Hydraulic transmission	Vehicle
Electromagnetic actuator	Electromagnetic transmission	Universal

1.1.3 Active Electromagnetic Suspension

The damping and stiffness of traditional automobile suspension systems are not adjustable, and it is difficult to balance vehicle comfort and operability. With the development of technology, electromagnetic active suspension can convert electrical energy into mechanical energy. Its structure is more compact, the system is more stable, the control ability is stronger, and the response is faster. Not only can it provide the vehicle with damping force, but it can also generate active electromagnetic force to control the attitude of the body, ensuring the safety of vehicle driving. Hence electromagnetic based active suspension has become a new type of suspension development trend.

Electromagnetic active suspension can be divided into magnetic levitation suspension type and motor suspension type according to the different structures[22-23]. Mirzaei S. and Saghaiannejad S. designed an active electromagnetic suspension system based on the magnetic levitation theory [24-25], which is mainly composed of silicon steel and coils,

and controls the output of damping by controlling the coil current. However, only a few researchers have proposed some design schemes and conducted some theoretical studies, and the magnetic levitation technology has not yet been applied on road vehicles.

For motor suspensions, Beno uses a rotating electric machine in an electronically controlled suspension [26-27]. Based on similar principles, Sude designed a new electromagnetic active suspension using a rotating motor and a ball screw, and conducted theoretical research on the problem of large equivalent inertia and structural impact [28-30]. Yu studied the same type of electromagnetic active suspension, improved the performance of the suspension system, and carried out bench experiments [31-34].

However, as the vehicle suspension movement is a linear motion, the early electromagnetic suspension generally use the rotating motor through the rotary-to-linear mechanical conversion to convert rotary motion into linear motion. Which makes the electromagnetic suspension structure complicated, which also increases the electromagnetic suspension instability and loss. Hence, a linear electromagnetic actuator suspension which can produce high linear thrust directly shows the advantage. Babak designed an electromagnetic suspension of a linear induction motor [35-36], discussed the influence of the internal structural of the suspension of electromagnetic force, and carried out a bench experiment using a prototype. The authors in [37] used a DC motor for the active suspension system, and pointed out that this type of active suspension has the advantages of high operating efficiency, convenient power factor control and high electromagnetic force linearity. The authors in [38] designed a linear switched reluctance motor active suspension. The suspension system has a simple structure and high reliability, but it has great thrust fluctuations.

1.2 Candidate High Force Density Linear Actuator Technologies for Electromagnetic Suspension

1.2.1 Current Problems with Linear Actuator Electromagnetic Suspension

According to the above analysis, because the linear actuator does not require an intermediate power transmission mechanism, the structure is simple, and it is more suitable for installation on a car suspension system with limited space. However, the linear actuator based on the electromagnetic active suspension of the automobile still has some problems and needs to be improved.

(1) The force density of linear motor reported in the literature is much lower than linear electromechanical actuation that uses rotary-to-linear transmission. Hence, to obtain the same thrust force, the linear electromagnetic actuator needs a much larger volume, weight and cost, even the volume of the linear actuator is larger than the rotary-linear actuator.

(2) In most of the modelling and control studies of electromagnetic active suspensions, the processing of the actuator is relatively simplified. The performance of the actuator is usually replaced by the motor constant, and in the model the structural characteristics and dimensions of the actuator are not accurately reflected. Hence, the performance of linear actuators with different structural characteristics may be inaccurate.

(3) In the analysis of electromagnetic force of electromagnetic suspension actuators, some studies have set it as a linear model of current. In fact, as the current increases, the electromagnetic force presents a nonlinear change under the influence of magnetic field saturation, which has an impact on the dynamic performance of the vehicle under peak conditions.

(4) In the experimental research of electromagnetic suspension actuators, most literature studies ignore the errors of actuators in actual manufacturing and assembly, such as eccentricity. This will cause friction and compromise performance of the actuator, which will affect the experimental results.

Therefore, this thesis will start from the electromagnetic suspension performance requirements, develop and optimize candidate high thrust force density linear actuators with different structural characteristics, and simulate the output performance under different working conditions. Then select an candiade design with the best performance for prototype construction, tests and validation.

1.2.2 Actuator Structure Feature Selection

Broadly speaking, all linear actuator topologys can be employed for electromagnetic suspension. However, since the electromagnetic suspension linear actuator must have the highest possible thrust force density, the linear permanent magnet (PM) motor is the choice of motor topology with its high thrust force density, simple structure, fast response, and good controllability. A number of candidate topologies, such as tubular, dual stator, vernier type, and magnetic screw for contactless rotary-to-linear high force density

transmission, etc., will be investigated. They all have potentials for significant increase in the force density of the linear actuator.

(1) In tubular topology, the windings are donought-shaped and have no end-windings, so the utilization rate of the windings is very high, thereby increasing the motor output thrust force. And because there is no lateral end effect, the tubular motor output force ripple is also small.

(2)Dual stator topology can place windings in both the inner and outer stators, so compared to the ordinary single stator structure, it can provide greater electrical loading, can generate greater thrust force under the same volumen [39], and improve the material and space utilization of the motor.

(3) Vernier structure uses the magnetic gear principle to modulate the magnetic field, instead of relying on the fundamental magnetic field, to achieve electromechanical energy conversion. A Vernier permanent magnet motor (VPM) combines the characteristics of PM motor and magnetic gear principle, so it can output high torque/force or high power density at low speed.

(4) In the structure of the magnetic screw, there is no direct mechanical contact between the rotational motion part and linear motion part, and the energy transfer is realized by magnetic field coupling like the mechanical screw. When it is integrated in a rotary motor, the force density of such a actuator can be significantly increased.

Table 1-2 listed the principle of different structural features to increase thrust force density.

Table 1-2 Principle of different structural features

Candidate topology/technology	Principle to increase thrust force density
Tubular	High utilization rate of the windings
Dual stator	High utilization rate of the volume
Vernier	Magnetic gear principle
Magnetic screw based	Rotary-to-linear magnetic gearing

1.3 Current State-of-the-art of High Force Density Linear Actuator

Linear electrical actuator is an equipment which can convert electrical energy into linear kinetic energy or vice versa without the need for any intermediate conversion

structure. A linear electrical actuator can be seen as an evolution of the rotating machine in the structure by radially cutting the machine, and then flattening it. Fig. 1-3 shows the conversion of a rotating electrical machine into a linear electrical actuator.

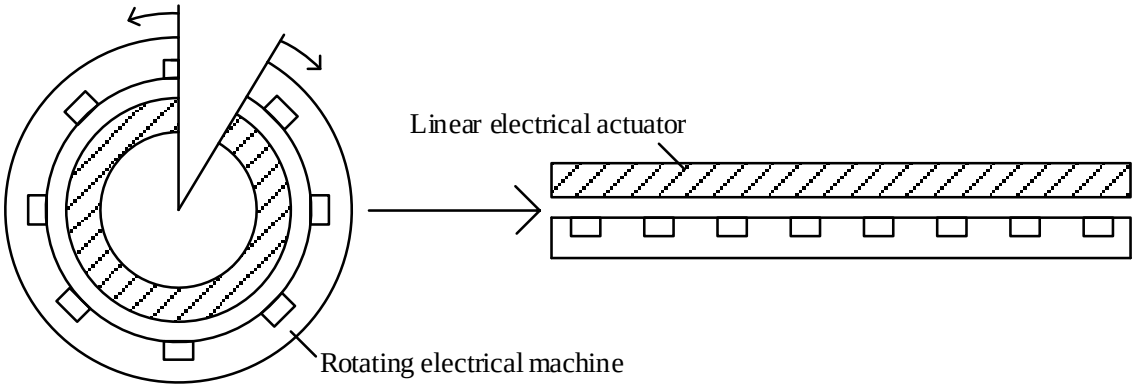

Fig. 1-3 Rotating electrical machine changes to linear electrical actuator

1.3.1 Permanent Magnet Linear Synchronous Actuator

Permanent magnet linear synchronous machine(PMSLM) combines the advantages of PM motors and linear motors. The main advantages of using PMLSM actuator include [40-41]:

(1) Direct drive. The mover of PMLSM is directly connected to the load, eliminating the need for intermediate mechanical transmission. It has the advantages of high speed, high acceleration, high positioning accuracy, high dynamic response, high efficiency, etc., and can achieve performance indicators that cannot be achieved by the rotating motor drive method.

(2) Relatively high thrust force density. The PMLSM has a large air gap flux density, and has a higher thrust force density compared with linear induction motors and switched reluctance linear motors. In addition, the semi-closed air gap structure of PMLSM is conducive to the heat exchange between the heat generated by the winding and the outside, the thermal load capacity of PMLSM is increased, so the current density of the motor winding can be designed to be larger. When the water-cooled structure is adopted, the thrust force density of PMLSM is further improved. However, the thrust force density of PMLSM is particularly insufficient compared to the combination of rotating machines and mechanical screws

(3) High reliability. PMLSM has a simple structure, without the mechanical friction of the intermediate parts, the wear of the parts is small, the maintenance is low, operation

safe and reliable, and the service life is long. Further use of air-levitation or magnetic-levitation rails can avoid mechanical contact and reduce movement noise.

(4) The stroke is easy to adjust without restriction. By laying the stator in the direction of movement, the stroke length of the mover can be extended indefinitely, and the modular design is more convenient.

Due to the features of the PMLSM structure, there are the following shortcomings in practical applications:

(1) Large thrust force ripple. Since the limited primary length of PMLSM, the PM breaks at the edge, which produces an end effect. The edge force caused by the end effect and the cogging force caused by the slotting effect will deteriorate the output thrust force performance, and effective methods must be taken to weaken the thrust force ripple.

(2) The control is difficult. When using PMLSM actuator, the load is directly connected to the mover, and external interference is transmitted to the motor mover without buffering. In order to ensure the stability and performance of the servo system, higher requirements are put forward for the robustness of the control system.

1.3.2 Tubular Linear Actuator

The evolved linear actuator in Fig. 1-3 is called the flat linear actuator, flat linear actuator along the vertical direction of linear motion direction may be rolled into a cylinder, thus forming a tubular linear actuator, as shown in Fig. 1-4. Its stator does not have end windings, so there is no lateral end leakage flux and additional impedance, and there is no net radial force on the cylindrical secondary, thereby reducing the linear bearing stress. Tubular PM actuators can offer high thrust density, high power density, high efficiency, no end-windings and excellent servo characteristics, this makes tubular PM actuators particularly attractive. However, due to the tubular structure, the space in the middle of the actuator cannot be effectively utilized. As schematically illustrated in Fig. 1-5, tubular PM actuators have a variety of configurations depending on the distribution of PMs and armature windings. Fig. 1-5 (a) shows the outer stator tubular PM actuator and Fig. 1-5 (b) shows the inner stator tubular PM actuator [42-43]. Fig. 1-5 (c) shows the tubular PM actuator which has axially magnetized PMs separated by iron core, and Fig. 1-5 (d) shows the tubular PM actuator using PMs Halbach array structure [41].

In [44] a general framework for the analysis and design of tubular linear actuator is described. In the paper the magnetic field distribution of radial PM machine technology, axial PM machine technology and Halbach PM machine technology are calculated analytically. The expressions of force and EMF prediction is also derived. And the analytical calculation is verified by FE analysis. The thrust density of radially magnetized, axially magnetized, and Halbach magnetized tubular PM actuators are compared under the same cooling condition, on the basis of analytical calculation [45]. It can be concluded that the Halbach magnetized actuator has high thrust force density with low force ripple, albeit the realization of the Halbach magnetization pattern is difficult. So in order to further optimize the axial and radially magnetised tubular PM actuator technology, the authors of [46] propose an improved axial tubular PM actuator topology, it is evident from the paper that the improved topology provides greater thrust force and uses less PMs.

The leading design parameters of the radially tubular PM actuator technology are optimized in [47]. As well as the analytical formula of open circuit EMF, thrust, iron loss, winding resistance and inductance and converter loss are derived and accounted. Besides, the Halbach tubular PM actuator technology is reported in [48]. Due to the ideal Halbach magnetized PMs is impractical, quasi-Halbach magnetization is a good alternative. It shows that quasi-Halbach magnetized PM actuators have lower air-gap harmonic content than conventional radial-magnetized PM actuators. These characteristics make it particularly suitable for low force ripple applications. In the paper, it can be concluded that the thrust fluctuation of the motor is mainly related to two parameters.

A high thrust force density tubular linear PM actuator for active vehicle suspension is described in [49-50]. It is shown that there are three key dimensional ratios in linear actuator design: outer radius/ inner radius, pole-pitch/ outer radius, middle PM width/ pole-pitch. The performance of the actuator is optimized and demagnetization risk are assessed.

The authors in [51-52] proposed transverse flux tubular linear PM actuator, the plane of the magnetic field lines of the main magnetic circuit of the motor is perpendicular to the motor motion plane, and has good control characteristics. Theoretically, the motor has the advantage of large thrust density, but the disadvantage is that the structure is complicated. The current research work mainly focuses on improving power factor, reducing magnetic leakage, and reducing cogging force. In addition, the authors in [53-

54] also proposed and carried out research on transverse flux cylindrical linear motors, which improved the utilization rate of PMs.

The authors in [55] proposed a built-in tubular linear PM actuator, the ring-shaped axial magnetizing PM and the ring-shaped magnetically conductive core are sequentially sleeved on the non-magnetically conductive shaft. The motor has a simple structure, can make full use of the reluctance force, and has the characteristics of high thrust force density and low processing cost. The disadvantage is that PMs have large axial magnetic leakage.

The authors in [56] proposed a coreless tubular linear PM actuator which does not have actual cogging. After the windings are arranged in a certain phase sequence, they are bonded by epoxy resin or fixed by other special methods. The working principle is basically the same as that of a slotted motor. The difference is that the slotless motor has large magnetic reluctance and fast armature response albeit low force density, so it has the advantages of stable thrust and wide load range.

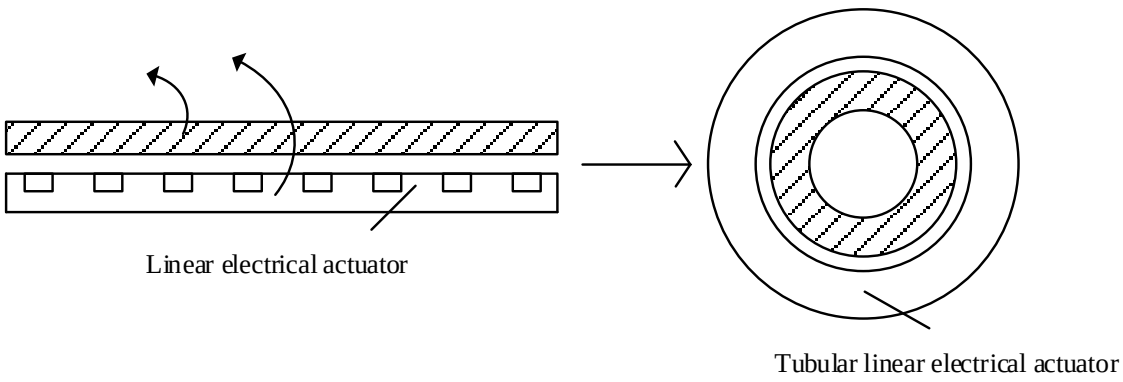

Fig. 1-4 Linear electrical actuator changes to tubular linear electrical actuator

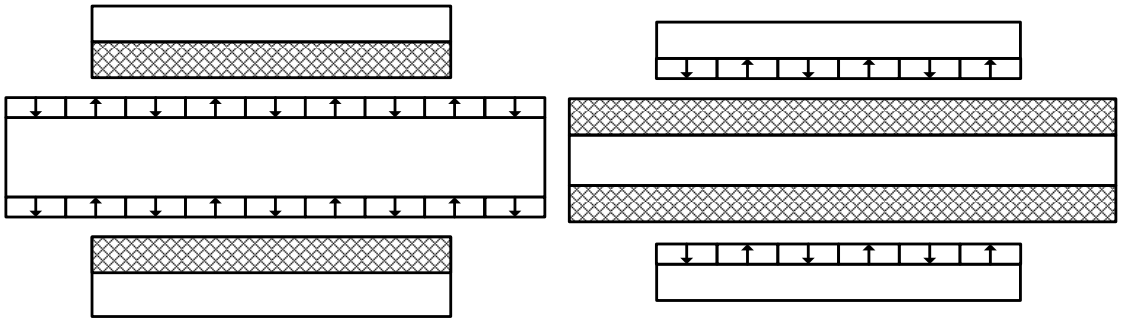

(a) (b)

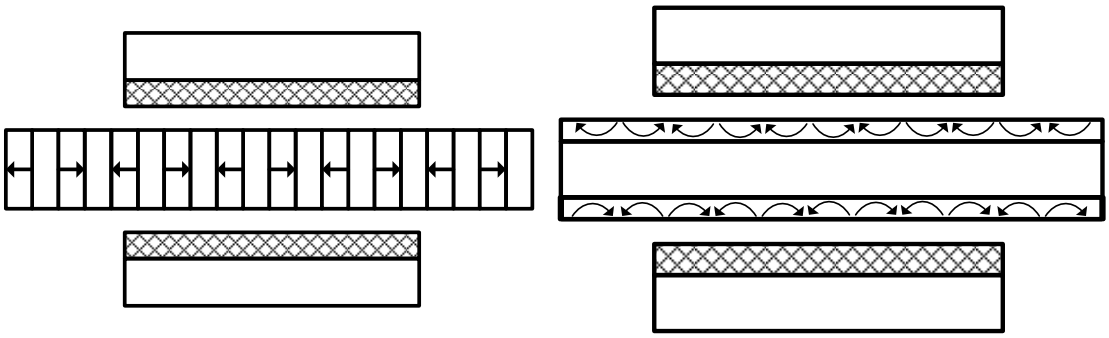

(c) (d)

Fig. 1-5 Typical tubular linear PM machine topologies (a) Internal radial PM machine technology (b) External radial PM machine technology (c) Internal axial PM machine technology (d) Halbach PM machine technology

1.3.3 Dual-stator Linear Actuator

A Dual-stator motor refers to a motor with two stators. For a linear motor, a dual-stator linear motor is equivalent to evolution a dual-stator rotating motor into a linear motor according to Fig. 1-3, but the air gap length on both sides of the stator becomes the same. The dual-stator motor linear motor makes more efficient use of space, resulting in greater thrust force density. And since there are stators on both sides of the mover, part of the thrust ripple of the mover can be offset by changing the structure of the teeth. For a dual-stator flat-plate linear motor, the stators on both sides increase the heat dissipation area, so that the motor can withstand a greater electrical load. For tubular dual-stator linear motors, the small contact area between the inner stator and the air is not conducive to the heat dissipation. The electrical load on the motor is reduced and the PMs are more susceptible to the risk of demagnetization.

The dual stator motor was first proposed by B. H. Smith in the form of an induction motor in 1966 [57]. Since then, the dual stator structure has been used in many different types of motors, from the early DC motors and induction motors, to the later PM synchronous motors and stepping motors. In many cases, it has advantages of high torque/force capability compared with single stator topologies.

A general dual stator motor will adopt one of the following two topologies: tubular concentric and parallel double-sided [58]. The dual-stator motor with a concentric structure is to place two stators radially on both sides of the mover, effectively using the internal space of the motor to increase the power density. Fig. 1-6 shows a cross-sectional view of a 9-slot 14-pole dual-stator tubular actuator which also exploits Vernier or magnetic gearing effect to increase force density.

In rotating electrical machines, a concentric dual-stator electrical machine generally adopts a cup-shaped rotor structure. However, it has been analysed that a rotating motor can have similar dual stator topologies [59-60] in the form of an axial flux type and a radial flux type.

In rotating PM motors, the use of a dual-stator design will increase the complexity of the motor's structure [61-62]. Hence, generally dual stator topologies are used in axial flux motors. Axial flux dual stator PM motors generally adopt a double air gap structure in which stators are placed on both sides of the rotor. In this way, heat dissipation on both stators can be facilitated.

The authors in [63-66] proposed a dual stator linear-rotary PM motor, which can perform rotation and linear motion at the same time. The authors in [67] proposed a tubular dual-stator PM motor for artificial heart. The motor structure has the advantages of low speed, high thrust and high reliability. A parallel dual stator and outer mover linear rotary PM machine is proposed in [68] for drilling robot, which combines a rotor and a linear mover. By adopting this structure, the torque and thrust force are improved. The authors in [69] improved and compared several dual stator linear stepping actuators for railways channels.

A dual-stator linear actuator may be adopted in a tubular topology. This will, however, increase structural complexity of the motor. Hence the dual-stator linear actuator has not been widely used.

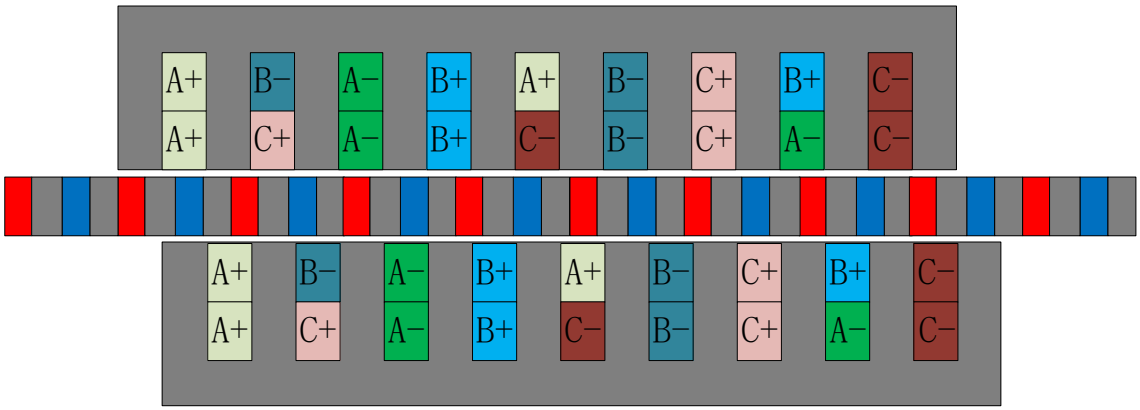

Fig. 1-6 9-slot 14-pole dual stator tubular actuator

1.3.4 Vernier Linear Actuator

Vernier permanent magnet (VPM) motor has received increasing attention in recent years. Compared with traditional PM motors, there is no essential difference in its

structure. It uses the magnetic gear principle to modulate the magnetic field, instead of relying on the fundamental magnetic field, to achieve electromechanical energy conversion. In the Vernier motor, the number of cogging slots n_s, the number of PM pole pairs p and the number of armature magnetic field pole pairs p_s conforms to the following relationship

$$p_s = p \pm n_s \tag{1-1}$$

The principle of VPM operation can be understood by the effect of magnetic gearing. K. Atallah and D. Howe proposed a concentric magnetic gear in 2001 [69]. This magnetic gear has a dual-rotor structure. The inner and outer rotors have PMs attached to the surfaces, and a stationary steel pole-pieces is placed between the two rotors. When the outer rotor and the inner rotor run at different speeds, the stationary steel pole-pieces plays a role in modulating the magnetic field, and the PMs on both the inner and outer rotors participate in torque transmission. In the magnetic gear, if the number of permanent magnet pole pairs of the high-speed rotor is p_1, the number of permanent magnet pole pairs of the low-speed rotor is p_2 and the number of magnetic modulating rings is n_f , the p_1, p_2 and n_f should satisfy

$$p_2 = p_1 \pm n_f \tag{1-2}$$

So the magnetic gear ratio G between the two different rotor speeds is given by:

$$G = \frac{p_1}{p_2} \tag{1-3}$$

Therefore, due to the reduction in speed, the torque is increased by a factor of $1/G$ on the low-speed rotor. Afterwards, based on the principle of magnetic gears, motors with many structures were designed, such as magnetic field modulation permanent magnet motors, tooth-pole vernier permanent magnet motors and split-tooth vernier permanent magnet motors, as shown in Fig. 1-7.

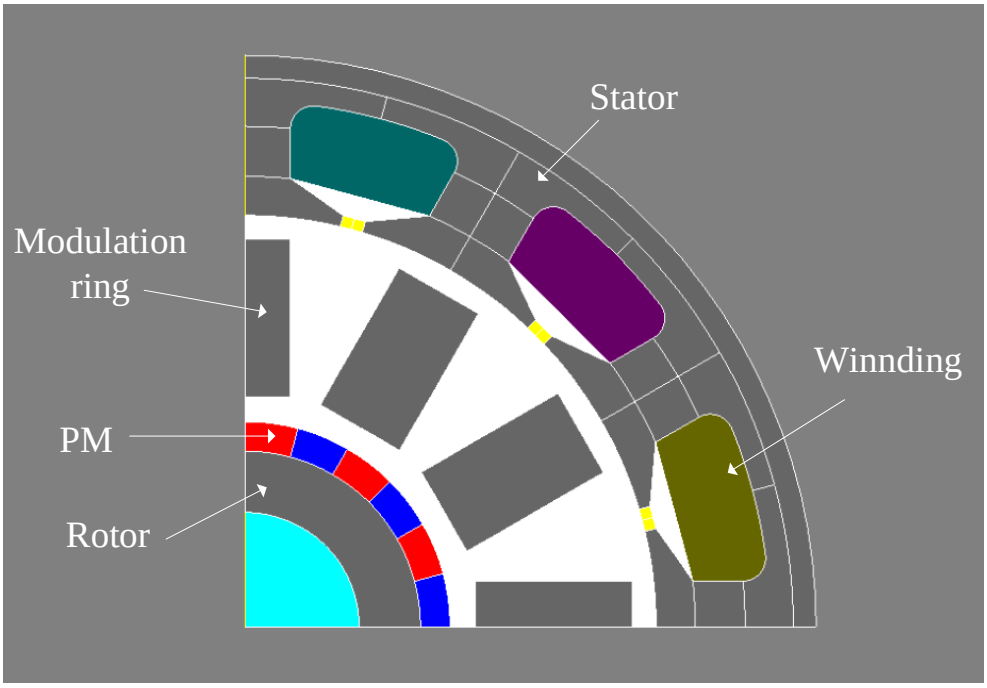
Stator
Modulation ring
Winnding
PM
Rotor

(a)

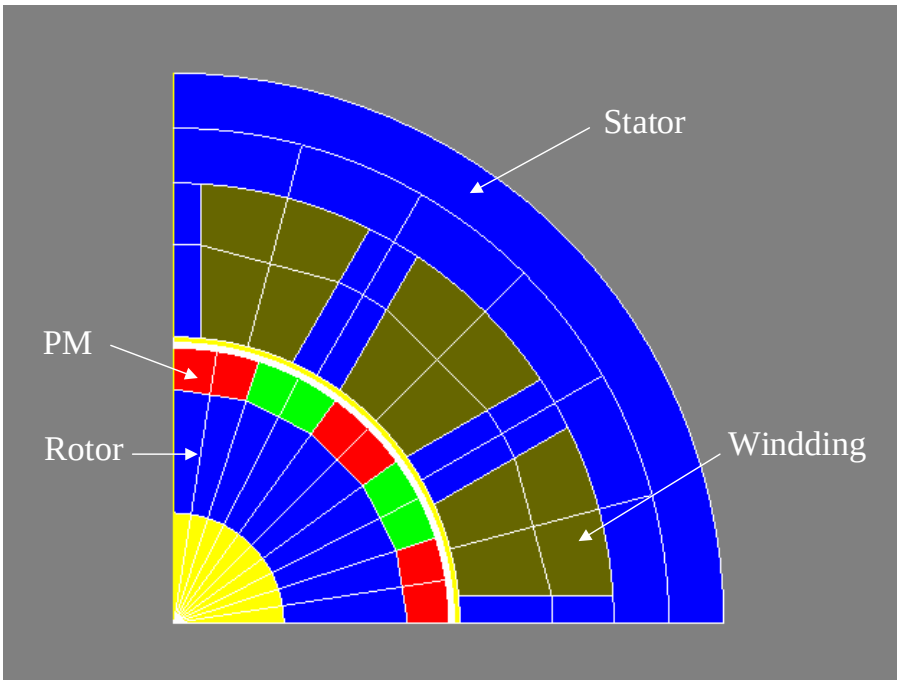
Stator
PM
Rotor
Windding

(b)

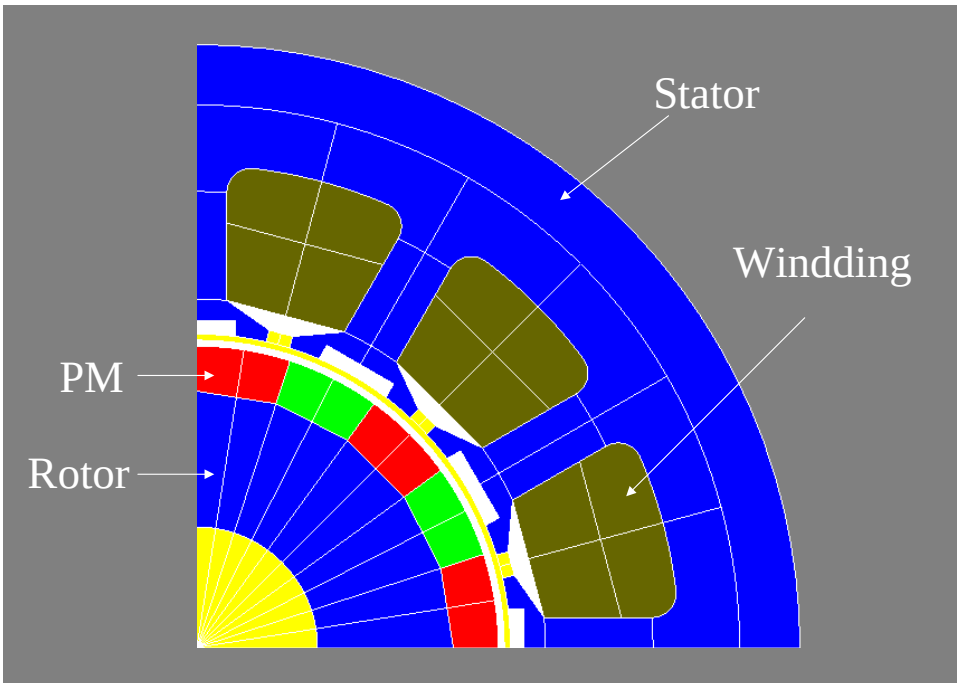

(c)

Fig. 1-7 Motor structure using the principle of magnetic gears (a) magnetic field modulation permanent magnet motor (b) tooth-pole vernier permanent magnet motor (c) split-tooth vernier permanent magnet motor

In 1999, T. A. Lipo proposed a PM Vernier motor consisting of 18 slots and 34 poles. [70-71]. The topology of this motor is very similar to traditional PM motor, with a single PM rotor and a single air gap. Flux modulation is achieved by the movement of the PM rotor with respect to the stationary teeth during operations. This motor realises the magnetic gear principle with one rotor and hence one layer of air gap, which greatly simplifies the mechanical structure. In addition, T. A. Lipo also proposed two stator structures suitable for PM Vernier motors, open slot stator and split-pole stator structures.

For a VPM motor, there is only one rotor. The magnetic gear effect occurs in the air gap in the form of harmonics. The magnetic density of the rotor permanent magnet passes through the cogging and reaches the armature to generate additional vernier torque. So for VPM, from (1-1), its gear ratio G_r is

$$G_r = -\frac{|p_r - n_s|}{p_r} = \frac{p_r - n_s}{p_r} \tag{1-4}$$

Similar magnetic gearing effect can be seen in Vernier machines and fractional slot PM machines. By way of example, Fig. 1-8 shows the schematic of a dual-stator tubular motor with 12-slot 20-pole Vernier topology and the resultant magneto-motive force (MMF) spectra. The magnetic field produced by the 2 pole-pair stator armature (p_s=2)

will be modulated by the 12-teeth (n_s =12) to produce 10 pole-pair magnetic field in the airgap, which interacts with the10 pole-pair PM mover (p=10) to produce thrust force.

The authors in [72] proposed a dual-excitation Vernier machine and compared it with the single rotor Vernier PM machine under the same volume and slot number. The dual rotor structure has larger air gap and adopts drum wingding configuration which effectively reduces the stator end winging length, so that the dual-excitation Vernier machine has higher torque and lower copper loss. The authors in [73] compared the rotor-PM Vernier machine, stator-tooth-PM Vernier machine and stator-yoke-PM Vernier machine. From the comparison results, the stator-tooth-PM Vernier machine has the least PM volume and the rotor-PM Vernier machine has the highest torque density. The authors in [74] presented a dual-stator spoke-type Vernier PM motor. There is a 180° electrical angle shift between inner and outer stators and the rotor adopts the spoke-type magnetic structure. The authors in [75] proposed a dual-stator line-start Vernier PM machine which combines the Vernier motor with a induction motor. The outer stator is for Vernier motor and the inner stator is for induction motor while both stators share one rotor whose outer surface is mounted with PMs and its inner side with conductive winding. The inner stator is energized first when the motor is running, when the rotor rotary at stable speed, the outer stator starts to connected to the grid and the inner stator is disconnected when the rotor has synchronised with the outer stator excitation.

In general, the principle of operation of rotating motors can be applied to linear motors albeit significant end effects in the linear motors may exist. There are many types of rotating Vernier motors, and the topologies of linear Vernier motors are also diverse. The author in [76] proposed a multi-tooth split-pole cursor linear motor with secondary surface-mounted PMs for wave power generation and discussed the control strategy. The simulation results verify the feasibility of such a motor for the direct-drive wave power generation. The authors in [77] compare the dual-sided linear PM Vernier machines with different rotor structure. The interior PM Vernier machine has the lowest force capacity while the surface-mounted PM Vernier machine has basically same force capacity as consequent-pole type Vernier machine. At present, the research on linear Vernier motors is not as much as rotary Vernier motors, but with the deepening understanding of the magnetic gears principle, more types of linear Vernier motors will be studied and applied.

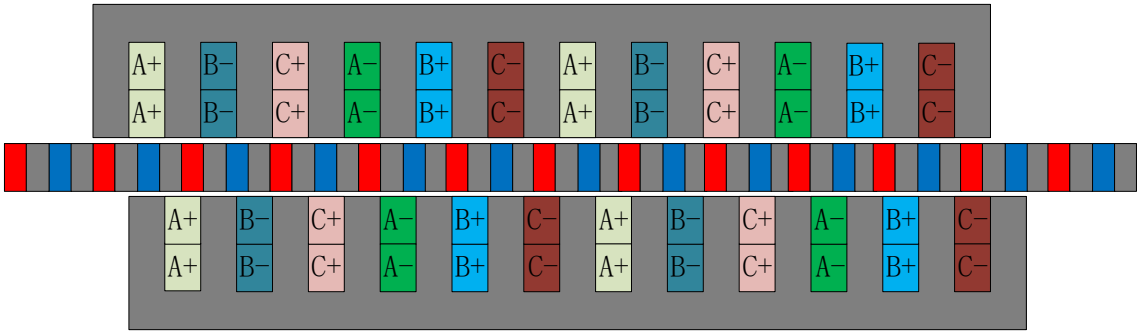

(a)

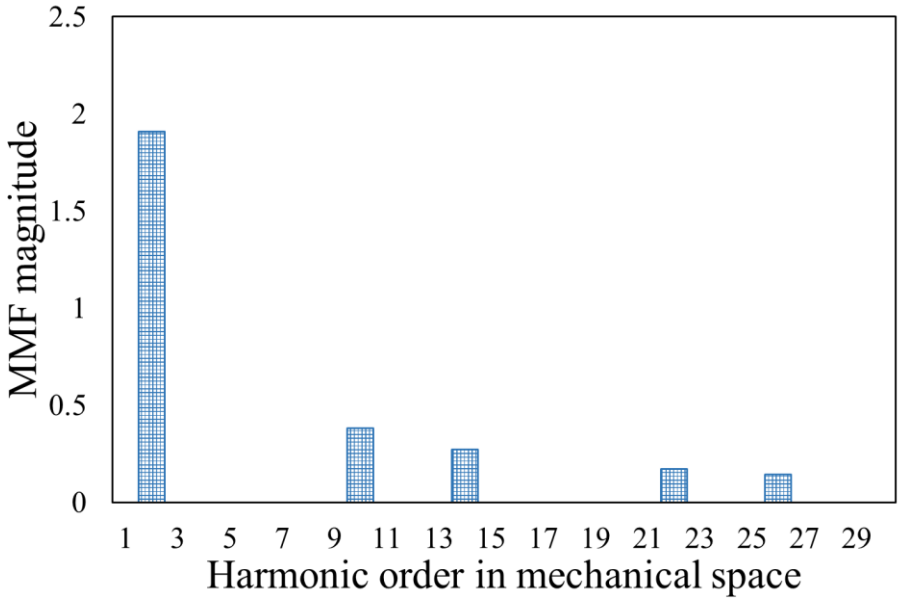

(b)

Fig. 1-8 12-slot 20-pole dual-stator vernier linear actuator (a) Actuator diagram (b) MMF spectra

1.3.5 Magnetic Screw

The authors in [78] developed a magnetic screw which can be used in linear electromagnetic actuators. Fig. 1-9 shows the magnetic screw structure and magnetic screw integrated in a rotary motor. It can be equivalent to a mechanical screw, but has no thread structure. Instead, the PMs are mounted on both sides of the magnetic screw components, and as a result of magnetic field interaction, magnetic torque and thrust force without direct mechanical contact are produced. Similar to the mechanical screw, the two parts move in synchronism; that is, whenever the nut rotates one revolution, the magnetic screw moves a distance λ known as lead, which equals to two times of the magnetic pole-pitch. According to the principle of conservation of energy, the relationship between torque T_n and the thrust force F_t can be established as,

$$T_n = \frac{\lambda}{2\pi} F_t \quad (1\text{-}5)$$

Therefore, when the appropriate magnetic pole-pitch and radius are selected, the magnetic screw can generate very high thrust force like a mechanical screw, and the structure is contactless and jam-free. And for a magnetic screw with a pole-pitch τ_p, the lead would be $2\tau_p$. So for a given linear speed, *v*, of the actuator, the shorter magnetic screw lead, the higher the angular speed of the rotating member of the screw. The gear ratio, *G*, can be defined as

$$G = \frac{\omega}{V} = 2\pi/2\tau_p = {}^{\pi}/_{\tau_p} \quad (1\text{-}6)$$

Where ω is the ratio of the rotor angular speed, and *v* is the actuator linear speed.

In [78], it is shown that the torque transfer relationship of a magnetic screw is similar to the mechanical screw, and in simulation, when the air gap is 0.8mm and the lead is great than 7mm, the thrust density can be greater than 10 MN/m^3. The force density of magnetic screw is more than an order of magnitude larger than that of a conventional linear electromagnetic motor. Therefore, the use of magnetic screw in an electromagnetic actuator is a way to solve low force density problem of the linear electromagnetic actuator.

A new type of electromagnetic energy conversion system is introduced in [79], which combines a motor with integrated direct-rotating magnetic screw. The interior of the motor device is a magnetic screw and the outer part is a three-phase winding motor.

The authors in [80] analysed the utility of magnetic screw in wave energy conversion, and studied its movement and mechanical properties. The results show that as the number of magnetic poles increases, the axial driving force does not change, and the driving torque will increase. In addition, the dynamic characteristics of the magnetic screw show that when the lead screw and the nut are driven, the fluctuation of the force and torque is about 1.1% and 1.3%, which is caused by the insufficient accuracy of the helical structure of the poles. The thrust curve of a magnetic screw under different dimensional parameters, the distribution of the magnetic flux density and the demagnetization effect are analysed in [81]. According to the design of the magnetic screw, the analysis shows that the accuracy of the drive can be guaranteed when the central angle of the pole piece is 15 °.

A magnetic screw with steel segments is reported in [82]. As the magnetic screw PM assembly is difficult, in order to simplify the installation of magnets in the magnetic screw, the iron core is placed between the PMs. In this structure the PMs and iron cores are alternately arranged and the magnetization direction of the iron core and the PMs is

aligned so that the flux can pass through the iron core to produce flux through its air gap. This magnetic screw offers a thrust force density of 2.83 MN/m^3.

The authors in [83] further analysed the magnetic screw mechanical loss and loss of magnetic energy. The results show that the prototype with a thrust of 17KN has an efficiency of about 80% at low load. The experimental and theoretical analysis of the loss of magnetic screw shows that the loss mainly comes from friction in the linear guide rail.

In [84] the design aspects of the magnetic screw are investigated. The effect of non-ideal spiral, demagnetization, impact of PM dimensions on force and scaling are analysed in detail. Due to helical PMs manufacturing process is not realistic, discrete PM blocks can be used, instead of the helical PMs.

The main goal of this thesis is to research, develop and optimise high thrust density linear actuators for active suspensions, and to construct and test a selected high force density actuator.

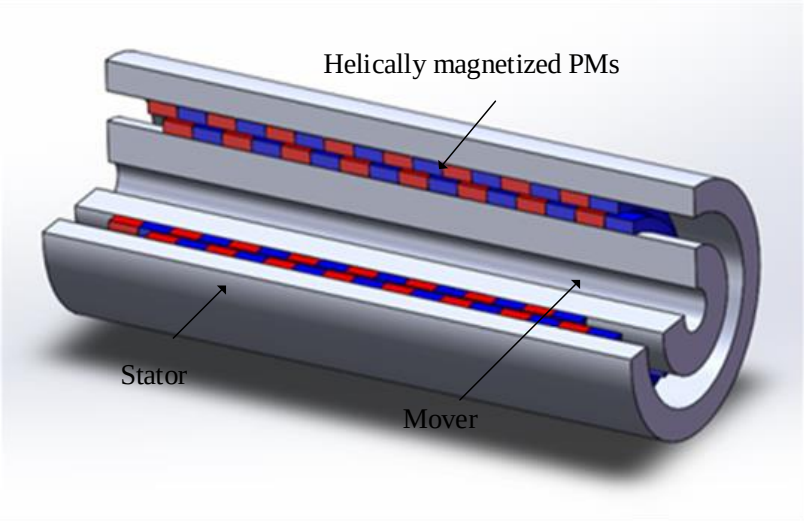

(a)

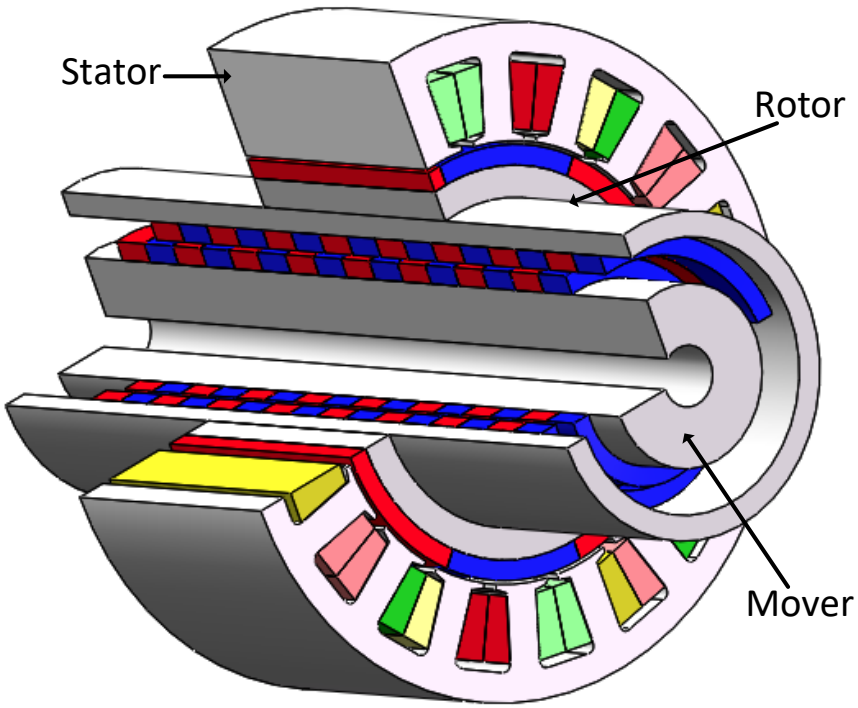

(b)

Fig. 1-9 Magnetic screw and magnetic screw with motor (a) Magnetic screw (b) Magnetic screw with motor

1.4 Outline of Thesis

The thesis is structured as follows:

Chapter 1 mainly outlines the challenges for active suspension systems and proposes candidates for high thrust force density linear actuators in such application, including a brief discussion of the current state-of-the art in this field. The outline and major contribution of this thesis are presented, and the publications to date are also listed.

Chapter 2. Following comprehensive assessment of candidate slot-pole combinations, an 18-slot 26-pole tubular PM Vernier motor and an 18-slot 28-pole tubular PM Vernier motor have been proposed and globally optimised against the target performance and constraints for an active suspension system. The demagnetization risk of the motor PMs is also analysed. The outcome is compared with conventional PM linear motor.

Chapter 3 investigates the potential of a dual-stator PM vernier linear motor. Through analysis and discussions of the advantages of the machine topology, three design variants with different pole-slot number combination are selected and their FE model established.

By incorporating the thermal model, global optimisations of the candidate machines are performed under the same set of specification and constraints. The electromagnetic performance of the optimised motors is subsequently analysed and assessed.

Chapter 4 has developed a high force density linear actuator with integrated magnetic screw. By combining a magnetic screw with a rotating PM machine, a high efficiency and high thrust force density actuator can be realised. According to the law of energy conservation, the transmission principle of the magnetic screw is explained. Further, an analytical mathematical model is established to predict the magnetic thrust force and force density. On this basis, the general design optimization process of the actuator is described. The magnetic screw part of the actuator is designed according to the design specification. Then the design optimisation of the matching rotary motor according to the output performance and geometric dimensions is subsequently carried out. The design of the actuator is further validated by 3D FE analysis.

Chapter 5 analyses the characteristics of unbalanced magnetic force (UMF) in a magnetic screw under static eccentricity. An analytical formula for UMF prediction has been derived. The UMFs have also been predicted by a full 3-D FE model of the magnetic screw and the results are compared with the analytical predictions. It is shown the UMF of a magnetic screw is much smaller than that of the tubular PM actuator of the same thrust force capability. This feature is very useful in the design of mechanical supporting structure and bearings.

Chapter 6 describes mechanical design and construction of the high force density linear actuator optimised in Chapter 4, and presents test results. All key mechanical components of the actuator including the motor housing are described in detail. For characterisation of the thrust force capability, the B-H curve of the magnets used in the prototype magnetic screw assembly are measured and accounted in the FE model. A test rig is designed and constructed. Motor torque characteristic test and mover static thrust force test have been performed on two different test rigs. The test process and test instruments are explained in detail. Test results are analysed and compared with prediction results.

Chapter 7 summarises the result and finding of the studies described in the thesis and points out the deficiencies and future research directions.

1.5 Major Contributions of Thesis

The major contributions of this thesis include two aspects. One is the development and optimisation of a number of candidate high thrust density linear actuators and comparison of their performance under the same set of specifications and constraints. The comparison of the results shows that the output thrust force density of the PM Vernier linear motor has a certain advantage compared with the conventional PM linear motor. The 12-slot, 20-pole design variant exhibits ~50% higher force capability with comparable power factor of the tubular PM machine under the same thermal condition. The double-side Vernier machine also has a linear thrust force-current characteristics up to the peak current loading. However, these advantages are obtained at the expense of the increased complexity of the stator structure and manufacturability.

The other one is the development of a high force density actuator with integrated magnetic screw and prototype construction and experimental demonstration. The test results demonstrate that the linear actuator with the integrated magnetic screw exhibits high force capability. The electromagnetic properties of the motor part and magnetic screw part of the actuator are in line with the optimized design results of the FE model. It has been shown that the friction force in the actuator mover is quite small during the test operation and the actuator can output maximum thrust force without slipping. Thus, the test results validate the machine optimization design, actuator mechanical design and test rig design.

1.6 List of Publications

Conference papers:

[C1] **Z. Liu** and J. Wang, "A High Force Density Linear Actuator for Active Suspension," 2019 12th International Symposium on Linear Drives for Industry Applications (LDIA), Neuchatel, Switzerland, 2019.

[C2] **Z. Liu** and J. Wang, "Design and testing of a high force density linear electromagnetic actuator," 2020 IEEE Energy Conversion Congress and Exposition (ECCE), Detroit, MI, USA, 2020.

[C3] **Z. Liu** and J. Wang, " Unbalanced Magnetic Pull in a Magnetic Screw," 2020 IET International Conference on Power Electronics, Machines and Drives (PEMD), 2021.

CHAPTER 2
High Force Density Tubular Linear Vernier Motor

This chapter mainly describes the development and design optimisation of a high force density tubular linear permanent magnet Vernier motor. The principle of operation of Vernier machine to achieve high thrust force density is first briefly outlined, and a selected machine topology is optimally designed against a defined set of specification. The design process includes selection of motor pole-slot combination, establishment of motor simulation model and thermal constrains, and global optimisation of leading parameters. The performance of the optimised machine is analysis and compared with an existing high force density tubular linear motor.

2.1 Introduction

Vernier permanent magnet (VPM) motor has received increasing attention in recent years. Compared with traditional PM motors, there is no essential difference in its structure. It uses the magnetic gear principle to modulate the magnetic field, instead of relying on the fundamental magnetic field, to achieve electromechanical energy conversion. A VPM motor combines the characteristics of PM motor and magnetic gear principle, so it can output high torque/force or high power density at low speed. Due to these merits, VPM motors are desirable in low-speed direct-drive applications [85].

The structure and principle of operation of a vernier motor may be understood by considering a magnetic geared motor (MGM), which may be formed by coaxially connecting a permanent magnet synchronous motor (PMSM) and a magnetic gear. The two may be independent entities, and the torque transmission principle is similar to a traditional PMSM connected to a gear box. K. Atallah and D. Howe proposed a concentric magnetic gear in 2001 [70]. This magnetic gear has a dual-rotor motor structure. The inner and outer rotors have PMs attached to the surfaces, and a stationary ferromagnetic (steel) pole-pieces is placed between the two rotors. When the outer rotor and the inner rotor run at different speeds, the stationary steel pole-pieces plays a role in modulating the magnetic field, and the PMs on both the inner and outer rotors participate in torque transmission, resulting in torque density being significantly increased. Since then, magnetic gears have derived many structures. For example, axial-flux magnetic gear [86], reluctance magnetic gear [87], cycloid magnetic gear [88], double-rotor planetary

magnetic gear [89] and a magnetic gear structure with tangential magnetized outer rotor PMs and radial magnetized inner rotor PMs [90], which are applied to many high torque density applications [70], [91]-[96]. However, since the magnetic gear in the MGM only plays the role of torque conversion and transmission, it does not generate torque by itself. Therefore, although the magnetic gear can increase the torque density of the motor, the torque density of the MGM topology may not be high compared to the motor connected to a mechanical gear box while its mechanic complexity and manufacturing cost are increased.

The name of the vernier motor can be traced back to the vernier reluctance motor proposed by C. H. Lee in 1963 [97]. It is different from ordinary reluctance motors. The stator tooth pitch of this reluctance motor is not equal to the rotor tooth pitch. A small rotor displacement can bring about a large air gap permeability change. In the process of rotor movement, the stator and rotor teeth of the motor are similar to the upper and lower scales of a vernier caliper, hence the name vernier motor. The first to apply the principle of magnetic gears to vernier motors was in 1999 when T. A. Lipo proposed a PM vernier motor consisting of 18 slots and 34 poles [71]. The topology of this motor is very similar to traditional PM motor, with a single PM rotor and a single air gap. Flux modulation is achieved by the movement of the PM rotor with respect to the stationary teeth during operations. This motor realises the magnetic gear principle with one rotor and hence one layer of air gap, which greatly simplifies the mechanical structure. Afterwards, many vernier motor structures have emerged [73-75]. The torque density of some structures that have been optimized are even 80% higher than commercial line-start PM machine [76].

In general, the principle of operation of rotating motors can be applied to linear motors albeit significant end effects in the linear motors may exist. There are many types of rotating vernier motors, and the structure of linear vernier motors is also diverse [77-78]. At present, the research on linear vernier motors is not as much as rotary vernier motors, but with the deepening understanding of the magnetic gears principle, more types of linear vernier motors will be studied and applied. Although the vernier structure can greatly increase the thrust force density of the motor, in order to generate a large gear ratio, the vernier motor mover often has more poles, which increases the inductive reactance of the motor and reduces the power factor. Therefore, the increase of thrust force density of the vernier motor is not unlimited, and motors with extremely high gear ratios often do not have practical value because of very low power factor.

This chapter develops and designs two candidate PM linear tubular fractional slot vernier motors, and compares their performance with an existing linear PM actuator for active suspension [98]. These two motors combine the advantages of PM motor, vernier motor, and tubular motor, with a simple structure, no end windings, low space harmonics, and simultaneous generation of PM thrust force and vernier thrust force. In order to make a fair comparison, the two candidate motors are optimally designed against the same specifications, volumetric and thermal constraints as those of the existing PM actuator [99]. Through the comparison of FE results, it has been shown that the tubular linear vernier motors of the two designs have certain advantages in thrust force density compared with the traditional linear motors for active suspension.

2.1.1 Magnetic Gear Principle

The principle of magnetic gears, as the name suggests, is the principle of torque or force transmission by magnetic means. This is achieved by the use of ferromagnetic pole-pieces to modulate the magnetic field of a PM rotor, so that the modulated magnetic field on one side interacts with the armature reaction field on the other side. Fig. 2-1 shows a schematic diagram of a magnetic geared motor which consists of three parts: a stator, a modulation ring and a rotor. Compared with traditional PM motors, the modulation ring is located between the stator and the PM rotor. As another rotating part of the motor, the modulation ring is composed of several modulation blocks of ferromagnetic materials uniformly distributed along the circumferential direction, which plays the role of magnetic field modulation.

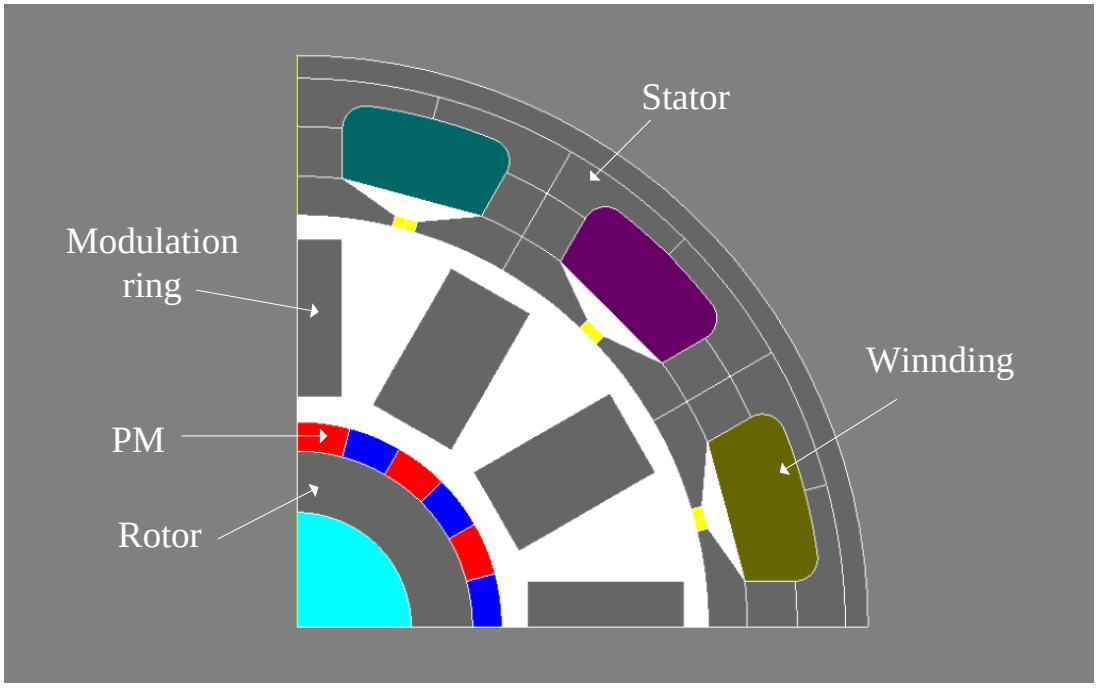

Fig. 2-1 Schematic diagram of a magnetic geared PM motor

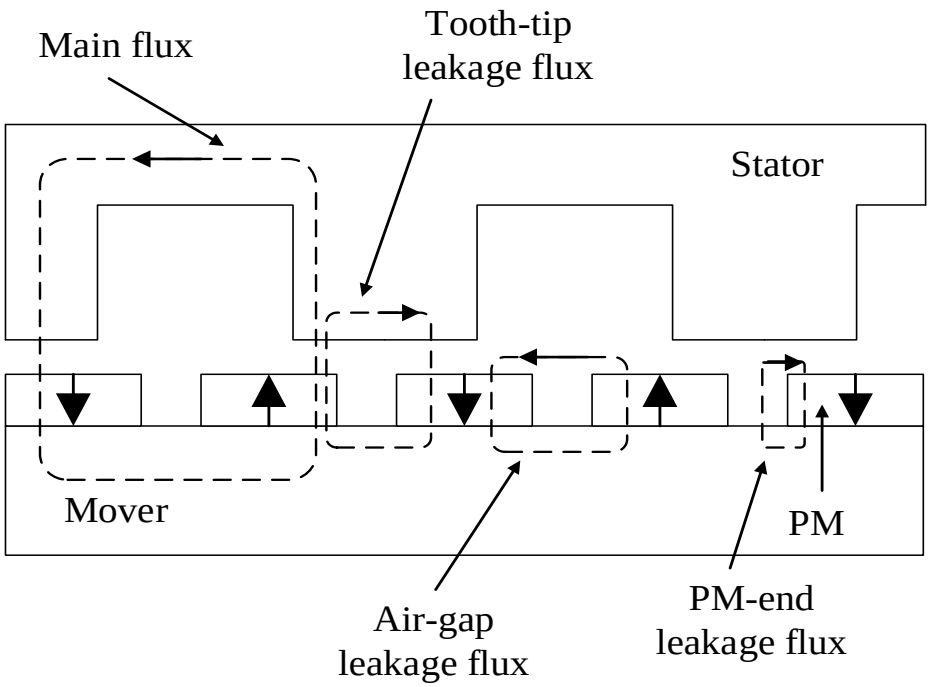

Fig. 2-2 Leakage flux of Surface-mounted PM linear vernier motor

For a vernier motor, it does not have a magnetic ring. Its function is replaced by the sloting (cogging) effect of the stator teeth, and the speed of the ferromagnetic modulating teeth is 0. The earlier version of a vernier machine uses multiple small teeth and multipole PMs for achieving high frequency modulation effect, hence high gear-ratio to exhibit high force density. However, this structure will cause serious magnetic flux leakage, especially the tooth tip leakage flux, as shown in Fig. 2-2, which lead to very low power factor [100].

Therefore, in the vernier motor, the main harmonics in the air gap are the PM harmonic of p_r pole-pairs, and the modulated harmonic of p_s pole-pairs, where $p_s = n_s - p_r$ and n_s is the number of teeth in the stator [85]. It is also possible to have $p_s = n_s + p_r$ but the design with $p_s = n_s - p_r$, yields a higher torque density. Therefore, the VPM motor studied in this chapter only considers $p_s = n_s - p_r$ unless otherwise stated.

When only the fundamental wave component is considered, the flux density of the PM field in air gap, B_{PM}, as shown in Fig. 2-3, can be expressed as:

$$B_{PM} = \frac{4}{\pi} B_{\delta} \sin\theta \qquad (2\text{-}1)$$

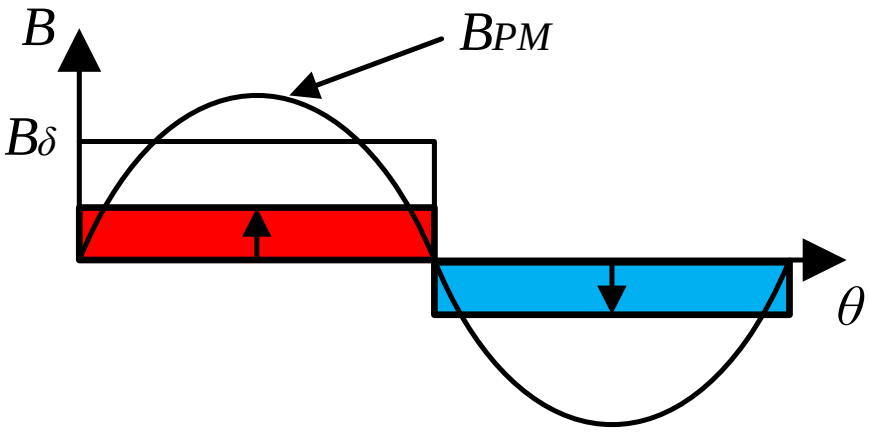

Fig. 2-3 No-load air gap PM flux density

where $B\delta$ is the amplitude of the PM flux density. Take the 18-slot 28-pole VPM motor as an example, spread it along the air gap as shown in Fig. 2-4. When the rotor rotation at a speed of n_m, the 14 pole-pair PM field is modulated by the 18 teeth, which produces the flux density wave B_{mo} of n_s - p_r = 4 pole-pairs in the air gap. This interacts with the 4-pole-pair (p_s = n_s - p_r = 4) armature reaction field of the stator winding to produce torque. The ratio of the harmonic speed of the PM flux density in air gap to that of the modulated magnetic field is the gear ratio G_r of the VPM motor:

$$G_r = -\frac{|p_r - n_s|}{p_r} = \frac{p_r - n_s}{p_r} \qquad (2\text{-}2)$$

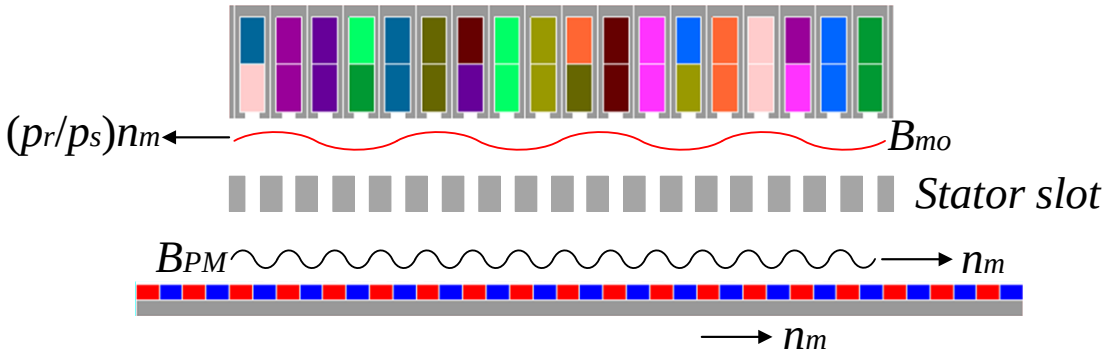

Fig. 2-4 Schematic diagram of main no-load working magnetic field of VPM linear motor

The negative sign indicates that the direction of travel of the modulated field is opposite to that of the PM rotor. When the axis of the PM coincides with the axis of phase A winding, the no-load back EMF of the phase A winding e_A is

$$e_A(t) = -\frac{d\Psi_{ph}}{dt} = k_{dp1} N_{ph} n_m D_1 l_{stk} \left(\frac{p_r}{p_s} B_{mo} + B_{PM}\right) \sin p_r n_m t \qquad (2\text{-}3)$$

where Ψ_{ph} is the flux linkage of each phase of the stator winding, D_1 is the inner diameter of the stator, l_{stk} is the length of the laminate, k_{dp1} is the fundamental winding factor of the stator winding, and N_{ph} is the number of turns in series per phase. According to (2-3), the no-load back EMF effective value E_{ph} is:

$$E_{ph} = \frac{k_{dp1} N_{ph} n_m D_1 l_{stk}}{\sqrt{2}} \left(\frac{p_r}{p_s} B_{mo} + B_{PM} \right) \quad (2\text{-}4)$$

When the three-phase VPM motor is supplied with symmetrical three-phase currents, the electromagnetic torque T_e is given by:

$$T_e = \frac{3 E_{ph} I_{ph}}{n_m} = \frac{\pi A k_{dp1} N_{ph} n_m D_1^2 l_{stk}}{2\sqrt{2}} \left(\frac{p_r}{p_s} B_{mo} + B_{PM} \right) \quad (2\text{-}5)$$

where I_{ph} is the effective value of the phase current, A is the electrical load, $A = \frac{6 N_{ph} I_{ph}}{\pi D_1}$ [101].

It can be seen from the formula (2-5) that the output torque of the VPM motor is divided into two parts, namely the PM torque and the vernier torque. Among them, the vernier torque accounts for a relatively small proportion. For the part of the vernier torque, when p_r/p_s increases, similar to an increase in gear ratio, the ratio of vernier torque will also increase. For the PM torque, although it is a dominant torque component, its output capacity is smaller than that of a traditional PM motor due to the need for a large slot openging for the modulation. Therefore, there is a trade-off in exploiting the venier torque in such PM machines.

2.1.2 High Force Density Linear PM Motor Example

In order to assess the thrust force density of the candidate tubular linear vernier motors, a reference design is defined. It is a 9-slot, 10-pole high thrust density PM tubular motor with quasi-Halbach magnetization developed for active suspension [99]. The schematic of the reference design is shown in Fig. 2-5, which will be employed for comparison in subsequent sections and chapters. For the Chapter 2 and Chapter 3, the size and output are compared, and for the Chapter 4, only the output is compared.

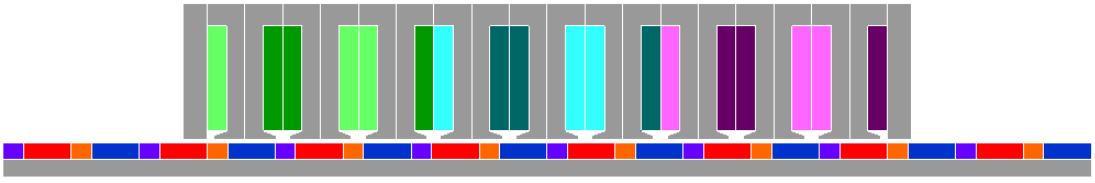

Fig. 2-5 9-slot 10-pole high thrust density PM linear tubular motor

Table 2-1 and Table 2-2 lists the main dimensions and thermal constraints, and the specification and performance indicators, respectively.

Table 2-1 Machine main dimensions and thermal constraints

Parameters	Value	Unit
Outer radius of stator	90	mm
Axial length of stator	200	mm
Remanence of magnets	1.15	T
Magnet height	6	mm
Air gap	1	mm
DC link voltage	42	V
Ambient temperature	40	^{o}C
Cooling	Air-cooled	

Table 2-2 Specification and performance indicators of 9-slot 10-pole PM tubular motor

Parameters	Value	Unit
Peak force capability	4000	N
Peak current at peak force	80.52	A
Rated speed	1.0	m/s
Rated thrust force	2000	N
Rated RMS current	57.00	A
Rated Peak current	81.00	A
Rated Force density	402	kN/m^3
Power factor	0.9	
Efficiency	0.781	

2.2 Possible Pole-slot Coordination of Linear Vernier Motor

In order to achieve the best possible thrust force density, it is first necessary to select suitable pole-slot number combinations of candidate designs. Based on the magnetic gearing principle described previously, possible pole-slot number combinations for a VPM machine can be obtained from $p_r = n_s - p_s$, where for a 3-phase machine the number of slots of the stator winding, n_s, must be an integer multiple of 3. And to achieve high thrust force density, only the VPM motors with G > 1 will be considered.

Table 2-3 listed the possible pole-slot number combinations of a VPM motor up to n_s = 24, where the number against a given n_s and p_s combination represents the number of PM pole-pairs over the n_s number of stator teeth. Only the combinations with G = $|p_s/p_r|$ <1 is shown. In assessing these options, the following considerations are given. First of all, because the main size of the motor must be consistent with the existing active suspension linear motor, too many or too few slots will weaken both the electromagnetic

and mechanical performances. Although a high gear ratio, such as p_s =1, p_r = 11, 14, 17, 20, …, etc., is conducive to a large Vernier torque, the PM torque will be compromised due to the low number of pole-pairs of the stator winding. In addition, as mentioned above, excessively high gear ratio will result in extremely low power factor which would increase the VA rating of the power electronic converter. The reference design has 9 slots and 10 poles, but its Vernier torque is negligible because the gear ratio is less than one and the modulation effect is small with the semi-closed stator teeth. Considering that too high gear ratio will bring very low power factor, the pole-slot number combinations of the PM vernier motor to be further studied in this chapter are 18 slots, 28 poles and 18 slots, 26 poles, as listed in Table 2-4, where the corresponding gear ratios are also given. Both options have a similar p_s to the reference design so that the PM torque contribution will be kept high while the gear ratio for the Vernier torque is 0.57 and 0.38, respectively.

Fig. 2-6 shows the schematic of the 18-slot, 26-pole VPM motor, where semi-closed teeth are illustrated for generality. Indeed, the slot opening will be a design parameter. The 18-slot, 28-pole VPM motor has the same winding distribution as the 18-slot, 26-pole option, shown in Fig. 2-6. Their armature reaction MMF waveforms and spectra are shown in Fig. 2-7. For the 28-pole machine, all odd space harmonics have been eliminated. And there are only 2nd, 14th, 22th, …harmonic orders. This is conducive to reduction of core loss and magnetic loss. And for the 26-pole machine, all even space harmonics have been eliminated.

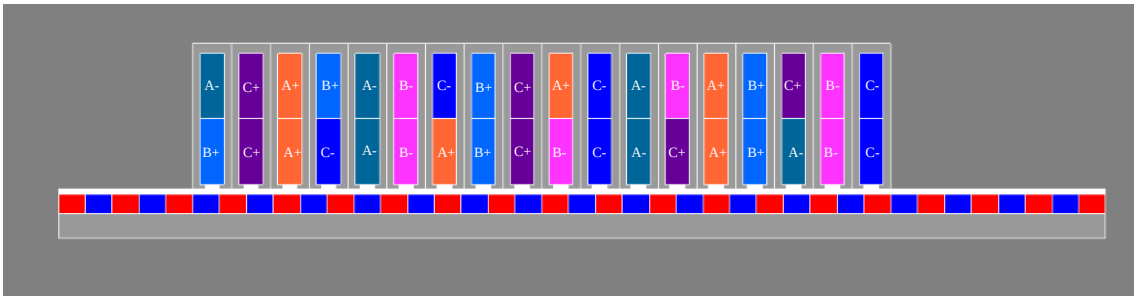

Fig. 2-6 18-slot 26-pole VPM motor winding distribution

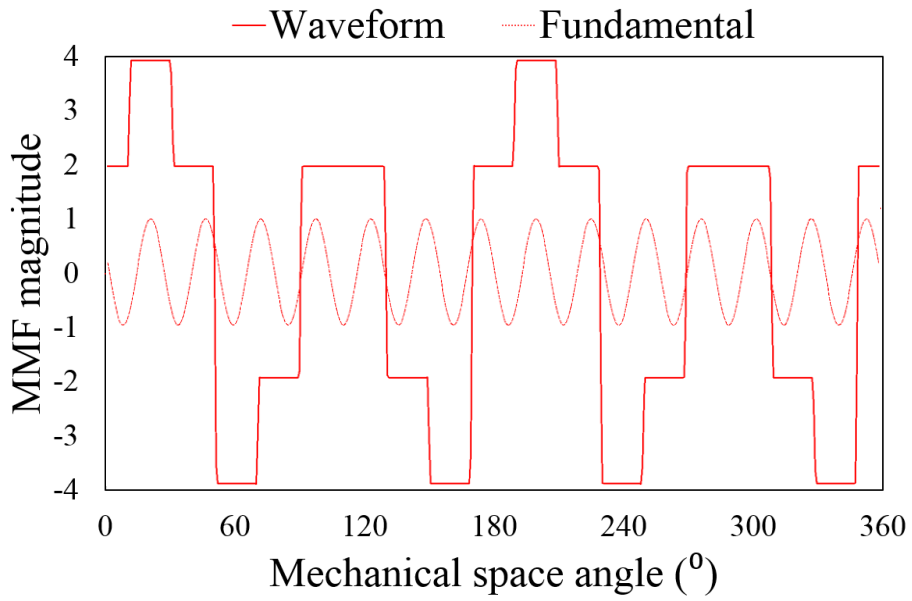
Waveform
Fundamental
MMF magnitude
4
3
2
1
0
-1
-2
-3
-4
0
60
120
180
240
300
360
Mechanical space angle (°)

(a)

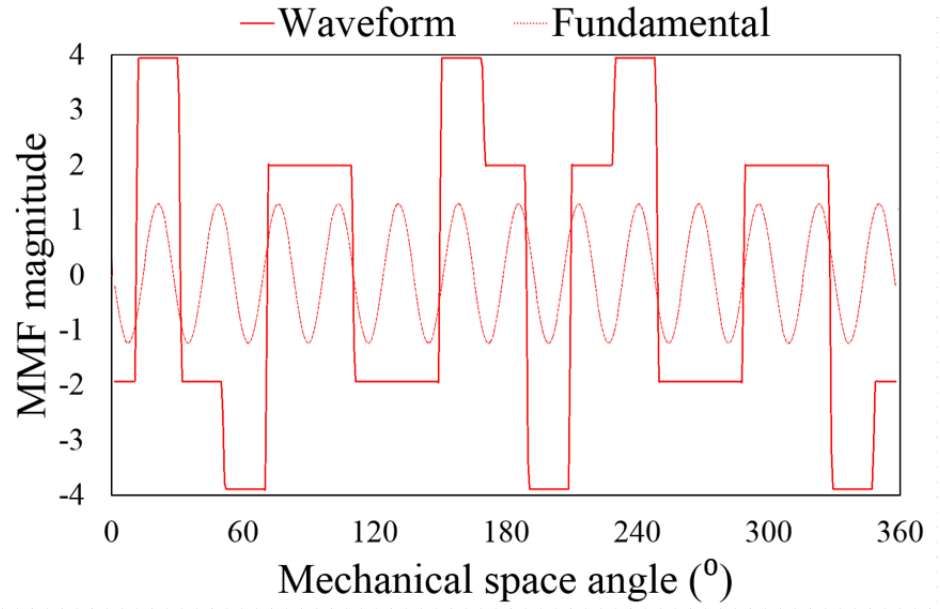
Waveform
Fundamental
MMF magnitude
4
3
2
1
0
-1
-2
-3
-4
0
60
120
180
240
300
360
Mechanical space angle (°)

(b)

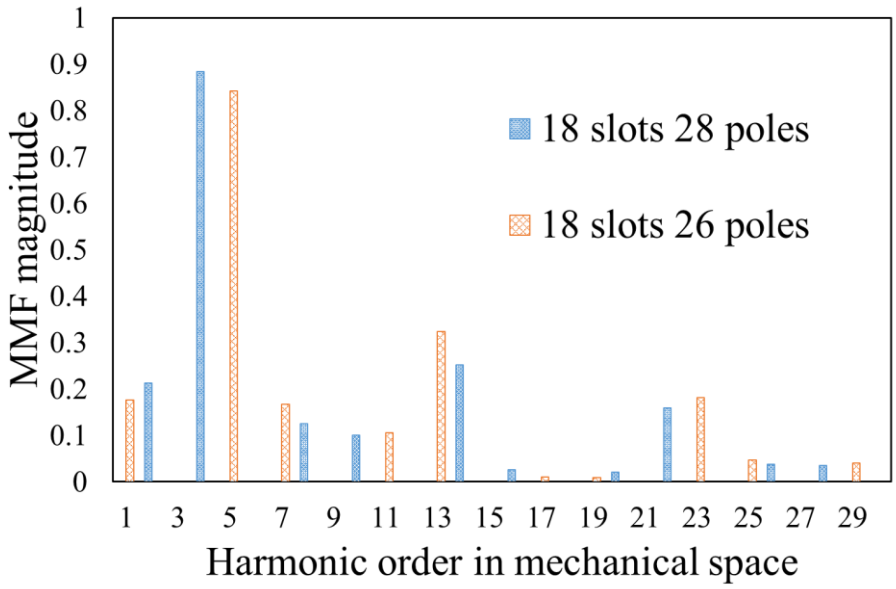

(c)

Fig. 2-7 MMF waveforms and spectra of candidates (a) 18 slots 28 poles (b) 18 slots 26 poles (c) Spectra

Table 2-3 Possible pole-slot number combinations of the VPM motor

	Number of pole-pairs of stator winding p_s										
Number of slot n_s	1	2	3	4	5	6	7	8	9	10	11
6	5	4									
9	8	7	6	5							
12	11	10		8	7						
15	14	13		11	10		8				
18	17	16	15	14	13	12	11	10			
21	20	19		17	16		14	13			
24	23	22		20	19		17	16		14	13
…											

Table 2-4 Gear Ratios in motor Candidates

n_s	p_r	p_s	G_r
18	14	4	-4/7
18	13	5	-5/13

With the 18-slot, 14-pole-pair design, the stator MMF harmonics that contribute to the torque production are of 4th and 14th orders while those of the 18-slot, 13-pole-pair variant are of 5th and 13th orders, as shown in Fig. 2-6 (c).

2.3 Finite Element Model of Tubular Linear Vernier Motor

After selecting the candidate pole-slot number combinations of the motor, the next step is to model, simulate and optimize the designs. In order to make a fair comparison of the candidate PM vernier tubular motors, the main dimensional parameters of the design variants, including the length of the stator, outer radius of the stator, air gap length and PM thickness are all kept the same. The performance of the candidate designs will be compared at the rated speed as 1 m/s with the same permanent magnet material grade N35M whose remanent flux density Br is 1.15T and relative recoil permeability is 1.05. Since the main dimensions of the candidate designs and the reference motor are the same, their heat dissipation area is the same. Therefore, in order to perform a fair comparison, the copper loss of the candidate designs is kept to the same value of 302W as that of the reference design. Although the machines under considerations have different core loss and magnet loss, these are relatively small and hence their influence is neglected.

The modelling, performance prediction and optimisation of the candidate PM vernier linear motors are performed by using an FE-based software, FLUX, from Altair together with the optimisation tool HyperStudy also from Altair. HyperStudy software can simulate the FE model in FLUX by entering the python program for global optimization. The optimisation process obtains the optimal parameters of the target under the condition of guaranteeing constraints through genetic algorithm. A flowchart of the optimisation process is illustrated in Fig. 2-8.

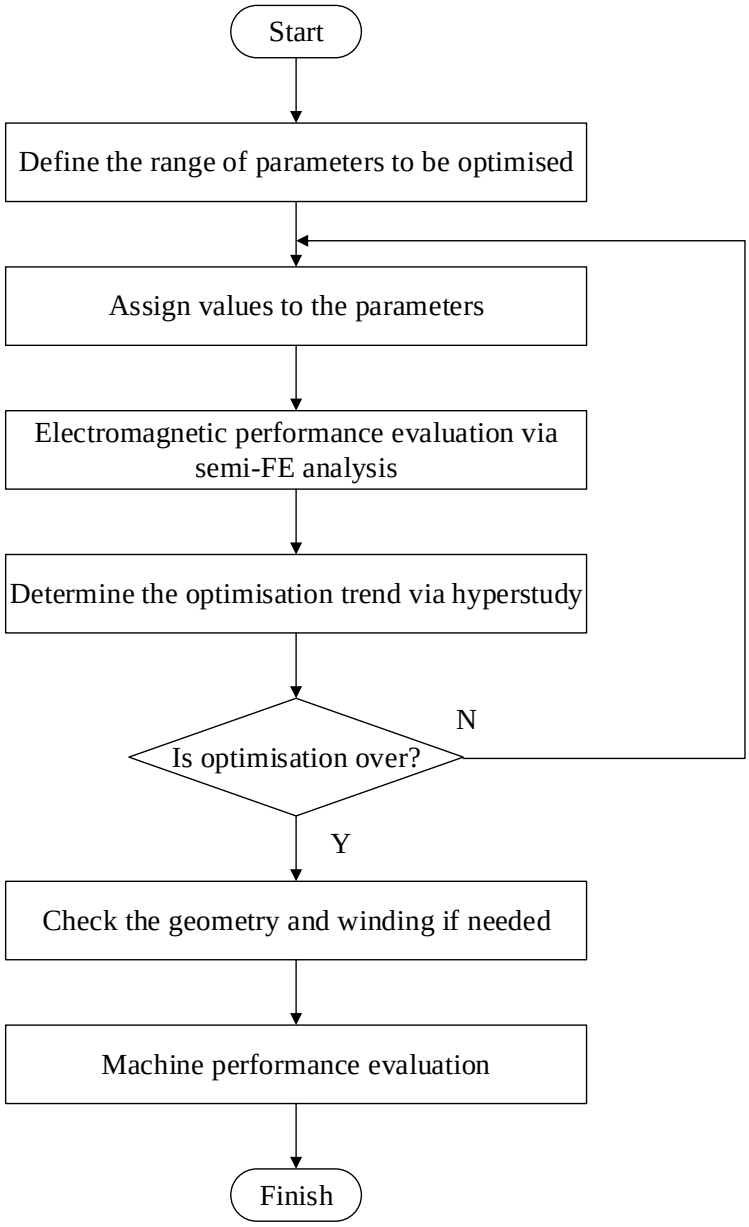

Fig. 2-8 Flowchart of the optimisation process

2.3.1 Leading Design Parameters

The leading design parameters to be optimised are shown in Fig. 2-9. Because the axial length and outer radius of the stator, the air gap length and the PM thickness are all kept the same as those of the reference design, they will not change in a optimization process. For a given candidate design, the pole-slot number combination, and the number of pole-pairs of the stator winding are also fixed while the pole pitch of the magnets and slot pitch are also determined. The six design parameters, including stator back iron thickness B_i, stator teeth width T_W, teeth tips width T_{TW}, teeth tips height T_{TH} and mover radius R_m, will be optimised. It is well known that the ratio of the outer stator radius to the mover radius, referred to as split ratio, has a significant influence on performance.

Since the outer radius of the motor is determined and fixed, the mover radius R_m directly determines the split ratio. When the split ratio of the motor is determined, the stator back iron thickness B_i and stator teeth width T_W determine the slot area and the magnetic saturation level, which are also important parameters that affect the motor performance. The teeth tips width T_{TW} and teeth tips height T_{TH} affect the air gap magnetic field and magnetic modulation, which influence the trade-off between the PM torque and Vernier torque.

When the slot area changes in the optimisation, and the current density and effective copper area will be adjusted accordingly to maintain the same copper loss of the reference design in the rated operation condition.

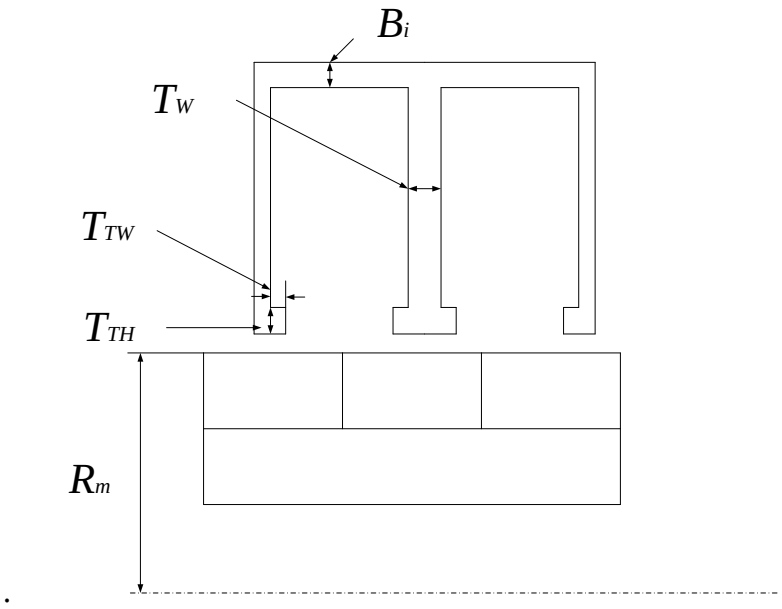

Fig. 2-9 Leading design parameters of PM vernier linear motor

2.3.2 18-slot, 28-pole Motor Optimisation

The motor uses distributed windings, and adopts T-shaped tooth structure. The magnets are radially magnetized and mounted on the mover surface. And for this optimisation the average force is the objective function.

The ranges of the leading parameters to be optimised in the 18-slot 28-pole PM Vernier are illustrated in Table 2-5. The optimisation trends of the leading design parameters are shown in Fig. 2-10 (a)~(e), and the optimisation objective, viz., the output force, is shown in Fig. 2-10 (f). The whole process was completed by 24 iterations. It can be seen that as the motor design parameters approach the optimal solution, the output thrust force of the motor continues to increase and reaches the maximum of 2113N. In

general, the variations of R_m, B_i and T_w during the optimisation represent a process to reach an optimal balance between the electric and magnetic loadings for the maximum thrust force under the thermal constraint, while the changes in T_{TW} and T_{TH} manifest the optimal trade-off between the PM and Vernier forces. The optimised geometry of the 18-slot 28-pole PM vernier linear motor is shown in Fig. 2-11 and the optimisation results are listed in Table 2-6.

Table 2-5 Parameter Ranges for the Optimisation of 18-slot 28-pole PM Vernier Linear Machine

Parameters	Description	Unit	Range
R_m	Mover radius	mm	56-62
B_i	Stator back iron thickness	mm	2.7-3.7
T_W	Stator teeth width	mm	2.8-3.6
T_{TW}	Teeth tips width	mm	1.9-2.8
T_{TH}	Teeth tips height	mm	1.9-2.7

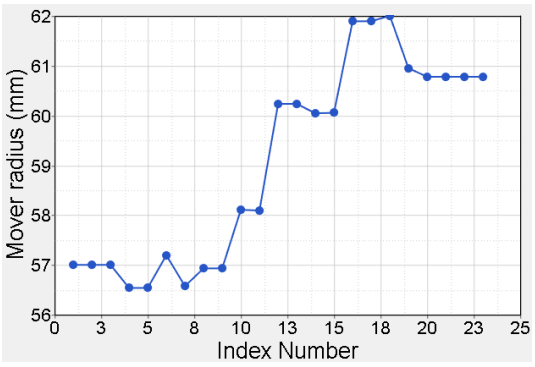

(a)

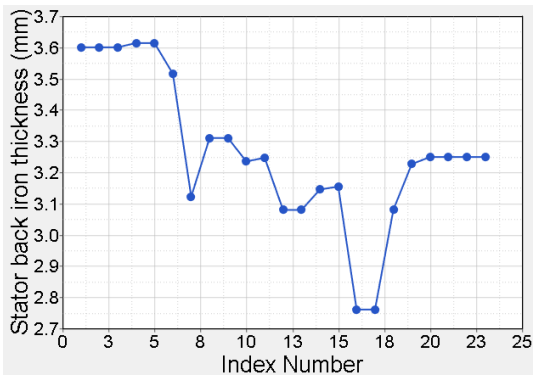

(b)

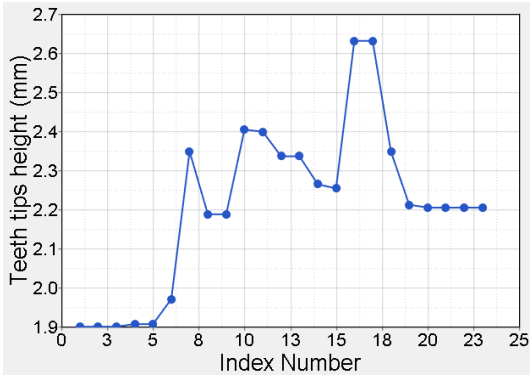

(c)

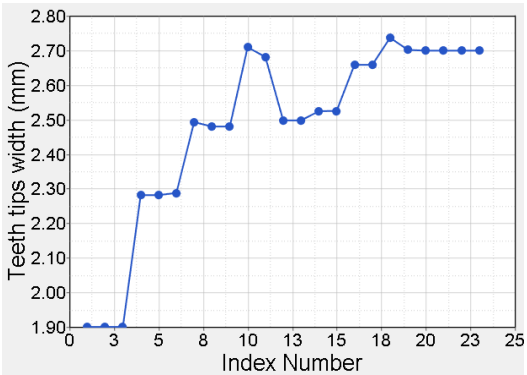

(d)

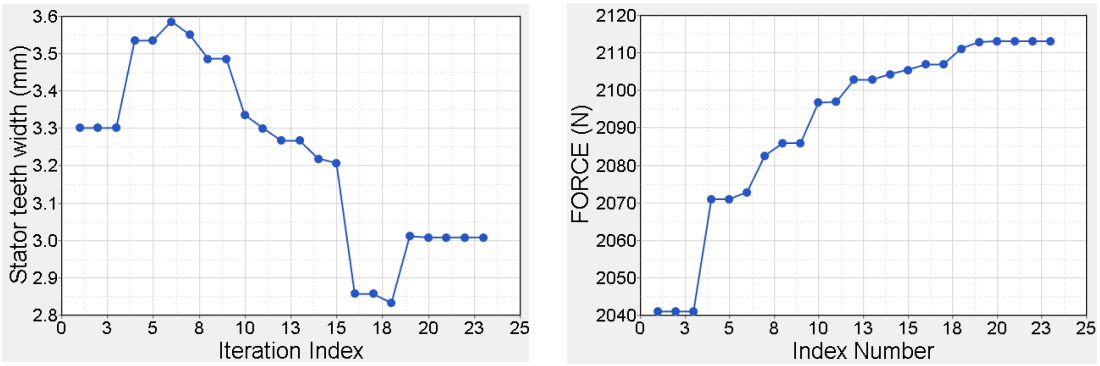

(e) (f)

Fig. 2-10 Optimisation trends of variables and objective (a) Mover radius (b) Stator back iron thickness (c) Tooth tip height (d) Tooth tip width (e) Stator tooth width (f) Output force

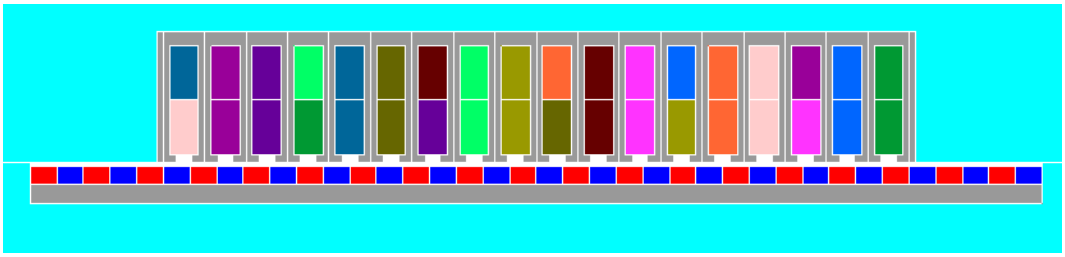

Fig. 2-11 Optimised geometry of 18-slot 28-pole PM vernier linear motor

Table 2-6 Optimised Parameters of 18-slot 28-pole PM Vernier Linear Machine

Parameters	Description	Unit	Value
R_m	Mover radius	mm	60.7
B_i	Stator back iron thickness	mm	3.25
T_W	Stator teeth width	mm	3
T_{TW}	Teeth tips width	mm	2.7
T_{TH}	Teeth tips height	mm	2.2

2.3.3 18 slot, 26-pole Motor Optimization

The ranges of the leading parameters to be optimised are illustrated in Table 2-7. The optimisation trends of the leading design parameters are shown in Fig. 2-12 (a)~(e), and the optimisation objective, the output force, is shown in Fig. 2-12 (f). The optimised geometry of the 18-slot, 26-pole PM vernier motor is shown in Fig. 2-13 and the optimisation results is listed in Table 2-8.

Table 2-7 Parameter Ranges for the Optimisation of 18-slot 26-pole PM Vernier Linear Machine

Parameters	Description	Unit	Range
R_m	Mover radius	mm	60-64.5
B_i	Stator back iron thickness	mm	2.3-3
T_W	Stator teeth width	mm	2.6-3.8
T_{TW}	Teeth tips width	mm	1.7-2.5

Parameters	Description	Unit	Range
T_{TH}	Teeth tips height	mm	1-2.2

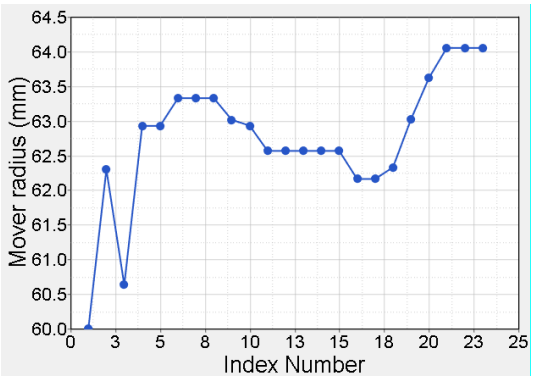

(a)

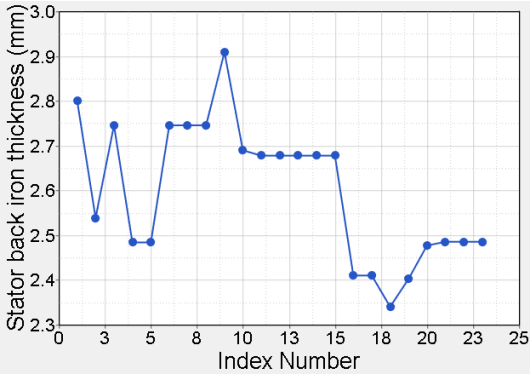

(b)

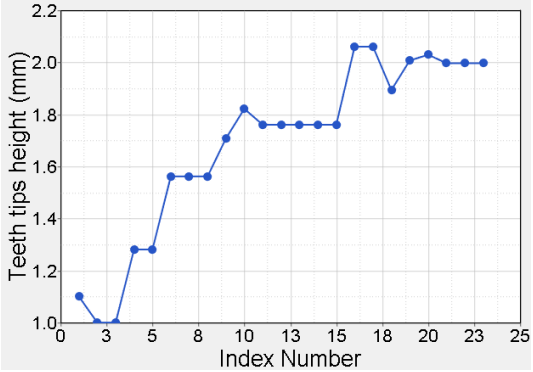

(c)

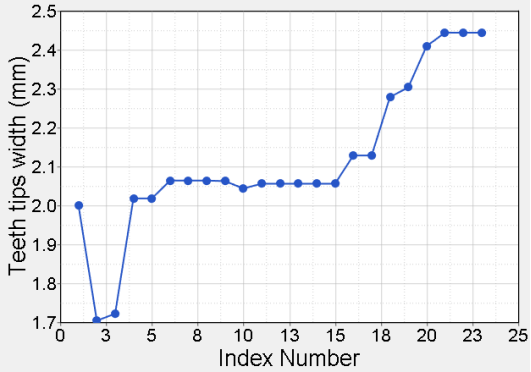

(d)

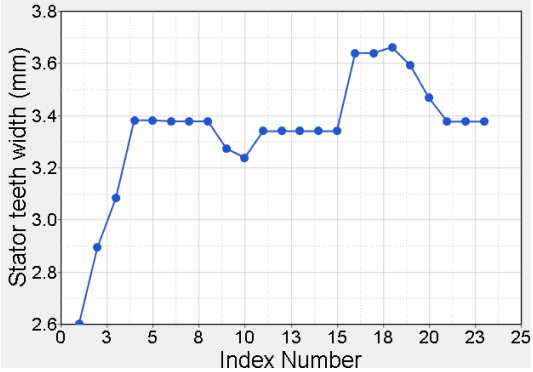

(e)

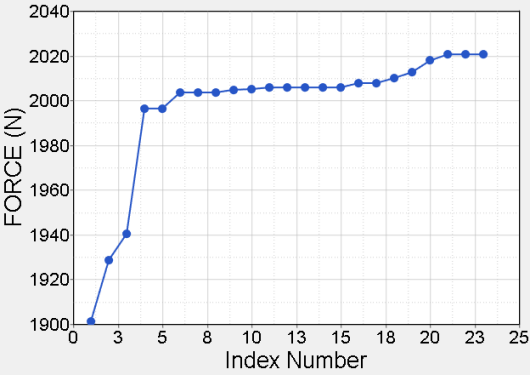

(f)

Fig. 2-12 Optimisation trends of variables and objective (a) Mover radius (b) Stator back iron thickness (c) Tooth tip height (d) Tooth tip width (e) Stator tooth width (f) Output force

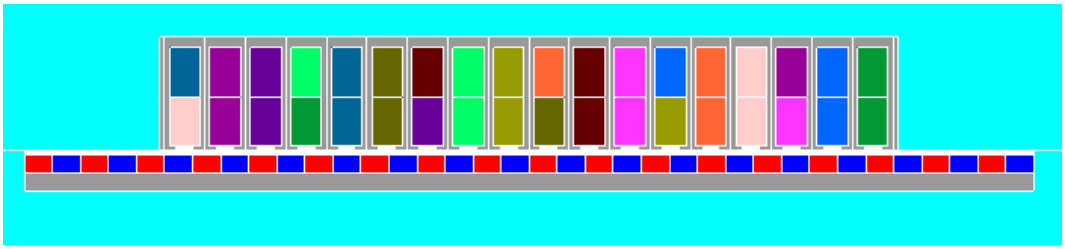

Fig. 2-13 Optimised geometry of 18-slot 26-pole PM vernier linear motor

Table 2-8 Optimised Parameters of 18-slot 26-pole PM Vernier Linear Machine

Parameters	Description	Unit	Value
R_m	Mover radius	mm	64
B_i	Stator back iron thickness	mm	2.5
T_W	Stator teeth width	mm	3.4
T_{TW}	Teeth tips width	mm	2.45
T_{TH}	Teeth tips height	mm	2

2.4 Performance Evaluation

2.4.1 Electromagnetic Performance

The phase back-EMF waveforms of 18-slot, 26-pole motor and 18-slot, 28-pole motor at the rated speed 1m/s are illustrated in Fig. 2-14. It can be seen that the waveforms of both the motors are sinusoidal, but high order harmonics are also visible, particularly in the 18-slot, 26-pole motor. These are caused by slotting and end effect of the stator, and will give rise to thrust force ripple in the motor. The back-EMF harmonic components of two motors are shown in Fig. 2-15. The back EMF of the 18-slot 26-pole motor contains a noticeable 3^{th} order harmonic while in the 18-slot, 28-pole motor, 27^{th} order and 29^{th} order harmonics are visible in the phase back-EMF. Although there is no constraints on phase back-EMF harmonics during the global optimisation, it can be seen that the motor back EMFs are not distorted in any significant manner.

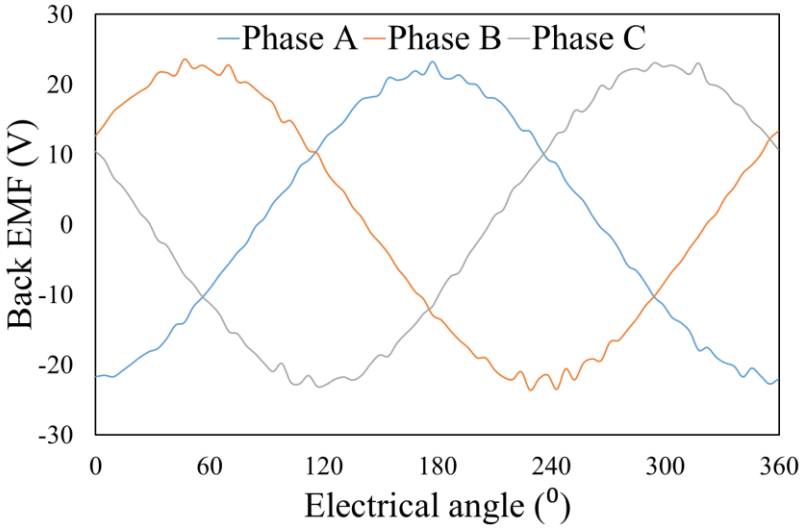

(a)

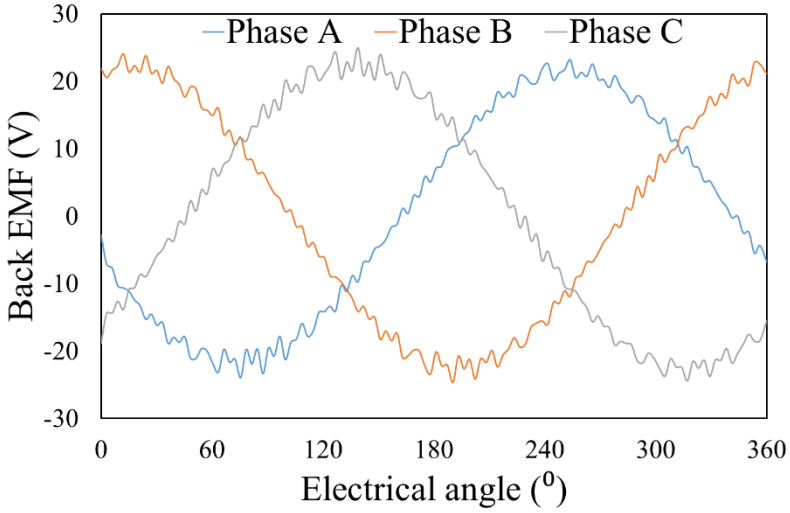

(b)

Fig. 2-14 FE-predicted phase back-EMF waveforms (a) 18-slot 26-pole motor (b) 18-slot 28-pole motor

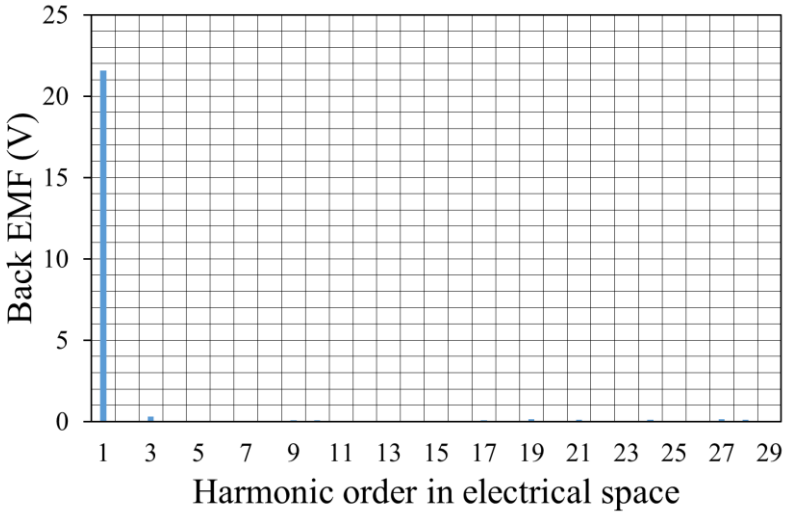

(a)

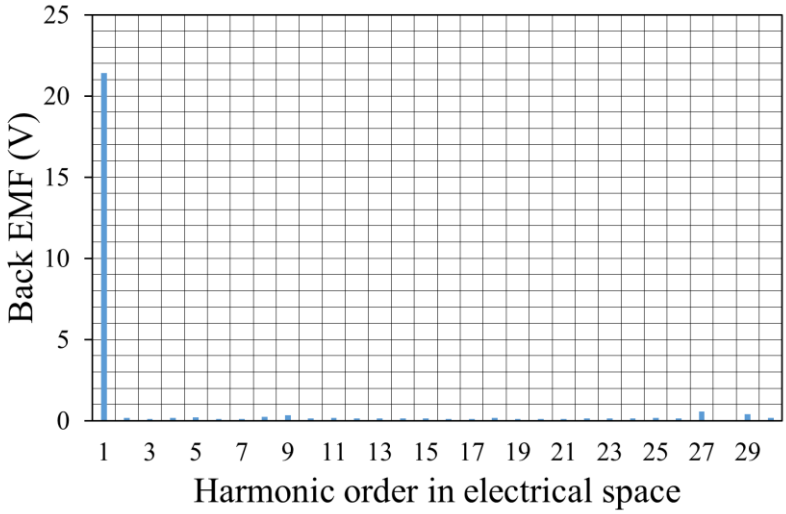

(b)

Fig. 2-15 Back-EMF harmonic component (a) 18-slot 26-pole motor (b) 18-slot 28-pole motor

The FE-predicted force waveforms of the two motors under the rated condition are illustrated in Fig. 2-16. The average forces of the 18-slot 26-pole motor is 2072N and that of the 18-slot 28-pole motor is 2113N. The force ripple of the former is 10% and the force ripple of the latter is 6%. The dominant force harmonic of the two motors is 2^{nd}, 4^{th} and 6^{th} orders, which can be observed in Fig. 2-17. This is because of the combine effects of the stator tooth cogging, and end effect cogging and the back-EMF harmonics. Studies have shown that tooth-effect cogging force is inversely proportional to the least common multiple (LCM) of the number of stator slots and the number of PM poles [102]. When the gear is relatively large, the parameter LCM of the VPM motor is also larger, leading to smaller tooth-effect cogging force. However, for the linear machines under study, the effect of cogging force, which manifests in the form of 2^{nd}, 4^{th} and 6^{th} harmonics is more significant. They can be minimised by a slight increase in the tooth width at both ends [103].

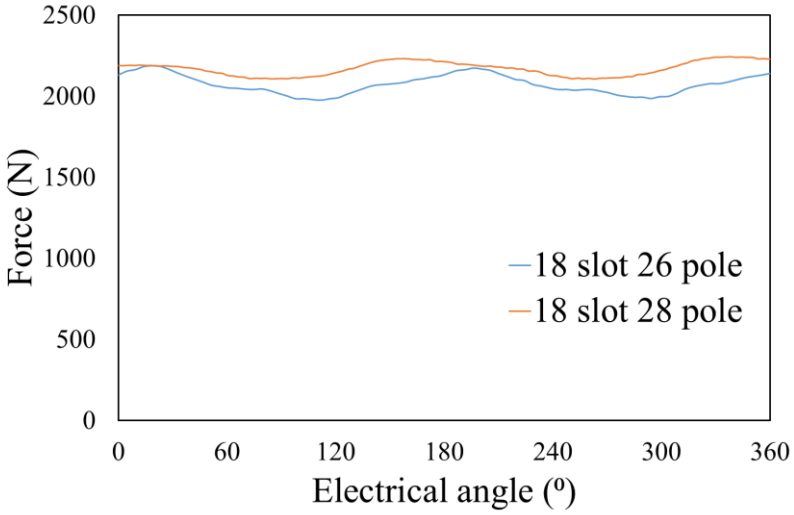

Fig. 2-16 FE-predicted rated torque waveform

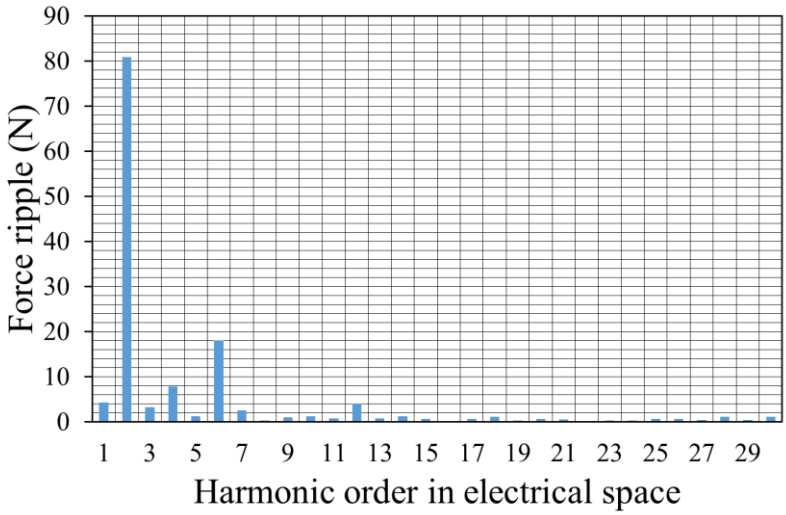

(a)

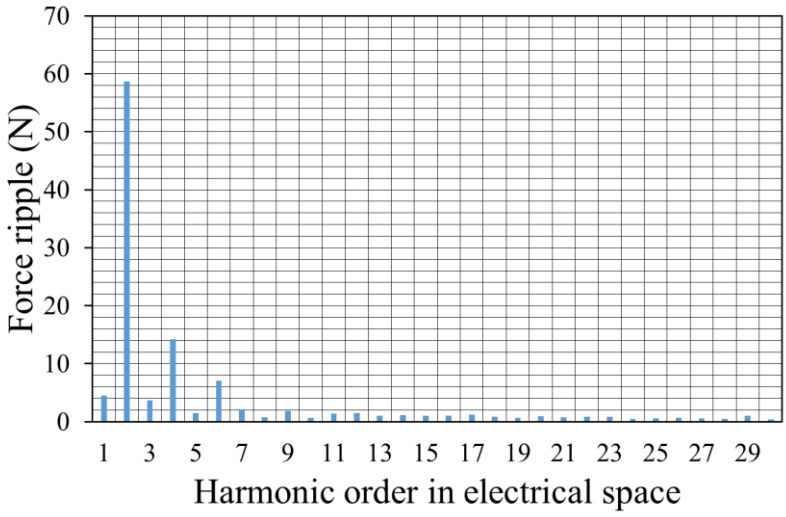

(b)

Fig. 2-17 Force ripple spectrum (a) 18-slot 26-pole motor (b) 18-slot 28-pole motor

Fig. 2-18 shows the variations of the thrust forces when the rms phase current increases from the rated to the maximum of twice the rated. It can be seen that the thrust forces of the two motor are not linearly proportional to the current. The ratio of the maximum thrust force to the rated thrust force of the 18-slot 26-pole motor is 1.6 and that of the18-slot 28-pole motor is 1.7. This is due to the fact that the 18-slot 26-pole motor is heavily saturated at the peak current, as shown in Fig. 2-19 and Fig. 2-20. Fig. 2-19 (a) shows the flux density of the 18-slot 26-pole motor at the rated current where the flux density at point A (stator back-iron) is 1.2T and the flux density at point B (tooth tip) is 2.3T. In contrast, Fig. 2-19 (b) shows the flux density of the machine at the peak current where the flux density at point A is 1.7T and the flux density at point B is 2.6T. Similar comparisons are shown in Fig. 2-20 for the 18-slot 28-pole motor at the rated and peak currents. At the rated current, the flux densities at points A (stator back-iron) and B (tooth tip) are 1.2T and 1.8T, respectively, while those at the peak current are 1.7T and 2.1T. It can be seen that the tooth tips of the18-slot 26-pole motor are more heavily saturated, which results in a slightly lower peak thrust force.

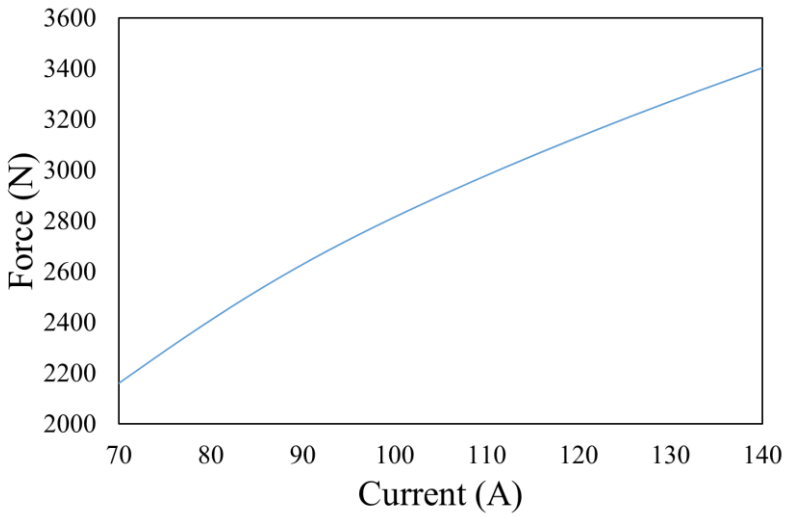

(a)

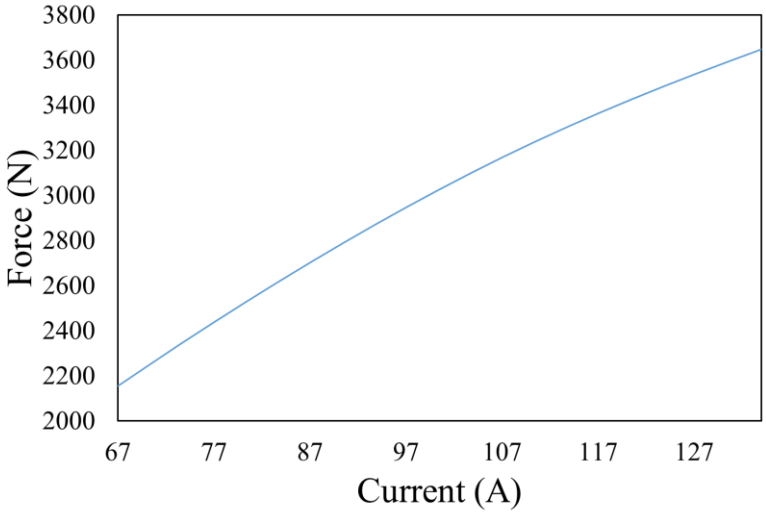

(b)

Fig. 2-18 Variations of thrust force with rms current (a) 18-slot 26-pole motor (b) 18-slot 28-pole motor

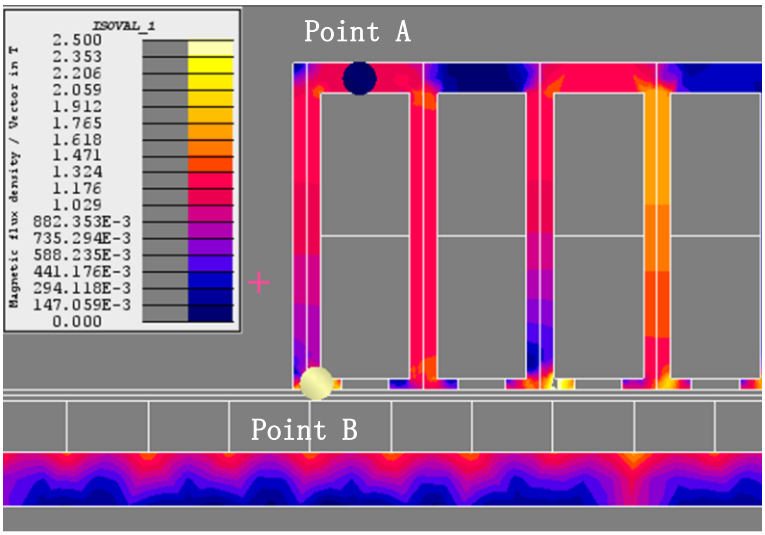

(a)

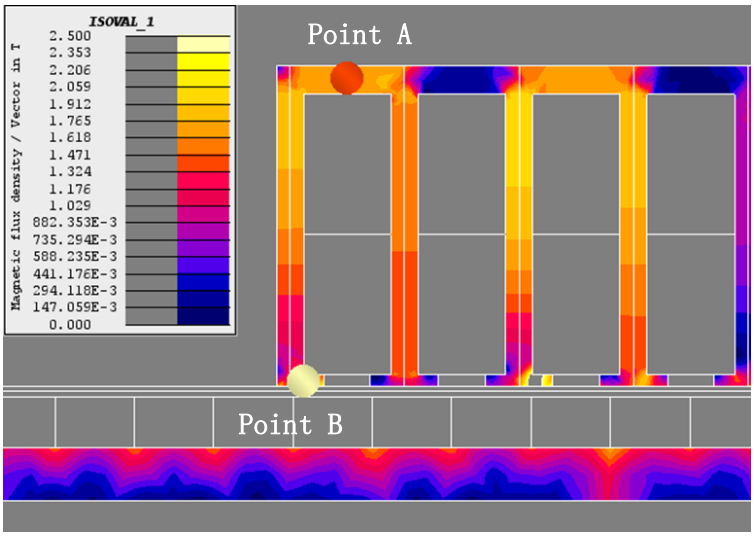

(b)

Fig. 2-19 Flux density of 18-slot 26-pole PM vernier linear motor (a) at rated current (b) at peak current

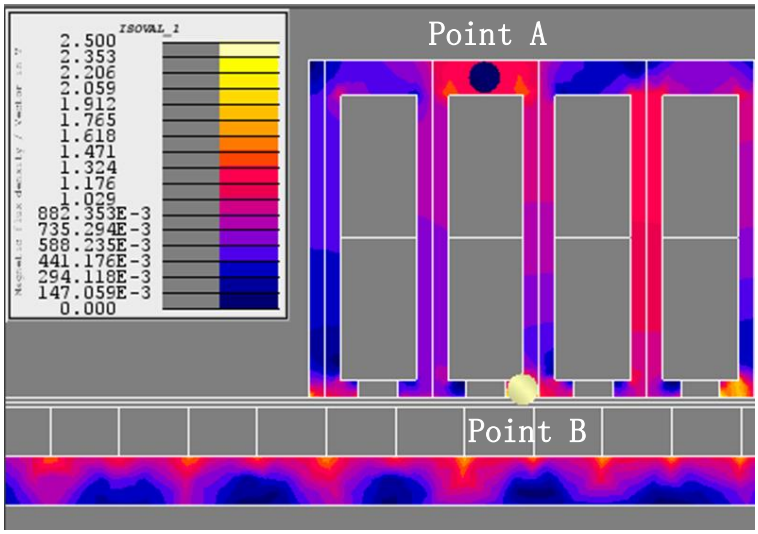

(a)

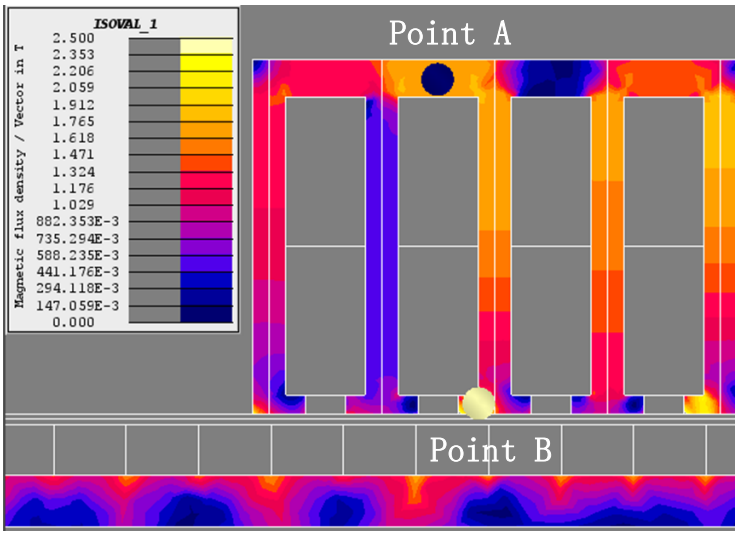

Fig. 2-20 Flux density of 18-slot 28-pole PM vernier linear motor (a) at rated current (b) at peak current

2.4.2 Demagnetization Analysis

Due to the high temperature of the vechicle itself, the PM vernier motors have more PM pole pairs and have to work in harsh environments, it is necessary to analyze the demagnetization risk of the motor magnets. Fig. 2-21 shows the N35M magnets demagnetization curve (Arnold Magnetic Technologies Corp 2016). In order to obtain the demagnetization knee point, it is necessary to first obtain the temperature of the motor magnets in the rated working state.

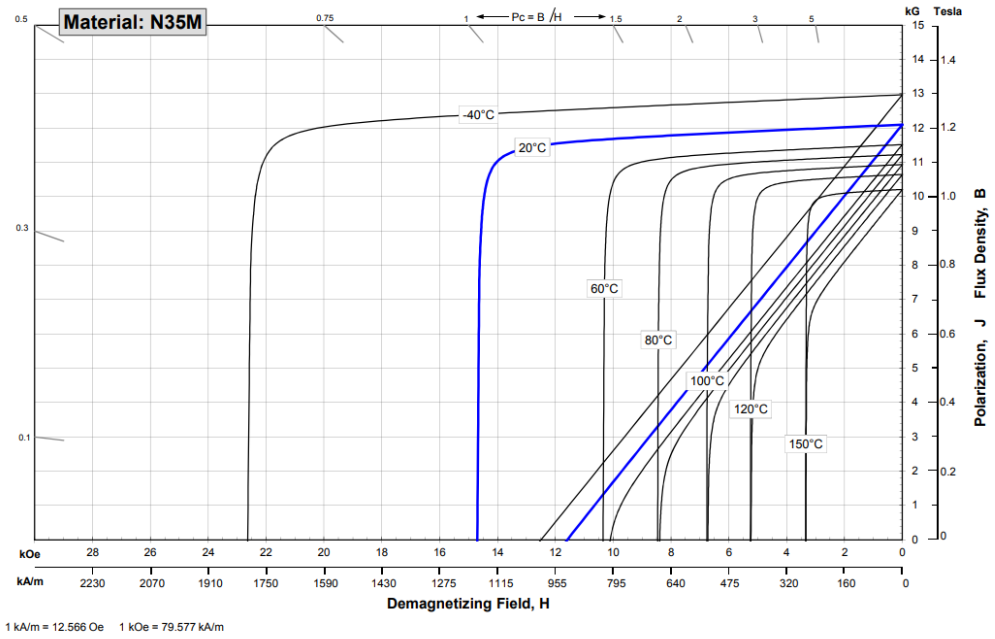

Fig. 2-21 N35M magnets demagnetization curve

Since the tubular linear motor has a symmetrical structure, only one radial cross section needs to be studied for the thermal distribution in the motor. Assuming that the motor only dissipates heat through its outer surface [22], the thermal network is shown in Fig. 2-22, where half a tooth pitch is modelled. P_{Cu} is the copper loss of the motor and P_{Fe} is the iron loss of the motor, the specific thermal resistances in the figure are given by:

$$R_{F1} = \frac{T_w}{4K_{Fe}\pi(R_h^2 - R_{ic}^2)}$$

$$R_{F2} = \frac{\ln(R_h/R_{cc})}{\pi K_{Fe} T_s}$$

$$R_{F3} = \frac{\ln(R_e/R_h)}{\pi K_{Fe} T_s}$$

$$R_{S1} = \frac{\delta_s}{K_{line}\pi(R_h^2 - R_{ic}^2)} \quad (2\text{-}6)$$

$$R_{S2} = \frac{\delta_s}{K_{line}\pi S_w R_h}$$

$$R_{W1} = \frac{S_w}{4K_{Fe}\pi(R_h^2 - R_{ic}^2)}$$

$$R_{W2} = \frac{\ln(R_h/R_{cc})}{\pi K_w S_w}$$

$$R_{S3} = \frac{R_S - R_m}{K_g \pi (T_s - S_o) R_s}$$

$$R_{S4} = \frac{R_{ic} - R_m}{K_g \pi S_o R_{ic}}$$

The motor geometric parameters required in (2-6) are shown in Fig. 2-23. K_w is the equivalent thermal conductivity of stator winding, K_{line} is the thermal conductivity of the slot line, K_g is the thermal conductivity of air gap, K_{Fe} is equivalent thermal conductivity of the stator core and δ_s is the slot line thickness. The thermal resistance representing the heat convection on the stator surface can be expressed as

$$R_C = 1/(\pi T_s R_e h_c) \quad (2\text{-}7)$$

where h_c is the thermal convection coefficient at the ambient temperature. Fig. 2-22 can be simplified to Fig. 2-23 for evaluating the temperature distribution. Where T_A is the ambient temperature point.

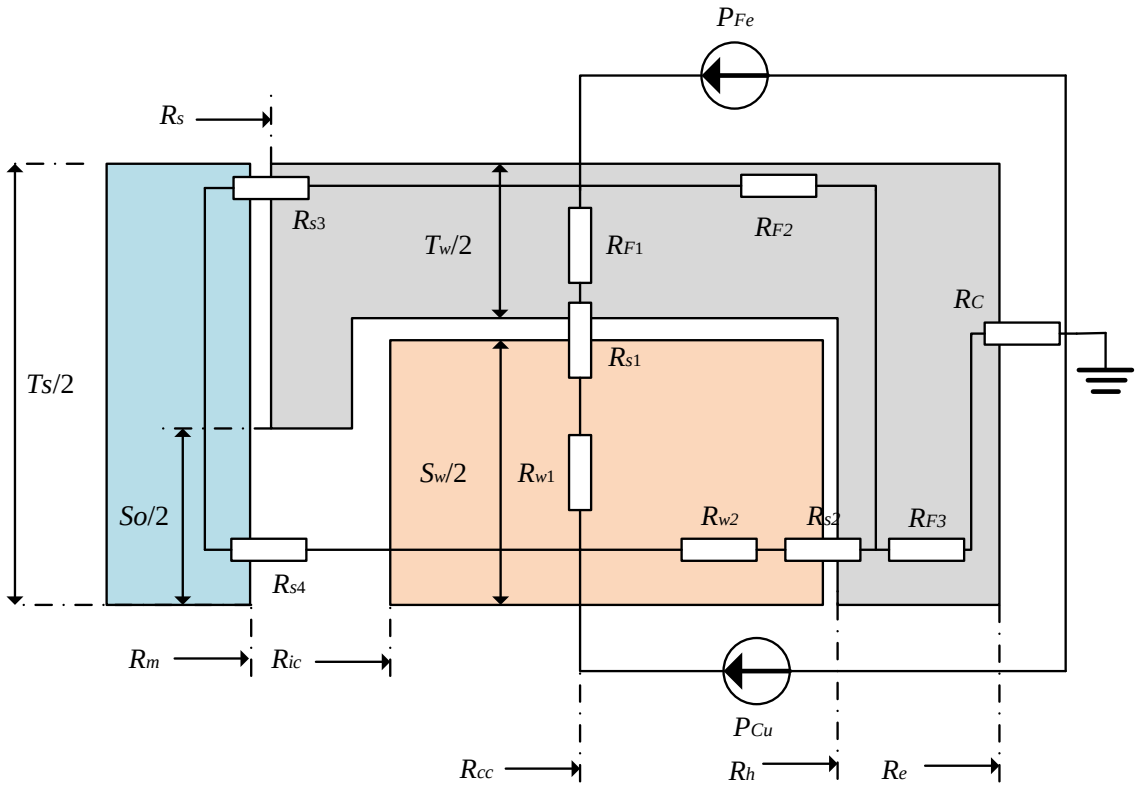

Fig. 2-22 Schematic of thermal model for tubular vernier PM motor

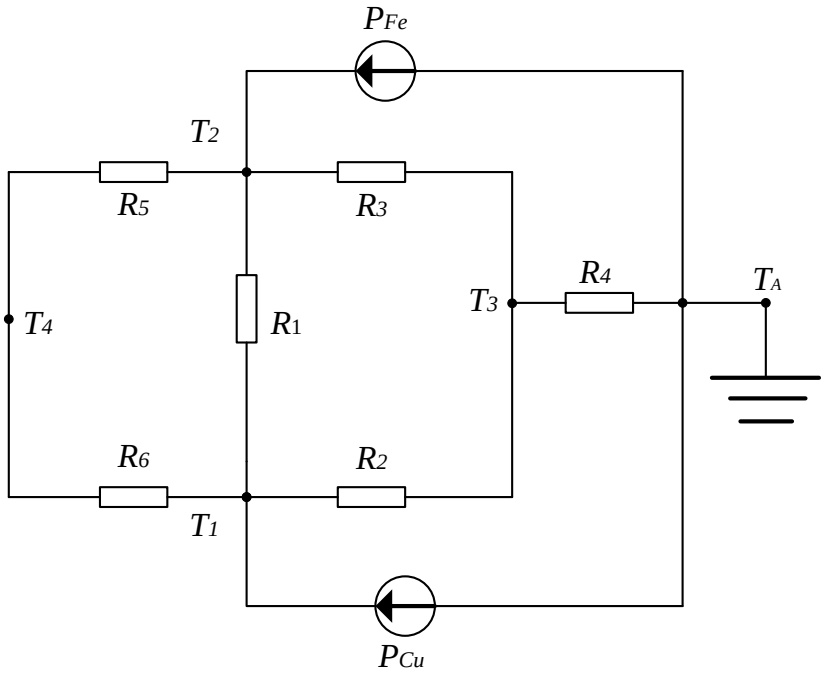

Fig. 2-23 Simplified thermal model

where

$$R_1 = R_{F1} + R_{S1} + R_{W1}$$

$$R_2 = R_{W2} + R_{S2}$$

$$R_3 = R_{F2}$$

$$R_4 = R_{F3} + R_C$$

$$R_5 = R_{S3}$$

$$R_6 = R_{S3}$$

Thus the temperature rises in the coil center T_1, the stator tooth T_2, back iron T_3 and the magnets T_4 can be predicted by

$$\begin{bmatrix} T_1 \\ T_2 \\ T_3 \\ T_4 \end{bmatrix} = \begin{bmatrix} G_1 + G_2 + G_6 & -G_1 & -G_2 & -G_6 \\ -G_1 & G_1 + G_3 + G_5 & -G_3 & -G_5 \\ -G_2 & -G_3 & G_2 + G_3 + G_4 & 0 \\ -G_6 & -G_5 & 0 & G_6 + G_5 \end{bmatrix}^{-1} \begin{bmatrix} P_{Cu} \\ P_{Fe} \\ 0 \\ 0 \end{bmatrix} \quad (2\text{-}8)$$

where G_1 G_2 G_3 G_4 G_5 and G_6 are the inverses of R_1 R_2 R_3 R_4 R_5 and R_6 respectively. In the calculations the copper loss is adjusted according to T_1 and while the core loss is kept to a constant value of 146W. In the analysis, the convection coefficient h_c is assumed to 22.

At the ambient temperature of 40 °C, the temperature rises of the mover magnets of the 18-slot, 26-pole motor and 18-slot, 28-pole are 105°C and 107°C, respectively.

The demagnetization risk analysis is to examine one representative magnet on the mover, as shown in Fig. 2-24, over one fundamental electric period to determine whether any part is partially demagnetised. The magnet is discretised into many small cells, and the flux density in the magnetization direction of each cell is evaluated. If the flux density in any time instant over an electric period is lower than the value at the demagnetization knee point, the corresponding cell will be partially demagnetised. The demagnetisation analysis is performed at the worst condition when the temperature of the motor magnets has reached steady-state temperature under rated operation and the maximum current is applied. The flux density at the knee point of the magnets at 150 °C and 0.7T in Fig. 2-21. By way of example, the flux density distributions at t = 0 in the designated are shown in Fig. 2-25 for the two designs. It can be seen that the flux density in the magnet outer surface close to the armature is significantly reduced. The partially demagnetized regions in an electric period are shown in Fig. 2-26. The magnet under the worst case condition has small regions at the bottom corners which suffer irreversible demagnetization. This has little influence on the thrust force as the demagnetised region is below 0.1% of the magnet volume.

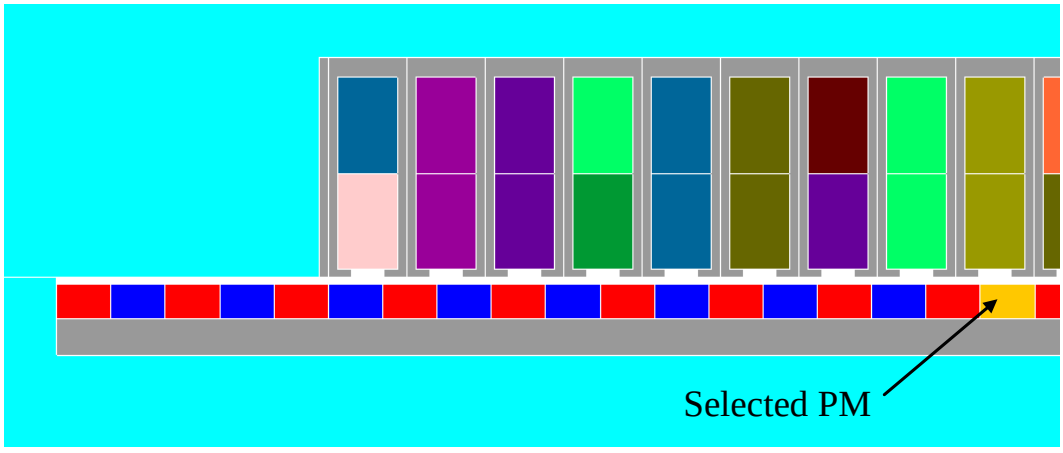

(a)

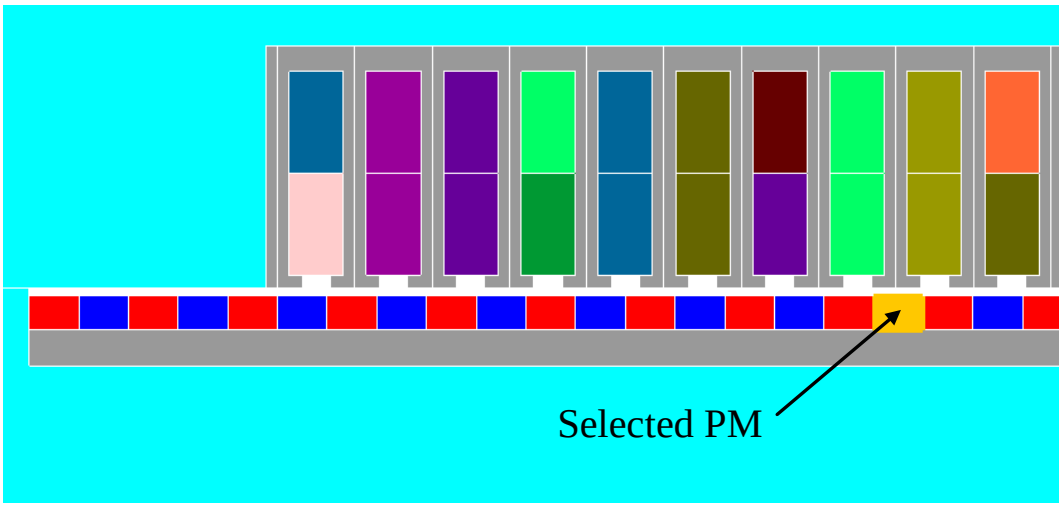

(b)

Fig. 2-24 The position of the selected PM (a) 18-slot 26-pole motor (b) 18-slot 28-pole motor

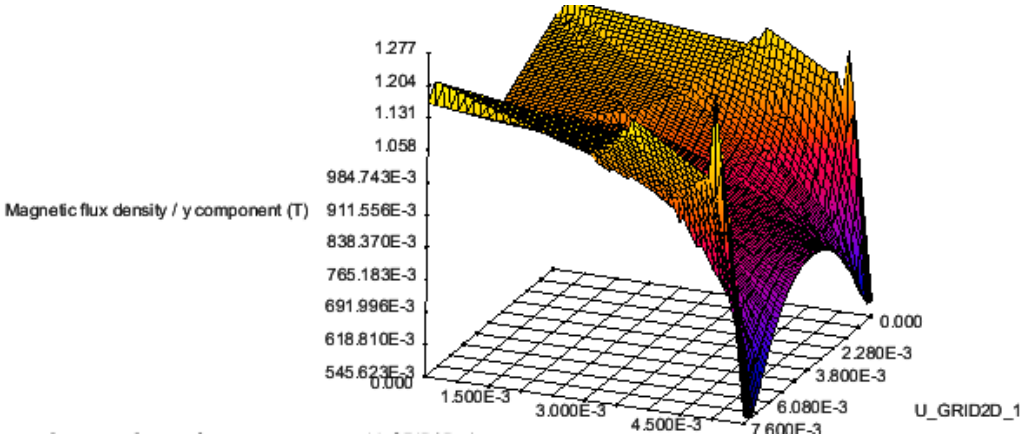

(a)

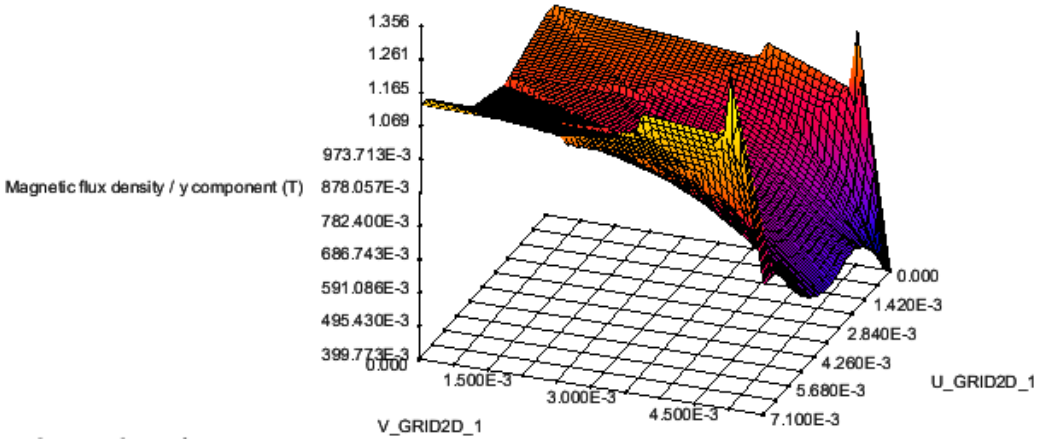

(b)

Fig. 2-25 PM flux density distribution at t=0 (a) 18-slot 26-pole motor (b) 18-slot 28-pole motor

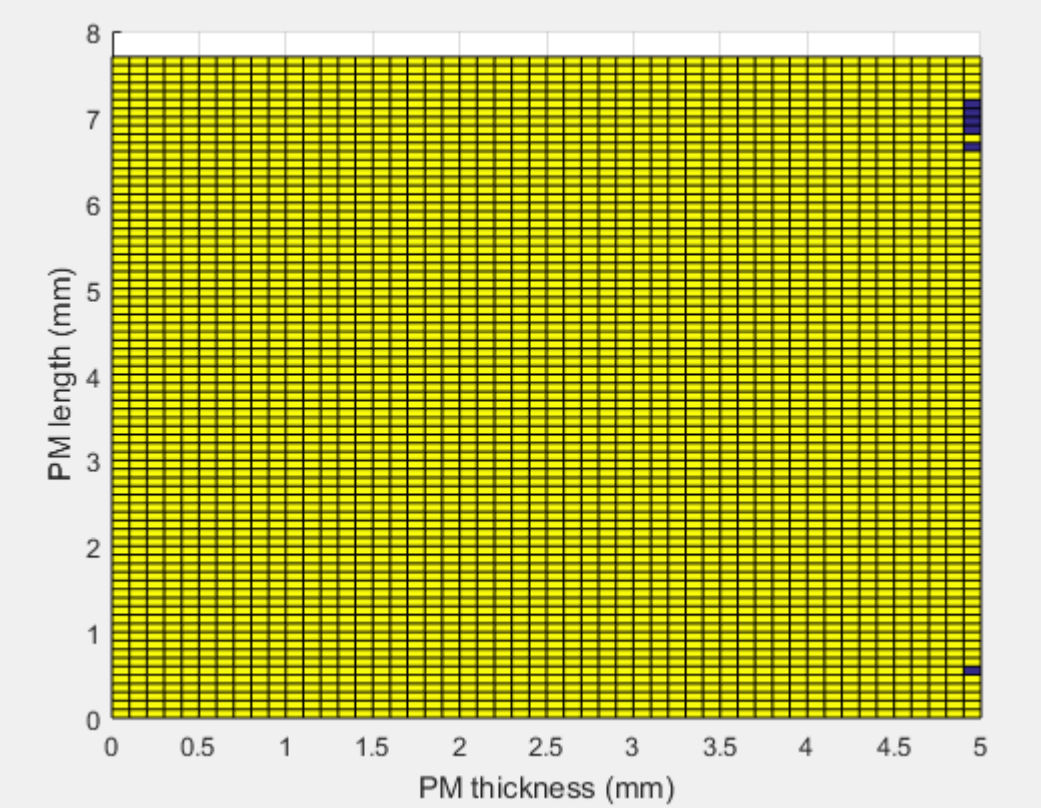

(a)

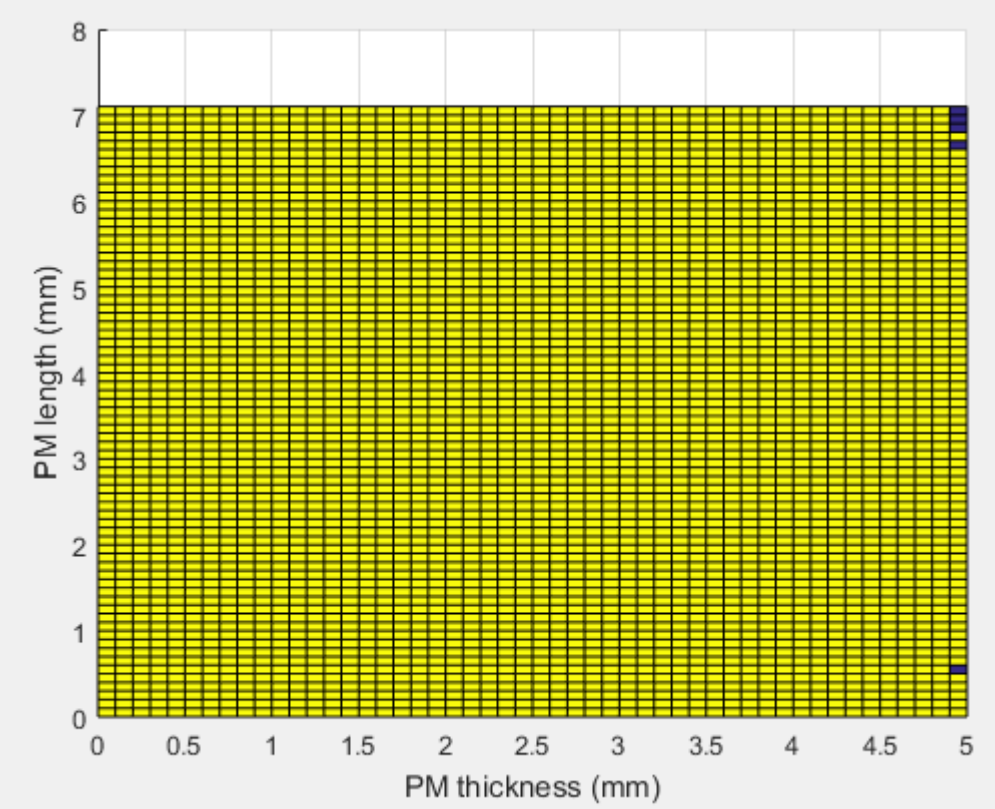

(b)

Fig. 2-26 Demagnetized regions (a) 18-slot 26-pole motor (b) 18-slot 28-pole motor

2.5 Comparison with Conventional Tubular Linear Motor

Fig. 2-27 shows performance comparison of the reference 9-slot 10-pole motor with the proposed designs, 18-slot 28-pole and 18-slot 26-pole, at their rated current. Compared with the reference motor, the proposed PM vernier linear motor has an average thrust increase about 10%, and the thrust ripple is less than half. This reflects the improvement of the torque density of the proposed motors by the magnetic gear principle, but under the same limitation of the copper loss, the PM vernier linear motors do not have much significant advantages.

However, as shown in Fig. 2-28, because the saturation level of the PM vernier linear motors is much higher, as the current continues to increase above the rated, the thrust force of the PM Vernier linear motors is obviously not as good as that of the reference linear motor. At the peak current, the output thrust force of the PM vernier linear motors is more than 5% lower than that of the reference motor, and in comparison of the two proposed PM vernier linear motors, the thrust force of the 18-slot 26-pole motor is further 5% lower than that of the 18-slot 28-pole motor.

Table 2-9 compares the thrust forces and key dimensions of the three designs. From the results, it can be seen that the PM vernier linear motor has certain advantages over the reference motor below and at the rated current, but it also consumes slightly more magnet material. For the proposed two motors, the performance of the 18-slot 28-pole motor is slightly better than the 18-slot 26-pole motor.

It has been shown that by exploiting the Vernier force in the proposed designs, the force capability below the rated current is slightly improved. This can be attributed to the Vernier force component but there is a trade-off between the PM force and Vernier force. Attempt to increase the Vernier force may reduce the PM force. Hence an optimal balance is reached via the optimisation, which tends to indicate the advantage gained in the proposed designs. However, similar to rotary Vernier motors, the proposed linear Vernier motors also suffer from high level of magnetic saturation in the stator tooth and back-iron region, which leads to a relatively poor peak force capability.

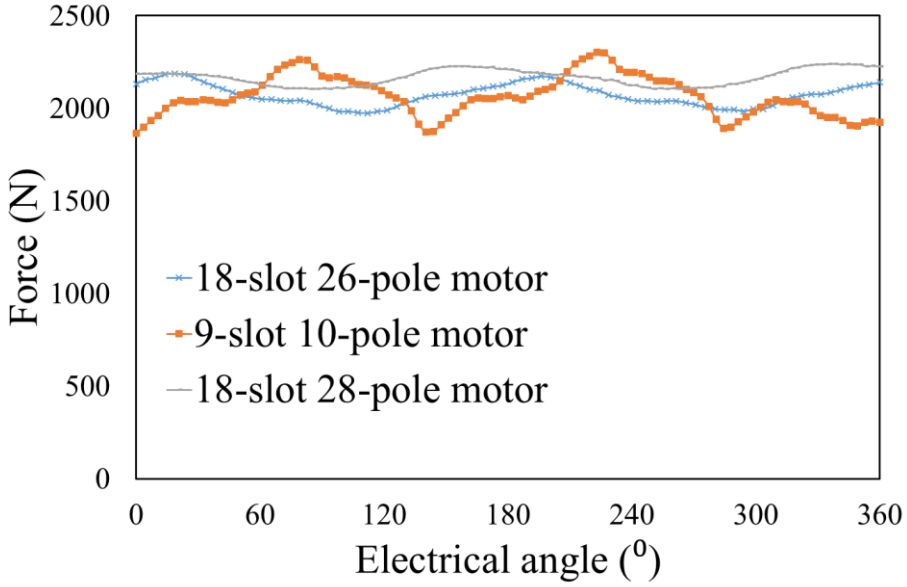

Fig. 2-27 Output force comparison at rated current

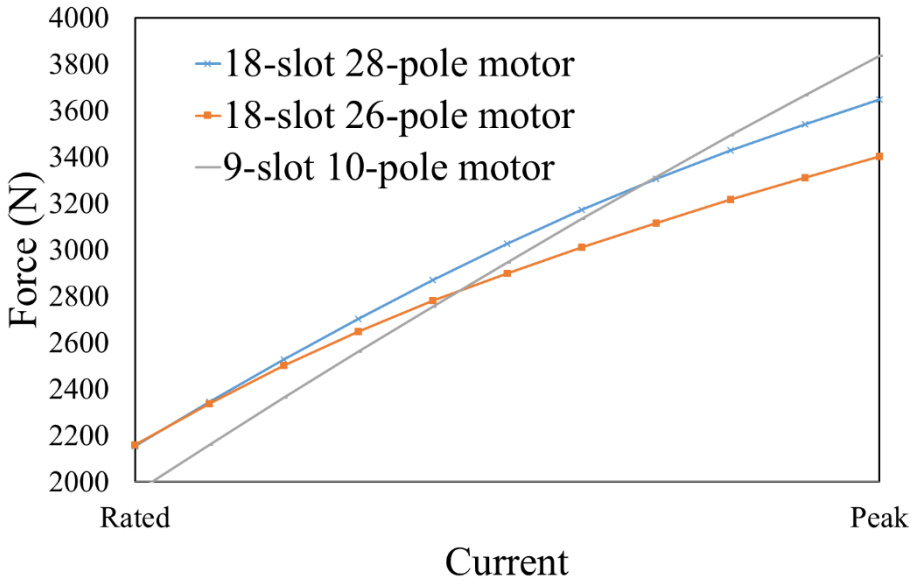

Fig. 2-28 Output force comparison from rated current to peak current

Table 2-9 Performance Comparison between 18/26 motor, 18/28 motor and 9/10 motor

	18/26	18/28	9/10
Rated Output Force	2159N	2184N	1953N
Rated Force Ripple	10%	6%	20%
Peak Output Force	3402N	3646N	3835N
Stator Back iron thickness	2.5mm	3.2mm	6.5mm
Stator Teeth Width	3.2mm	3mm	10.7mm
Power Factor	0.53	0.6	0.9
PM Volume	3.8e5mm^3	3.6e5mm^3	3.5e5mm^3

2.6 Summary

An 18-slot 26-pole tubular PM vernier linear motor and an 18-slot 28-pole tubular PM vernier linear motor have been proposed and globally optimised subject to the same volumetric and thermal constraints of the reference motor. Their risk of demagnetisation under the worst condition is also assessed.

The comparison result shows that the output thrust force density of the PM vernier linear motors has a certain advantage over the reference linear motor, being about 10% higher below and up to the rated current, while the cogging force of the vernier motors is also smaller. However, as the motor current increases, the thrust force of the vernier motors become lower due to relatively high saturation. When the maximum current is reached, the output thrust density of the PM vernier linear motor is more than 5% lower compared with the reference motor. In addition, the Vernier motor designs use slightly more magnet material. Therefore, the vernier linear motor designs in this chapter do not have a significant advantage over the reference motor.

CHAPTER 3
Design and Modelling of Double-sided, Tubular Vernier PM Motors

This chapter investigates double-sided, tubular, Vernier permanent magnet (DTVPM) motors for high force density applications. The potential of high force density and high power factor which results with this type of machines are exploited and a design process of 3 different pole-slot combinations is described. The design process includes selection of motor pole-slot coordination, thermal modelling, establishment of motor simulation model, and global optimization of leading design parameters. The simulation results will be compared with existing high force density tubular linear motor and those studied in Chapter 2, including electromagnetic, thermal and demagnetization performance. The results show that with same copper loss the DTVPM machine has larger thrust force and thrust force density, high power factor and low risk of demagnetization.

3.1 Introduction

From the results in Chapter 2, it can be concluded that, while maintaining the same electrical load, the thrust force density of the vernier linear motor with a small gear ratio has no significant advantage compared to the conventional high thrust density density linear motor. One of the most significant shortcomings of the vernier motor is its low power factor. The main reason is that the vernier motor mover adopts more pole pairs, which leads to increased motor magnetic flux leakage. Hence the back-emf is low and more magnetic energy in the form of leakage flux is stored in the machine, causing lower motor power factor. If the thrust force density of the motor is increased by raising the gear ratio of the vernier motor, this will further deteriorate the power factor, being even lower than 0.4 [104]. Although such kinds of motor improves the thrust density, it has no practical application value as the voltage-Ampere rating of the inverter is significantly increased. Therefore, how to solve the conflict between high gear ratio and low power factor is the key to improving the thrust force density of the linear PM vernier motor

The work in [105] proposed a 24-slot 44-pole double-sided Vernier PM rotatory motor. The motor consists of three layers, namely the outer stator, the rotor and the inner stator. There are no teeth tips structure in the inner and outer stator slots, and there is a 90 degree phase difference between the two. The rotor adopts the spoke-array magnets structure, which produces PM flux linking both the inner and outer stator windings. The motor windings have 2 pole pairs, combined with a 24-slot stator and 44-pole rotor to

form the Vernier structure. The motor has the advantages of high thrust force density capability and significantly high power factor > 0.9, which are derived from the unique features of the machine topology that exploits Vernier principle while minimising leakage flux[106].

In the past years, this type of rotary motors has been further studied [107], and many dual-sided structures have been derived that increase the thrust density by conducting magnetic circuits on both sides of the stator. Very recently, this type of motor structure has also been applied to the linear motor of both flat and tubular topologies[108-109]. However, comprehensive assessment of machine performance under thermal constraints and risk of demagnetisation have not been reported in literature.

To exploit the potential of such motor topology in high force density applications, a tubular version is investigated in this chapter. Unlike the usual single-sided motors, the double-sided structure can more effectively use the internal space of a tubular motor, and the double-layer air gap also increases the air gap area of the motor magnetic field, which can greatly improve the output performance of the motor. However, the double-sided structure also brings difficulties in construction and manufacturing, and the motor is more prone to eccentricity and thermal dissipation problems. The rotor adopts axially magnetized ring magnets being sandwiched between magnetic pole-pieces. The inner and outer stators are displaced by 90 electrical degrees, which provides a permeable path for the PM flux when the mover travels to any position. This Vernier magnetic structure greatly improves of the PMs utilization while minimising flux leakage. Consequently, the thrust density of the motor is further improved due to the increase of the PM flux density and magnetic gearing while the power factor of the motor has also been greatly improved.

The aim of this chapter is to assess the performance of the double-sided, tubular, Vernier permanent magnet (DTVPM) motor for high force density applications, and compare it with the single-sided Vernier linear motors. To examine the influence of magnetic gear ratio on thrust force density and power factor, machines with three different pole-slot combinations and hence three gear ratios are optimally designed under thermal constraints, and their performance is analysed under the same electrical load, including no-load back EMF, thrust force and demagnetization risk.

This chapter is organized as follows. In Section 3.1, the reasons for the high power factor and thrust force density of the DTVPM motor are analysed. In Section 3.2, three gear ratios which result with the pole slots combinations of (9 slots, 14 poles), (12 slots,

20 poles) and (18 slots, 32 poles) are discussed and their structures established. In Section 3.3, the motor is globally optimized against the leading design parameters of the motor, and the influence of each parameter is discussed. In Section 3.4, the performance of three candidate motors is analysed and compared. Finally, Section 3.5 summarizes the key findings.

3.1.1 Power Factor

Many literatures have pointed out that a Vernier motor suffers from a lower power factor compared to the conventional motor, especially when the gear ratio is increased, the power factor of a Vernier motor will be further reduced. This makes the Vernier motor need to use a larger size inverter to achieve the same output power, which increases the cost and limits applications of Vernier motor.

Although the operating principle of a Vernier machine introduces the magnetic gearing effect, its electrical governing equations are the same as those in a conventional PM synchronous motor, so if the resistance of stator windings is neglected and d-axis current I_d = 0, as shown in Fig. 3-1, the power factor can be evaluated by

$$\cos\theta = \frac{1}{\sqrt{1+(\frac{I_q X_q}{E_0})^2}} = \frac{1}{\sqrt{1+(\frac{I_q L_q}{\Psi_{PM}})^2}} \tag{3-1}$$

where Ψ_{PM} is the PM fundamental flux linkage, X_q is the inductive reactance, L_q is the q-axis inductance and E_0 is the back EMF. Therefore, power factor is determined by L_q/Ψ_{PM}. While 3-phase winding configuration of a Verner machine is similar to that of a conventional synchronous PM machine, as the gear ratio increases, one pole-pair of the stator has larger number of the mover PM poles. Further, in order to achieve a better magnetic field modulation effect, the slot opening of the stator teeth is generally larger. Consequently, the mover PMs produce greater flux leakage, which reduces the amplitude of the fundamental in the air gap. In addition, significant high order harmonic armature reaction field exist as a result of flux modulation. Hence the synchronous inductance of the stator winding also increases. In order to improve the power factor of the motor, it is necessary to increase the utilization of PMs and reduce the flux leakage.

Therefore, due to the special structure of the DTVPM machine, the PM utilization rate of the motor is greatly improved, thereby improving the power factor. With a high power factor, the machine can designed with a larger gear ratio, which improves the thrust force density.

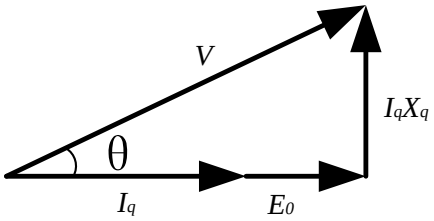

Fig. 3-1 Phasor diagram of DTVPM machine

3.1.2 Force Production of DTVPM machines

For the DTVPM machine under study, there are two reasons for the increase of thrust force density. On the one hand, the machine adopts double-sided structure with more magnets on the mover, which increase the force production surface area in the two air-gaps; and on the other hand, the machine can have a pole-slot combination with high gear ratio. In order to quantify the improvement brought by the high gear ratio, it is necessary to obtain the specific output thrust force percentage of different thrust force components.

A 12-slot 20-pole DTVPM machine is discussed as an example where a 2 pole-pair stator winding (p_s=2) is arranged in 12 slots (n_s=12) and interacts with 10 pole-pairs PM mover (p_r=10). The slot/pole number combination conforms to the Vernier principle formula $p_r=n_s-p_s$ and the resultant gear ratio G_r=0.2, which is a relatively higher than those described in Chapter 2. According to the method introduced in the Chapter 2, Fig. 3-2 shows the armature reaction harmonics model without PMs and stator slots, and the resultant radial flux density of the armature reaction field in air gaps is shown in Fig. 3-3. According to Fig. 3-3, the amplitudes of the 2th, 10th and 14th harmonics are larger than the other harmonics, where the 2nd armature reaction magneto-motive force (MMF) harmonics generate thrust force under the gear effect with the 10 pole-pair PM MMF harmonic. In addition, the 10^{th} MMF of the armature reaction field interacts the 10 pole-pair PM field to produce another thrust force. Fig. 3-2 (a) and Fig. 3-2 (b) show the schematics of 10 pole-pair PM field interaction with the 2th and 10^{th} armature reaction MMF harmonics, respectively. The corresponding air gap radial flux densities are shown in Fig. 3-4.

The force contribution of the two force components can be evaluated by FE analysis. Fig. 3-5 shows the calculation results of the FE simulation model of the two interactions where the results of both are displayed and compared with the total thrust force. It can be seen that the magnetic gearing effect contributes 33% of the total thrust force and the

conventional PM machine principle contributes 66% of the thrust force. Compared with the motor structure shown in Chapter 2, the thrust force Contributed by the magnetic gear effect is approximately doubled.

As will be shown subsequently, the no-load back-emf of the stator winding is relatively large compared with conventional Vernier machines of similar gearing effect. Consequently, the power factor is also high.

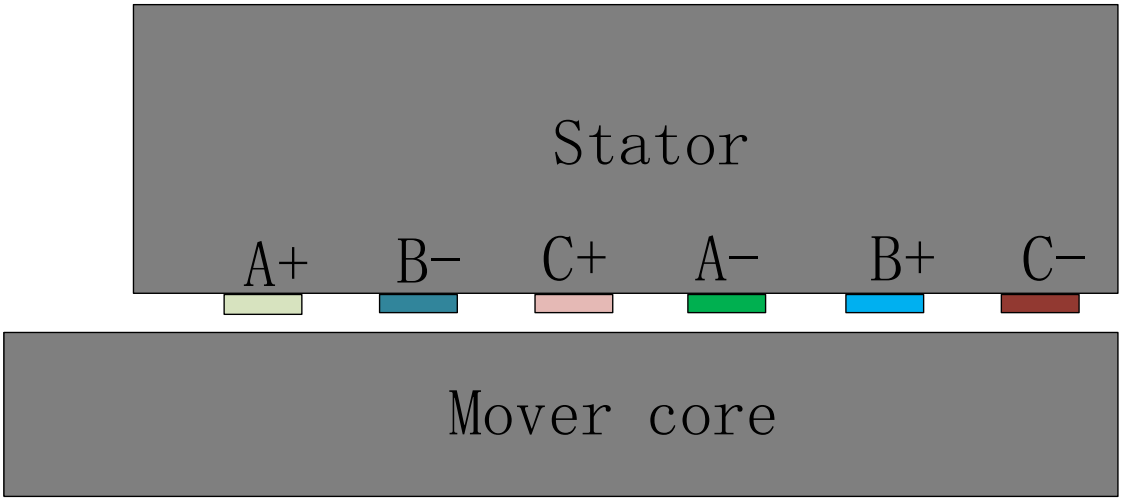

(a)

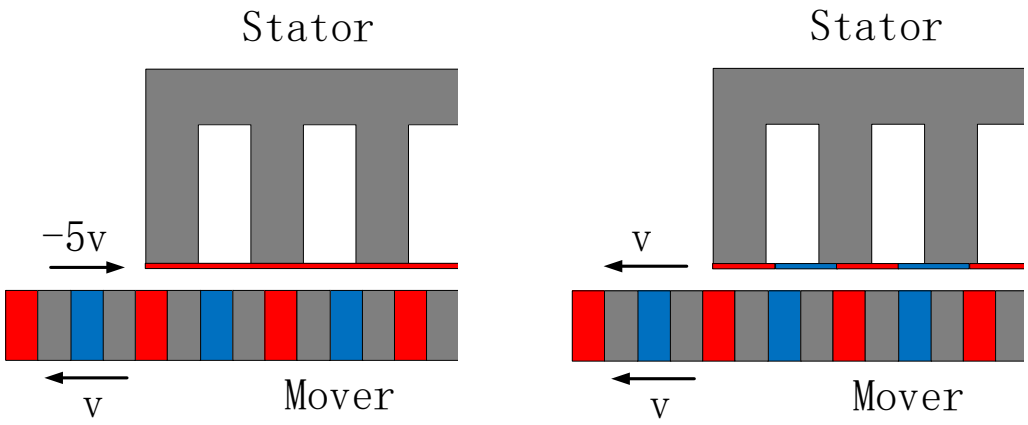

(b) (c)

Fig. 3-2 Interaction of the MMF harmonics (a) A model without PMs and stator slots (b) 10th PM and 2th armature reaction MMF (b) 10th PM and 10th armature reaction MMF

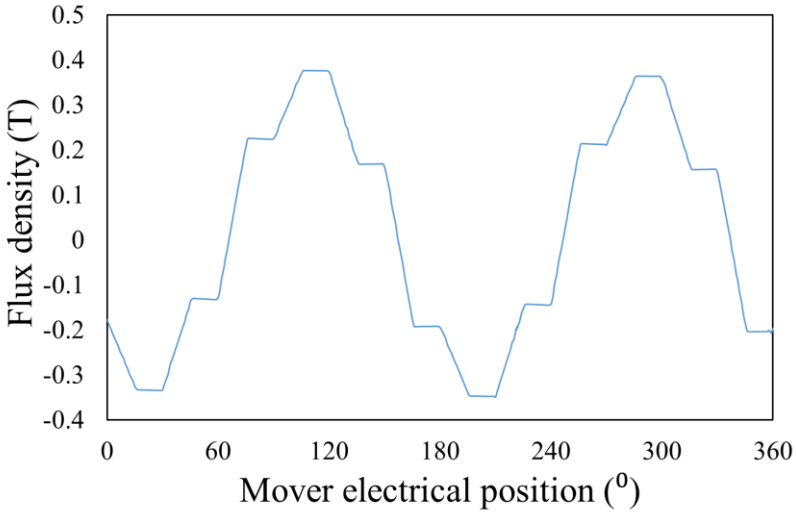

(a)

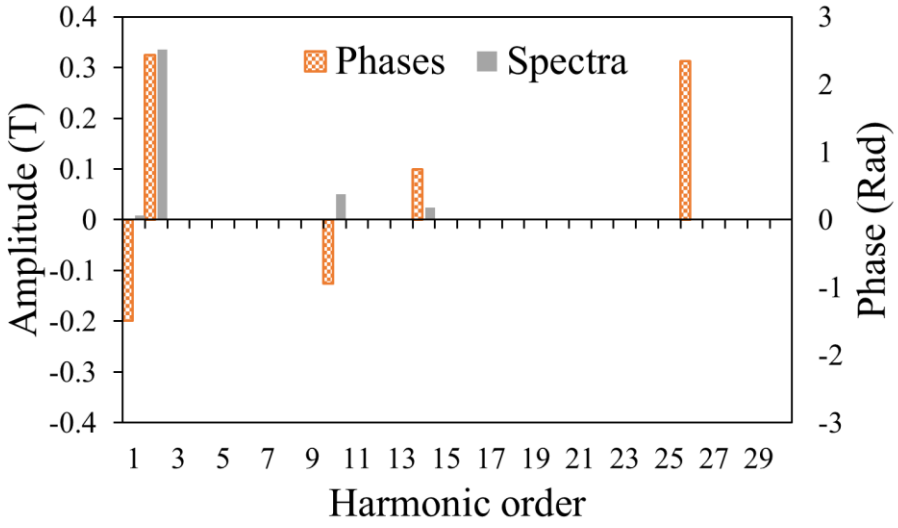

(b)

Fig. 3-3 Radial flux density of armature (a) Air gap waveform (b) Spectrum and phases

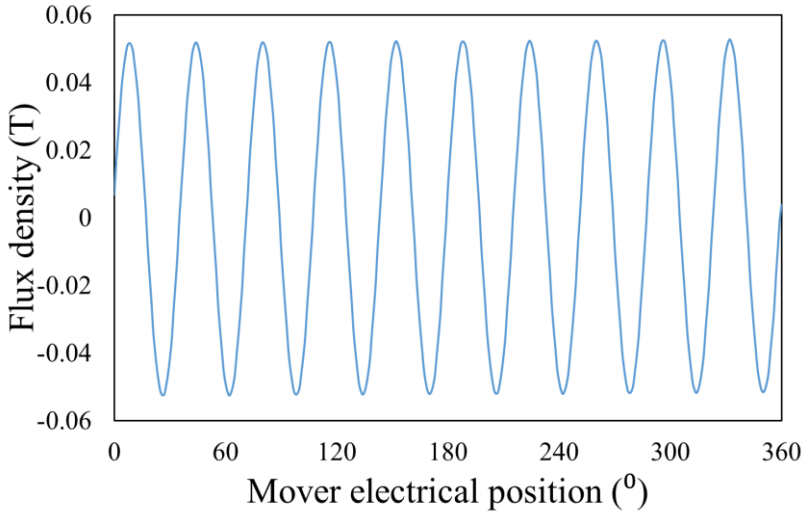

(a)

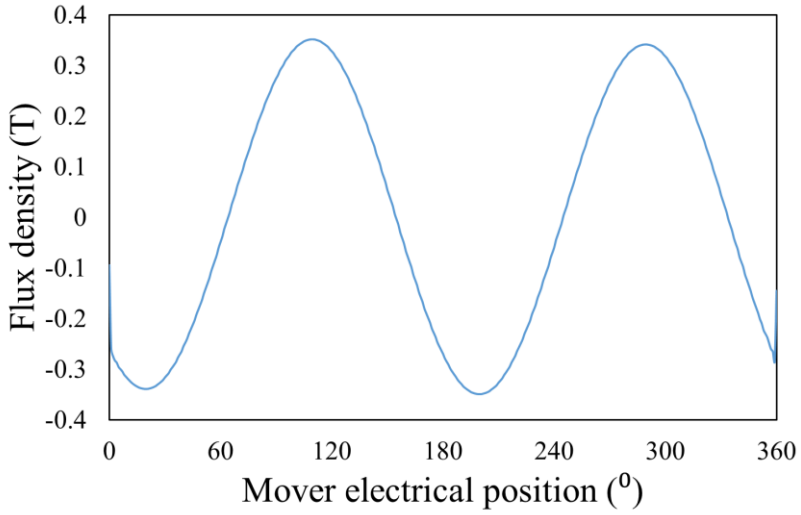

(b)

Fig. 3-4 Radial flux density of sinusoidal magnetized PM (a) 10 pole pairs (b) 2 pole pairs

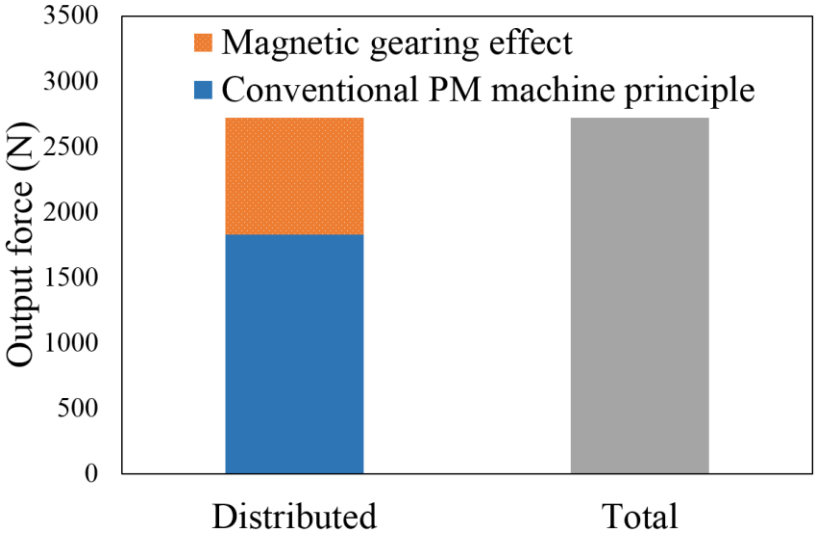

Fig. 3-5 Contributions of two force components in DTVPM machine

3.2 Machine Topology and pole-slot combinations

In order to study the influence of gearing on machine performance, three candidate pole-slot combinations are considered. They are (9-slot, 14-pole), (12-slot, 20-pole) and (18-slot, 32-pole) machines whose schematics are shown in Fig. 3-6, where axi-symmetrical tubular structure is assumed. Similar to the structure of the rotatory Vernier motor counterpart [105], the inner and outer stators have a phase shift of 90 degrees, which provides more permeable path for the PM flux and hence reduce flux leakage. In order to reduce the influence of the end effect, a half-tooth width iron core is added on both sides of the machine. Since the main purpose of the study is to evaluate force

capability and power factor, the cogging force resulting from the end-effect is not minimised.

In order to make a fair comparison, the design specification, and thermal and volumetric constraints are the same as in Chapter 2. That is, the same permissible winding copper loss, the same operating speed and the same main size of the motor are employed in the design. As the main size of the machine is determined, the greater the number of slots, the smaller the tooth width of the stator. To ensure sufficient mover stiffness, the axial length is also kept the same as the reference design, in order to ensure the mechanical strength of the stator teeth. This limits the maximum number of slots of the machine to 18. It should be noted that the 9-slot machine has unconventional winding configuration and contains sub-harmonics. Nevertheless, it is considered for the purpose of performance comparion.

As high power factor is one of the advantages, the three DTVPM condidates can be designed with relatively high gear ratios. Thus, the number of stator armature pole pairs of the three candidates is 2, and as the number of slots increases, their gear ratio is also increasing. The gear ratios of three candidate designs are listed in Table 3-1, and their armature reaction MMF waveforms and spectra are shown in Fig. 3-7.

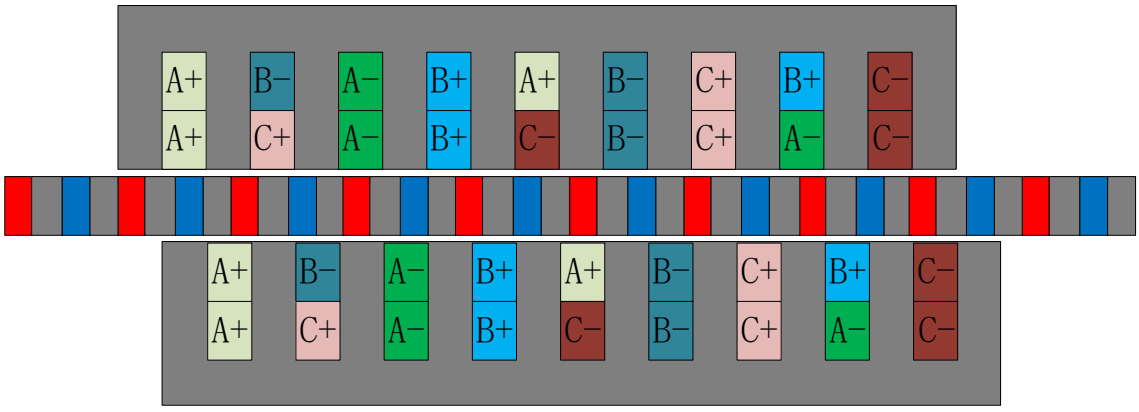

(a)

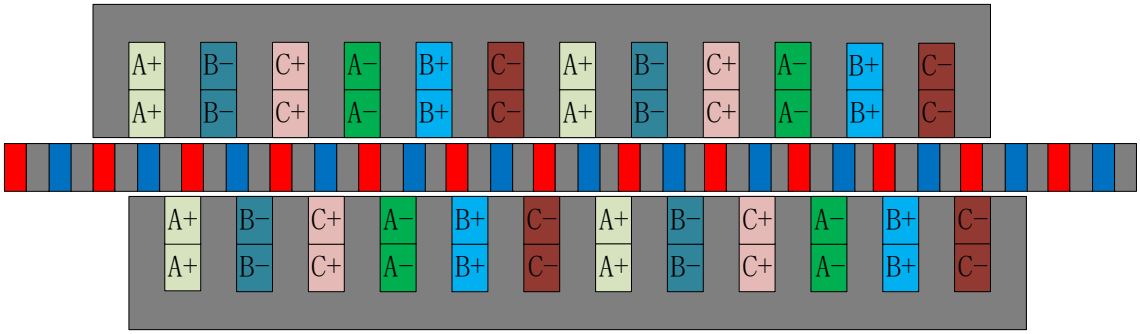

(b)

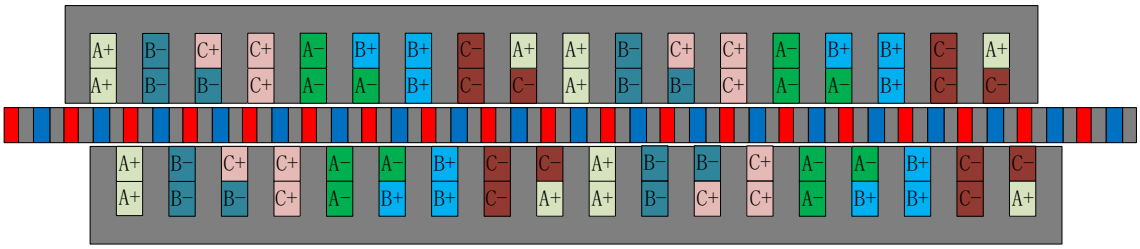

(c)

Fig. 3-6 Candidate DTVPM topologies (a) 9-slot 14-pole (b) 12-slot 20-pole (c) 18-slot 32-pole

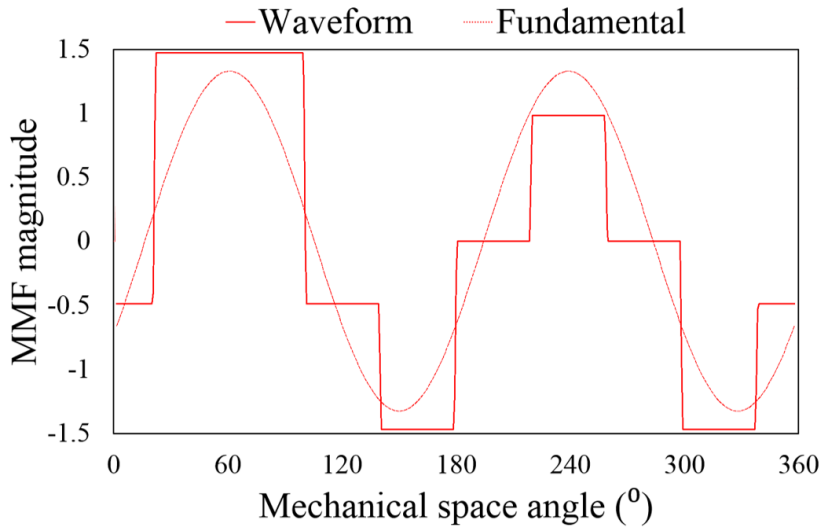

(a)

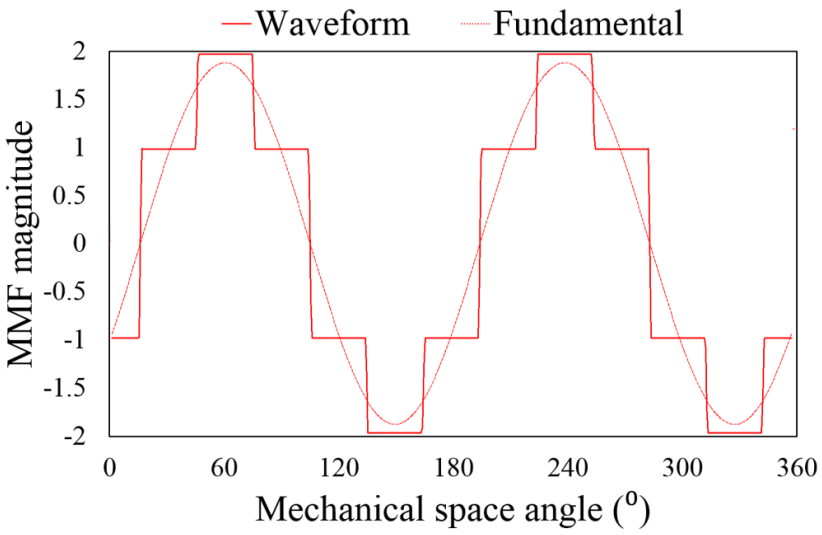
Waveform
Fundamental
MMF magnitude
2
1.5
1
0.5
0
-0.5
-1
-1.5
-2
0
60
120
180
240
300
360
Mechanical space angle (°)

(b)

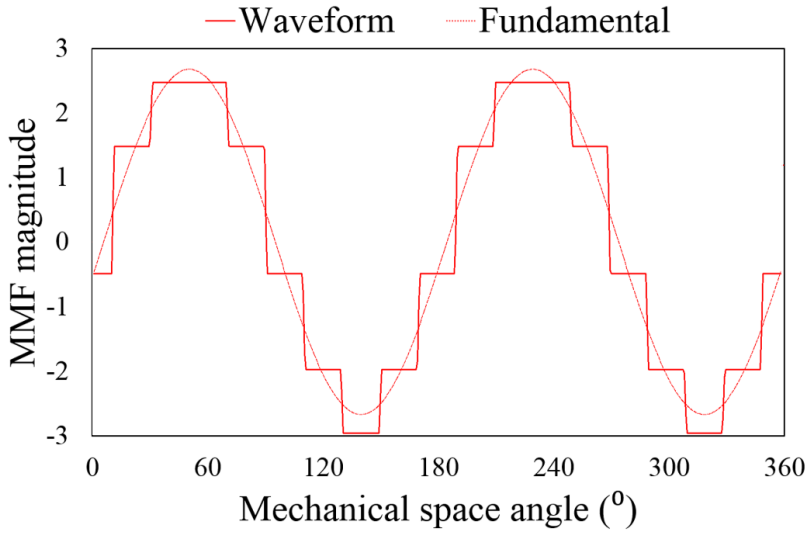
Waveform
Fundamental
MMF magnitude
3
2
1
0
-1
-2
-3
0
60
120
180
240
300
360
Mechanical space angle (°)

(c)

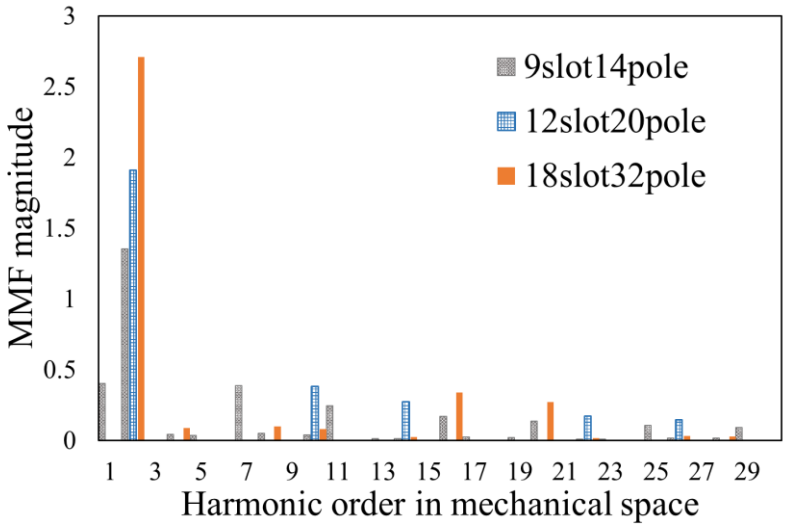
9slot14pole
12slot20pole
18slot32pole
MMF magnitude
3
2.5
2
1.5
1
0.5
0
1
3
5
7
9
11
13
15
17
19
21
23
25
27
29
Harmonic order in mechanical space

(d)

Fig. 3-7 MMF waveforms and spectra of candidates (a) 9-slot 14-pole (b) 12-slot 20-pole (c) 18-slot 32-pole (d) Spectra

Table 3-1 Gear Ratios in DTVPM Candidates

N_s	p_r	ps	G_r
9	7	2	-2/7
12	10	2	-1/5
18	16	2	-1/8

3.3 Motor Leading Design Parameters and Global Optimisation

Although the design specification and constraints of the candidates are the same as in Chapter 2, the machine topology is very different from those of a single-sided Vernier motor. When the main sizes of the machine, namely, the outer diameter and active stator length are kept the same, the outer surface area of the Vernier motor remains the same, so the motor has the same heat dissipation capacity when the copper loss is the same. However, the copper loss of the DTVPM machine is distributed between the inner and outer stators, and the heat dissipation capacity of the inner stator is much smaller than that of the outer stator. Therefore, for the DTVPM candidates, it is essential to include the thermal constraints in the global optimization. For the sake of comparison, the properties of PM and soft magnetic materials of the candidates are the same as those in Chapter 2.

3.3.1 Motor Leading Design Parameters

The leading design parameters of the machine to be optimised are shown in Fig. 3-8. The axial length of the stator, the outer radius of stator and both inner and outer air gap lengths for the three candidates are kept the same. For a given pole-slot number combination, the pole-pitch and slot-pitch can be determined. And in order to simplify the structure and reduce the number of optimization parameters, the machine has no teeth tips. Hence, there are six parameters, including the stator back iron thickness B_i, the stator teeth width T_W, mover core width R_w, the mover core height R_l and inner bore radius of the outer stator R_m , to be optimized. Since the outer diameter of the motor is fixed, the inner bore radius of the outer stator R_m directly determines the split ratio of the outer stator, and it together with mover core height R_l determines the split ratio of the inner stator. These two directly influence the area of the two air gaps, and electrical and magnetic loadings of the machine. Hence, they have the most important impact on the output thrust force. When the split ratio of the motor is determined, the stator back iron thickness B_i

and stator teeth width T_W determine the slot area and the magnetic saturation level and the stator teeth width T_W also affects the DTVPM slot modulation ability. The mover core width R_w and PM length R_l directly determines the size of the DTVPM mover, including the volume of the PM, which is also an important parameter for motor performance and cost-effectiveness.

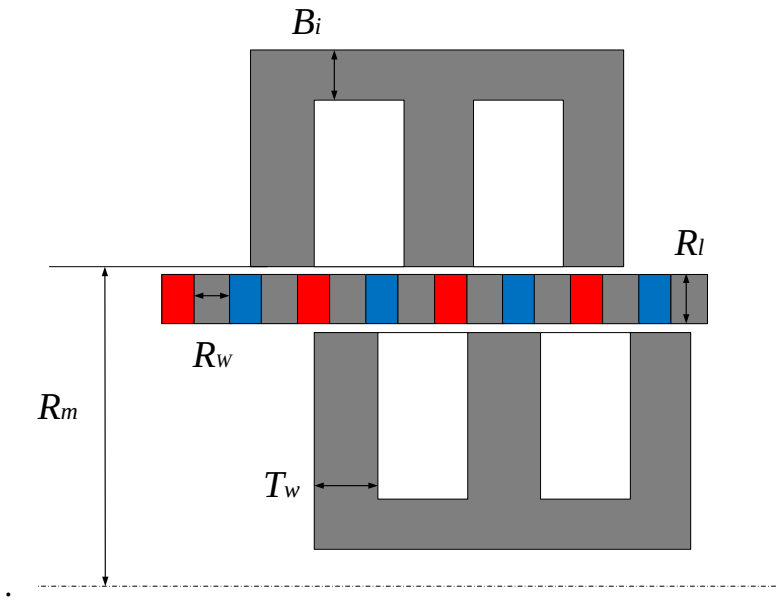

Fig. 3-8 Leading design parameters of PM vernier linear motor

3.3.2 Motor Thermal Model and Constraints

Since the tubular linear motor is a symmetrical structure, only the cross section of a half slot-tooth needs to be studied for the thermal distribution in the motor when the end-effect is neglected. Assuming that the motor dissipates heat through the outer surface of the outer stator and inner surface of the inner stator, the representative thermal network is shown in Fig. 3-9, where half a tooth pitch is modelled. P_{Cu1} and P_{Cu2} are the copper loss of the outer and inner windings, respectively, and P_{Fe1} and P_{Fe2} are the iron loss of the outer and inner stators, respectively. The specific thermal resistances in the figure can be derived based on the principle of thermal conduction and convection [98], and they are given by

$$R_{F1} = \frac{T_w}{4K_{Fe}\pi(R_{h1}^2 - R_{s1}^2)}$$

$$R_{F2} = \frac{\ln(R_{h1}/R_{cc1})}{\pi K_{Fe} T_s}$$

$$R_{F3} = \frac{\ln(R_{e1}/R_{h1})}{\pi K_{Fe} T_s}$$

$$R_{S1} = \frac{\delta_s}{K_{line}\pi(R_h^2 - R_{s1}^2)} \quad (3\text{-}2)$$

$$R_{S2} = \frac{\delta_s}{K_{line}\pi S_w R_{h1}}$$

$$R_{W1} = \frac{S_w}{4K_{Fe}\pi(R_{h1}^2 - R_{S1}^2)}$$

$$R_{W2} = \frac{\ln(R_{h1}/R_{cc1})}{\pi K_w S_w}$$

$$R_{S3} = \frac{R_{S1} - R_{m1}}{K_g\pi(T_s - S_o)R_{s1}}$$

$$R_{S4} = \frac{R_{S1} - R_{m1}}{K_g\pi S_o R_{S1}}$$

$$R_{F4} = \frac{\ln(R_{m1}/R_{m2})}{\pi K_{Fe} T_s}$$

$$R_{S5} = \frac{R_{m2} - R_{s2}}{K_g\pi S_o R_{S2}}$$

$$R_{S6} = \frac{R_{m2} - R_{s2}}{K_g\pi(T_s - S_o)R_{s2}}$$

$$R_{W3} = \frac{S_w}{4K_{Fe}\pi(R_{s2}^2 - R_{h2}^2)}$$

$$R_{W4} = \frac{\ln(R_{cc2}/R_{h2})}{\pi K_w S_w}$$

$$R_{F5} = \frac{T_w}{4K_{Fe}\pi(R_{s2}^2 - R_{h2}^2)}$$

$$R_{S7} = \frac{\delta_s}{K_{line}\pi(R_{s2}^2 - R_{h2}^2)}$$

$$R_{W3} = \frac{S_w}{4K_{Fe}\pi(R_{s2}^2 - R_{h2}^2)}$$

$$R_{W4} = \frac{\ln(R_{cc2}/R_{h2})}{\pi K_w S_w}$$

$$R_{S8} = \frac{\delta_s}{K_{line}\pi S_w R_{h2}}$$

$$R_{F6} = \frac{\ln(R_{cc2}/R_{h2})}{\pi K_{Fe} T_s}$$

$$R_{F7} = \frac{\ln(R_{h2}/R_{e2})}{\pi K_{Fe} T_s}$$

The relevant motor geometric parameters for computing these are also shown in Fig. 3-9. K_w is the equivalent thermal conductivity of stator winding, K_{line} is the thermal conductivity of slot line, K_g is the thermal conductivity of air gap, K_{Fe} is equivalent thermal conductivity of stator core and δ_s is the slot line thickness. Unlike the other thermal resistances in the figure, the thermal resistance represents the heat convection on the stator surfaces can be expressed as

$$R_{C1} = 1/(\pi T_s R_{e1} h_c)$$

$$R_{C2} = 1/(\pi T_s R_{e2} h_{c1}) \quad (3\text{-}3)$$

where h_c is the thermal convection coefficient at the room temperature and h_{c1} is the thermal convection coefficient of inner surface of the inner stator. In Fig. 3-9 there are many thermal resistances connected in series on different branches, in order to facilitate analysis, Fig. 3-9 can be simplify to Fig. 3-10.

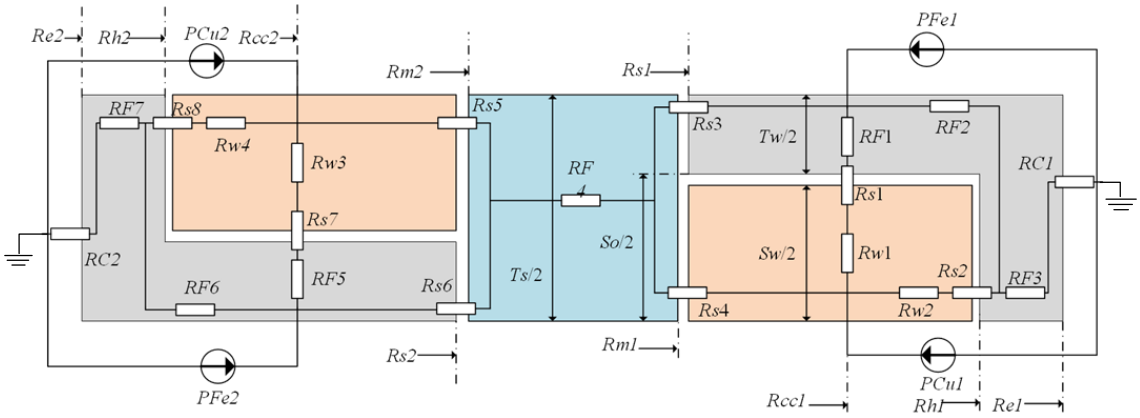

Fig. 3-9 Schematic of thermal model for DTVPM

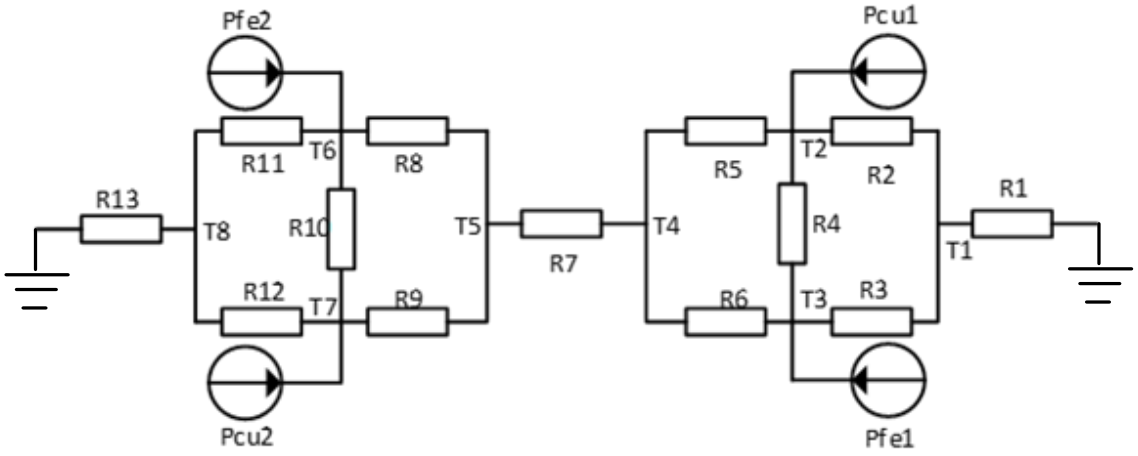

Fig. 3-10 Simplified thermal model

where

$$R_1 = R_{F1} + R_{S1} + R_{W1}$$

$$R_2 = R_{W2} + R_{S2}$$

$$R_3 = R_{F2}$$

$$R_4 = R_{F3} + R_{C1}$$

$$R_5 = R_{S3}$$

$$R_6 = R_{S4}$$

$$R_7 = R_{F4}$$

$$R_8 = R_{S5}$$

$$R_9 = R_{S6}$$

$$R_{10} = R_{F5} + R_{S7} + R_{W3}$$

$$R_{11} = R_{W4} + R_{S8}$$

$$R_{12} = R_{F6}$$

$$R_{13} = R_{F7} + R_{C2}$$

Thus the temperature rises in the outer stator back iron T_1, the outer stator tooth T_2, the outer stator coil center T_3, the mover PM T_4, and T_5, the inner stator coil center T_6, the

inner stator tooth T_7 and the inner stator back iron T_8, can be solved by a 7-order matrix calculation. In the calculations the copper loss is 302W and while the core loss is kept to a constant value of 146W. In the analysis, the convection coefficient h_c is assumed to be 22W/m^2/C and because the inside area of DTVPM machine is much smaller than the outside surface. The convection coefficient of inner surface h_{c1} is assumed to 4. At the ambient temperature of 40 °C [39]. Generally, the maximum working temperature of H grade winding insulation is 180 °. In order to ensure the safety of motor operation, the thermal constraints of the inner and outer stator windings of the motor are set to 160 °. So the global optimization of the DTVPM machine to achieve the maximum force is performed under the following constrains: (1) Fixed stator outer radius; (2) Fixed air-gap length; (3) Fixed stator length; (4) Fixed copper loss; (5) Fixed slot packing factor; (6) Maximum permissible winding temperature.

3.3.3 Motor Global Optimization

Fig. 3-6 shows the structures of the (9-slot, 14-pole), (12-slot, 20-pole) and (18-slot 32-pole) DTVPM candidates. The leading parameters and their range to be optimised are illustrated in Table 3-2. The optimisation is performed in Flux-2D in conjunction with Altair HyperStudy platform, where computationally efficient optimisation algorithm can be selected. The thermal constraint is incorporated into the optimisation process via Python script language.

The optimisation trends of the leading design parameters are shown in Fig. 3-11 (a)~(e), and the optimisation objective, viz. the output force, is shown in Fig. 3-11 (f). The whole process was iterated 24 times via construction of responses surfaces with a genetic algorithm to ensure a global optimal is reached. It can be seen that as the motor parameters approach the optimal solution, the output thrust of the motor continues to increase. The optimised geometries of the candidate machines are shown in Fig. 3-12 and the optimisation results are listed in Table 3-3.

It can be seen from the global optimization in Fig. 3-11, except for the two variables, namely, the stator tooth width T_W, and the mover core width R_w, which change with the different pole-slot number combinations, the other leading parameters tend to be in a similar range when the main size is determined. And from Fig. 3-11 (g), it can be seen that the winding temperatures of the three machines are all close to the maximum temperature, which shows that the three DTVPM has been optimized to the thermal limit. As can be seen in Fig. 3-11 (f), the output thrust forces of the three candidates do not

increase proportionally with the gear ratio when the copper loss is kept same. The 12-slot 20-pole motor which has a gear ratio between the other two has the highest average thrust force.

Table 3-2 Parameter Ranges for the Optimisation

Parameters	Description	Unit	Range
R_m	Outer stator inner radius	mm	56-70
B_i	Stator back iron thickness	mm	0-12
T_W	Stator teeth width	mm	0-14
R_W	Rotor core width	mm	0-8
R_L	PM length	mm	0-25

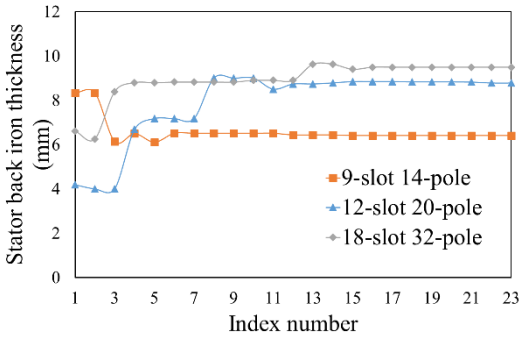

(a)

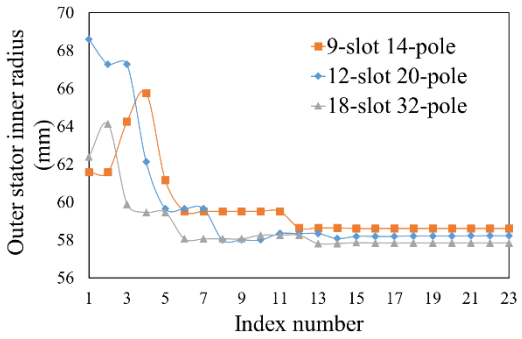

(b)

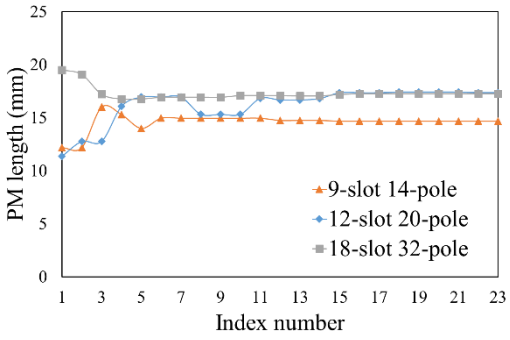

(c)

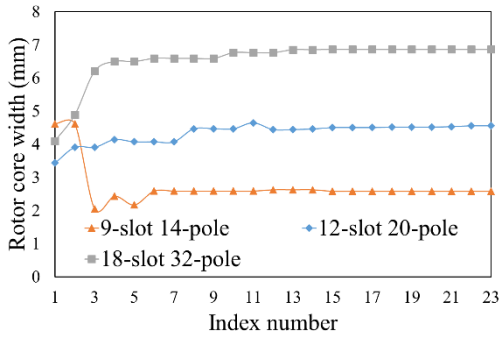

(d)

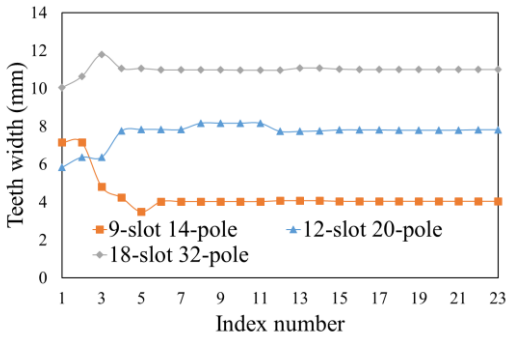

(e)

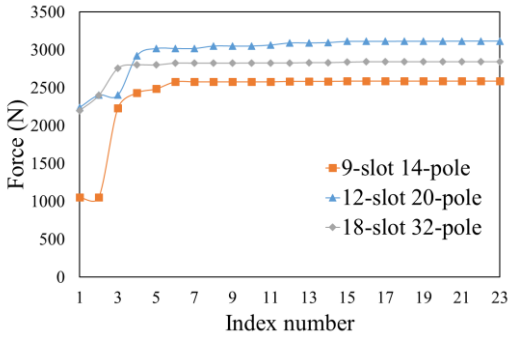

(f)

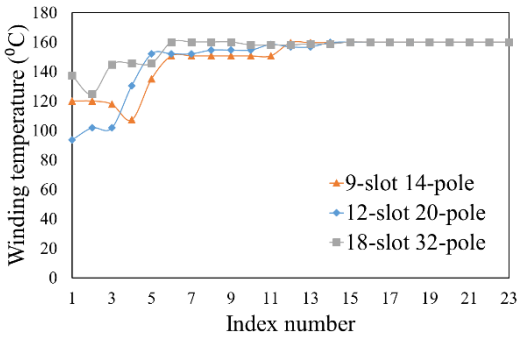

(g)

Fig. 3-11 Optimisation trends of variables and objective (a) Stator back iron thickness (b) Outer stator inner bore radius (c) PM length (d) Mover core width (e) Teeth width (f) Output force (g) Winding temperature

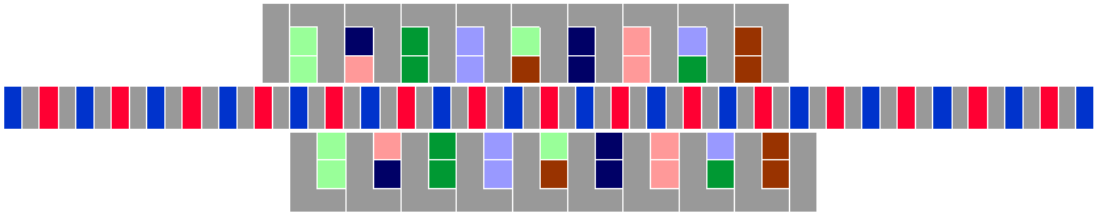

(a)

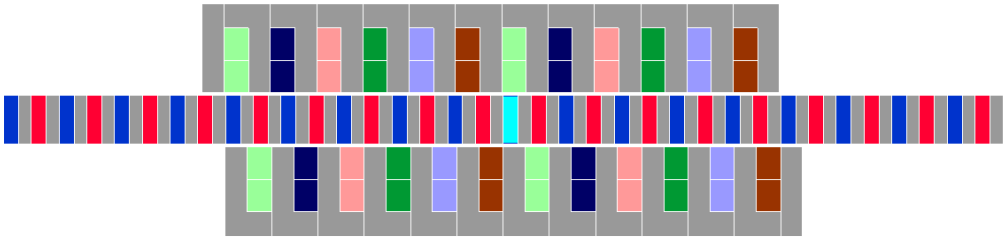

(b)

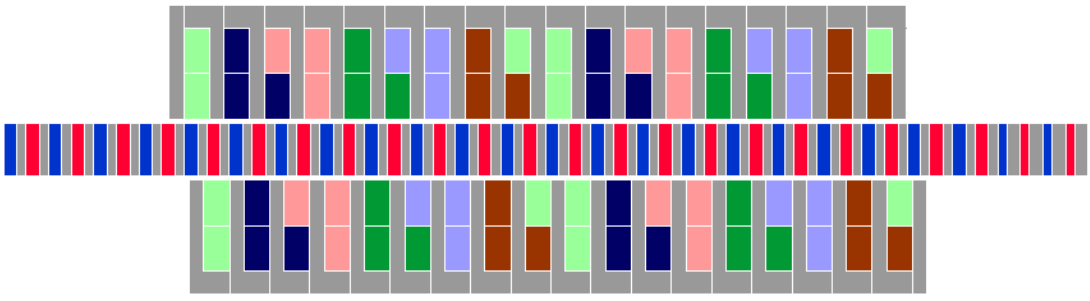

(c)

Fig. 3-12 Optimised geometry of DTVPM candidates (a) 9-slot 14-pole (b) 12-slot 20-pole (c) 18-slot 32-pole

Table 3-3 Optimised Parameters of DTVPM candidates

Parameters	9-slot 14-pole	12-slot 20-pole	18-slot 32-pole
R_m	58.6	58.2	57.8
B_i	6.4	8.7	9.4
T_W	4	7.8	11
R_W	2.5	4.5	6.8
R_L	14.6	17.3	17.2

3.4 Performance Evaluation

3.4.1 No-load Flux Linkage and Back EMF

Phase A flux linkage waveforms per turn and their spectra of three optimised designs at the rated speed of 1m/s is illustrated in Fig. 3-13. It can be seen that the back-EMF waveforms of the three are all very close to sinusoidal, and the 12-slot 20-pole design has the largest back-EMF amplitude, which is also in line with the thrust force result of the global optimization Although there is no constraints on phase back-EMF harmonics during the global optimisation, it can be seen that the motor back EMF is not distorted in any significant manner. Hence, no fine-tuning of the geometry to minimise the back EMF harmonics is needed.

The magnetic flux density distributions of the optimised designs and the initial mover position are shown in Fig. 3-15 and Fig. 3-16. It can be seen from Fig. 3-15 that the magnetic flux leakage of the DTVPM machines is significantly reduced compared with the single-sided Vernier motor. The PM flux lines not only link with the stator winding on one side but also the winding on the other side of the stator, which greatly improves the utilization of the PMs of the DTVPM machine. It can be seen from Fig. 3-16 that when the three candidate machines are at no load, the maximum flux density levels in the stator back-irons and stator teeth are about 1.65T and 1.35T when the local saturation in the stator teeth corners is neglected. It is close to the iron core saturation level of the soft magnetic materials used. The flux density of the machines at the rated operating point and the peak force operating point will be discussed in the next sub-section.

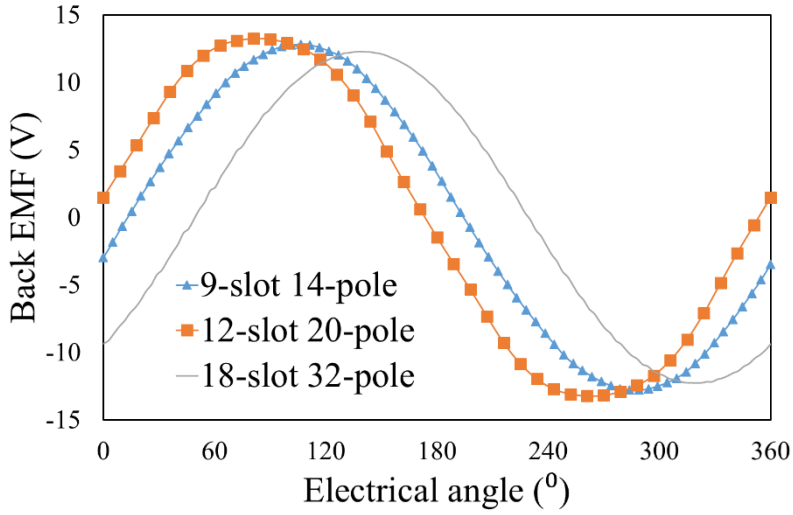

(a)

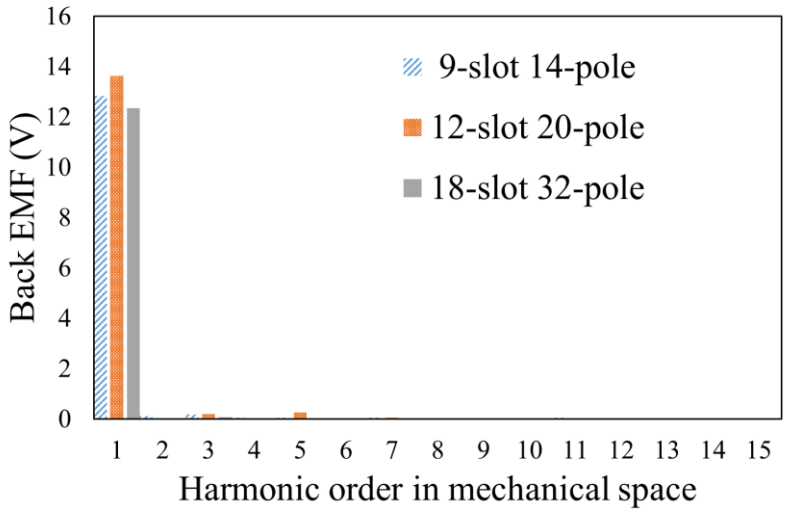

(b)

Fig. 3-13 FE-predicted phase back-EMF (a) Waveform (b) Spectra

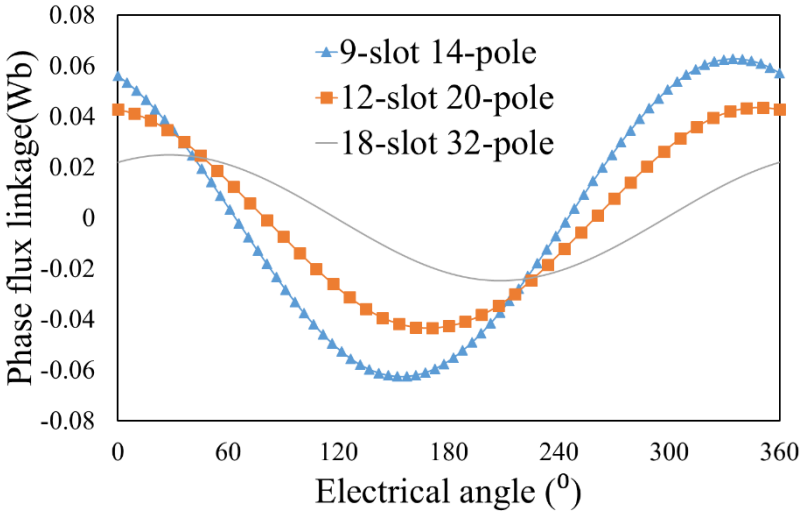

(a)

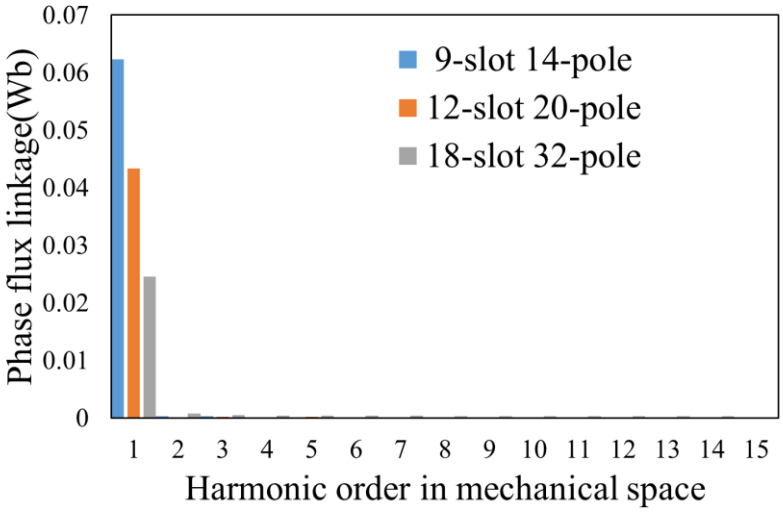

(b)

Fig. 3-14 FE-predicted phase flux linkage (a) Waveform (b) Spectra

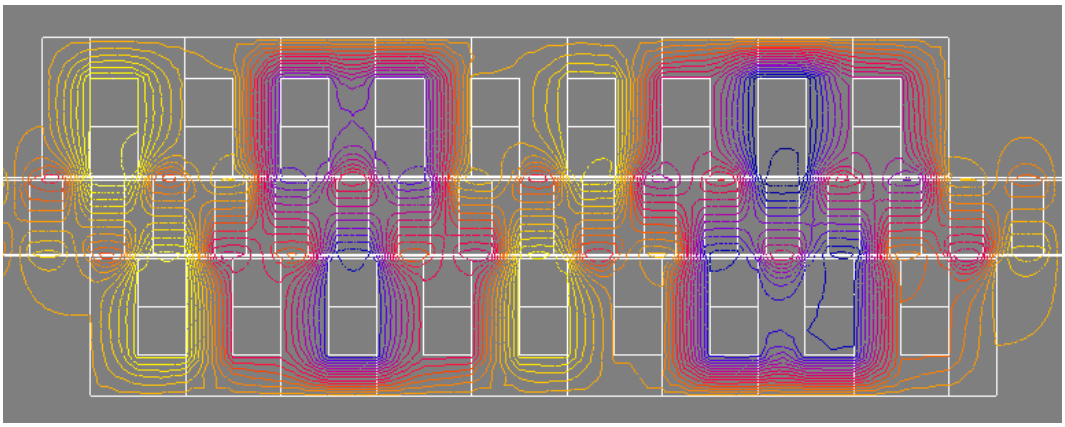

(a)

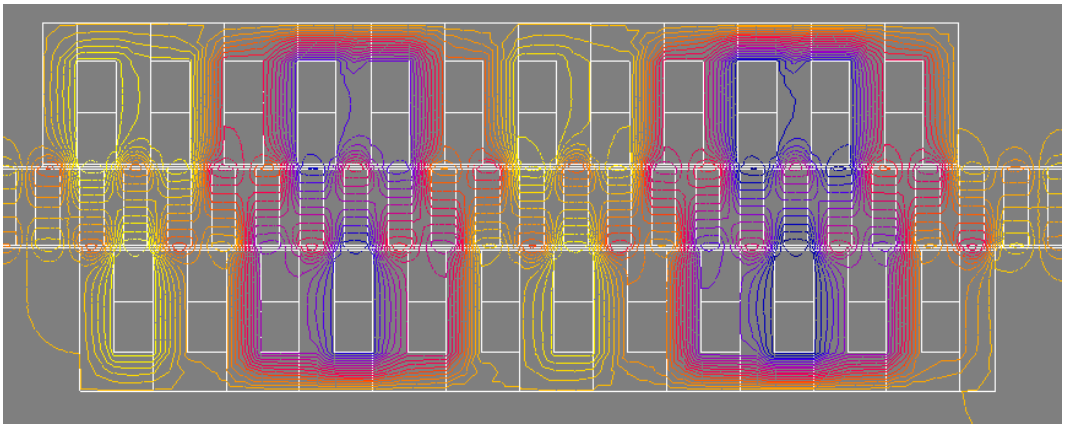

(b)

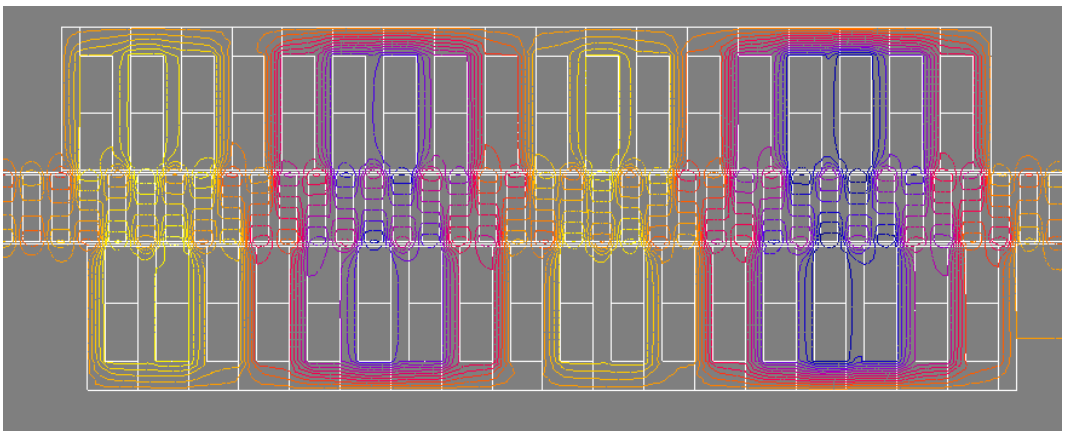

(c)

Fig. 3-15 Back-EMF harmonic component (a) 9-slot 14-pole (b) 12-slot 20-pole (c) 18-slot 32-pole

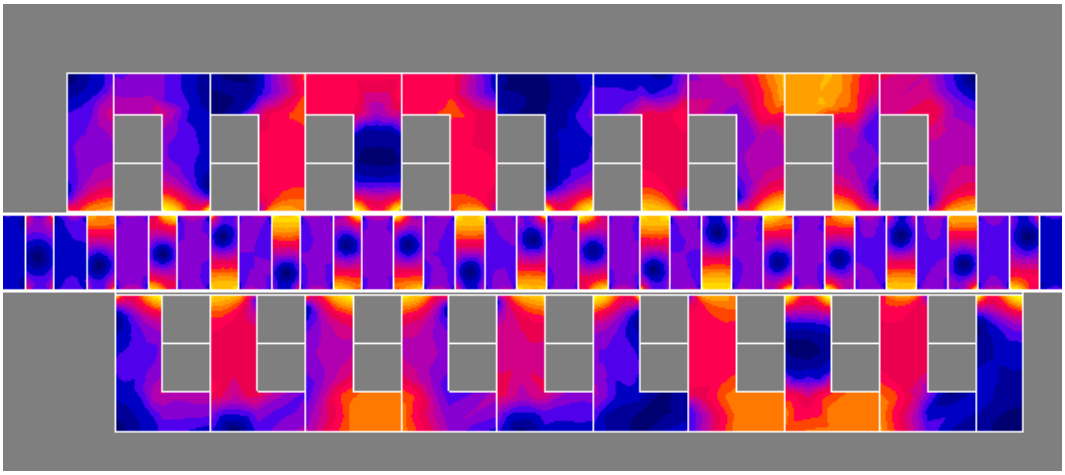

(a)

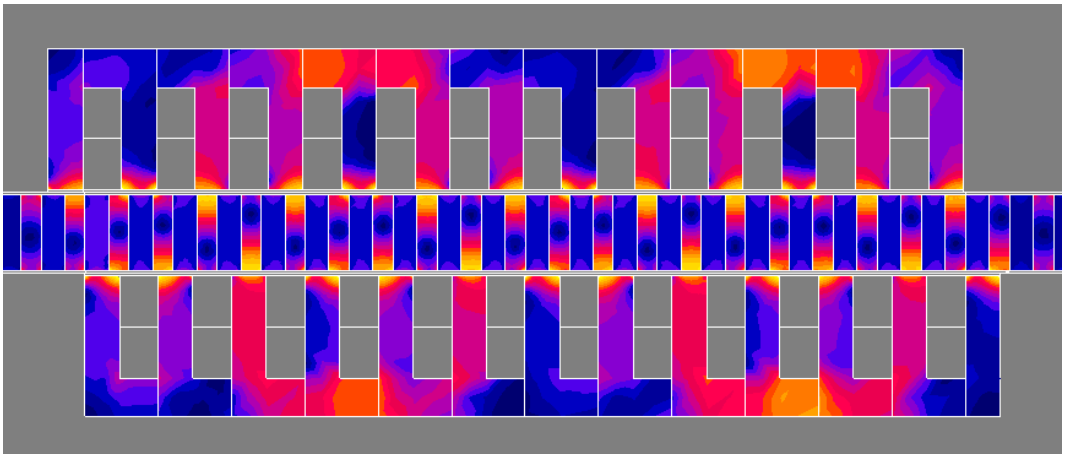

(b)

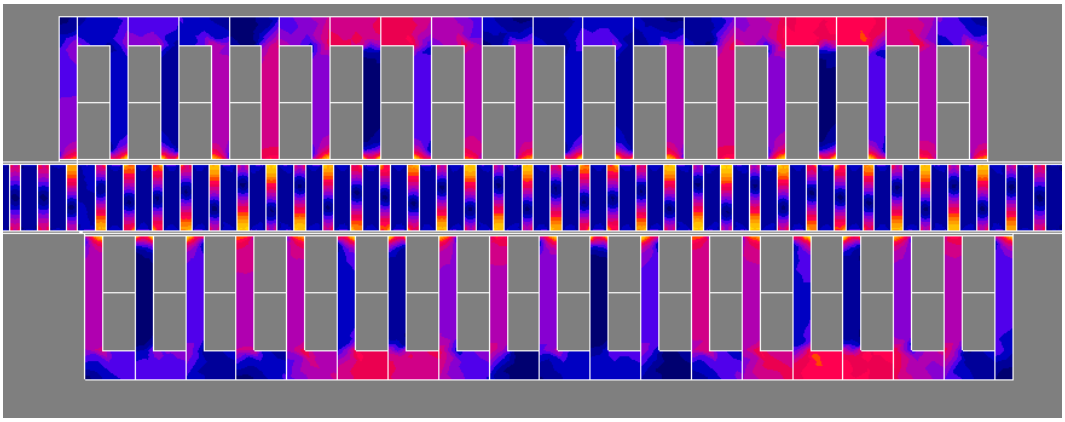

(c)

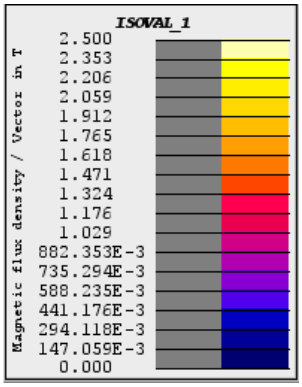

(d)

Fig. 3-16 Comparison of flux density distribution at no load (a) 9-slot 14-pole (b) 12-slot 20-pole (c) 18-slot 32-pole (d) Scale

3.4.2 Force Capability and Power Factor

The FE-predicted rated and peak force waveforms of the three designs are illustrated in Fig. 3-17 and Fig. 3-18. The peak forces are computed at twice the rated electrical loading. The thrust force and power factor of the three designs are compared in Table 3-4. It can be seen from the results that although the gear ratio of the 12-slot 20-pole machine is not the highest, it has the best thrust force capacity and power factor. The 18-slot 36-pole design has the highest gear ratio, but its amplitude of the fundamental flux linkage is lower, and its average thrust force is the lowest.

It can be seen from the back EMF that the 12-slot 20-pole DTVPM has the highest back EMF amplitude, which shows that the pole slot combination has a higher utilization rate of PM. But there is no significant difference in its magnetic cloud map. As the current increases, when the DTVPM reaches the maximum thrust force, the fundamental harmonic amplitudes of the three DTVPM become closer. This may be that the DTVPM is too saturated, which reduces the output capacity of the 12-slot 20-pole DTVPM which

has the highest degree of saturation at no-load working condition. And as mentioned in the Chapter 2, since the 12-slot 20-pole DTVPM has the smallest LCM, its cogging thrust force is the largest.

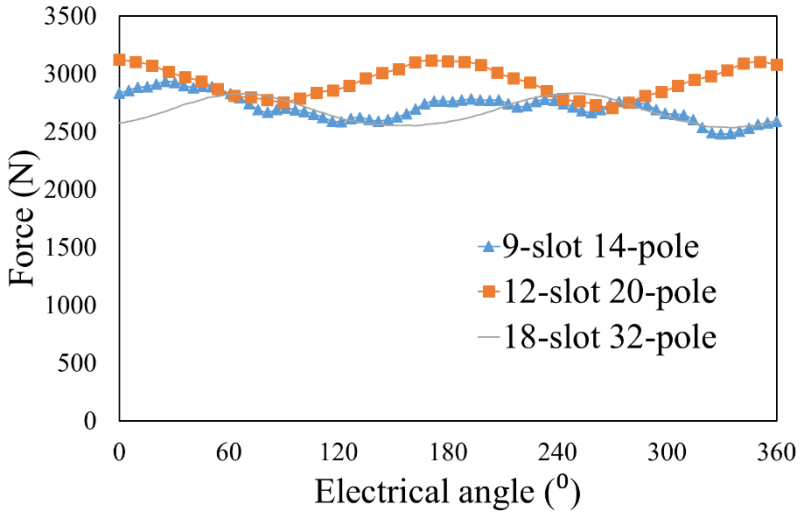

(a)

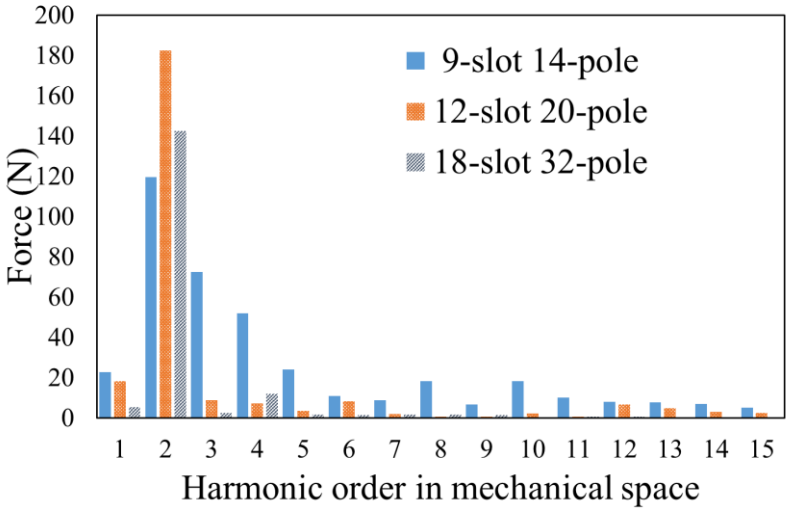

(b)

Fig. 3-17 FE-predicted rated force (a) Waveforms (b) Spectra of force ripples

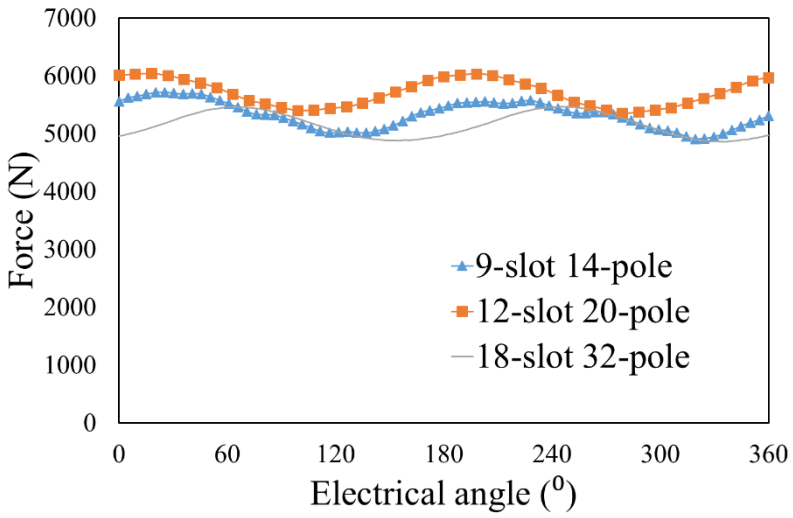

(a)

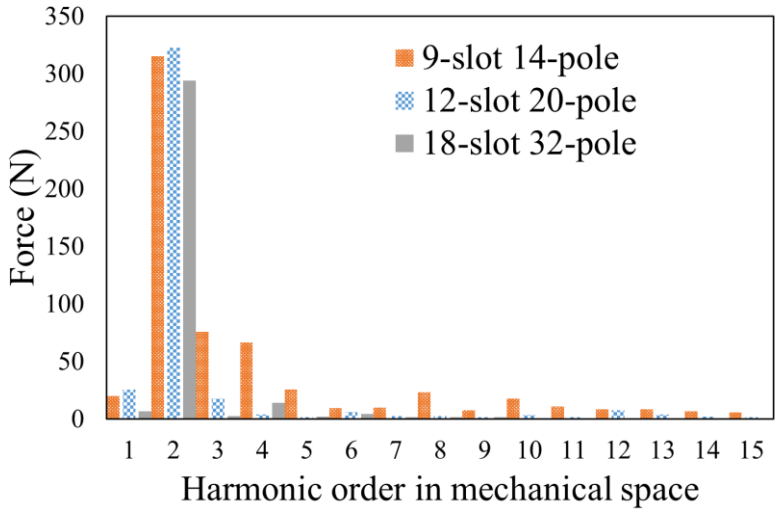

(b)

Fig. 3-18 FE-predicted peak force (a) Waveforms (b) Spectra of force ripple

Fig. 3-19 shows the variations of thrust force with rms current, where the minimum current on the curve is the rated rms current and the maximum current is the rms peak current. It can be seen that the thrust forces of the three motors are almost linearly proportional to rms current. The ratios of the maximum thrust force to the rated thrust force of the (9-slot 14-pole), (12-slot 20-pole) and (18-slot 32 pole) design variants are 1.96, 1.92, and 1.96, respectively. It is worth mentioning that all three machines have a relatively high saturation under no-load conditions. Thus, the good force-current linearity suggests that this machine topology is less sensitive to magnetic saturation. It can be seen from Fig. 3-20 that when the three DTVPM are at the rated load (current), the maximum flux density in the main body of the stator back-irons and stator teeth in all three machines are about 1.88T and 1.58T, respectively. In contrast, Fig. 3-21 shows the flux density

distributions when the three machines are at the peak load. The maximum flux density of the stator back-iron and stator teeth are about 2T and 1.7T. In such a saturated condition, the machine can still output such a high thrust close to twice of the rated.

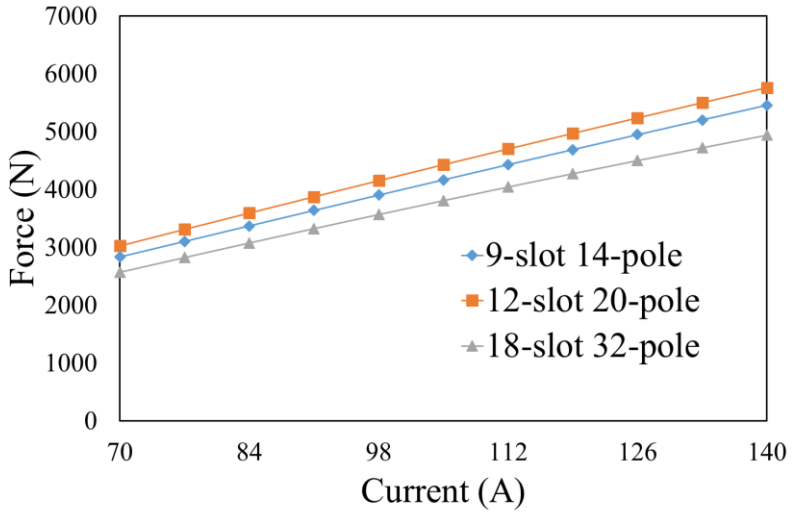

Fig. 3-19 Variations of thrust force with rms current

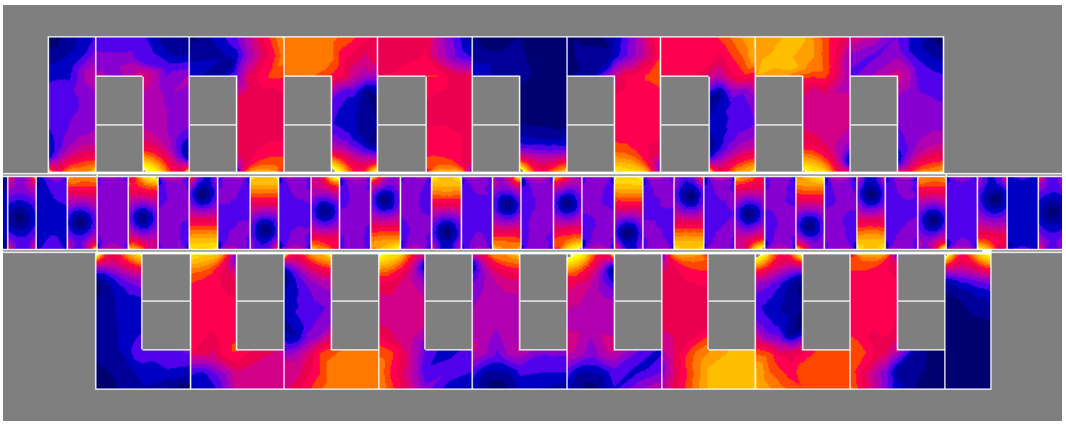

(a)

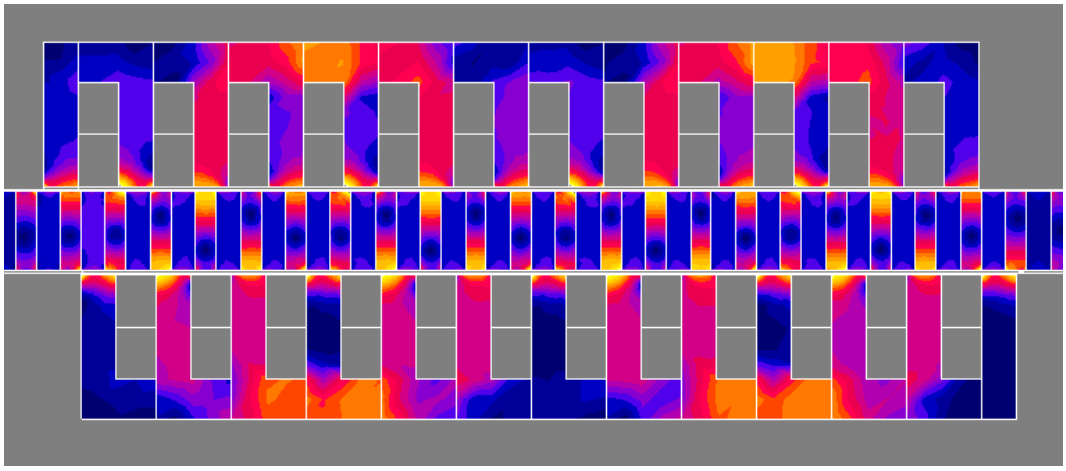

(b)

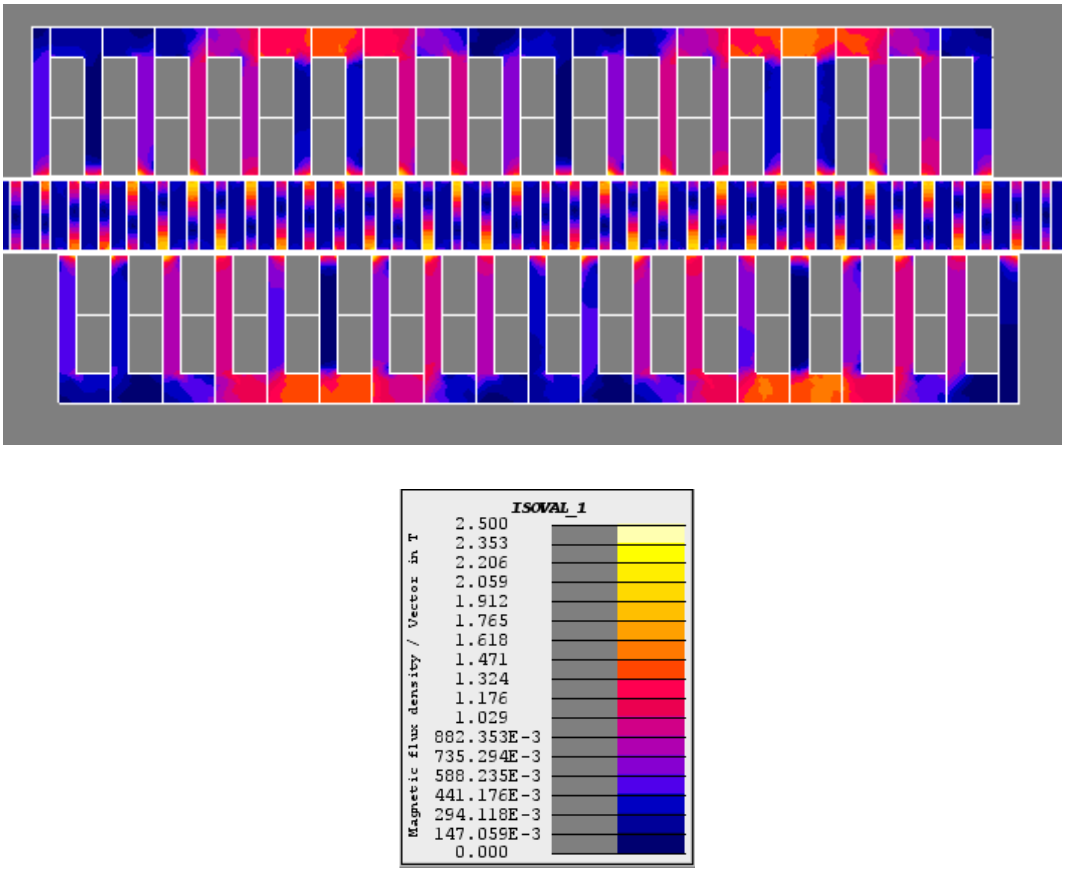

Fig. 3-20 Comparison of flux density distribution at rated load (a) 9-slot 14-pole (b) 12-slot 20-pole (c) 18-slot 32-pole (d) Scale

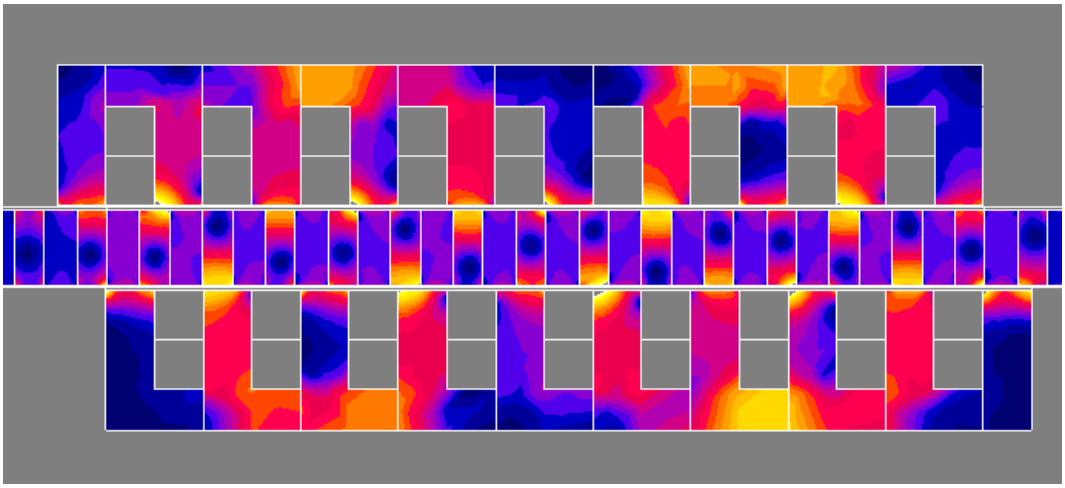

(a)

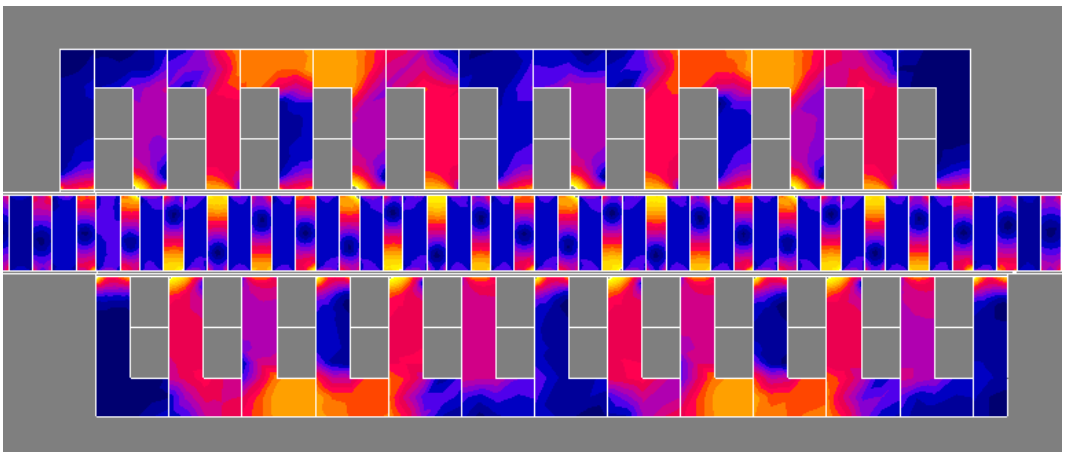

(b)

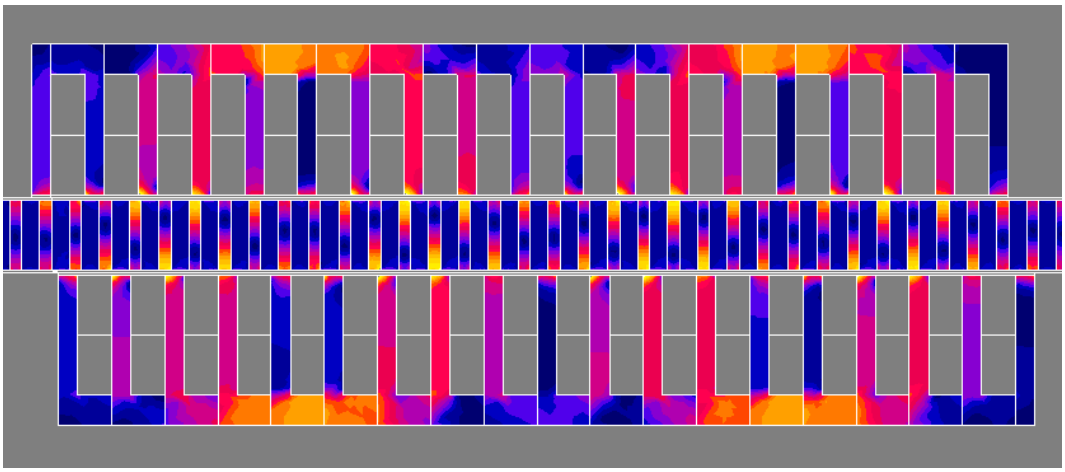

(c)

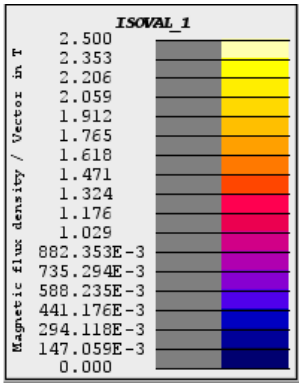

(d)

Fig. 3-21 Comparison of flux density distribution at peak load (a) 9-slot 14-pole (b) 12-slot 20-pole (c) 18-slot 32-pole (d) Scale

Table 3-4 Performance Comparison of DTVPM

Parameters	9-slot 14-pole	12-slot 20-pole	18-slot 32-pole
Rated force (N)	2713	3014	2674
Peak force (N)	5326	5713	5151
Power factor	0.74	0.94	0.83
Rated Force ripple	13	12.3	12.3

Parameters	9-slot 14-pole	12-slot 20-pole	18-slot 32-pole
PM volume($mm^{3)}$	3.8e5	3.6e5	3.5e5

3.4.3 Demagnetization Analysis

Due to the difficulty of dissipating heat from the stator windings in the double stator structure, PM material with high temperature grade N35UH is selected in the design. Fig. 3-22 shows the N35UH magnets demagnetization curve (Arnold Magnetic Technologies Corp 2016). In order to obtain the demagnetization knee point, it is necessary to first obtain the temperature of the motor PM in the rated working state. From the thermal model described previously, the predicted mover temperature at the rated current for three motor is from 172 to176 C^o.

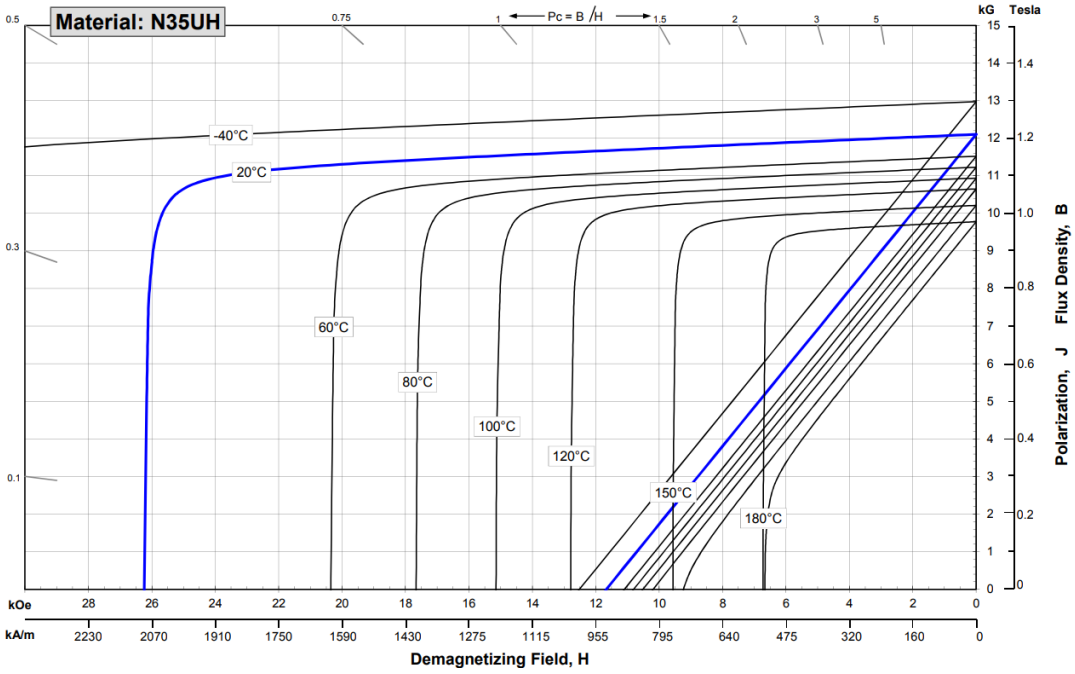

Fig. 3-22 N35UH magnets demagnetization curve

The demagnetization risk analysis is performed by discretising PM on the motor movers, as shown in Fig. 3-23 in blue colour, into many small cells, and computing the resultant flux density in the magnetization direction in each cell over one electrical period under the peak load conditions and the magnet temperature at the rated condition. If the minimum flux density in a cell over one electrical period is lower than the demagnetization knee point, it is considered to be irreversibly demagnetised. Otherwise, it is not. When the motor is running at the peak current, it is assumed that the temperature of the motor magnets has reached the steady-state rated operating temperature. Therefore, the knee point of the motor PM is 180 ℃ and 0.3T in Fig. 3-22. The flux density

distributions in a mover magnet of the three machines at t = 0 is shown in Fig. 3-24. It can be seen that the magnet magnetic density in the interface region with the mover core is significantly reduced due to inter-pole flux leakage. Hence the magnets in this region are more vulnerable. The resultant partial demagnetization is shown in Fig. 3-25. It can be seen that when the machines operate in the peak load conditions, a small part of the mover magnets will have the risk of demagnetization. This may be caused by the special PM array structure. Two PMs with opposite magnetization directions are arranged very close in order to enhance the air gap flux density. However, the magnetic field produced by one magnet also contributes to demagnetising field of the other. Such phenomenon has also been reported in [106].

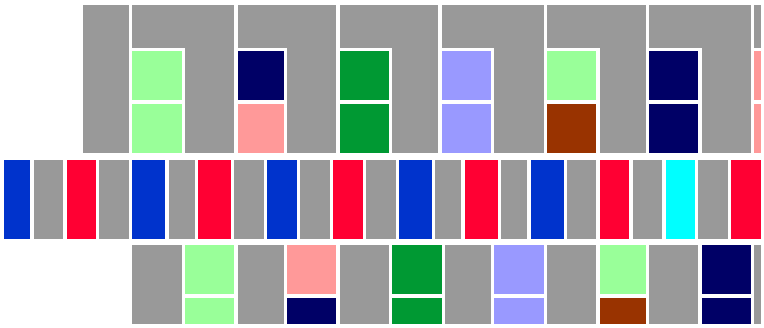

(a)

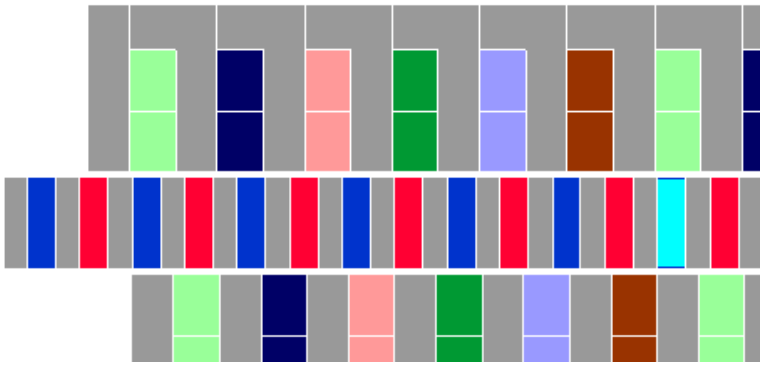

(b)

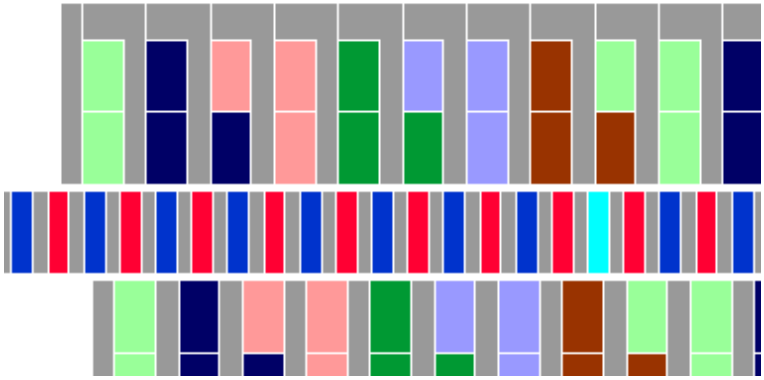

Fig. 3-23 The position of the selected PM (a) 9-slot 14-pole (b) 12-slot 20-pole (c) 18-slot 32-pole

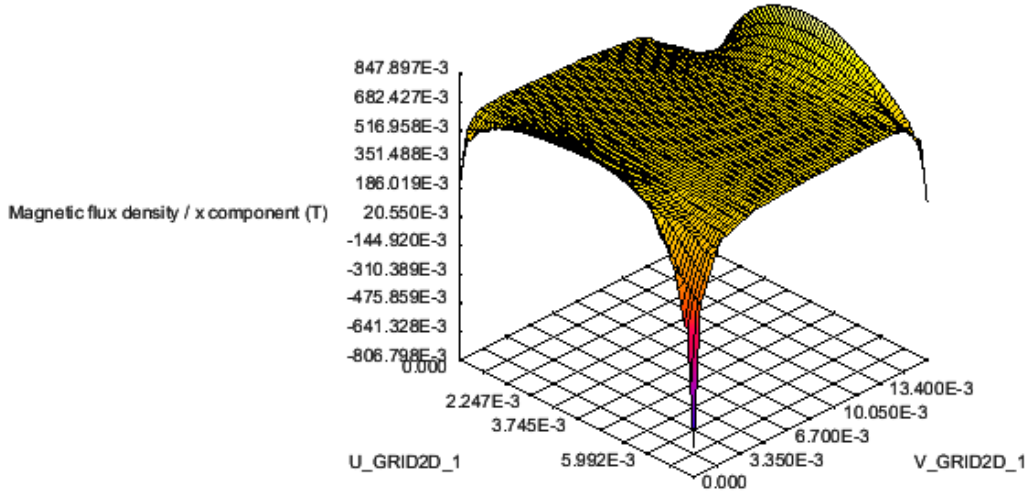

(a)

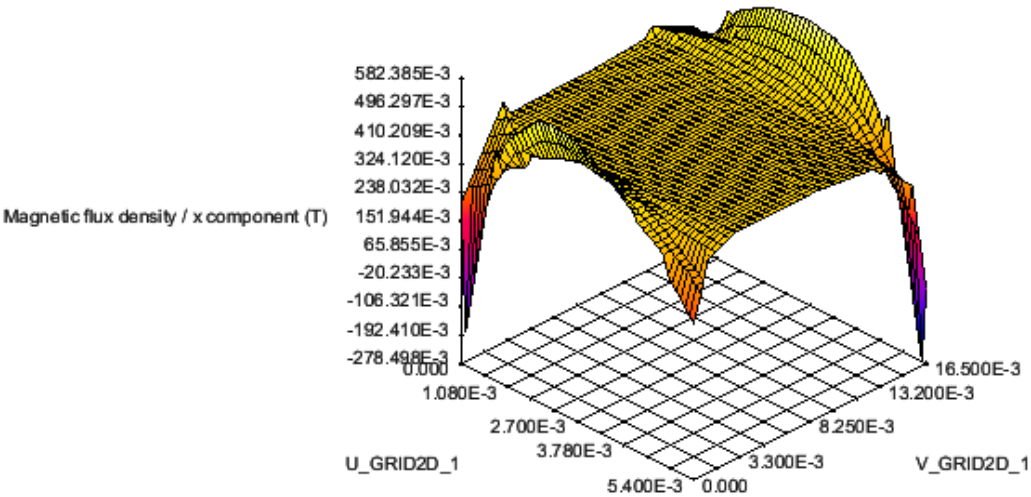

(b)

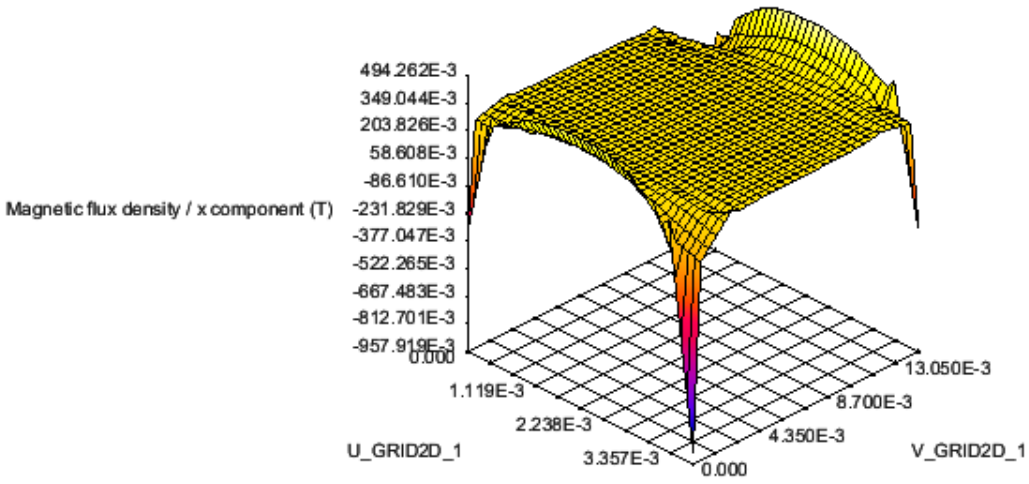

Fig. 3-24 PM flux density distribution at t=0 (a) 9-slot 14-pole (b) 12-slot 20-pole (c) 18-slot 32-pole

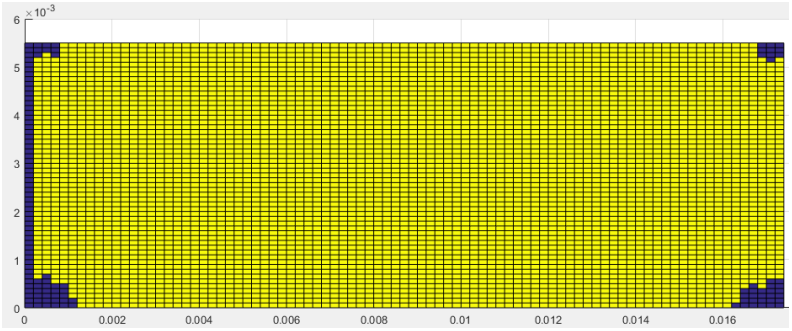

(a)

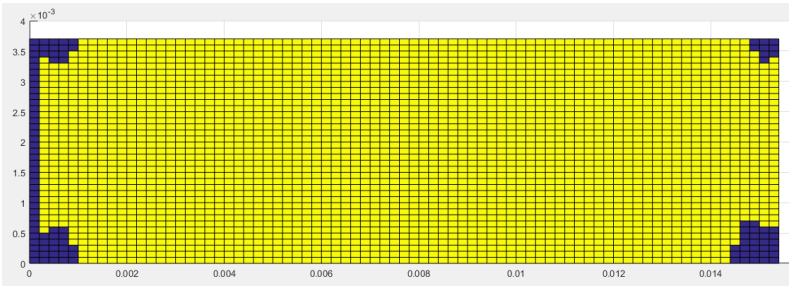

(b)

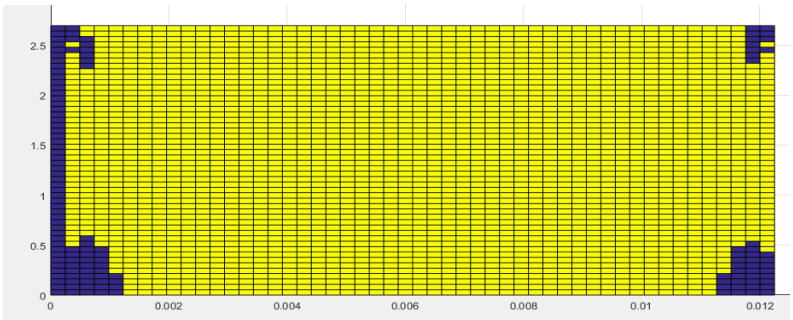

(c)

Fig. 3-25 Demagnetized regions (a) 9-slot 14-pole (b) 12-slot 20-pole (c) 18-slot 32-pole

3.4.4 Thrust Force with Demagnetised PMs at Peak load

Due to the poor heat dissipation capacity of the double stator structure, the PMs of the motor will produce irreversible demagnetization under peak current, and this part of the demagnetization will also affect the thrust force capacity of the DTVPM. In order to reduce the influence of the partial demagnetization of the PM, axial air-gaps are introduced between the mover core and axially PMs, as illustrated in Fig. 3-26. As the demagnetization of the PMs used for the three pole-slot combination is inconsistent. Table 3-5 shows the values of the axial air-gaps g_{ax} and mover pole pitch Tp for three DTVPMs and Fig. 3-27 shows the 9-slot 14-pole FE model with axial air-gaps.

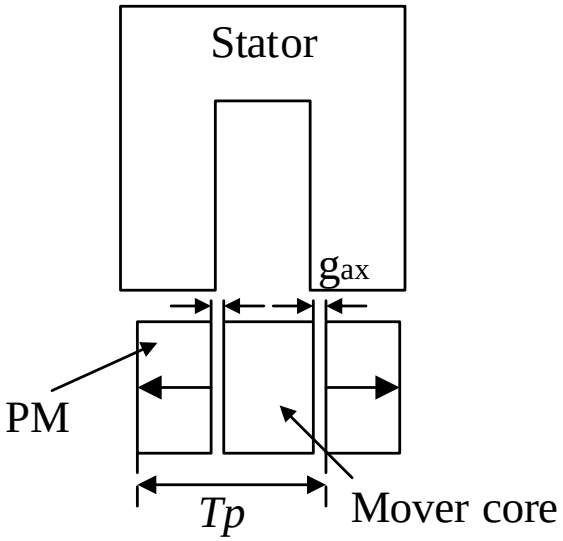

Fig. 3-26 Mover PMs with axial air-gaps

Fig. 3-27 9-slot 14-pole FE model with axial air-gaps

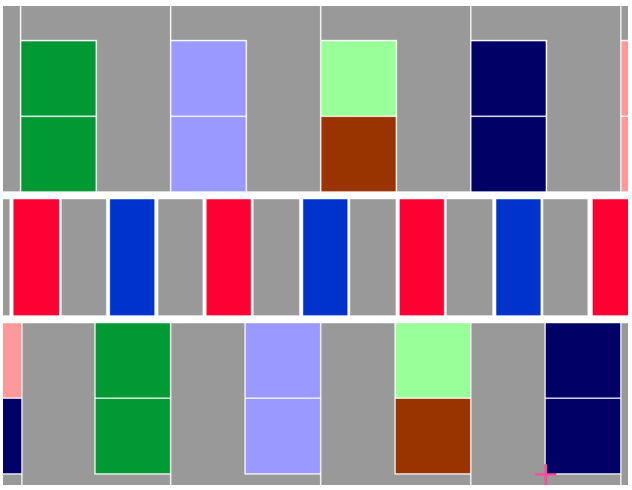

Table 3-5 Axial air-gaps between PM and mover core

Parameters	9-slot 14-pole	12-slot 20-pole	18-slot 32-pole
Tp(mm)	5.5	3.7	2.7

Parameters	9-slot 14-pole	12-slot 20-pole	18-slot 32-pole
g_{ax}(mm)	0.5	0.5	0.4

Fig. 3-28 shows the variations of thrust force with PM air gap and no PM air gap. Due to the loss of PMs, the thrust force curve of the three DTVPM s are similarly trending down. It is worth mentioning that since the cogging force of the linear motor is very sensitive to the air gap, a part of thrust force curve of the 9-slot 14-pole design has a different trend. And Fig. 3-29 compares the variations of thrust force with rms current with PM air gap and no PM air gap, where the minimum current on the curve is the rated rms current and the maximum current is the rms peak current. It is evident that in three DTVPMs the two trends are close, but as the current increases, the loss of motor thrust force output also increases. Table 3-5 listed the reduction of M volume and thrust force, compared with the reduction of PM volume, the reduction of DTVPM peak and rated thrust force is half of that. And even though the 12-slot 20-pole design loses the most PM volume, it still has an advantage in thrust force output.

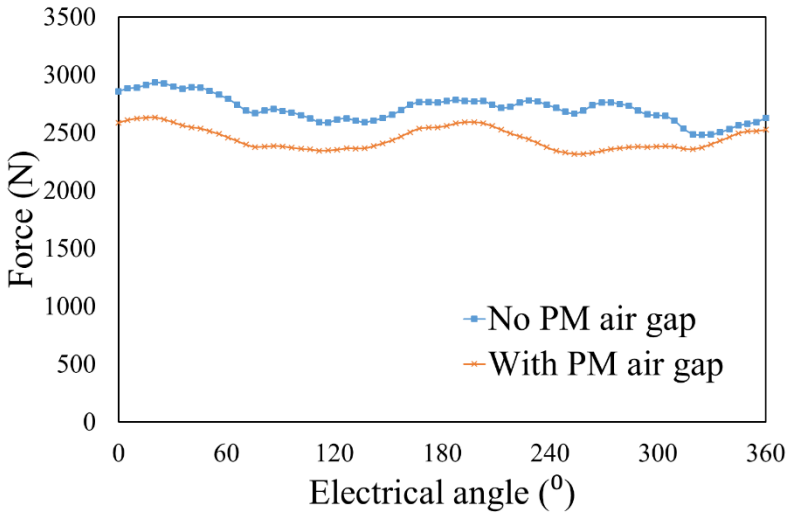

(a)

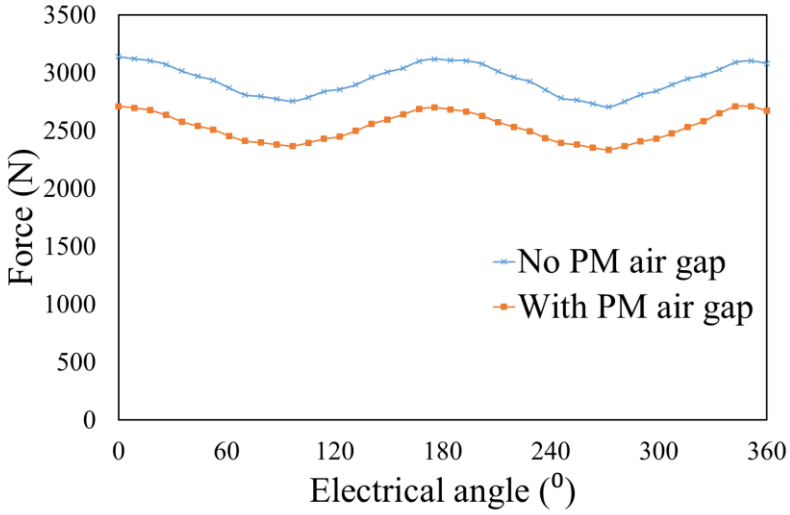

(b)

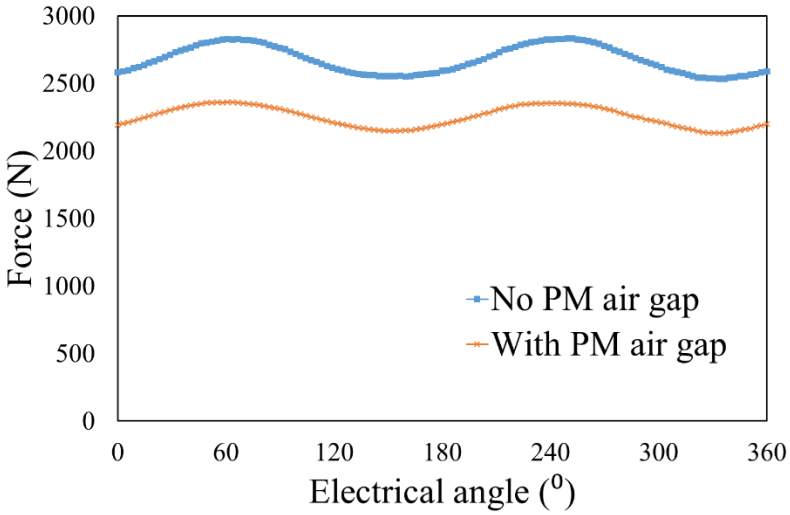

(c)

Fig. 3-28 Thrust force with PM air gap and no PM air gap (a) 9-slot 14-pole (b) 12-slot 20-pole (c) 18-slot 32-pole

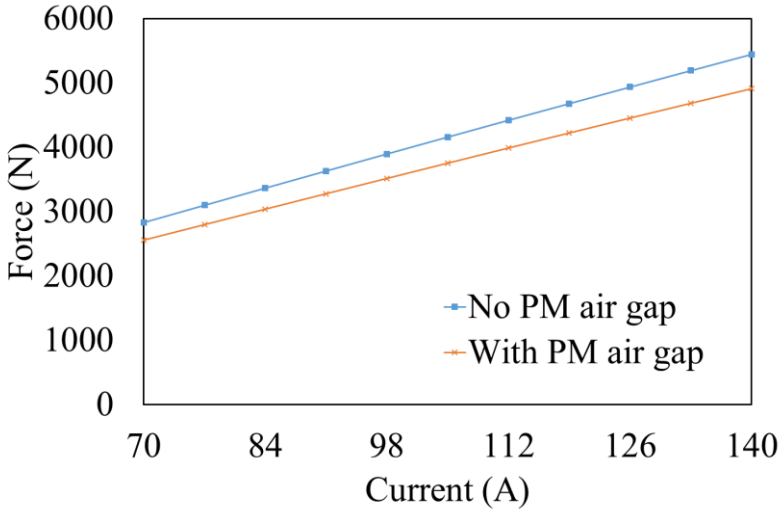

(a)

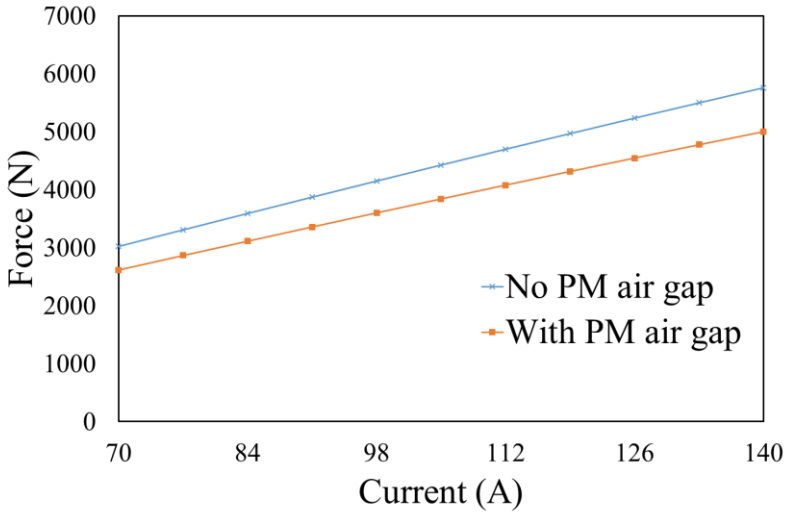

(b)

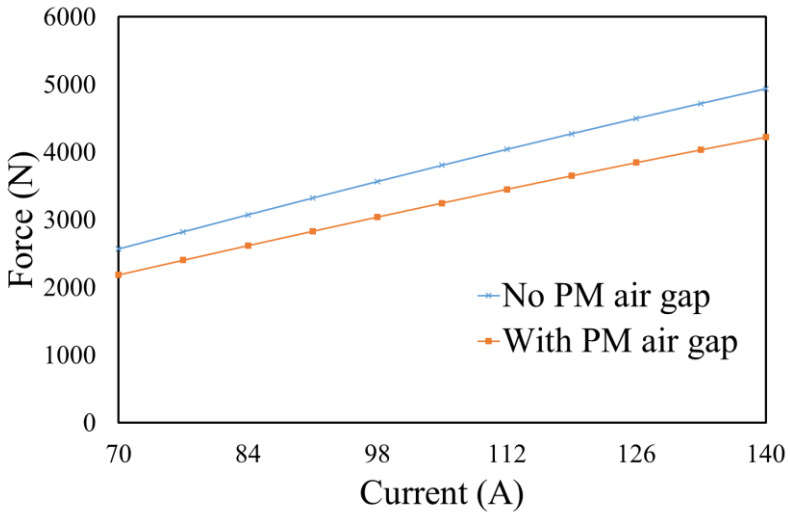

(c)

Fig. 3-29 Thrust force with the stator current with PM air gap and no PM air gap (a) 9-slot 14-pole (b) 12-slot 20-pole (c) 18-slot 32-pole

Table 3-6 Reduction of PM volume and thrust force

Parameters	9-slot 14-pole	12-slot 20-pole	18-slot 32-pole
Reduced PM volume	18%	27%	29%
Reduced rated force	9.6%	13.4%	14.9%
Reduced peak force	9.7%	13.1%	14.6%

3.5 Summary

In order to find a linear actuator topology with higher thrust density, this chapter investigate the potential of a double-sided PM vernier linear motor. Through analysis and

discussions of the advantages of the machine topology, three design variants with different pole-slot number combination are selected and their FE model established. For a fair comparison, the motor design employs the same specification and constraints described in Chapter 2, including volumetric constraints. Table 3-7 shows the output performance comparison of the dual stator structure vernier motor, the single stator structure vernier motor and the surface mount permanent magnet motor in Chapter 2 and Chapter 3.

Since the double-sided stator differs from a conventional tubular machine in thermal dissipation, a representative thermal model for predicting steady-state temperature of the candidate machine has been developed. By incorporating the thermal model, global optimisations of the candidate machines are performed under the same set of specification and constraints. The electromagnetic performance of the optimised motors are subsequently analysed. It has been shown that the two proposed candidates have a very good thrust force capability and high power factor which are derived from the unique features of the candidate topology. In addition, the thrust force of the motor will not be affected by demagnetization in the worst working conditions.

The comparison of the results shows that the output thrust force density of the PM vernier linear motor has a certain advantage compared with the conventional PM linear motor. The 12-slot, 20-pole design variant exhibits ~50% higher force output capability with comparable power factor, compared with the tubular PM machine designed for the same application under the same thermal condition [98]. The comparison is performed under the same main size and input, but the vernier structure uses more PMs and has a lower power factor. The double-side Vernier machine also has a linear thrust force-current characteristics up to the peak current loading. However, these advantages are obtained at the expense of the increased complexity of the stator structure and manufacturability.

Table 3-7 Performance Comparison of VPM

Parameters	9/14	12/20	18/32	18/26	18/28	9/10
Rated force (N)	2713	3014	2674	2159	2184	1953
Peak force (N)	5326	5713	5151	3402	3646	3835
Power factor	0.74	0.94	0.83	0.53	0.6	0.9
Rated Force ripple	13	12.3	12.3	10	6	20
PM volume($mm^{3)}$	3.8e5	3.6e5	3.5e5	3.8e5	3.6e5	3.5e5

CHAPTER 4
Design and Modelling of Magnetic Screw Linear Actuator

This chapter investigates a high force density linear electromagnetic actuator which integrates a magnetic screw with a rotary permanent magnet(PM) motor. The integrated linear actuator is denoted as magnetic screw linear actuator (MSLA). The principle of magnetic screw is briefly outlined and an analytical expression that can be used to predict thrust force density of a magnetic screw is established. The concept that integrates the magnetic screw into a rotary PM motor is described. Determining the key parameters affecting thrust force density provides a theoretical basis and technical insight for general optimization of an MSLA. The design process includes selection of motor pole slot number coordination, establishment of MSLA finite element model and global optimization of the leading parameters. The predicted results show that the MSLA has a thrust force density much greater than that of a conventional linear electromagnetic motor.

4.1 Introduction

The challenge for acticve suspension linear actuator is that it has to achieve both high thrust force density, high reliability, high dynamic performance and direct thrust capability. The previous two chapters studied the vernier linear actuator, and designed a dual-stator vernier linear actuator that can significantly increase the thrust force density. However, the force density of a linear electromagnetic actuator is fundamentally limited by achievable magnetic flux density in airgap and the current density in the armature winding under a thermal constraint. It has been shown in [106] that a linear PM actuator can achieve a force density of ~0.6 MN/m^3 with water cooling jacket, which is still far below required force density in many applications.

4.1.1 Magnetic Screw

In order to further enhance the thrust density of linear electrical actuator, a magnetic screw structure is developed which can be used in linear electromagnetic actuator. In 1998, W. A. Smith proposed the original structure of the magnetic screw and applied it to the field of artificial heart [108]. The rotary motion was converted into linear motion through helix magnetic transmission. Due to the limitation of the development and design with low grade PM material, it has not attracted widespread attention. In 2011, a high-thrust-force density magnetic screw actuator was proposed by employing rare-earth permanent

magnets [109]. The operating principle of the magnetic screw is analysed in detail and its electromagnetic thrust force is calculated analytically. Its predicted thrust force density can reach more than 10MN/m^3 which is more than an order of magnitude larger than the conventional linear electromagnetic motor.

In 2013, Rasmussen proposed an axial magnet embedded magnetic screw structure [110-111], which is easy for demonstrating the principle. Due to structure simplification, in which circular magnets are inserted in holes in the helix path on the surface of the cylindrical back-irons, to approximate the helical magnetic patterns, the magnets are poorly utilised, and the output thrust force is not unsatisfactory. H. A. Toliyat proposed a design idea of variable "torque-thrust" and "angle-displacement" magnetic screw by changing the number of pole pairs of the spiral PMs and the lead, and gave basic conclusions [112-113]. F. Gao conducted research on magnetic screw with variable pole pairs, supplementing the relationship between pole pair and magnetic field modulation [114]. In order to obtain an approximate helix magnetic field, S. Pakdelian uses segmented magnetic blocks to approximate to helix PM patterns [115]. The test results show that in the field of low-speed transmission, compared with tubular PM linear motors of the same size, the magnetic screw has absolute advantages in terms of thrust force density, loss, weight, volume and material cost.

Based on the PM magnetic screw structure, K. Lu proposed an electromagnetic magnetic screw [116]. This magnetic screw mover is composed of a helix slot and coil, thus generates a helix magnetic field through electric excitation. The structure simplifies the processing difficulty of the mover, and saves the amount of PM materials. And, by adjusting the amplitude of the current, it can respond to the load changes in time. But compared to the PM magnetic screw structure, its thrust force density is reduced by about 75%. At the same time, Q. Wang proposed a PM-inductive sub-type hybrid excitation magnetic screw structure [117], which makes the magnetic screw air gap magnetic field adjustable. However, compared with the PM magnetic field, the magnetic flux density is much smaller, which makes the effect of electric excitation not obvious enough.

Therefore, in this chapter, in order to obtain a linear actuator structure with greater thrust force density, the design object adopts a structure with PMs on both sides of the air gap with the largest flux density.

4.1.2 Magnetic Screw Linear Actuator with PM Motor

Since the magnetic screw cannot directly generate thrust, magnetic screws requires additional input structure. As the PM motor itself has a high torque density, the rotating PM motor integrated magnetic screw can exert its advantages, such as very high force density and direct thrust force capability. The torque from the rotary PM machine converted to linear thrust force by the magnetic screw has the same advantage of a mechanic lead screw, but is contactless and hence free from jamming.

From late 2000s, many magnetic screw motors were proposed. S. Pakdelian directly connects the magnetic screw structure with the motor shaft [118], which drives the magnetic screw rotor to rotate, so that the linear thrust force can be applied to the mover. This magnetic screw uses segmented vertical PMs to approximate helix PMs. The rotor of the magnetic screw motor is on the inner side and the mover is on the outer side. The mover is connected to the test rig guide rail to prevent it from rotating. Compared with the conventional linear tubular motor, the output thrust density of magnetic screw motor actuator is an order of magnitude higher. However, due to the high price of the approximately helix PMs, the magnetic screw motor may lose its advantage for long stroke and low thrust force applications. Z. Ling proposed a radially magnetized magnetic screw actuator with discretized PMs [119]. The segmented PMs of the magnetic screw are cut along the spiral direction, making the structure closer to the helix PMs. And the assembly uses the iron core slotted to cooperate with the PM bulge, which makes the PMs distribution more accurate. This structure simplifies the processing and assembly difficulty of the magnetic screw, and can also achieve a good output thrust force. J. Ji introduced the Halbach array structure and designed a magnetic screw motor for artificial heart [120]. This actuator direct combination a SPM motor and a magnetic screw, and the two share same rotor. The whole structure from the outside to the inside is the motor stator, rotor, and magnetic screw mover, and the PM structures of the SPM motor and magnetic screw are all Halbach arrays. The predicted results show that the output thrust density of the magnetic screw motor using the Halbach array is increased by about 72%.

The aim of this chapter is to design a magnetic screw motor for active suspension applications and establish general design principles and analysis methods for this kind of high thrust force density linear electromagnetic actuator. The process is to design the magnetic screw and SPM motor separately according to the design specification and

constraints, and combine the two to establish an overall dynamic simulation FE model, and perform testing verification in the subsequent chapters.

The rest of this chapter is organized as follows. In section 3.2, the structural characteristics and operating principles of the magnetic screw is introduced and the influence of its leading design parameters on thrust force density analysed. In section 3.3, the concept of a linear actuator which integrates a magnetic screw with a rotary PM motor to achieve high force density is presented. According to the design specification and constraints, an 8-pair pole magnetic screw is designed and analysis. In section 3.4, a matching 18-slot 8-pole SPM motor is designed. In Section 3.5, a 3D FE model of the MSLA is established, and its output performance is analysed. Finally, section 3.6 summarizes the key findings.

4.2 Magnetic Screw Topology and Principle

Fig. 4-1 shows the magnetic screw structure. It is composed of a pair of helically magnetized magnets deployed on the outer surface of a mover iron core and the inner surface of a rotary iron core. When the rotor rotates, the interaction of the inner and outer helix PMs generates thrust force on the mover.

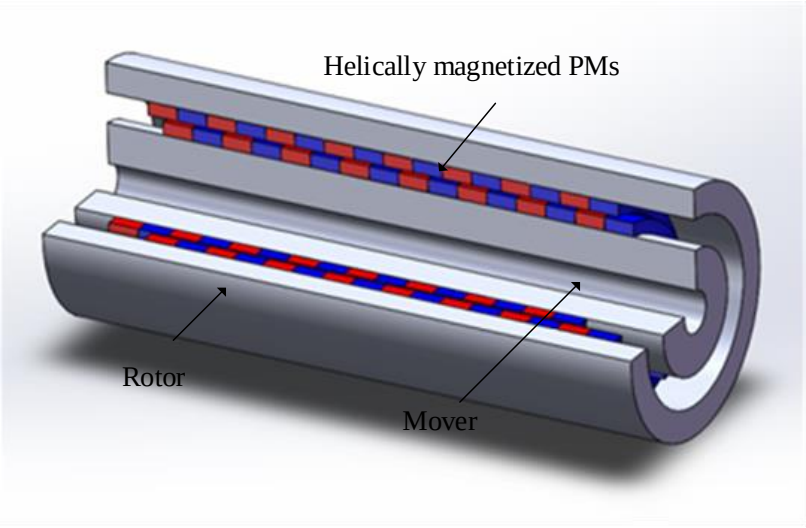

Fig. 4-1 Magnetic screw

4.2.1 Analysis of Magnetic Screw Thrust Force

In the structure of the magnetic screw, there is no mechanical contact between the rotor and the mover, and the energy transfer is realized by magnetic field coupling. The output of linear mechanical energy on the mover can be realized by inputting rotating mechanical energy on the rotor.

The axial thrust force of the magnetic screw is generated by the mutual coupling between the PM fields of the rotor and the mover. As shown in Fig. 4-2 (a), when the centre of the north or south poles of the helix PMs on the mover and rotor is aligned with each other, the rotor angular displacement with respect to the mover $\theta_r = 0$, and the mover linear displacement with respect to the rotor $z_d = 0$. In this position, the magnetic field distribution in the air gap has no axial component, and the thrust force $F_t = 0$N.

When the rotor rotates an angle of θ_r, the relative position z_d between the rotor and mover changes accordingly. The helix PMs on the rotor and mover develop radial and axial components of flux density in the air gaps, which then generates thrust force F_t. It can be seen from the continuity of thrust force that as the rotor rotation angle θr changes, the thrust force F_t will reach peak at a certain position. In a pair of pole magnetic screw, when the rotor rotation angle $\theta_r = \pi/2$, the relative displacement between the rotor and the rotor reaches $z_d = \lambda/4$, where λ is defined as the lead of the magnetic screw as shown in Fig. 4-2 (b), the thrust force F_t is maximum at this position.

With the further increase of the rotor angle θ_r, the axial component of the air gap magnetic field gradually decreases, and the amplitude of the thrust F_t also gradually decreases. When the helix PMs on the rotor and mover are aligned in the opposite magnetization directions, the air gap has no axial magnetic field component, as shown in Fig. 4-2 (c), the thrust force becomes $F_t = 0$N.

It can be seen that the output thrust force of the magnetic screw is determined by the relative position of the rotor and the mover. When the load does not exceed the maximum thrust force, the rotor and the mover will remain at a certain relative position to achieve continuous thrust force output. When the load exceeds the maximum thrust force, sliding will occur between the rotor and the mover, which will not cause mechanical irreversible damage to the magnetic screw and serve as overload protection feature of the magnetic drive.

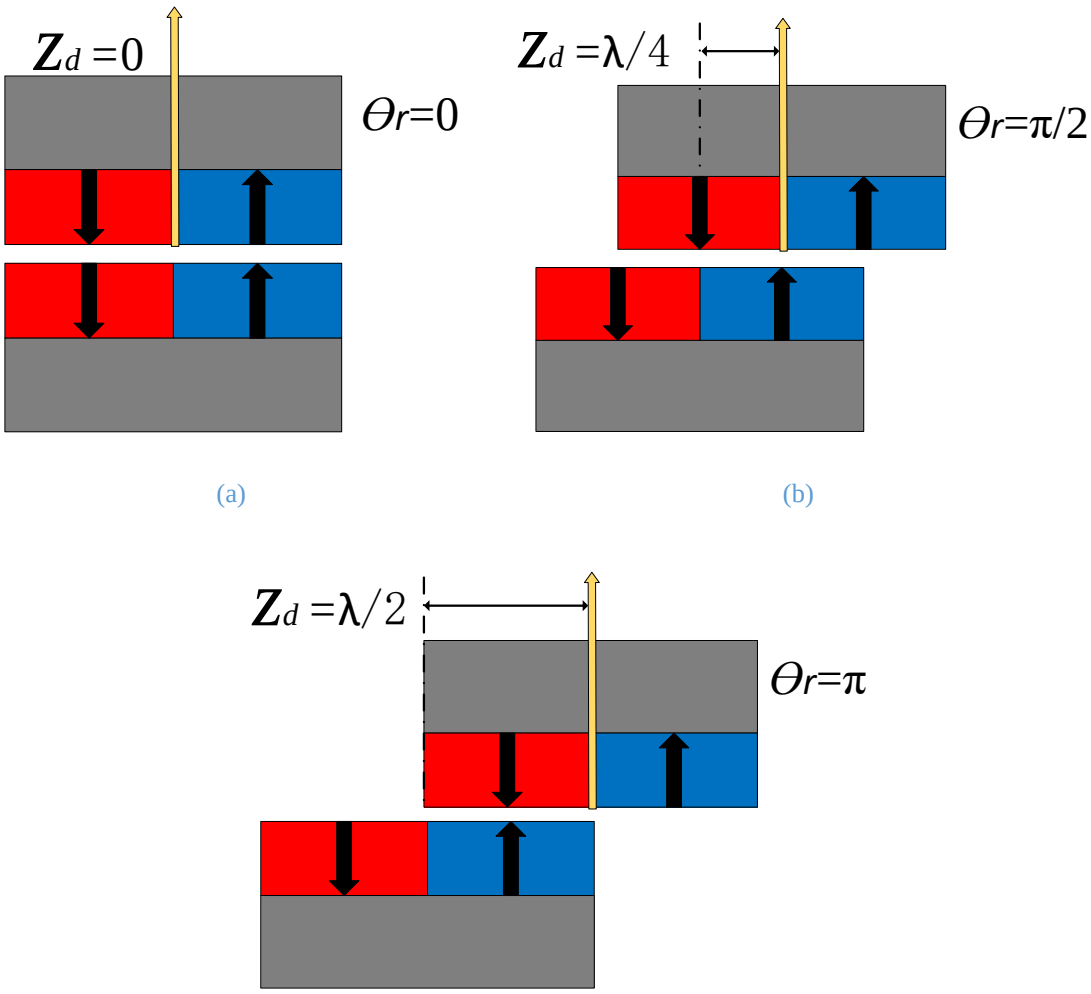

Fig. 4-2 Angle-displacement diagrams of magnetic screw (a) N and S aligned in the same magnetization direction (b) at peak thrust force position (c) N and S aligned in opposite magnetization direction

4.2.2 Magnetic Screw Transmission Mechanism Analysis

Similar to the mechanical screw, the two parts move in synchronism; that is, whenever the nut (rotor) rotates one revolution, the magnetic screw mover moves a distance λ known as the screw lead, which equals to two times of the magnetic pole-pitch. According to the principle of conservation of energy, if the loss is neglected, the rotational power P_r of the rotor and the linear motion power P_t of the mover should be equal. The relationship between torque T_n and the thrust force F_t can be drawn, by

$$P_r = T_n \times \omega_r = F_t \times v_t = P_t \tag{4-1}$$

$$T_n = \frac{\lambda}{2\pi} F_t \tag{4-2}$$

where ω_r and v_t are rotor angular speed and mover linear speed. Therefore, when the appropriate magnetic pole-pitch and radius are selected, the magnetic screw can generate

very high thrust force like a mechanical screw, and the structure is contactless and jam-free. And for a magnetic screw with a pole-pitch τ_p, the lead will be $2\tau_p$. For a given mover torque, the shorter the magnetic screw lead, the higher the mover thrust force and the rotor angular speed. The gear ratio, *G*, can be defined as:

$$G = \frac{\omega_r}{v_t} = 2\pi/2\tau_p = {}^{\pi}/_{\tau_p} \tag{4-3}$$

4.2.3 Magnetic Screw Analytical Thrust Force Calculation

As shown in Fig. 4-1, magnetic screw adopts a surface-mounted helix PM structure with alternately magnetization direction. Hence there is a three-dimensional helix magnetic field in the working air gap between the rotor and the mover. Generally, the three-dimensional FE method is a more accurate tool for calculating the distribution of this helix magnetic field. However, the three-dimensional FE method has the disadvantages of complex preliminary processing and long calculation time; while the analytical method has the characteristics of simplicity and speed, which facilitates the rapid solution of the air gap magnetic field distribution. Therefore, first, the helix magnetic circuit model is used to analyse the thrust force of the magnetic screw, and then the FE method is used to verify the analytical results.

For a magnetic screw, in order to obtain a larger thrust force density, the length of its working air gap g should be as small as possible within the controllable range of machining. If the air gap length of the magnetic screw is much less than the PM pole pitch, τ_p, the field distribution can as approximate as axially symmetric. The analytical calculation method of thrust force is as follows. First, to establish the magnetic field distribution of the radially magnetized PMs on the mover; second, to obtain equivalent current sheet model of the rotor magnets; finally, interacts the mover magnetic field with the rotor current sheet to generate axial electromagnetic thrust force.

In order to approximate the magnetic field distribution in the air gap of the magnetic screw, the following ideal conditions are assumed:

1) In the z direction the field distribution is axially symmetric and periodic;

2) The back-irons of the nut and screw are infinitely permeable.

Hence, taking the magnets region and the airspace region as the solution region, as shown in Fig. 4-3 (a), then the B-H relationships are given by

$$B = \begin{cases} \mu_0 H & \text{airspace region} \\ \mu_0 \mu_r H + \mu_0 M & \text{magnets region} \end{cases} \tag{4-4}$$

where μ_r is the relative recoil permeability and μ_0 is the permeability of the airspace; M is the remanent magnetization, which is determined by the remanence of the magnets, B_{rem}, $M = B_{rem}/\mu_0$, in the cylindrical coordinate system, the remanent magnetization M is expressed as

$$M = M_r e_r + M_z e_z \tag{4-5}$$

where M_r and M_z are the radial and axial components of the remanent magnetization.

Since the PM uses radial magnetization, the remanent magnetization M only contains the radial component M_r, and the axial component M_z =0. Assuming that the surface of the mover magnet is an isomagnetic potential surface, the distribution of the radial component of the magnetization at the mover surface, as shown in Fig. 4-4, can be expressed as

$$M_r = \begin{cases} -M_0 & -\frac{\tau_p+\tau_m}{2} \le z \le -\frac{\tau_p-\tau_m}{2} \\ 0 & -\frac{\tau_p-\tau_m}{2} \le z \le \frac{\tau_p-\tau_m}{2} \\ M_0 & \frac{\tau_p-\tau_m}{2} \le z \le \frac{\tau_p+\tau_m}{2} \end{cases} \tag{4-6}$$

where τ_m is the axial width of the magnets. Expand the PM magnetomotive force shown in Fig. 4-4 into a Fourier series

$$M_r = 4B_{rem}/\mu_0 \sum_{n=1,2,\ldots}^{\infty} \frac{\sin(2n-1)\pi\alpha_p/2}{(2n-1)\pi} \cos m_n z_d \tag{4-7}$$

where $\alpha_p = \tau_m/\tau_p$ is PM pole pitch coefficient, and m_n is given by

$$m_n = \frac{(2n-1)\pi}{\tau_p} \tag{4-8}$$

In order to calculate the magnetic field of the mover PMs, it is necessary to solve the Laplace/Poison equation of the magnetic vector potential A in the magnets region and the airspace region as

$$\begin{cases} \nabla^2 \times A_{\mathrm{I}} = 0 & \text{airspace region} \\ \nabla^2 \times A_{\mathrm{II}} = -\mu_0 \times M & \text{magnets region} \end{cases} \tag{4-9}$$

In (4-9), "I" and "II" represent the airspace region and the magnets region respectively. Combining (4-7) and (4-9), the boundary and interface conditions that the air gap magnetic field A must satisfy are given in (4-10)

$$B_{\mathrm{Iz}}|_{r=R_s} = 0,\ \ B_{\mathrm{IIz}}|_{r=R_r} = 0,$$

$$B_{\mathrm{Iz}}|_{r=R_m} = B_{\mathrm{IIz}}|_{r=R_m},\ \ H_{\mathrm{Iz}}|_{r=R_m} = H_{\mathrm{IIz}}|_{r=R_m} \tag{4-10}$$

$$\begin{cases} \dfrac{\partial}{\partial z}\left(\dfrac{1}{r}\dfrac{\partial}{\partial z}(rA_{\mathrm{I}\theta})\right)+\dfrac{\partial}{\partial r}\left(\dfrac{1}{r}\dfrac{\partial}{\partial r}(rA_{\mathrm{I}\theta})\right)=0 & \text{airspace region} \\ \dfrac{\partial}{\partial z}\left(\dfrac{1}{r}\dfrac{\partial}{\partial z}(rA_{\mathrm{II}\theta})\right)+\dfrac{\partial}{\partial r}\left(\dfrac{1}{r}\dfrac{\partial}{\partial r}(rA_{\mathrm{II}\theta})\right)=\sum_{n=1,3,5\ldots}^{\infty} P_n \sin m_n z & \text{magnets region} \end{cases}$$

(4-11)

where P_n=4 B_{rem} sin($n\pi$/2) k_c/(μ_0 $n\pi$). Subsequently, using the analytical method proposed in [6], the radial and axial components of the magnetic field distribution expression in the airspace region are obtained as

$$B_{\mathrm{Ir}}(r,z) = -\sum_{n=1,3,5..}^{\infty}[a_{\mathrm{In}}BI_1(m_n r)+b_{\mathrm{In}}BK_1(m_n r)]\cos(m_n z)$$

$$B_{\mathrm{IIr}}(r,z) = -\sum_{n=1,3,5..}^{\infty}[a_{\mathrm{In}}BI_0(m_n r)-b_{\mathrm{In}}BK_0(m_n r)]\sin(m_n z) \tag{4-12}$$

where BI_0(•) and BI_1(•) is modified Bessel functions of the first kind, BK_0(•) and BK_1(•) is modified Bessel functions of the second kind; and a_{In} and b_{In} are the coefficients associated with the nth harmonic component. They are given in [6].

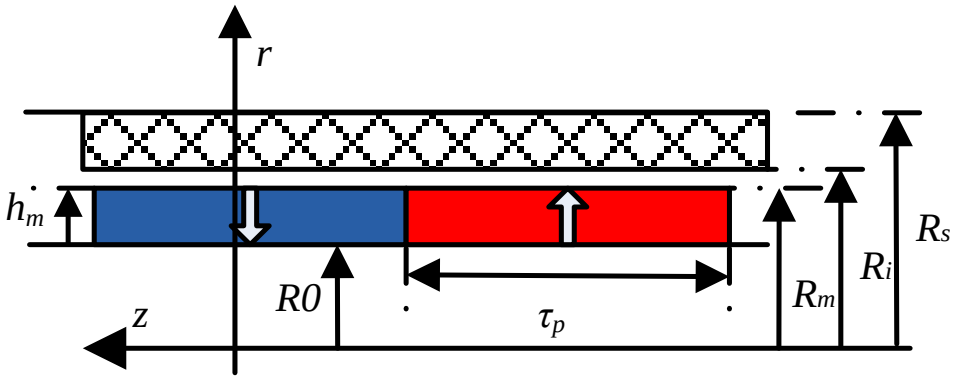

(a)

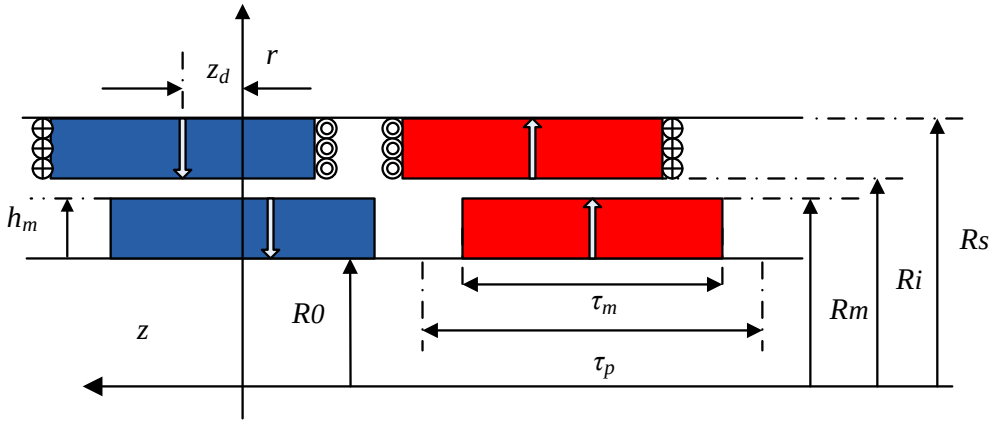

(b)

Fig. 4-3 Axially symmetrical model (a) Field regions (b) Equivalent current sheet model

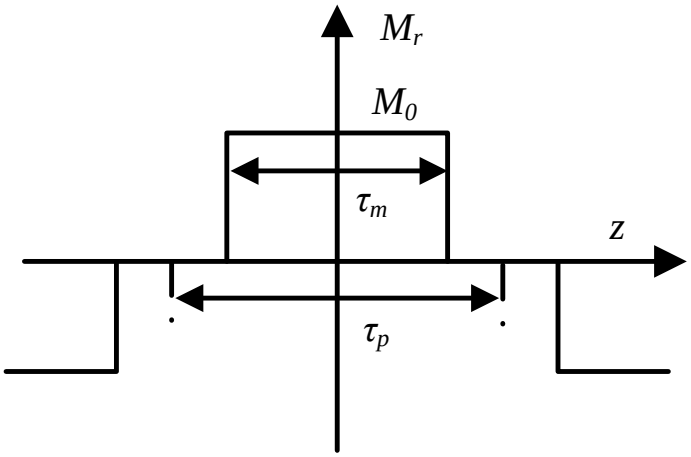

Fig. 4-4 Magnetomotive force distribution of translator

In the next step, the magnets in the rotor are represented by the equivalent current sheet, as shown in Fig. 4-3 (b). The linear thrust force F as a function of the axial displacement z_d is given by

$$F = \int (J_C \times B) dS = 2\pi p J_C \sum_{n=1,2,\ldots} K_n \sin(m_n z_d) \tag{4-13}$$

where Jc is the equivalent current density of the magnets on the rotor (nut), and p is the number of pole-pairs of the magnets. And K_n can be obtained by

$$K_n = K_{rn} \sin(m_n \tau_m / 2)$$

$$K_{rn} = \int_{R_{is}}^{R_{0s}} [a_{In} B I_1(m_n r) + b_{In} B K_1(m_n r)] \, r dr \tag{4-14}$$

where $R_i = R_0 + h_m + g$ and $R_s = R_{is} + h_m$, where R_0 is the outer radius of the magnetic screw back-iron, and h_m is the magnets thickness; τ_m is the magnet pole width of the magnetic

screw. The analytical force prediction in (4-13) will be used to select leading design parameters of the magnetic screw in the subsequent section.

4.3 Magnetic Screw Design and Optimisation

Without loss of generality, the development of a high force density linear electromagnetic actuator is aimed for active vehicle suspension. The design specifications of the linear actuator are given in Table 4-1. These are based on the studies reported in [121]. The main output requirements are the same as those of the linear vernier actuator in the previous two chapters.

The linear actuator shown in Fig. 4-5 will be designed to achieve the required specification. It integrates a magnetic screw inside the rotor hub of the rotary PM machine. The magnets for the rotary PM machine is deployed on the outer surface of the rotor hub while the magnet arrays of the magnetic screw are attached to the inner surface of the hub. Thus, the ferromagnetic hub provides flux return paths for the magnets on both surfaces. However, the flux for the rotary machine is predominantly in the radial direction while that of the magnetic screw in the axial direction. Consequently, the magnetic coupling between the rotary machine and the magnetic screw is not significant. This allows the designs of the PM rotary machine and magnetic screw to be performed separately. And because the magnetic screw does not have loss, high operating temperature may be avoided. This facilitates use of high-performance, low cost PMs with low temperature grade. From (4-13), it can be concluded that the thrust force of magnetic screw is proportional to the square of the PM remanence *Brem*. Therefore, the performance of the PM material will significantly affect the thrust force performance of magnetic screw. Therefore, the PM material uses high-performance PMs N42UH and its properties are shown in Table 4-2. In this initial study, the magnets with relatively high temperature grade are employed to ensure they are not accidently demagnetised during tests.

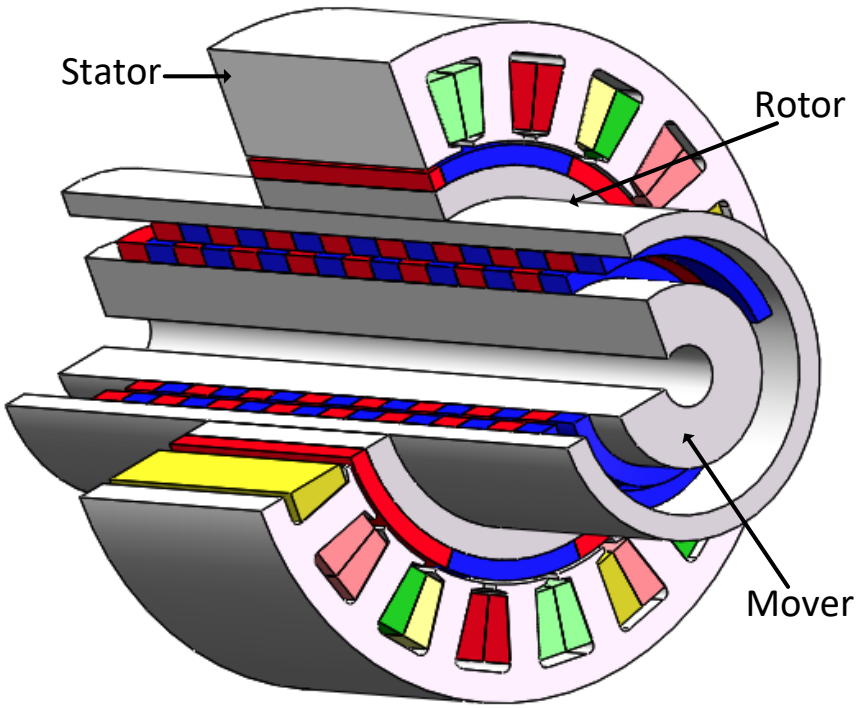

Fig. 4-5 3-D schematic of the MSLA

Table 4-1 Active suspension design specification

Parameters	Unit	Value
Maximum short-time thrust force	N	4000
rms force	N	2000
Maximum speed	m/s	2
rms speed	m/s	2
Cooling method		Air cooling
Stroke	mm	+/- 100

Table 4-2 N42UH material properties

Parameters	Unit	Value
Magnet remanence	T	1.27~1.35
Coercivity	KA/m	1990
Max. temperature	^{o}C	180
Maximum Energy Product	KJ/m3	330
Mass density	g/cm3	7.5
Electrical Resistivity	Ω• cm	180

4.3.1 Magnetic Screw Leading Design Parameters

Since the maximization of the force density of the active suspension is of particular importance, the leading design parameters of the magnetic screw should be further optimized. The optimization variables, namely the magnet thickness *hm*, pole-pitch *τp*,

thickness of inner back iron *Rb1*, thickness of the outer back iron *Rb2* and the radius of inner back iron *Ro* are shown in Fig. 4-6. Among them, the magnet thickness *hm*, pole-pitch *τp*, radius of the inner back iron *Ro* are key parameters that affects the thrust force performance. The inner back iron *Rb1*and the outer back iron *Rb2* determine the saturation in the back-irons, and to a certain extent also affect the thrust force output. Since the outer side of the magnetic screw mover needs to be protected by a non-metallic sleeve, the air gap is selected as 1mm. In order to facilitate the analysis of the leading design parameters, the initial values of the design variables are given in Table 4-3.

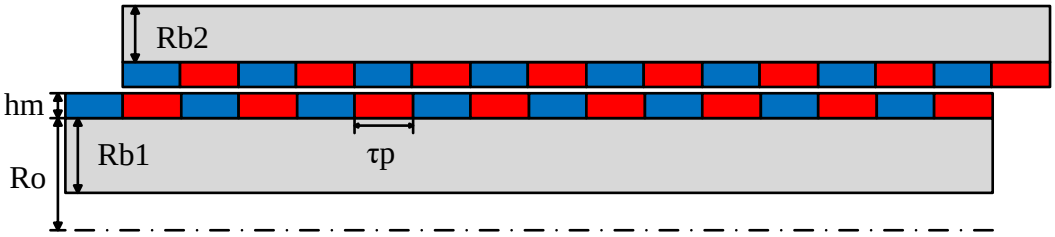

Fig. 4-6 Leading design parameters of the magnetic screw

Table 4-3 Initial values of the design variables

Parameters	Symbol	Value
Thickness of inner back iron	*Rb1*	10mm
Thickness of outer back iron	*Rb2*	10mm
Magnet thickness	*hm*	4mm
Air gap	*g*	1mm
Radius of inner back iron	*R0*	20mm
Pole pair	*p*	10
Pole-pitch	*τp*	7mm

4.3.2 Magnetic Screw Optimization and Analysis

For the magnetic screw, since there are only PMs on both sides of the air gap, under the condition that the PM remanence *Brem* and the PM thickness *hm* remain unchanged, the thrust output of the magnetic screw is determined by the effective working area of the air gap. Therefore, the main parameters that determine the output is the radius of inner back iron *Ro* and the active length.

With the initial values of the design variables, Fig. 4-7 shows the variation of the output force with the mover active length while the effective working area of the air gap are kept constant. It can be seen that by keeping the effective working area constant, as the effective length increases and the radius of inner back iron decreases, the magnetic screw thrust force hardly changes. As the magnetic screw is a tubular structure, the area

is proportional to the product of the radius and axial length while the volume is proportional to the product of radius square and the axial length. Hence, the force density will be inversely proportional to the radius. Reducing the radius of the inner back iron will significantly increase the thrust force density of the magnetic screw. However, too small inner back iron radius will lead to very long effective axial length and compromise mechanical stiffness of the device. So with consideration of these factors, the radius of inner back iron *Ro* is selected for 18mm.

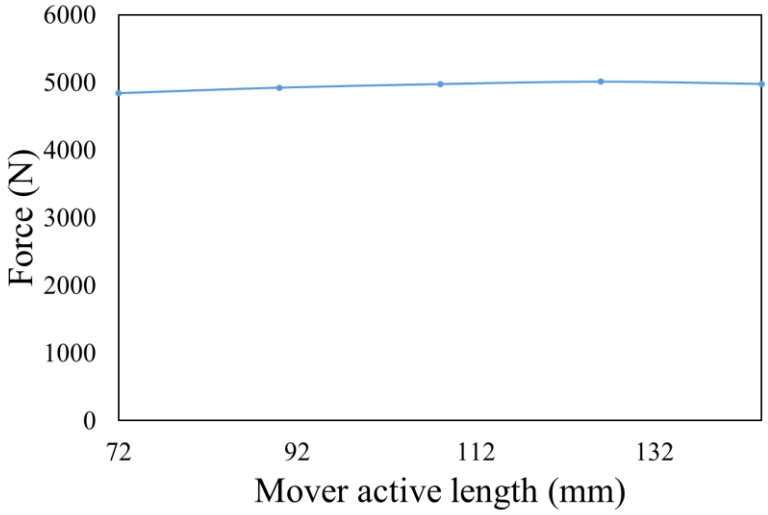

(a)

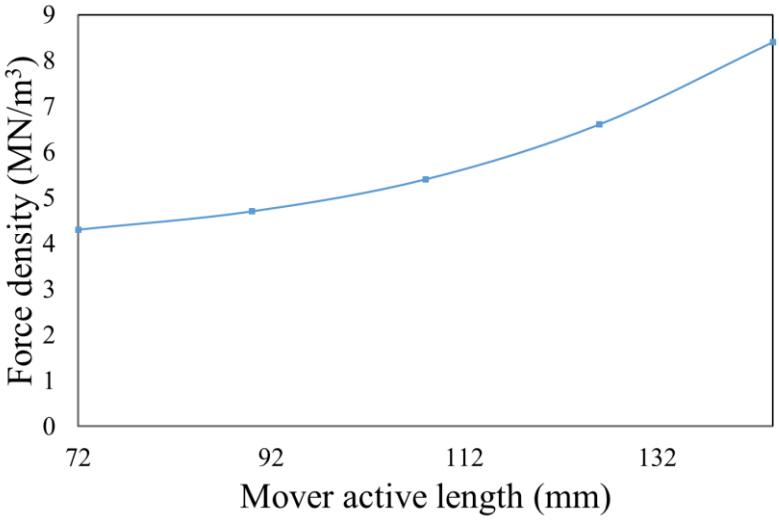

(b)

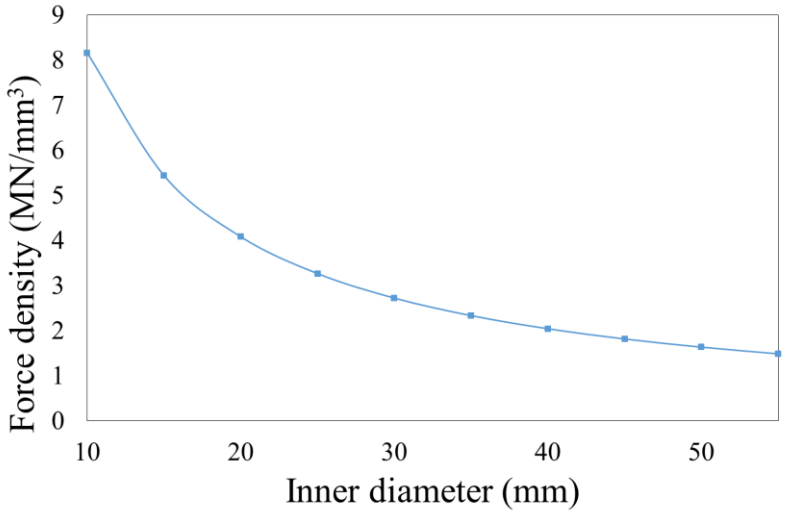

(c)

Fig. 4-7 Variation of output with mover parameters (a) Thrust force with active length (b) Thrust force density with active length (c) Thrust force density with inner diameter

Since the inner back iron radius *Ro* is set to 18mm, the effective length of magnetic screw can be determined. For a given effective length, the pole-pitch τ_p determines how many pole-pairs the magnetic screw has. Too few poles will reduce airgap shear stress and increase the thickness of the back-irons, and too many poles will cause excessive inter-pole magnetic flux leakage. Since the magnetic screw pole pitch τ_p will also affect the flux density in the air gap, it is very important to optimize the PM dimensions. Fig. 4-8 shows the variation of the force density with respect to the magnet thickness *hm* and pole-pitch τ_p. It can be seen that as the pole pitch τ_p increases, the magnetic screw thrust force density first increases and then decreases, and after the *hm* reaches a certain thickness, its thrust force density no longer increases. As a result, the thrust force density of the magnetic screw can be maximized by adjusting *hm* and τ_p. Then, based on the considerations of size, weight and cost the magnet thickness *hm* is selected to be 4 mm and the pole-pitch τ_p selected to be is 9 mm.

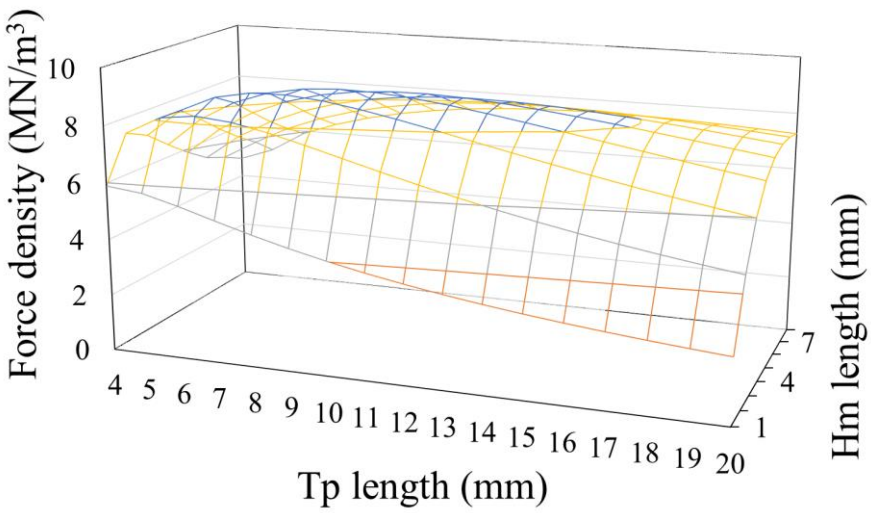

Fig. 4-8 Variation of output with magnet thickness and pole-pitch

When *hm,* τ_p and *Ro* are optimized, the output performance of the magnetic screw is determined. *Rb1* and *Rb2* can be designed to ensure that the magnetic screw back-iron is not heavily saturated. The influence of back-iron thickness on flux density is shown inFig. 4-9. It can be seen that the increase of the both inner and outer back iron thickness can reduce the flux density. However, when inner back iron and outer back iron reaches 7 mm and 6 mm the flux density of back iron reduces to below 1.5T. Hence, based on the considerations of size, weight and cost, the inner back iron thickness is selected to be 7 mm and the outer back iron thicknesses selected to be 6 mm. Although the previous optimization has taken into account the back iron saturation, localised the back iron saturation still need to be examined. The optimised geometries of the magnetic screw are shown in Fig. 4-10 and overall leading design parameters optimisation results are listed in Table 4-4.

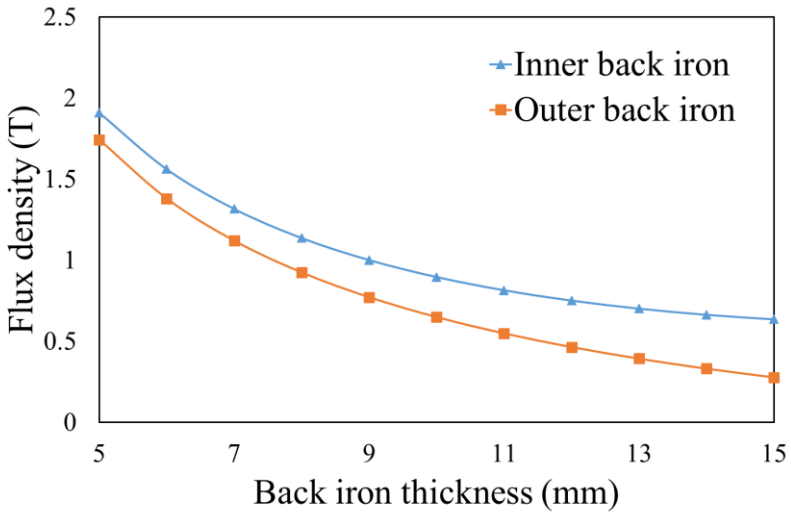

Fig. 4-9 Variations of flux density in the back irons with back iron thickness

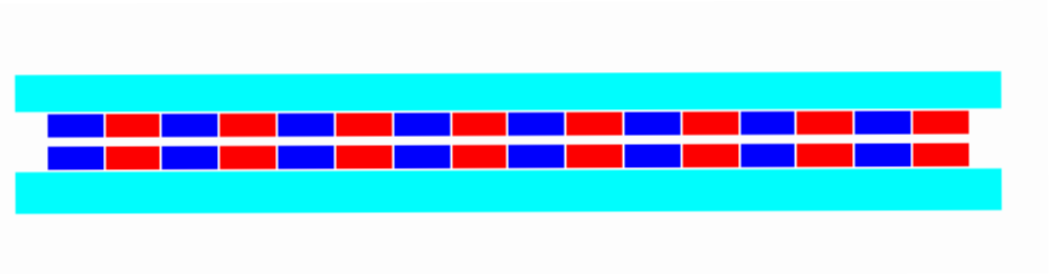

Fig. 4-10 Optimised geometry of magnetic screw

Table 4-4 Leading design parameters of magnetic screw

Parameters	Symbol	Value
Thickness of inner back iron	*Rb1*	7mm
Thickness of outer back iron	*Rb2*	7mm
Magnet thickness	*hm*	4mm
Air gap	*g*	1mm
Radius of inner back iron	*R0*	28mm
Pole pair	*p*	8
Pole-pitch	*τp*	9mm

4.3.3 Magnetic Screw FE Simulation Results and Verification

A 2D FE model of the magnetic screw has been built and simulated. This model assumes axi-symmetrical field distribution and hence is an approximation of the helically distributed magnetisation in a magnetic screw. As will be shown in the subsequent section, the 3D predicted results are very close to the 2D prediction. Hence the 2D model captures the key features of the device while being much more computationally efficient. The 2D predicted magnetic field distribution in 3 relative rotor positions are shown in Fig. 4-11. It can be seen that there is no axial flux density magnetic component in the air gap at the 0 °and 180 °rotor positions, and Maxwell stress tensor the airgap according to shear stress is zero. Hence the thrust force is 0. When the mover displacement is half a pole pitch or the corresponding electrical position is 90 °, the axial flux density in the air gap reaches the maximum, which generates thrust force and verifies the principle of magnetic screw thrust force generation.

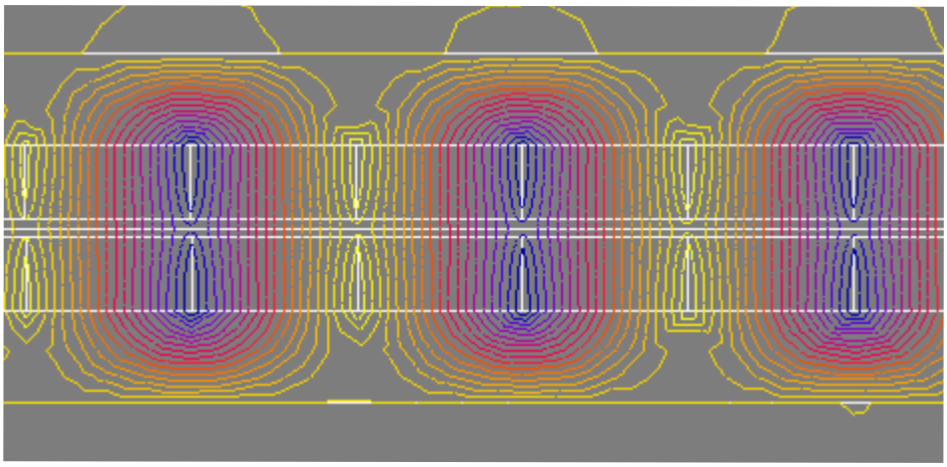

(a)

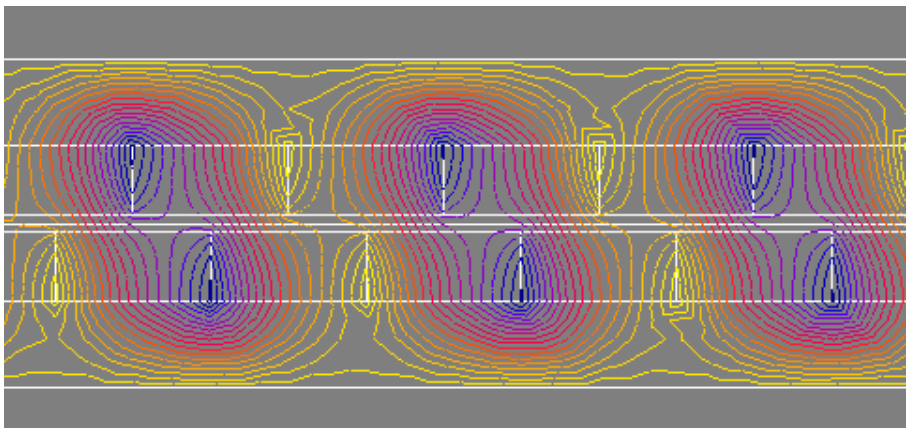

(b)

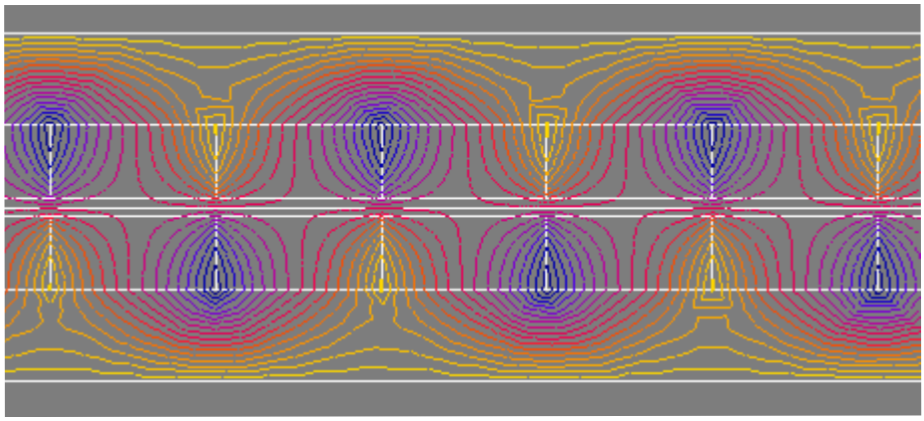

(c)

Fig. 4-11 2-D FE model magnetic field distribution (a) 0 °position (b) 90 °position (c) 180 °position

Fig. 4-12 and Fig. 4-13 show the magnetic field distributions in the radial and axial directions of the air gap at the 90 °mover position. Since the magnetic screw has 8 pole pairs PMs, there are 8 periods of magnetic field distribution over the entire effective

length. Performing FFT analysis on the radial and axial magnetic fields respectively, both main harmonic orders are 8.

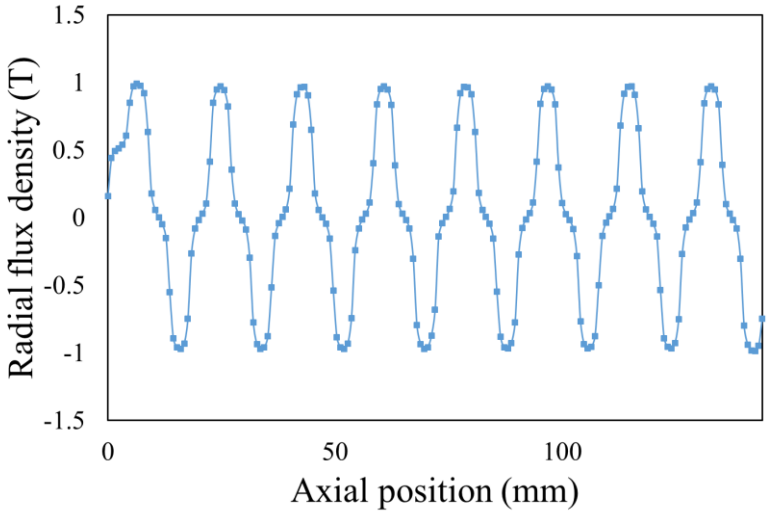

(a)

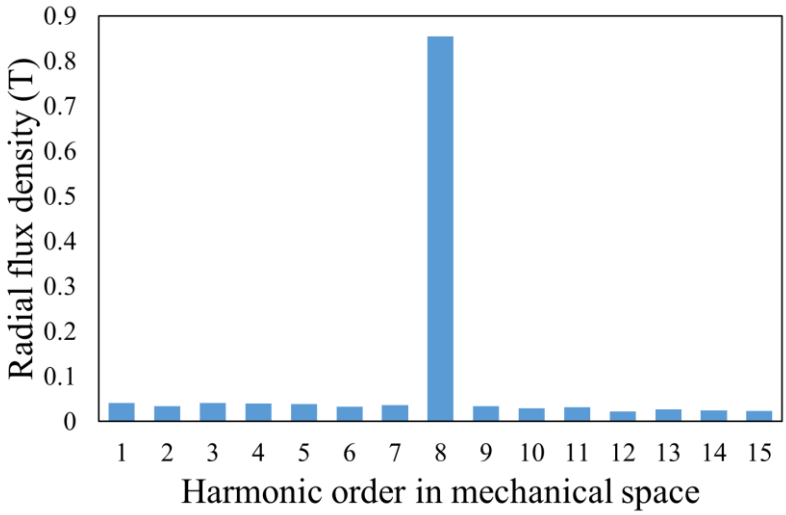

(b)

Fig. 4-12 Air gap radial magnetic field (a) Waveform (b) Spectra

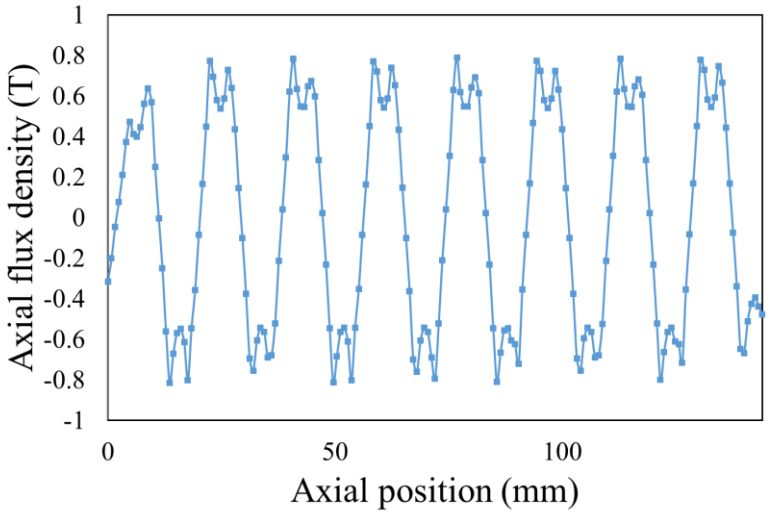

(a)

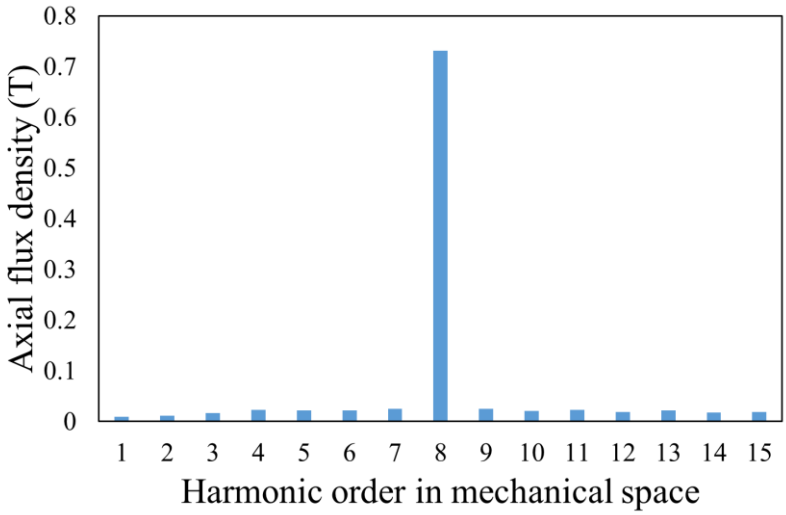

(b)

Fig. 4-13 Air gap axial magnetic field (a) Waveform (b) Spectra

The magnetic flux density distribution of the optimised magnetic screw is shown in Fig. 4-14 . It can be seen that the flux density of most parts of the back-iron is about 1.2T except for the local saturation position which reaches 1.7T. So there is no risk of over-saturation in the whole magnetic screw structure. Fig. 4-15 compares the analytically and 2-D FE predicted thrust force in the case of running the entire pole pitch. It is shown that, the analytical prediction agrees very well with the 2-D FE result, the peak force of the FE prediction is 5234N and that of the analytical prediction is 5118N. After calculation, it can be shown that a thrust force density in excess of 8.4MN/m^{3}can be achieved for air gap length of 1 mm.

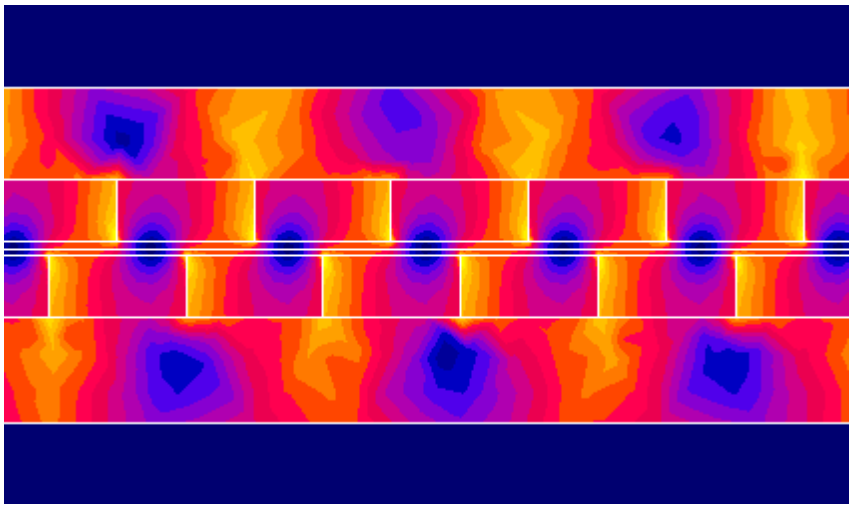

(a)

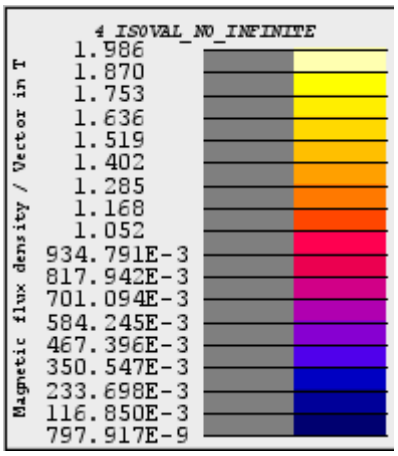

(b)

Fig. 4-14 Flux density distribution at 90 °mover position (a) Flux cloud (b) Scale

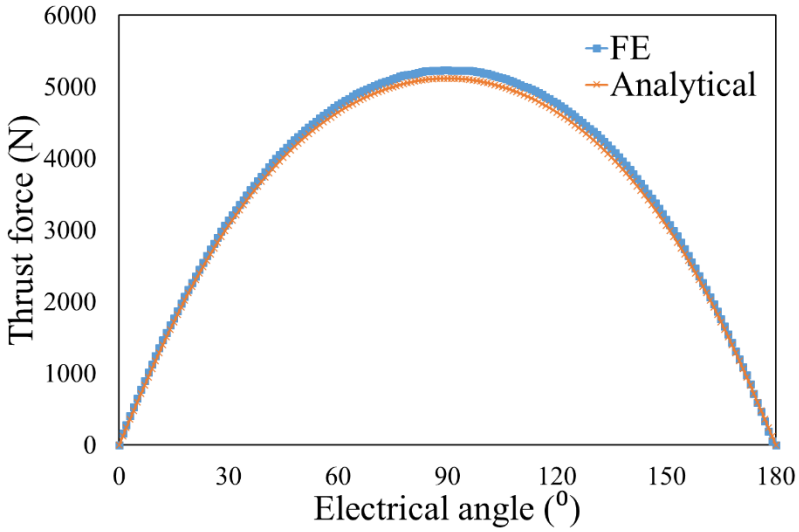

Fig. 4-15 Comparison of analytically and FE predicted thrust force variation

4.4 18-slot, 8-pole Motor Design and Optimisation

As the screw cannot provide its own power, it is necessary to design a matching motor to provide power. From (4-1) to (4-3), as the axial peak force of screw is 4000N, the lead of the screw is 18mm, the peak torque of the motor is 11.5Nm. And with the peak magnetic screw velocity of 2m/s, the maximum motor speed is 6666 rpm. The requirements and constraints of the motor are shown in Table 4-5.

Table 4-5 Design specification of machine

Specification	Unite	Value
Base speed	rpm	3500
Rated torque	Nm	6
Peak torque	Nm	12
Rated output power	kW	2.2
Rotor inner radius	mm	32
Current density	A/mm^2	4
DC link voltage	V	600

4.4.1 Motor Structure Selection

As the motor design needs to match the magnetic screw, the design specification of the machine for the active suspension is given in Table 4-5. As observed, this machine requires limited rotor diameter with high torque density and high power density, so a fractional-slot surface-mounted permanent magnet (SPM) motor is used as the drive motor topology. And because the magnetic screw of the MSLA uses high-performance PMs, the motor structure should minimize the loss on the rotor.

In [121] a fractional-slot winding configurations and associated pole-slot combinations for PM machines are described. Fig. 4-16 shows the schematic of 18-slot, 8-pole winding configuration and Fig. 4-17 shows armature reaction MMF waveforms and spectra. It can be seen in Fig. 4-17 (b) all odd space harmonics have been eliminated. In additional to the 4^{th} order working harmonic, the remaining harmonics are n=2, 14, 22. In this way this kind of winding configurations can improve torque density and efficiency of the machine. And because the 18-slot, 8-pole structure has less harmonic content, the MSLA selects the 18/8 SPM as the motor part.

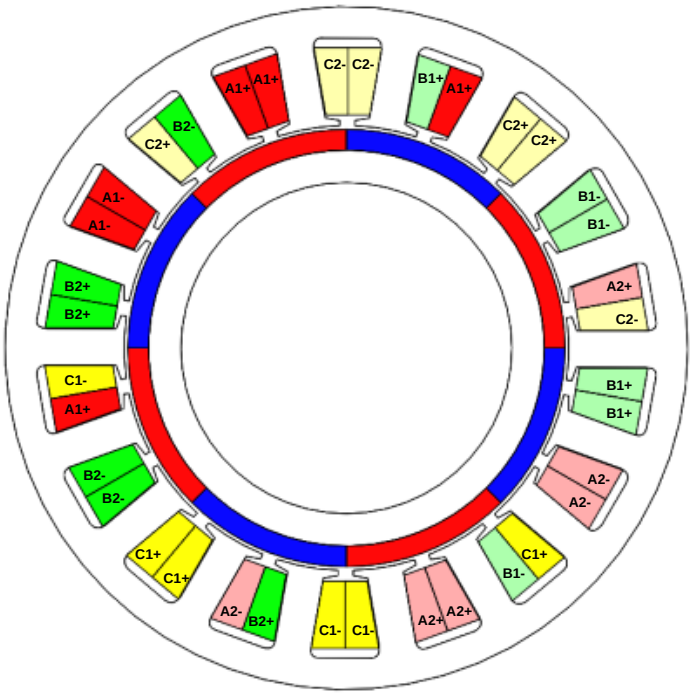

Fig. 4-16 Schematic of proposed 18-slots, 8-pole PM machine

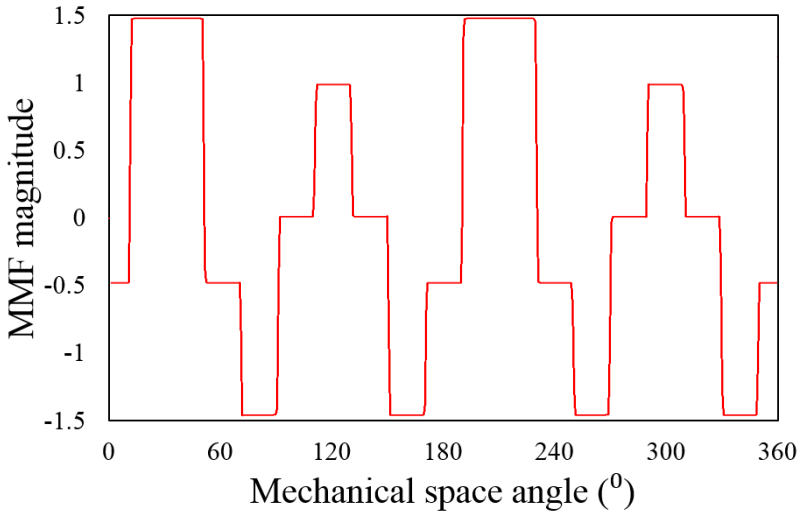

(a)

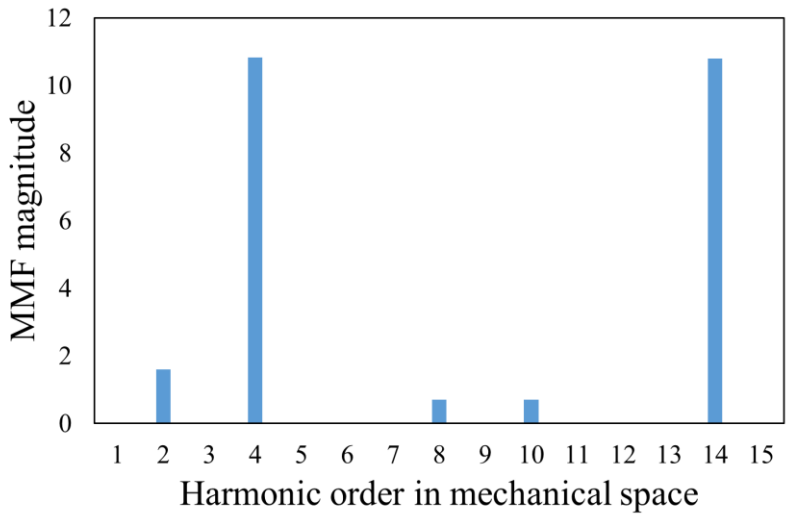

(b)

Fig. 4-17 MMF waveform and spectra of 18-slot, 8-pole machine (a) MMF waveform (b) Spectra

4.4.2 Motor Main Size Calculation and Leading Parameters

Because the inner diameter of the motor is much larger than a conventional motor, it is necessary to determine the basic design specifications of the motor prior to the initial design. Based on the required torque/power and the dimension equations, the initial values of the basic parameters of the motor can be calculated and selected.

As discussed above, the 18-slot, 8-pole SPM topology is selected as the drive motor for the magnetic screw. Due to the need to maximize the torque density, the size of the motor design should be as small as possible. So the motor needs to be optimally designed and the leading design parameters are initially estimated as follows.

1) According to the characteristics of magnet BH curve, and selected air gap length, the permanent magnet operating point, and permanent magnet type are selected.

2) Estimate the rotor dimension and the stator diameter and armature length. Initial selections of these parameter can be made based on the following governing theory.

In the AC motor, the output power P_N of the motor is

$$P_N = mEI \tag{4-15}$$

where m and I are the number of phases and the phase current. The phase electromotive force of armature winding, E, is given by

$$E = 4k_B f N k_{w1} \emptyset \tag{4-16}$$

where N is the number series turns per phase winding, f is the fundamental electric frequency and Φ is the phase magnetic flux linkage per pole which can be obtained by

$$\emptyset = B_\delta a_i \tau L_2 \tag{4-17}$$

where B_δ and L_2 are the peak fundamental air gap flux density and active length of the motor armature, and τ is the pole pitch which is related to the rotor diameter D_1 and number of pole-pair p by

$$\tau = \frac{\pi D_1}{2p} \tag{4-18}$$

The motor line load A can be evaluated by

$$A = 2m \frac{NI}{\pi D_2} \tag{4-19}$$

where D_2 is the stator inner bore diameter and from (4-15), (4-16) and (4-19), the following is derived:

$$\frac{D_1 L_2 n_N}{P_N} = \frac{6.1}{a_1 K_B K_{w1} A B_\delta} \tag{4-20}$$

where K_B, and K_{w1} are the magnetic field coefficient and fundamental winding factor, respectively, and n_N is the rotor rated (base) speed. Because the permanent magnet rotor for the rotary machine is placed outside of the magnetic screw rotor, its inner radius must be equal to the outer radius of the screw rotor of 32 mm. The stator inner bore diameter D_1 and the length of armature L_2 are estimated to be 86mm and 60mm, respectively in order to meet the specifications. After determining the stator inner radius and active length, the PM thickness is chosen for 4mm to provide good performance. Since the required motor output torque is determined, the selection of the outer diameter of the motor will take into account the winding area and the stator size of the motor. As the motor is naturally air-cooled, its continuous current density must be less than 4A/mm^2, so the area of the winding can be calculated. The cross section of the fractional-slot PM machine is shown in Fig. 4-16 . Two set of phases are denoted as A1, B1, C1 and A2, B2, C2 with polarity as indicated by+ and −. The magnets are shown in red and blue are magnetized in opposite directions.

Fig. 4-18 shows the leading design parameters of fractional-slot PM motor. As calculated from (4-20) the stator inner bore radius is 43mm and the active length of 42mm. As the motor rotor needs to be equipped with a sleeve, considering the manufacturing tolerances the air-gap length is assumed to be 0.75mm. Hence, there are four parameters, including the ratio of the rotor outer radius Rb_6 to the stator outer radius Rb_5, the stator

teeth width *TWS*, the mover core height Rb_3 and stator back iron thickness Rb_4, to be optimized. The M270-35A electrical steel is used for the stator laminations and the rotor use the same soft magnetic iron material DT4 as the magnetic screw. The motor PMs uses N35UH with its remanence of 1.2 T and coercivity of 1.04.

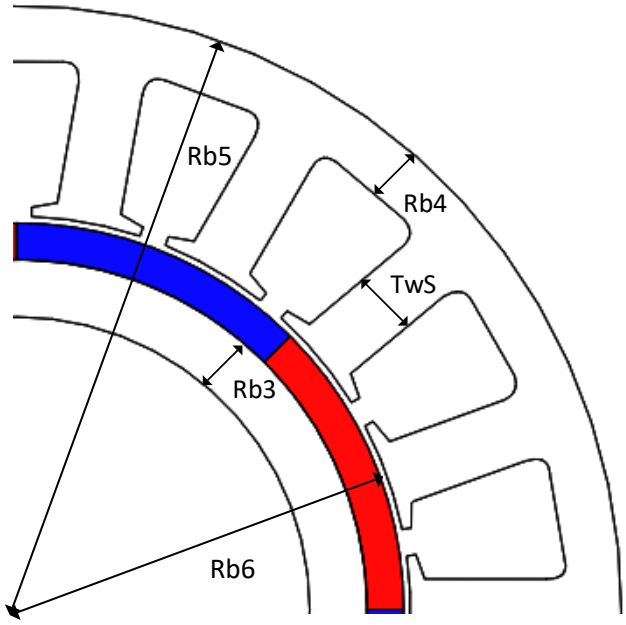

Fig. 4-18 Leading design parameters of fractional-slot PM motor

4.4.3 Motor Global Optimization

In order to maximize the MSLA thrust force density, all four motor leading parameters are globally optimized to achieve the maximum torque density under the following constrains: (1) Fixed rotor inner radius; (2) Fixed air-gap length; (3) Fixed active length; (4) Fixed stator winding current density; (5) Fixed Motor output torque between 6-6.5Nm. Here, a conservative motor current density is adopted, so that the temperature rise of winding can be controlled within a reasonable range, and the thermal performance of the motor will be verified later.

Fig. 4-19 shows the mesh division during the global optimization of the motor. In order to obtain more accurate results, the motor uses high-quality meshing. The optimisation is performed in Flux-2D in conjunction with Altair HyperStudy platform, where computationally efficient optimisation algorithm can be selected. The thermal constraint is incorporated into the optimisation process via Python script language. The optimised geometries of the machines is shown in Fig. 4-20 and the optimisation results are listed in Table 4-6.

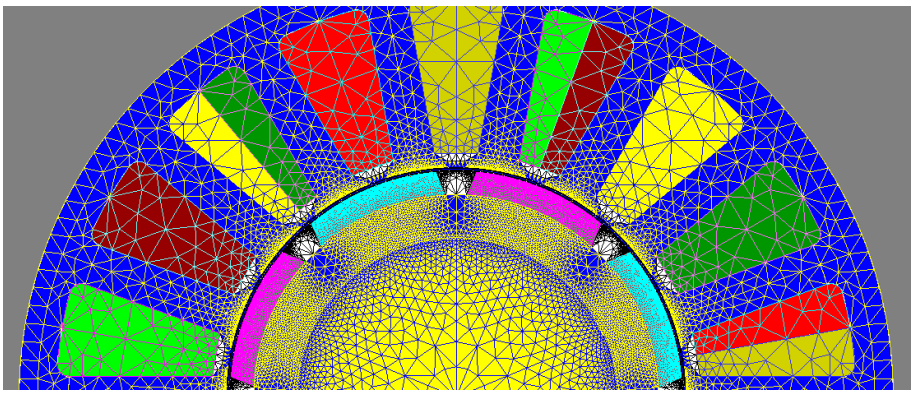

Fig. 4-19 Mesh of 18 slot 8 pole motor FE model

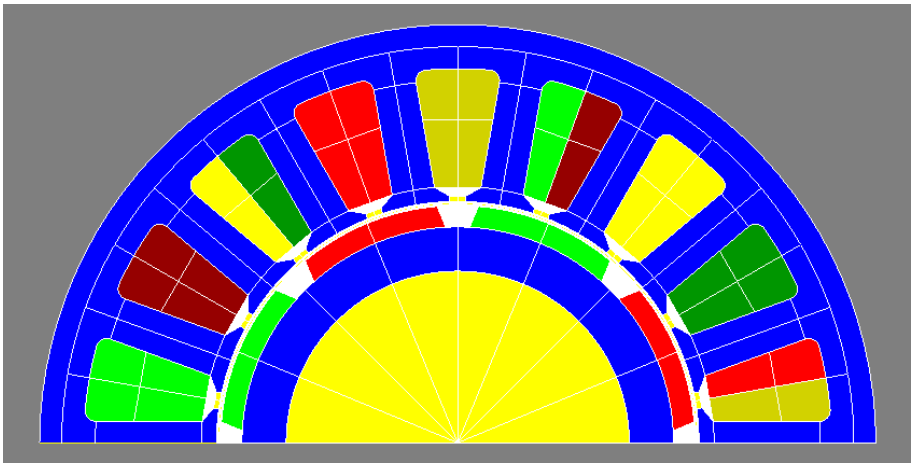

Fig. 4-20 Optimised geometry of 18 slot 8 pole motor

Table 4-6 Optimized Parameters of 18 slot 8 pole motor

Specification	Value
Stator outer radius	74mm
Stator inner radius	44mm
Air gap	0.75mm
Rotor outer radius	39.25mm
Rotor inner radius	27mm
Active axial length	39mm
Magnet depth	4mm
Magnet arc	160 °
Tooth width	7mm
Back iron thickness	6mm

4.4.4 18 Slot 8 Pole Motor FE Simulation Results and Verification

Phase back-EMF waveforms and their spectra at the rated speed of 3500rpm is illustrated in Fig. 4-21. It can be seen that the phase shift angle between each phase is 120°, and due to the influence of the third harmonic, as shown in Fig. 4-21 (b), the back-EMF waveform of the motor is saddle-shaped.

The magnetic flux line distributions of the optimised design is shown in Fig. 4-22. It can be seen that, since the rotor PM has a pole arc of 160^0, the inter-pole magnetic leakage is relatively small.

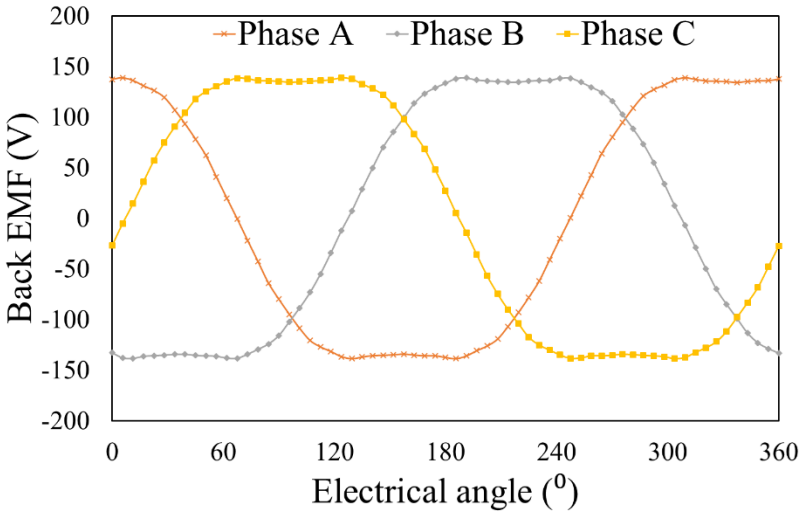

(a)

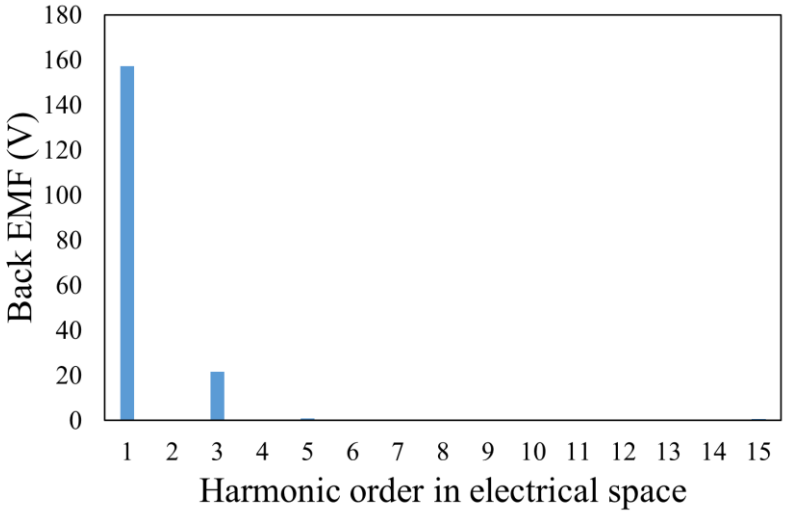

(b)

Fig. 4-21 FE-predicted phase back-EMF (a) Waveform (b) Spectra

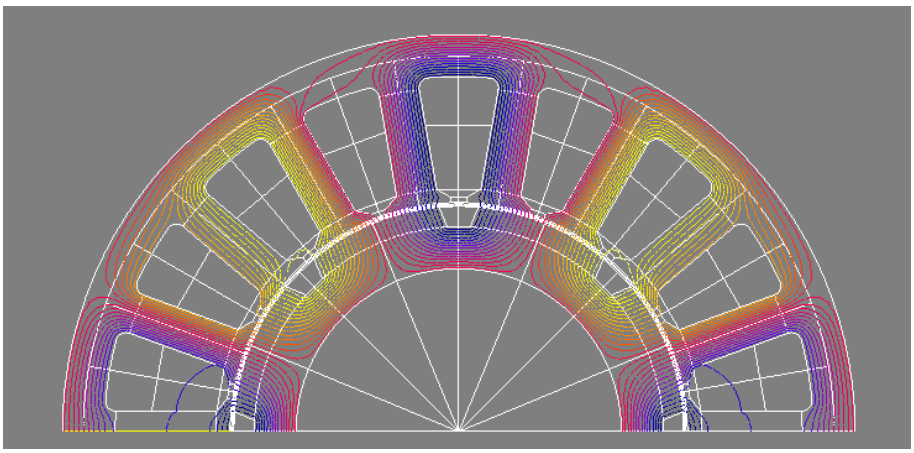

Fig. 4-22 Flux line of 18 slot 8 pole motor

The FE-predicted rated and peak torque waveforms of the motor is illustrated in Fig. 4-23 and Fig. 4-24. And Fig. 4-25 shows the flux density distributions when the machines are at the rated load and peak load, respectively. The peak torque is computed at twice the rated electrical loading. The average rated torque is 6.02Nm which meets the requirement of 6Nm. The torque ripple is 9% and its dominant harmonic is 6^{th} and 12^{th} order, which can be observed in Fig. 4-23 (b). The average peak torque is 11.97Nm which is almost twice the rated average torque and the torque ripple is 6.4%. It can be seen from Fig. 4-25 (a) that when the 18 slot 8 pole motor at the rated load (current), the maximum flux density of the stator and rotor is about 1.88T and 1.58T, respectively. In contrast, Fig. 4-25 (b) shows when the machines is at the peak load. The maximum flux density of the stator and rotor is about 2T and 1.7T, respectively.

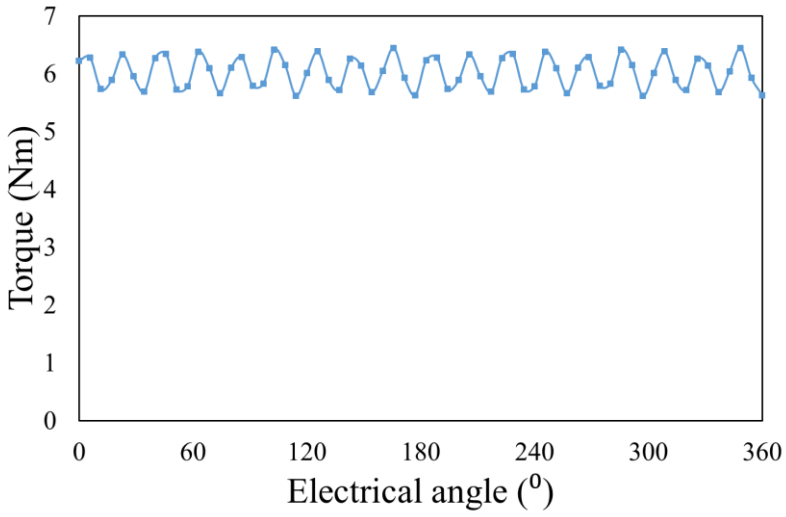

(a)

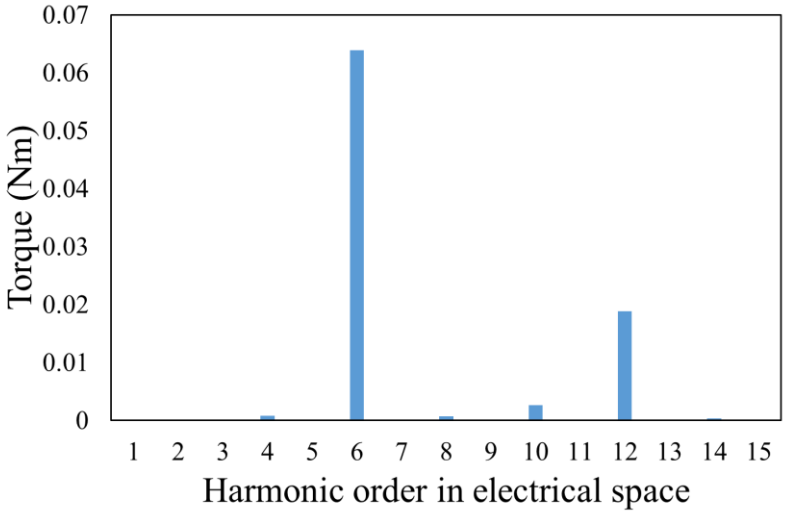

(b)

Fig. 4-23 FE-predicted rated torque (a) Waveforms (b) Spectra of force ripples

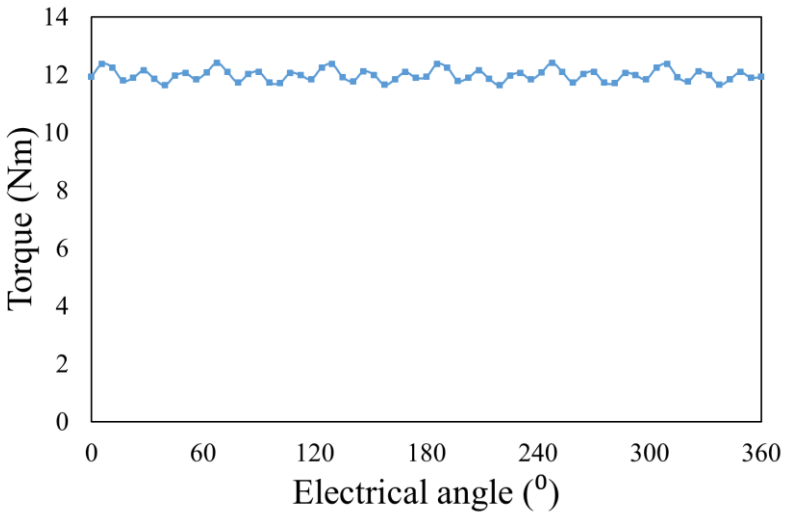

(a)

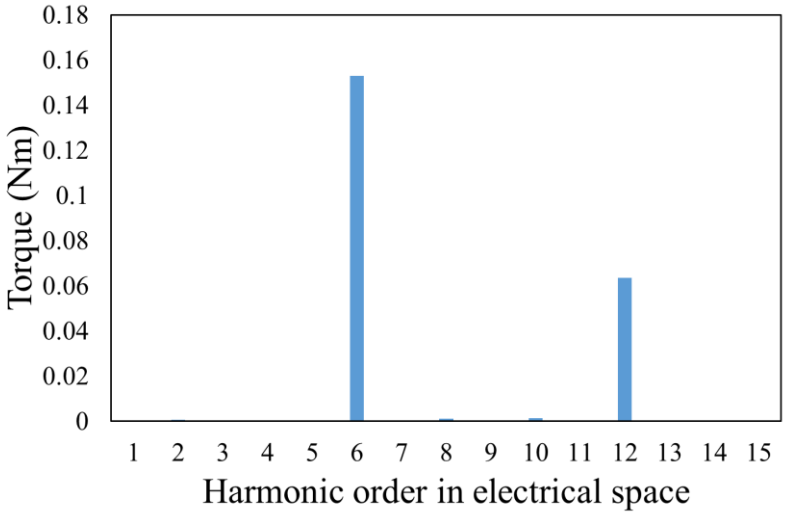

(b)

Fig. 4-24 FE-predicted peak torque (a) Waveforms (b) Spectra of force ripples

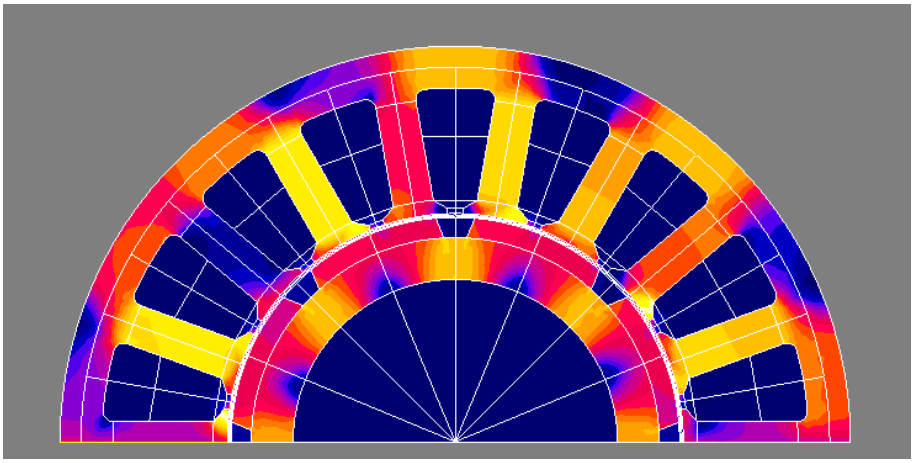

(a)

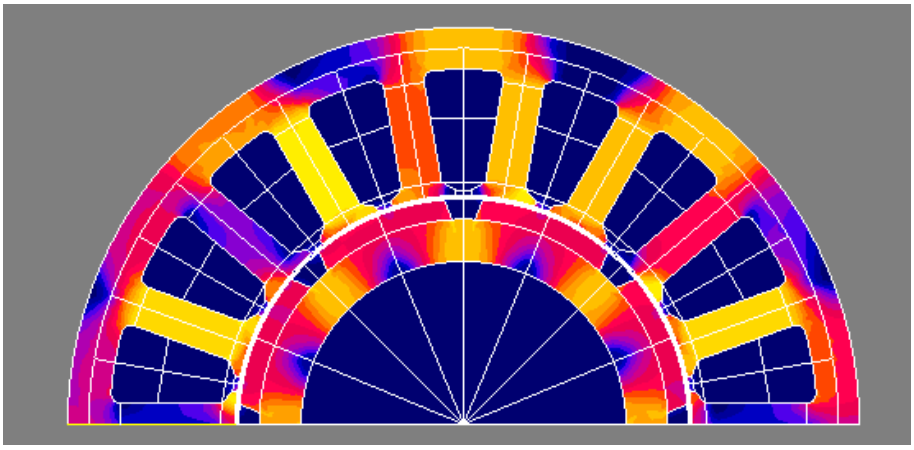

(b)

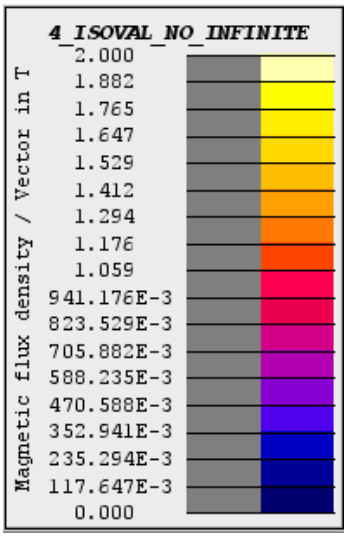

(c)

Fig. 4-25 Flux density distribution of 18 slot 8 pole motor (a) Rated load (b) Peak load (c) Scale

Since the inner part of the MSLA incorporates the magnetic screw structure which uses high-performance PMs, its temperature rise should be limited to prevent demagnetisation. Hence, it is necessary to minimize the loss of the motor. Fig. 4-26 shows the eddy current loss in the rotor magnets and back-iron, and the iron loss of the 18-slot, 8-pole motor. The iron losses of the machine is calculated using Bertotti losses equation by FEM under the rated working condition. As can be seen the iron losses is 57.71W and eddy current loss 12.37W, the eddy current loss is much smaller than copper loss.

In order to gain insight of the eddy current loss in the rotor back iron, three circular lines are set in the rotor back-rion, as shown in Fig. 4-27 (a). The flux density of these three lines under rated conditions is obtained through simulation, and the results are shown in Fig. 4-26 (b). It can be seen that as the line goes deep into the motor rotor back-iron, the flux density gradually reduced. Fig. 4-28 shows the eddy current density in colour diagram of the motor rotor under rated working conditions. Since odd harmonics have been eliminated in the 18 slot 8 pole motor, and the remaining 2^{nd} harmonic is very week, the eddy current loss is primarily due to the 14^{th} and 20^{th} harmonics, which cannot penetrate deeply into the back-iron. Therefore, the eddy current loss is distributed in the regions close to magnet surfaces.

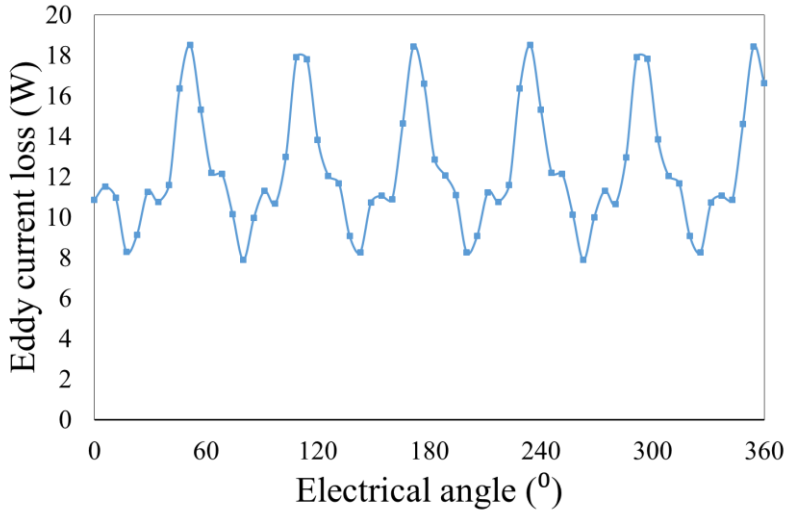

(a)

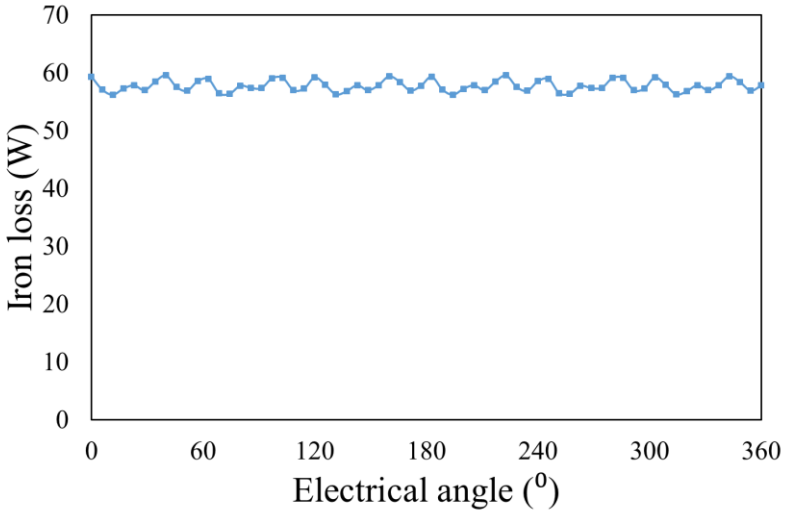

(b)

Fig. 4-26 Variation machine loss (a) Eddy current loss (b) Iron loss

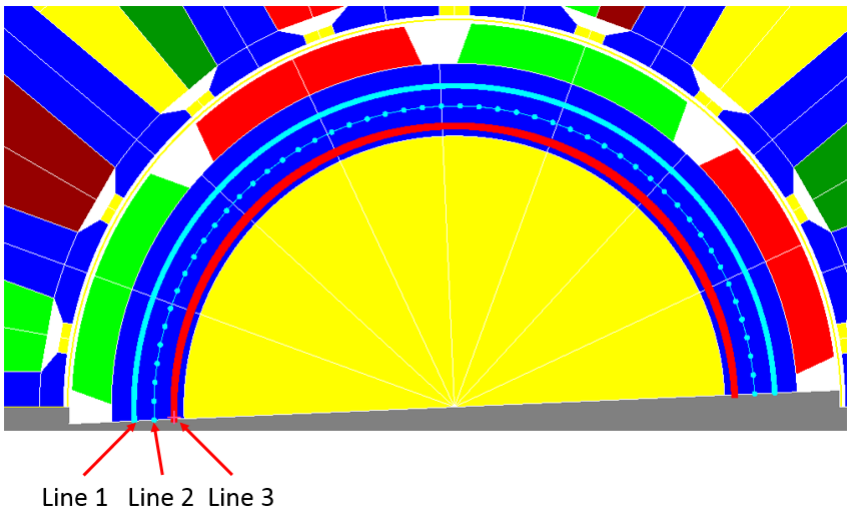

(a)

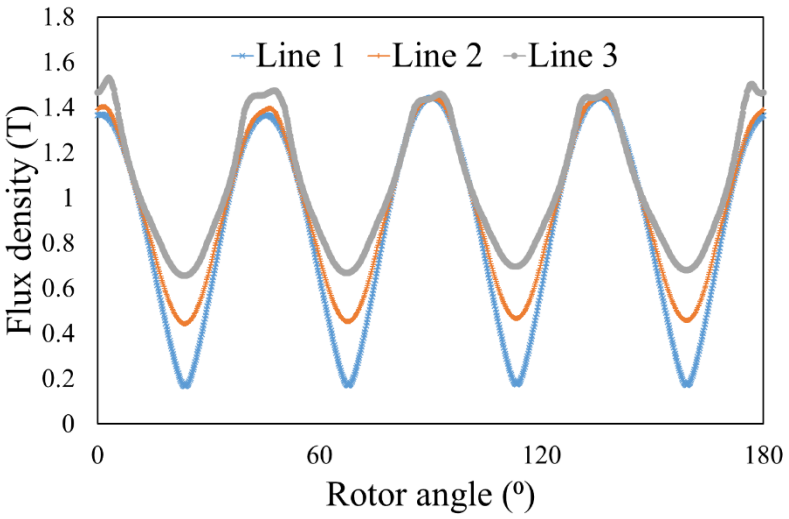

(b)

Fig. 4-27 Rotor flux density (a) Location diagram (b) Waveforms

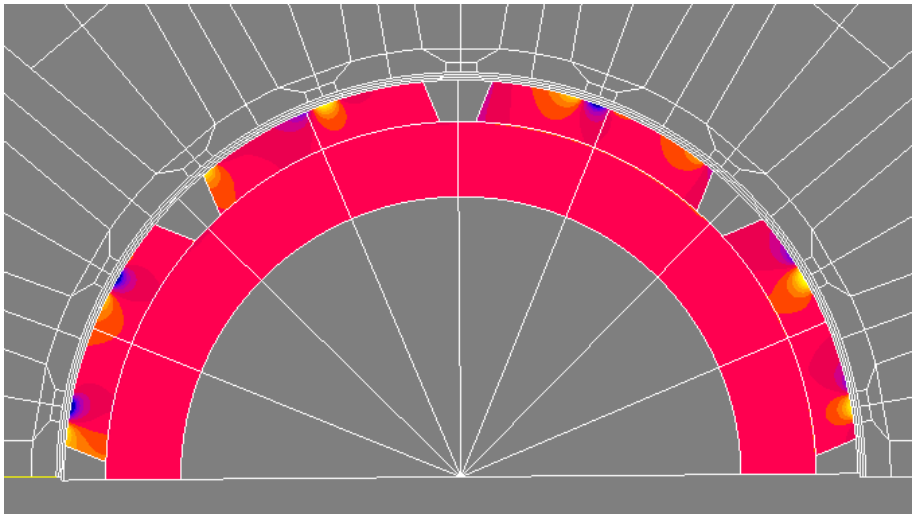

(a)

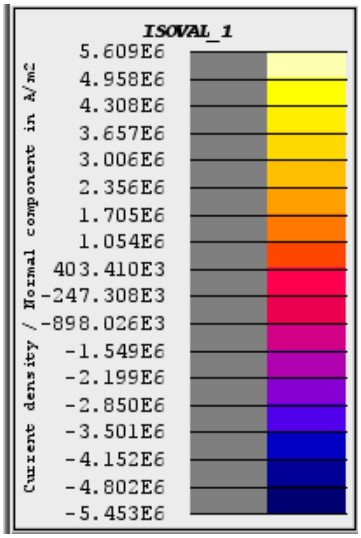

(b)

Fig. 4-28 Rotor current density (a) Cloud (b) Scale

Although there is less loss on the rotor, it is necessary to predict the temperature of motor at continuous working condition. If the motor continues to run at an excessively high temperature, the PM will be subject to the risk of irreversible demagnetization and undesirable reduction in lifetime.

The detailed thermal analysis is performed in Motor-CAD which developed by Motor Design Limited. The motor cooling method is set to air cooling and the ambient temperature is set to 40°C. The thermal analysis at the rated load conditions and base speed, i.e. 6Nm and 3500rpm is performed and results are shown in Fig. 4-29.

It can be seen that the maximum winding temperature of the motor under the rated conditions is 118°C, and the maximum temperature of the rotor magnets is 106°C. This is because the motor has a larger copper loss and a smaller rotor loss. The temperature of windings and PM under working conditions is lower than the permissible temperature of both, indicating that the machine can be rated for a long time. The performance indicators of the optimized motor at the rated operation are summarised in Table 4-7.

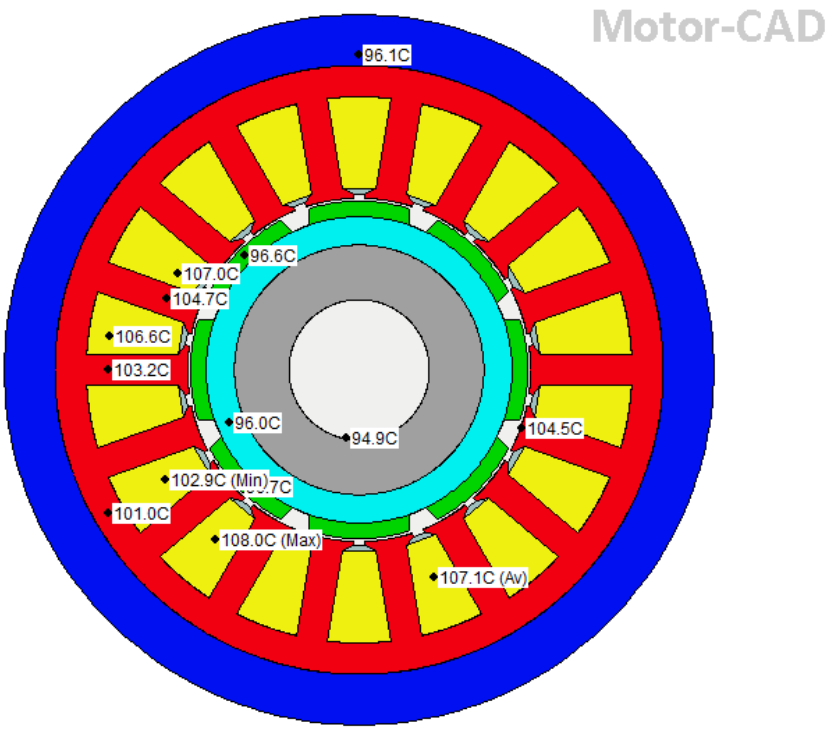

Fig. 4-29 Thermal analysis results at rated torque and base speed

Table 4-7 Performances of 18 slot 8 pole motor

Specification	Value
Rated torque output	6.02Nm
Rated output power	2.2kW
Rated (base) speed	3500 rpm
Rated current	10A (peak 20A)
Eddy current loss	12.37W
Iron loss	57.71W
Copper loss	58.12W
Max winding temperature	118°C
Motor efficiency	0.951

4.5 3D FE Modelling and MSLA Electromagnetic Performance Evaluation

Since the actual action of the MSLA is combined by the magnetic screw and the rotary PM machine, a 3D FE model is require to predict its performance more accurately. Fig. 4-30 shows the 3D FE model of the MSLA. The main components from the outside to the inside is the motor stator, rotor and magnetic screw mover. Since the motor and the magnetic screw share the same rotor, the degree of magnetic saturation is the superposition of the two.

Fig. 4-31 shows the mesh of the 3D MSLA rotor model and the predicted magnetic saturation at the rated torque and speed. In order to obtain accurate results, a time-consuming high-precision mesh is used. It can be seen that despite the superposition of the motor and the magnetic screw flux density, the MSLA rotor does not suffer from very high saturation, which is also reflected in the output thrust force as shown in Fig. 4-32. It can be seen that the three predicted thrust force variation with the electrical displacement are relatively consistent. The difference between the waveform shapes is mainly due to the analytic calculation, which ignores the influence of the saturation effect of the magnetic yoke, and the FE model will be affected by the end effect.

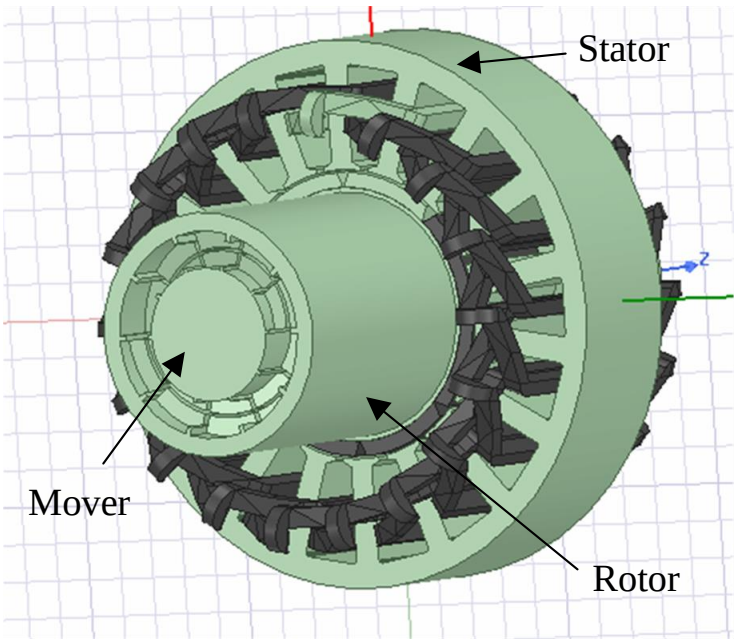

Fig. 4-30 3D FE model of MSLA

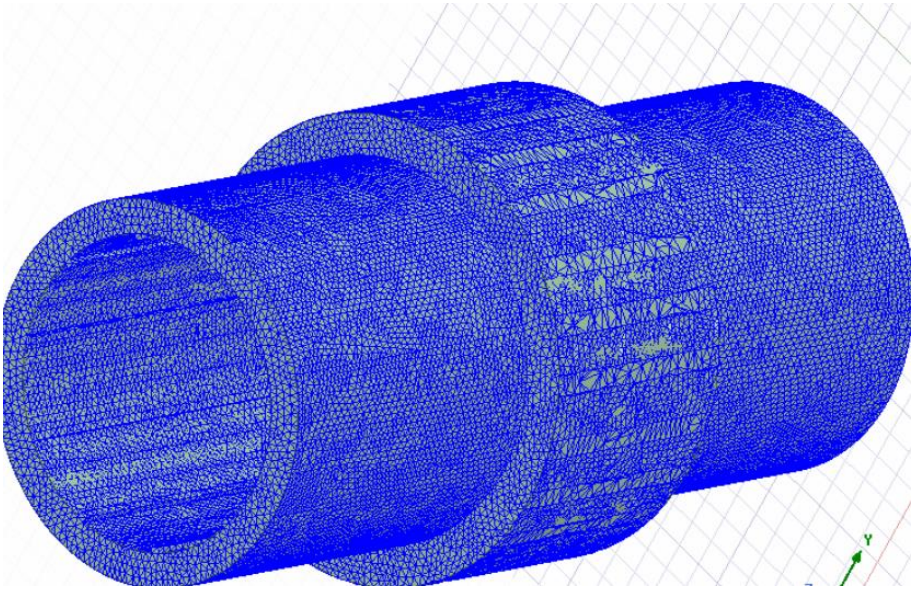

(a)

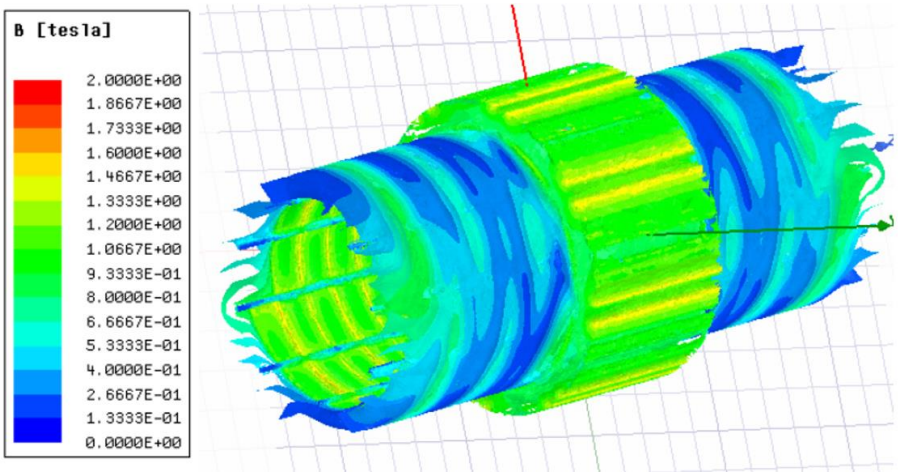

(b)

Fig. 4-31 Rotor 3D model (a) Mesh (b) Flux density distribution

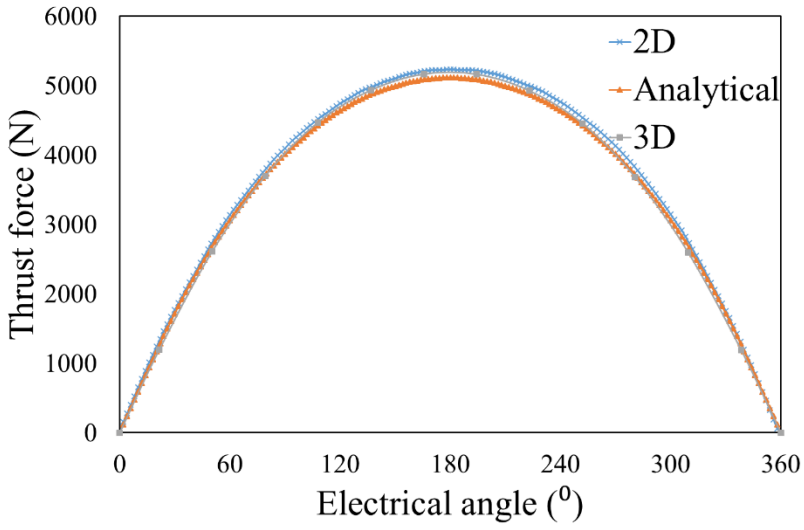

Fig. 4-32 Comparison of analytically, 2D and 3D FE predicted thrust force variation

As the magnetic screw and the motor share a rotor, the magnetic screw rotor part can be regarded as a shaft. By setting the shape and material of the shaft as the parameters of the magnetic screw rotor in MotorCAD, the thermal condition of the MSLA in operation can be simulated. Fig. 4-33 (a) shows the 3D thermal analysis model of the motor, the entire motor shell has a heat sink, the size of hollow shaft is same as the magnetic screw rotor, and the shaft length is the effective length of the magnetic screw rotor. Fig. 4-33 (b) and Fig. 4-33 (c) show the thermal distribution on the front and side of the motor. It can be seen that after adjusting the size of the motor shaft, the temperature distribution of the motor does not change significantly. Both the motor and the magnetic screw PMs need to withstand about 100°C under the rated conditions.

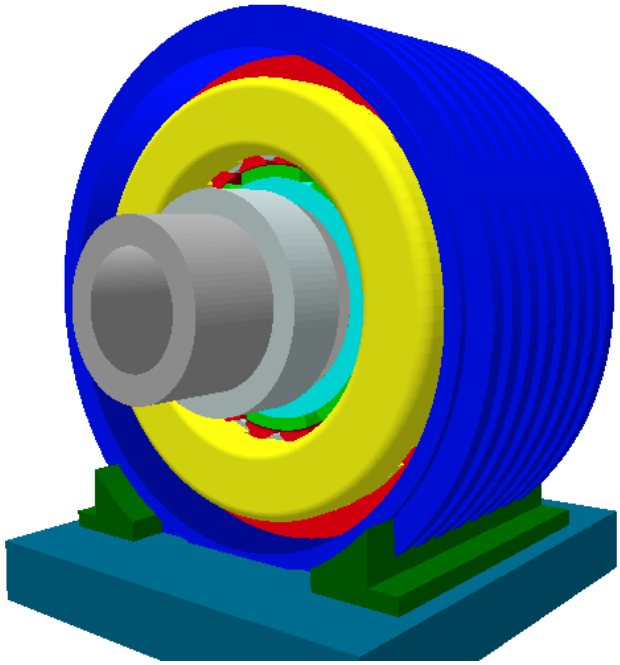

(a)

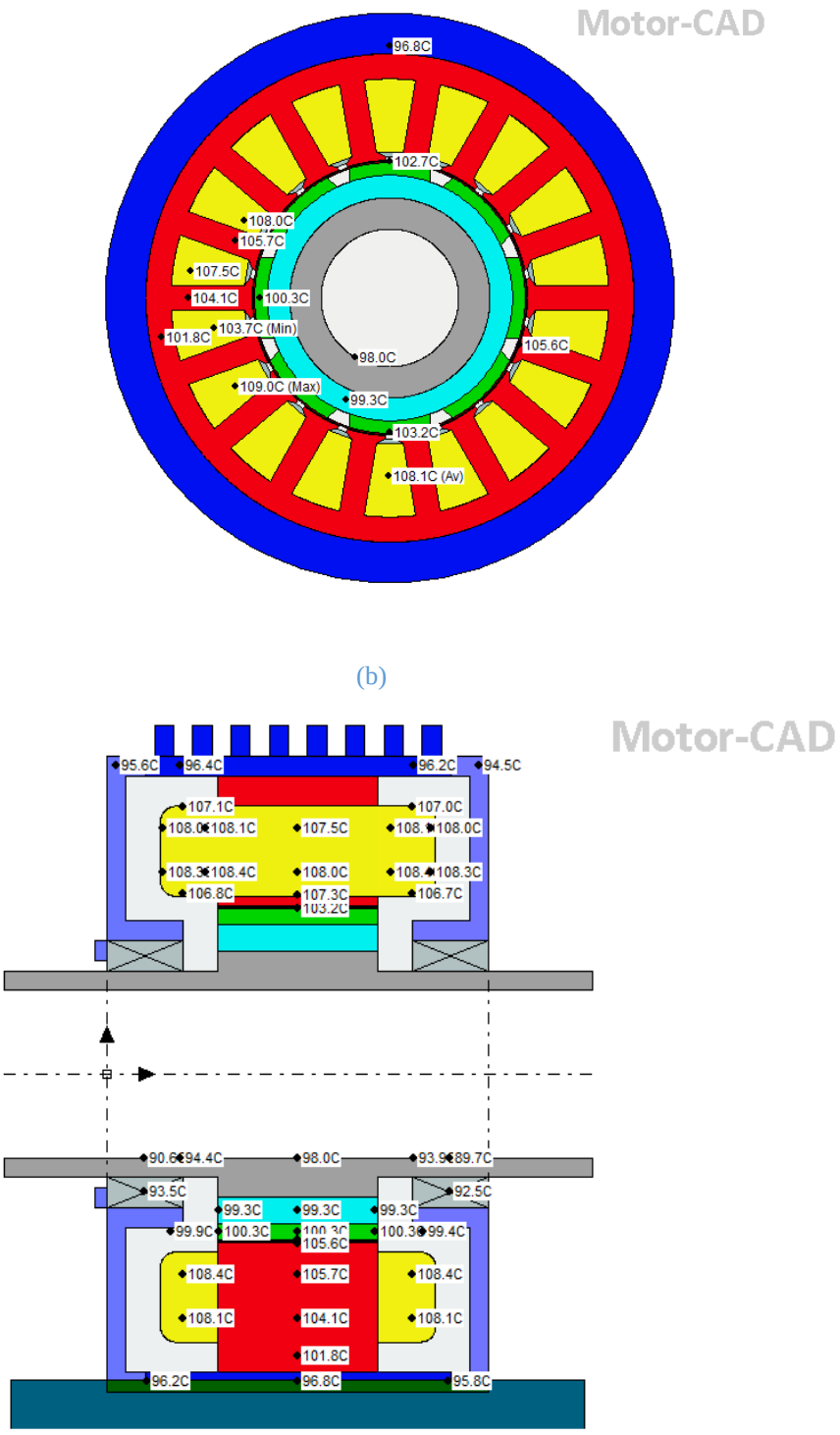

Fig. 4-33 Thermal analysis of MSLA (a) 3D model (b) Motor front (c) Motor side

In order to pursue high peak thrust force density, the MSLA magnetic screw part uses high-performance PMs with poor heat receiving capacity, so it is necessary to analyze the demagnetization risk. Fig. 4-34 shows the N35UH and N42UH magnets demagnetization curve. Since both of motor and magnetic screw PMs have to bear temperature close to 100°C, it can be seen from Fig. 4-34 that the flux density in the motor PMs needs greater

than 0T and that in magnetic screw PMs needs greater than -0.1T under peak force conditions to avoid the risk of demagnetization.

Fig. 4-35 shows the flux density of the PMs of the motor at the peak load and PMs of the magnetic screw at the maximum thrust force point (Arnold Magnetic Technologies Corp 2016). It can be seen that the minimum flux density of both point is greater than 0T so there is no risk of demagnetization during operation.

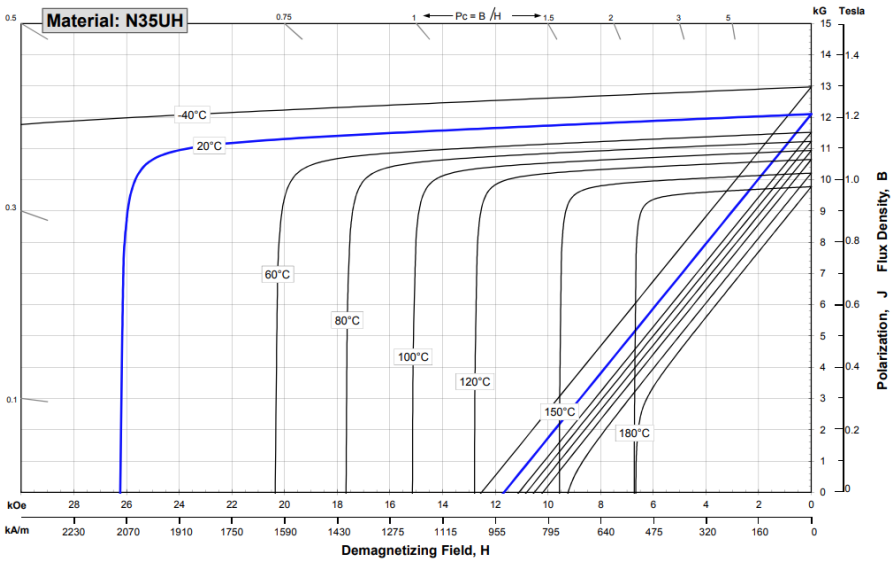

(a)

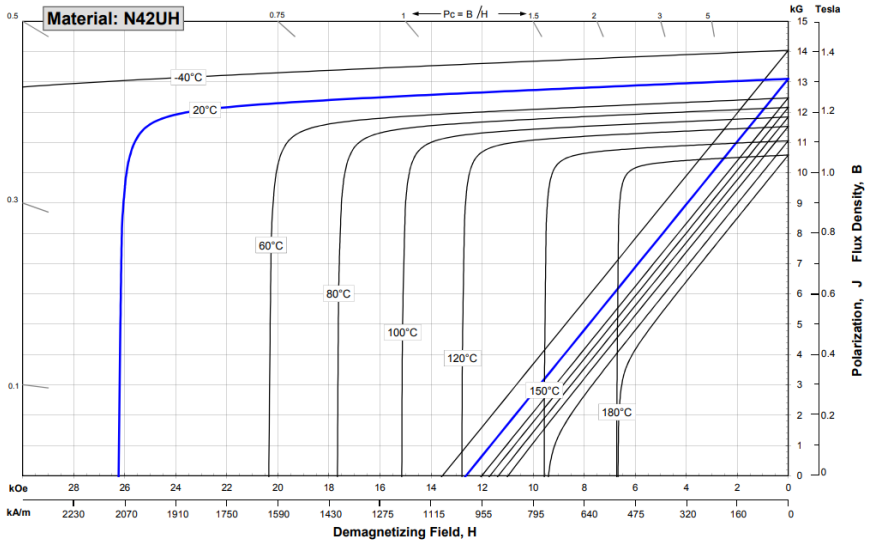

(b)

Fig. 4-34 Magnets demagnetization curve (a) N35UH (b) N42UH

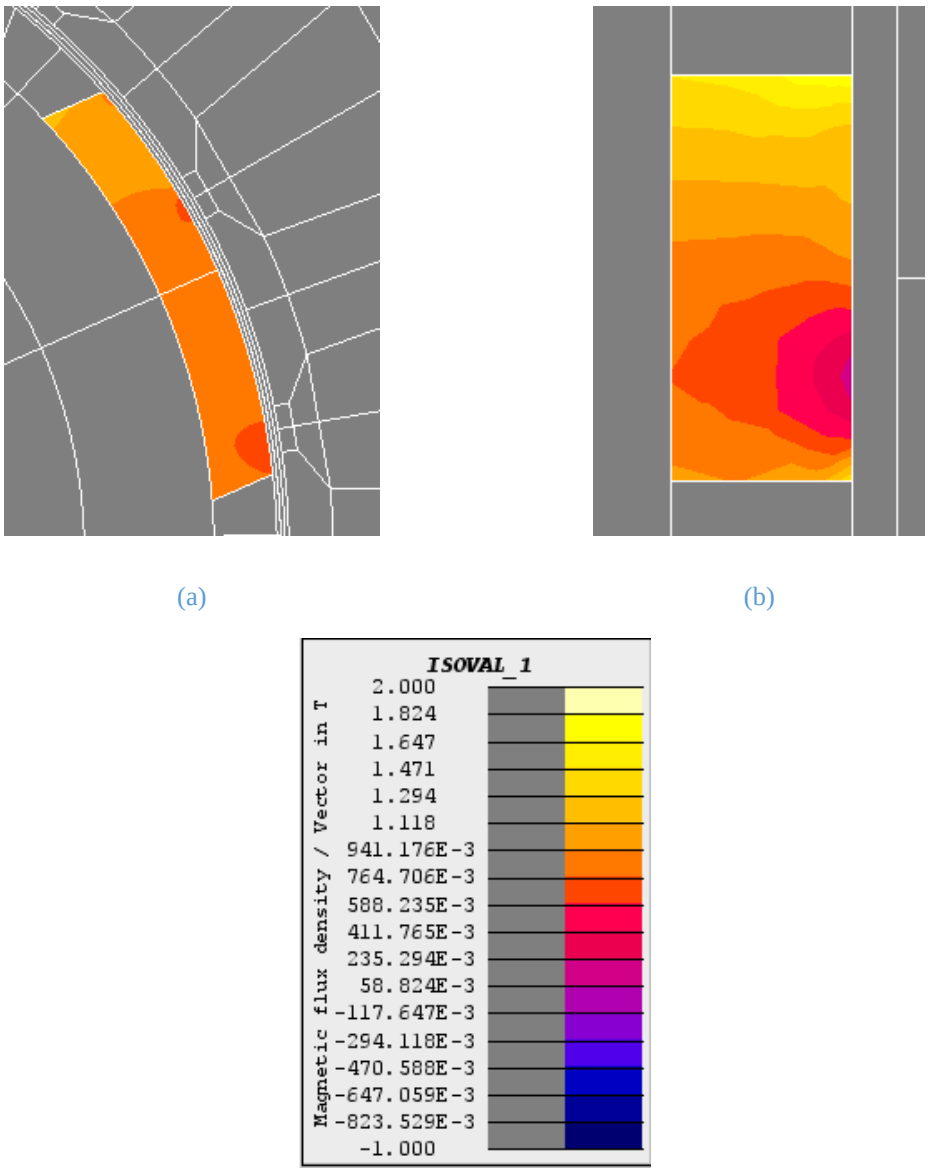

(a) (b)

(c)

Fig. 4-35 Magnets flux density (a) Motor PM (b) Magnetic screw PM (b) Scale

By integrating the magnetic screw, the peak thrust force of the MSLA is 5234N and resultant force density of such linear actuator reach 4.55MN/m^3, which is more than an order of magnitude higher than the current state-of-the art linear electromagnetic actuator under the same cooling condition. This shows that the design of the MSLA has a great potential for the target application and beyond.

4.6 Summary

In order to meet the application requirements of active suspension with high thrust force density and high reliability, this chapter has developed the MSLA actuator with integrated magnetic screw structure. The magnetic screw based on the helix magnetic force transmission mechanism can achieve high thrust force density and non-contact

force/power transmission. By combining it with a rotating PM machine, a high efficiency and high thrust force density MSLA actuator can be constructed.

According to the law of energy conservation, the transmission principle of the magnetic screw is explained. Further, an analytical mathematical model is established to predict the magnetic thrust force and force density density. On this basis, the general design optimization process of the MSLA is proposed.

First, the magnetic screw part of the MSLA is designed according to the design specification. In order to achieve high thrust force density theoretically, the magnetic screw structure should be long and thin. This, however, compromises mechanical properties of the actuator. The leading design parameters of the magnetic screw are determined based on a mover radius that yields good stiffness. The design optimisation of the matching motor according to the output performance and geometric dimensions is subsequently carried out. Since the screw magnetic part and the motor part share the same rotor, special attention has been paid to the magnetic saturation in the rotor back-iron, the losses and thermal analysis. The design of the MSLA is further validated by 3D FE analysis.

From the simulation results, the designed MSLA exhibits high thrust density and high efficiency while meeting the design specification and free from jamming. In subsequent chapters a prototype is manufactured and tested for validation.

CHAPTER 5
Unbalanced Magnetic Pull in a Magnetic Screw

This chapter investigates the unbalanced magnetic force(UMF) produced by translator eccentricity in a magnetic screw. The principle of eccentricity is briefly outlined and an analytical expression that can be used to predict UMF of a magnetic screw is established. A 3D magnetic screw model with helically magnetized permanent magnets(PMs) has been built and simulated in ANSYS Maxwell with different eccentricities. Comparing the finite element (FE) simulation and analytical calculation results, there is a certain difference in the UMF of the magnetic screw, which is also caused by the asymmetry of the magnetic screw structure. And compared to the linear tubular PM motor with the same thrust force capability, the magnetic screw has a much smaller UMF, which eases the mechanical design of the device, albeit it is dependent on relative mover position. Furthermore, a simplified 3D tubular permanent magnet model is proposed to reduce computational burden. It is shown that the eccentric force of the helically magnetized PM structure can be estimated by simulation of the simpler tubular PM structure.

5.1 Introduction

The last chapter designed a MSLA that can provide high thrust force density, but in the linear actuator testing, it is often troubled by the friction generated by machining and the UMF. Since the magnetic screw rotor needs to rotate when the mover moves linearly, its structure requires two sets of bearings, and its motor housing needs to be divided into more sections. Because of manufacturing tolerance of each motor housing section, the assembly of multiple housings will result in greater tolerance progression. And because the two sets of bearings will also cause errors in assembly the air gap between the rotating and translating elements of a magnetic screw may not be uniform. This eccentricity will generate radial UMF, which will cause additional friction, vibration and noise, and accelerate bearing wear.

Since the effective length of a linear electromagnetic actuator with a long stroke is generally much larger than that of a rotating motor, this problem is often more serious in linear actuators. In many applications, such as artificial heart, magnetic screws are required to operate in high stability and low vibration [120]. The linear actuator designed in this thesis is applied to the active suspension, it needs a lot of fast reciprocating motion in application. So if its UMF is too high, the mover is prone to deformation after long-term operation. And as the air gap on one side decreases, the UMF on this side will become higher, and the eccentricity of the mover will deteriorate rapidly under high-

frequency working conditions. This will reduce the stable performance and service life of the magnetic screw. So to ensure reliability and safety, the risk of UMF is comprehensively assessed under worst conditions, and preventative measure devised at the design stage.

5.1.1 Machine Eccentricity

In a rotating electric machine, the radial electromagnetic force acting on the surface of the rotor and stator is much larger than the tangential electromagnetic force which produces torque. However, if the axis of the stator and the rotor coincide with no eccentricity, the air gap between them is evenly distributed and the radial forces cancel each other out. In fact, the geometric eccentricity between the stator and rotor of the machine is inevitable due to factors such as machining error, assembly error and bearing wear, resulting in UMF [124].

General rotor geometric eccentricity is mainly divided into static eccentricity, dynamic eccentricity and mixed eccentricity [125-126]. Static eccentricity is caused by factors such as manufacturing errors and assembly errors. After installation, the axis of the stator and rotor do not coincide. If eccentricity on any section along the motor axis is the same, it is collectively referred to as radial eccentricity [127-128], as shown in Fig. 5-1 (a). In practice, however, due to assembly errors and other reasons, the center lines of the stator and rotor are usually not parallel, resulting in angular misalignment, which is static angular eccentricity [129], as shown in Fig. 5-1 (b). The air gap changes along the axial direction but the minimum air gap position is fixed.

Dynamic eccentricity is a situation where the rotation center of the rotor does not coincide with its axis, which is usually caused by factors such as machining errors and bearing wear [130-131]. The position of the smallest air gap is rotating, so the eccentric force is always changing. In addition, the unbalanced mass distribution of the rotor, that is, the centrifugal force generated by the motor during operation, will also cause dynamic eccentricity [132]. Moreover, the radial displacement of the rotor increases significantly near the critical speed, so the relative eccentricity is more serious and may even cause the stator and rotor rubbing. Mixed eccentricity refers to the situation where static eccentricity and dynamic eccentricity exist simultaneously, and this is a most likely case in a real rotory or linear electrical machine.

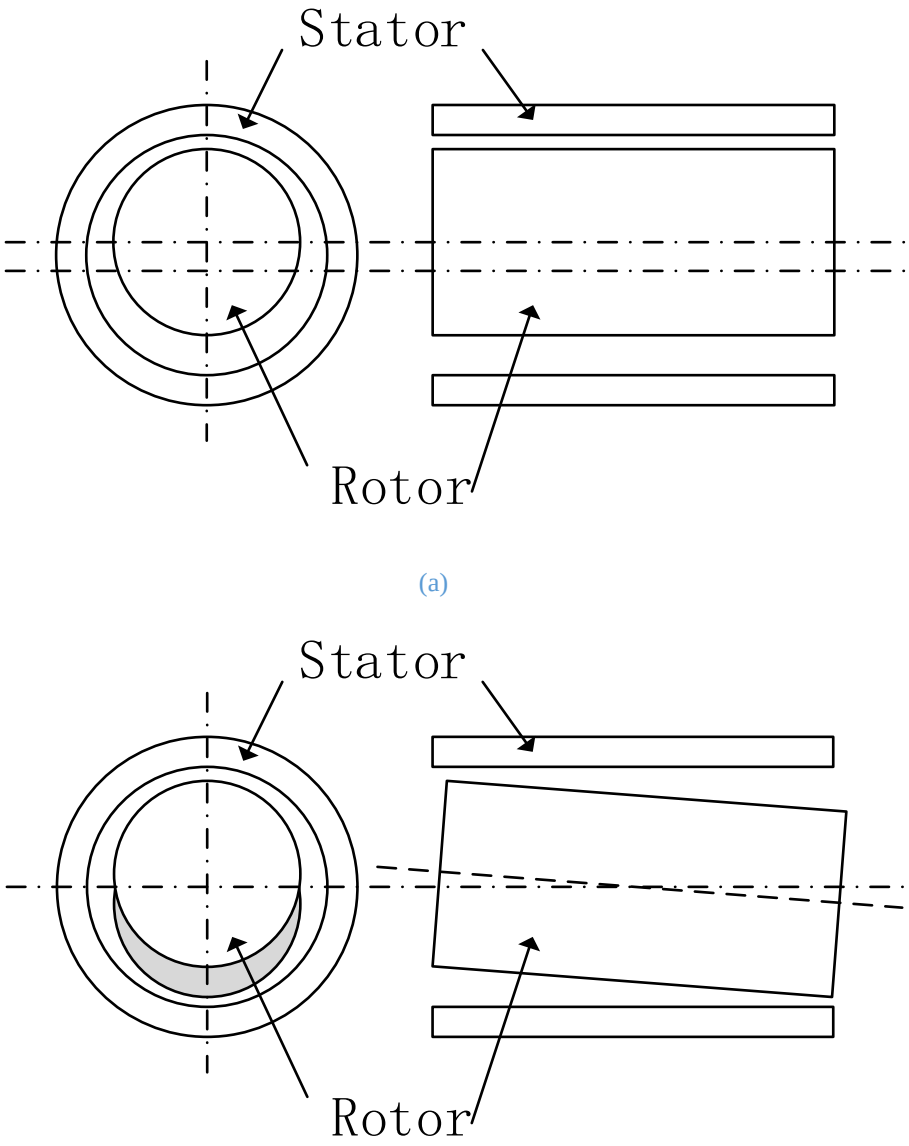

Fig. 5-1 Machine static eccentric (a) Radial eccentricity (b) Angular eccentricity

5.1.2 Unbalanced Magnetic Force of Rotary Motors

Due to the geometric eccentricity between the stator and the rotor, the air gap of the motor is no longer uniform and its magnetic field is distorted, so the radial force acting on the rotor is no longer balanced and an UMF is generated. The direction of the UMF points from the centre of the rotor to the stator where the air gap is the smallest, so that the rotor continues to deviate from the centre of the stator, which causes the UMF to increase further. This positive feedback mechanism shows that the unbalanced magnetic tension has negative stiffness characteristics, which weakens the lateral load-bearing capacity of the rotor shaft, causes the natural frequency of the system to decrease [133],

produces higher vibration and noise levels [134], and causes bearing wear and even stator and rotor friction [135].

As early as the beginning of the 20th century, scholars had observed the existence of UMF [136], and used linear models to derive theoretical formulas. Behrend [137] put forward the hypothesis that the magnetic density in the air gap is inversely proportional to the length of the air gap, resulting in a linear expression of the UMF. Later Covo [138] considered magnetic saturation and improved the linear model. Tenhunen [139] verified the correctness of Covo's equations through experiments. Richard [140] discussed the effect of linear and nonlinear materials on the UMF under different loads. Dorrel [141] proposed a different analytical method from the past to obtain the UMF generated by the eccentric rotor, which can flexibly deal with various winding conditions. Pillai [142] considered the rotor tilt and coning motion, and established the approximate analytical expression of the UMF caused by the rotor static eccentricity. Bortoli [143] analyzed the UMF of various stator coils when the rotor is eccentric. Li et al. [144] used the conformal mapping method to establish the UMF model of the PM motor considering the cogging factor. Lundström et al. [145] used the law of conservation of energy to calculate the UMF considering the shape deviation of the generator rotor.

The expression of the linear model is easy to use and has sufficient accuracy when the eccentricity is small. In engineering applications, linear empirical formulas are often used for calculations [146]. However, UMF is a typical nonlinear force [147]. When the eccentricity increases, the error of the linear model also increases, and the noise and vibration of the rotor increase significantly [148].

5.1.3 Unbalanced Magnetic Force of Linear Actuator

While there is a wide range of papers dealing with the UMF of rotary motors, relatively little work is dedicated to analysis of UMF in linear actuators, although they are more susceptible to UMF during operation due to long axial distance between two bearing supports in machines with long stroke. 2D and 3D finite element (FE) models of linear tubular motors were used to analyse the UMF in [149-152]. Marignetti [153] derived an analytical formulation of the no load magnetic field distribution in tubular IPM machines with translator eccentricity. Wang [154] assessed the UMF of double-sided linear switched reluctance machine and Zouaghi [155] investigated the UMF of a quasi-Halbach magnetized PM linear motor.

5.2 Analytical Formulation of Magnetic Field with Mover Eccentricity in a Magnetic Screw

UMF will appear when the stator and rotor are geometrically eccentric. Its nonlinearity and negative stiffness effects have an important impact on the characteristics of the magnetic screw. In order to study the magnetic field distribution of the magnetic screw in air gap. This chapter makes the following assumptions when calculating the unbalanced magnetic tension

(1) The relative permeability of the core is infinite;

(2) Ignore the magnetic saturation of the core;

(3) The inner surface of the stator and the outer surface of the rotor are both smooth cylindrical surfaces.

Fig. 5-2 (a) shows the 2D longitudinal cut view of a magnetic screw and Fig. 5-2 (b) shows the shows the 3D model of the magnetic screw, which is used in active suspension applications and is capable of more than 5000N thrust force with an effective stroke of 150mm. It should be noted that a periodic repeat of the magnetic field along the axial direction of the device spans 360º electrical degrees. Thus, the linear displacement θ in electrical degree is related to the linear mechanical displacement z by $\theta = 180z/T_p$, where T_p is the pole-pitch of the magnetic screw, as shown in Fig. 5-2 (a).

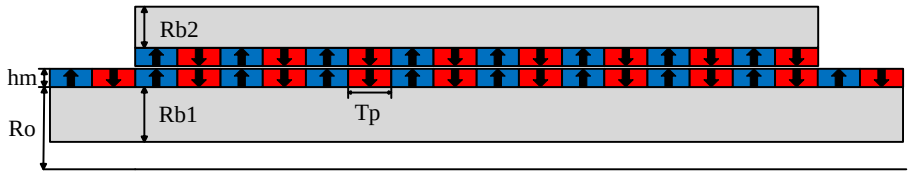

(a)

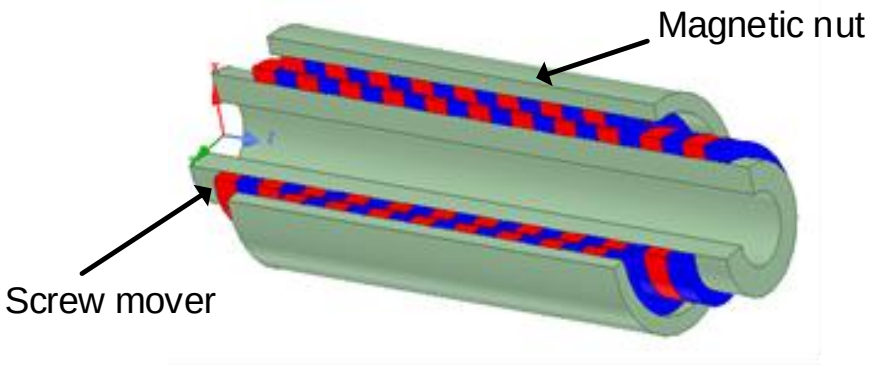

(b)

Fig. 5-2 Schematic of a magnetic screw (a) 2-D longitudinal cross section view (b) 3D model

5.2.1 Air-Gap Length Distribution of Magnetic Screw

Since the magnetic field of the magnetic screw acts on the air gap, the length of the air gap has a significant influence on the magnetic field. Therefore, in order to study the magnetic field in the eccentric air gap, it is first necessary to determine the air gap length at each angle.

Fig. 5-3 (a) shows the cross-sectional structure of the non-eccentric two-pole magnetic screw. Where R_1 is the outer radius of the screw mover, R_i is the inner radius of the magnetic nut and $g0$ is the air gap length without eccentricity. The PMs of the magnetic screw is magnetized radially. And because the magnetic screw PMs is a spiral structure, the front view of magnetic screw cross-sectional has only one pole on both the magnetic nut and screw mover, which appears as one color.

Fig. 5-3 (b) shows the cross-sectional structure of the eccentric magnetic screw. This chapter only studies the case where the screw mover has static eccentricity and no static angular eccentricity. So in the coordinate system O'xy, the screw mover center O and the magnetic nut center O' have a deviation of e in the y direction. When the screw mover moves in a straight line, its center is always higher than the center of the magnetic nut, that is, the maximum and minimum positions of the air gap remain unchanged at all times, with $g0$-e in the positive direction of the y-axis and $g0$+e in the negative direction of the y-axis, respectively.

In eccentric cross section of magnetic screw, as the angle of the mover θ changes, the air gap width g' also changes. When point A is not on the y axis, aob and ao'b are two right triangles with the same base. From the right triangle formula:

$$R_i \cos\theta' - (R_1 + g')\cos\theta = e \tag{5-1}$$

$$R_i \sin\theta' = (R_1 + g')\sin\theta \tag{5-2}$$

Add (5-1) and (5-2) squares to get

$$(R_1 + g')^2 + 2e(R_1 + g')\cos\theta + \left(e^2 - {R_i}^2\right) = 0 \tag{5-3}$$

Solving (5-3), the air-gap length g' can be calculated as a function of θ and e as

$$g' = -e\cos\theta \pm \sqrt{{R_i}^2 - e^2\sin^2\theta} - R_1 \tag{5-4}$$

Since e is much smaller than R_i , $\sqrt{{R_i}^2 - e^2\sin^2\theta}$ approximately equal to R_i (5-4) can be simplified to

$$g' = g_0 - e\cos\theta \tag{5-5}$$

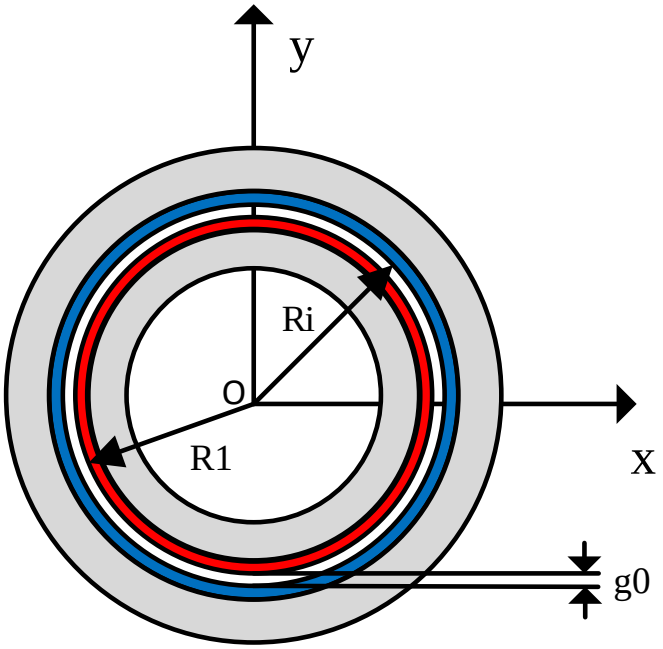

(a)

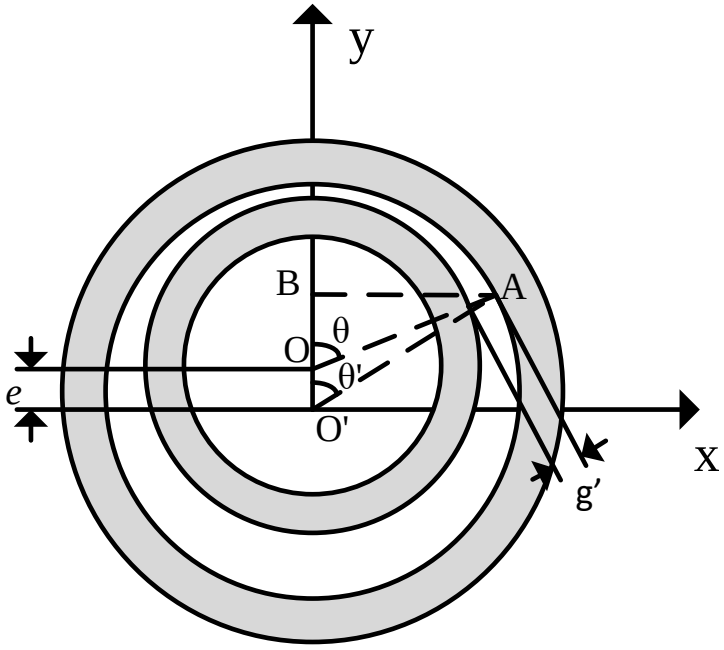

(b)

Fig. 5-3 Front view of a magnetic screw (a) Non-eccentric cross section (b) Eccentric cross section

5.2.2 Eccentric Magnetic Field

As shown in Fig. 5-4, the structure of the magnetic screw with eccentricity has not changed, but its air gap length changes with the angle of the mover θ. Fig. 5-4 (a) shows the longitudinal cut view of the magnetic screw at a given θ position, where the dimensions for the analytical calculation of the magnetic field distribution, are given by $R_m=R_1+hm$, $R_i=R_1+hm+g'$ and $R_s= R_1+2*hm+g'$. The tubular magnetic field model is used to analyze the UMF of the eccentric magnetic screw, where the pair of the magnets on the rotary part of the screw are represented by their equivalent current sheets. FE method is used to verify the analytical results.

As has been described in Chapter 4, the radial and axial components of the magnetic field distribution expression in the airspace region are obtained as

$$B_{\mathrm{Ir}}(r,z) = -\sum_{n=1,3,5..}^{\infty} [a_{\mathrm{In}} BI_1(m_n r) + b_{\mathrm{In}} BK_1(m_n r)] \cos(m_n z)$$

$$B_{\mathrm{Iz}}(r,z) = -\sum_{n=1,3,5..}^{\infty} [a_{\mathrm{In}} BI_0(m_n r) - b_{\mathrm{In}} BK_0(m_n r)] \sin(m_n z) \qquad (5\text{-}6)$$

The constants associated with the n[th] harmonic, a_{In}, b_{In}, are determined by satisfying the following boundary conditions

$$B_{\mathrm{Iz}}|_{r=R_s} = 0, \quad B_{\mathrm{IIz}}|_{r=R_1} = 0,$$

$$B_{\mathrm{Iz}}|_{r=R_m} = B_{\mathrm{IIz}}|_{r=R_m}, \quad H_{\mathrm{Iz}}|_{r=R_m} = H_{\mathrm{IIz}}|_{r=R_m} \qquad (5\text{-}7)$$

where R_s varies as the air gap g' changes. Therefore, the radial force generated by the current sheets and the PM field along z-direction is

$$F_r = \int (J_\theta \times B_z) \cos\theta \, dV \qquad (5\text{-}8)$$

where V is the total area of the current sheets. When the magnetic screw does not have eccentricity, the magnetic field is the same at different angle θ, and the integral of cosθ is 0 from 0 to 2π. The forces in different directions are mutually offset, and the whole screw mover is free from radial force. But when the magnetic screw is eccentric, the air gap magnetic field at different angles θ is different, so the UMF per pole can be obtained from the following integration:

$$F_r = \int_{z-\tau w/2}^{z+\tau w/2} \int_0^{2\pi} \int_{R_i}^{R_s} J B_{\mathrm{Iz}}(r,z) \cos\theta \, r \, dz dr d\theta \tag{5-9}$$

which can be written as

$$F_r = 2\pi J_C \sum_{n=1,2,\ldots} K_n \cos(m_n z_d) \tag{5-10}$$

where z_d and τ_m are the axial displacement of mover and magnet pole length as shown in Fig. 5-4

$$K_n = K_{zn} \sin(m_n \tau_m / 2)$$

$$K_{zn} = \int_0^{2\pi} \int_{R_i}^{R_s} [a_{In} B I_0(m_n r) - b_{In} B K_0(m_n r)] \cos\theta \, r \, dr d\theta \tag{5-11}$$

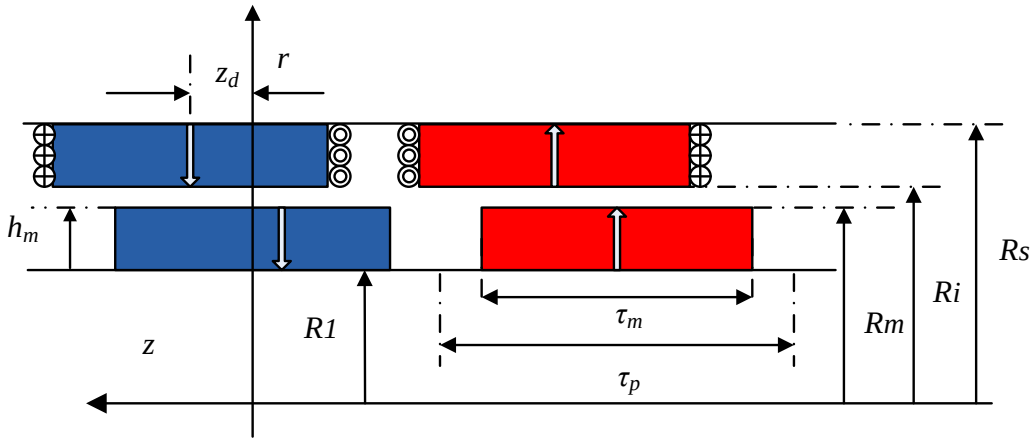

(a)

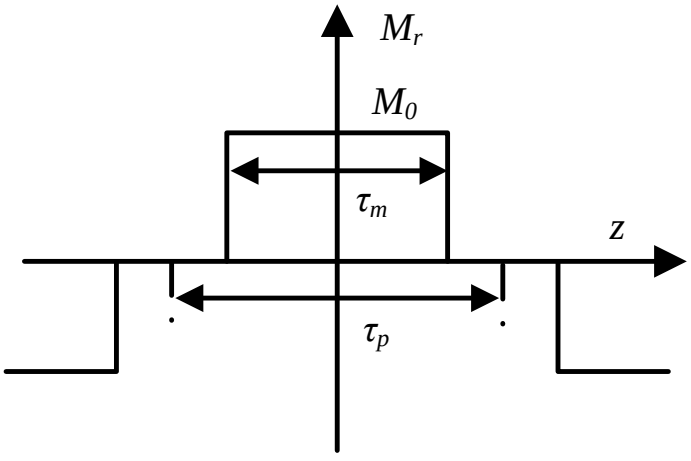

(b)

Fig. 5-4 Field region of eccentric magnetic screw (a) Field region (b) Magneto motive force distribution

5.2.3 Analytical UMF prediction

The analytical UMF prediction in (5-11) will be obtained for a 8 pole pair magnetic screw as shown in Fig. 5-2 whose main design parameters are given in Table 5-1.

Fig. 5-5 (a) shows the variation of analytically predicted UMF of the magnetic screw with mover displacement in electric degree when the eccentricity changes from 0.05mm to 0.15mm. The eccentric position is along the y-axis, the higher the eccentricity, the narrower the air gap length in the positive y direction. The mover linear displacement (angle) 0 ° corresponds to the magnetic screw 0N thrust force position, where z_d=0, as shown in Fig. 5-6 (a). At this position, the radial flux density in the air gap where the current sheets are located is 0 while the axial flux density is the strongest. Hence, the magnetic screw UMF reaches its maximum at this position for a given eccentricity. For the case studied, the maximum UMF with 0.15mm eccentricity is (197N). When the mover linear displacement (angle) is 90 °, z_d=1/2τ_m, as shown in Fig. 5-6 (b), the magnetic field in the radial direction is the strongest while the magnetic field in the axial direction where the current sheets are placed is 0. The resultant magnetic screw UMF is 0N. The UMF characteristics over -90^0~0 linear displacement are the mirror images of those shown in Fig. 5-5 (a). The UMF of the magnetic screw varies periodically for each 180^0 repeat of linear displacement angle θ.

Fig. 5-5 (b) shows the maximum UMF changes with eccentric length. When the eccentric length increases, the maximum UMF increases linearly. When the eccentricity is 0.15mm, the maximum UMF is 3.7% of the maximum thrust force of the magnetic screw.

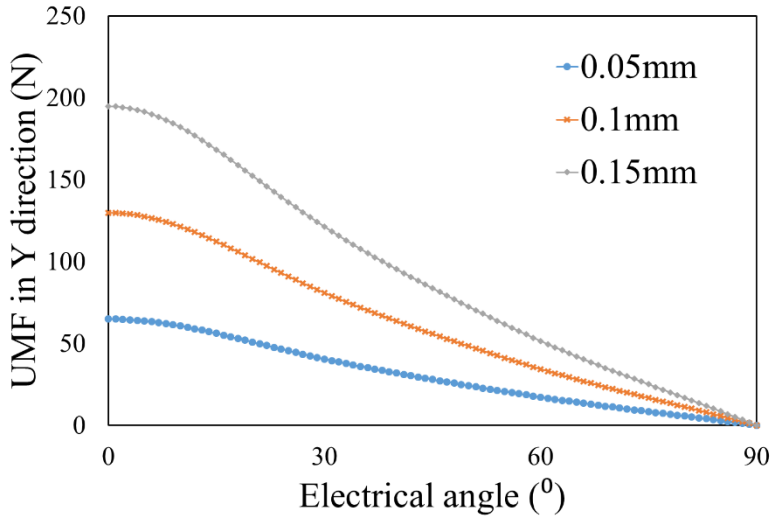

(a)

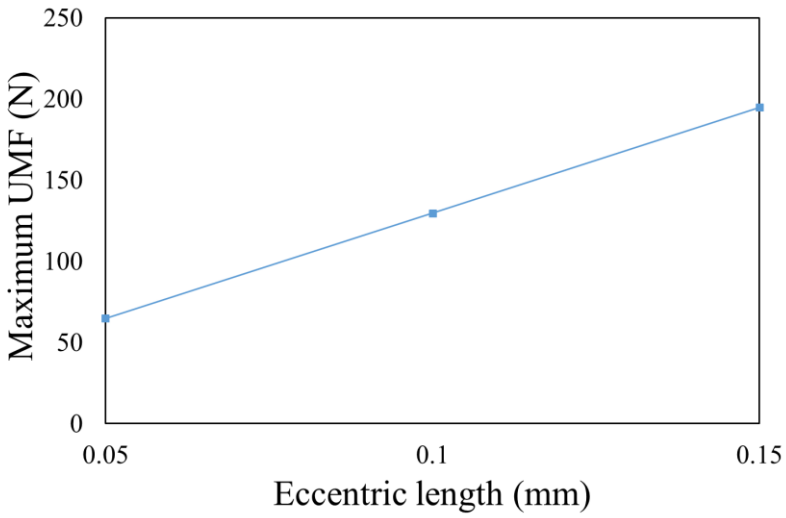

(b)

Fig. 5-5 Analytical UMF prediction (a) Under different eccentricity (b) Maximum UMF comparison

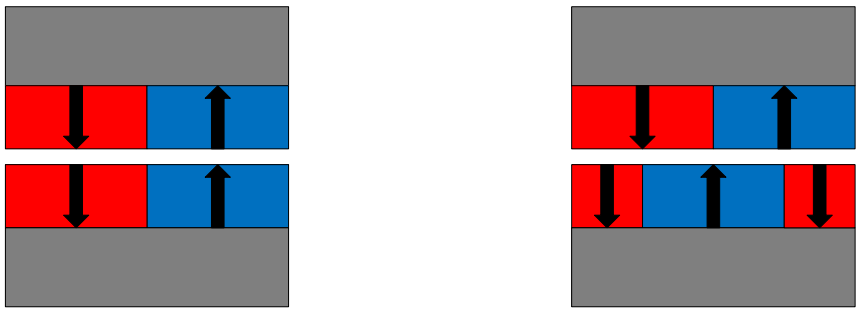

(a) (b)

Fig. 5-6. Magnetic screw PM position (a) 0o angle. (b) 90o angle

Table 5-1 Main design parameters of magnetic screw

Parameters	Symbol	Value
Outer radius of the screw mover	*R1*	28mm
Magnet thickness	*hm*	4mm
Air gap without eccentricity	*g0*	1mm
Remanence of PM	B_{rem}	1.3T
Pole pair	*p*	8
Pole-pitch	*τm*	9mm

5.3 3-D FE Analysis and Comparison

In order to get more accurate results, the predictions from the derived analytical expression for UMF should be compared with 2-D and 3-D FE analyses. However, unlike conventional linear tubular motor, the magnetic field distribution in a magnetic screw is asymmetrical and the fringing fields at two ends of the devices are different. Therefore, the general 2D model simulation may not be very accurate. The simulation of eccentric

force in the magnetic screw requires 3D FE analysis. Because of the unconventional structure of the magnetic screw, construction of the 3D model and its simulation is more complicated and time consuming.

5.3.1 3-D FE Mover Eccentricity Model

Since it is difficult to draw 3D helically PMs in the simulation software ANSYS Maxwell, the model of the magnetic screw is imported from SolidWorks for FE analysis of the magnetic screw UMF due to mover eccentricity, as shown in Fig. 5-7. Because the end effect of the helically magnetised PM of the magnetic screw cannot be expressed periodically, the length of the UMF model is the same as the thrust force model. And since the length of the mover of the magnetic screw is longer than the length of the magnetic nut under normal working conditions, a pole pair distance is extended on both sides of the mover. When the 3-D FE simulation is running, the magnetic screw mover does not move linear, but the magnetic nut rotates, which is equivalent to the linear displacement of screw mover and the end effect at both ends will not be significantly changed.

To ensure prediction accuracy, it is important to use appropriate mesh generation process. Fig. 5-8 shows 2 different 3D model meshes of the magnetic screw used to predict its UMF. Fig. 5-8 (a) shows the meshes automatically generated by the software, and Fig. 5-8 (b) shows the active refined meshes. It can be seen that the density of active refined meshes is much higher than that of automatically generated meshes. Since the magnetic screw has a large volume compared with rotating motors whose FE volume can be effectively reduced by symmetry, improving the quality of the meshes will greatly increase the 3-D FE simulation time. In the case of active refined high-quality meshes, the simulation time of a 90 °electrical cycle exceeds one week.

With high-quality meshes, prediction accuracy improves. Fig. 5-9 shows the resultant flux density distribution on the inner surface of the magnetic nut. Since the magnetic screw is only equipped with PMs, its flux density should exhibit the helical pattern of the PM deployment. In Fig. 5-9 (a), the flux density distribution predicted with the automatically generated meshes appears to be inaccurate as discontinuous field is seen in various places. In Fig. 5-9 (b), the flux density distribution of the magnetic nut predicted with the fine mesh generation exhibits clearly the smooth helical pattern. Therefore, in order to obtain the UMF of the magnetic screw as accurately as possible, although this

will greatly increase the time of computer simulation, the active refined meshes is selected for simulation.

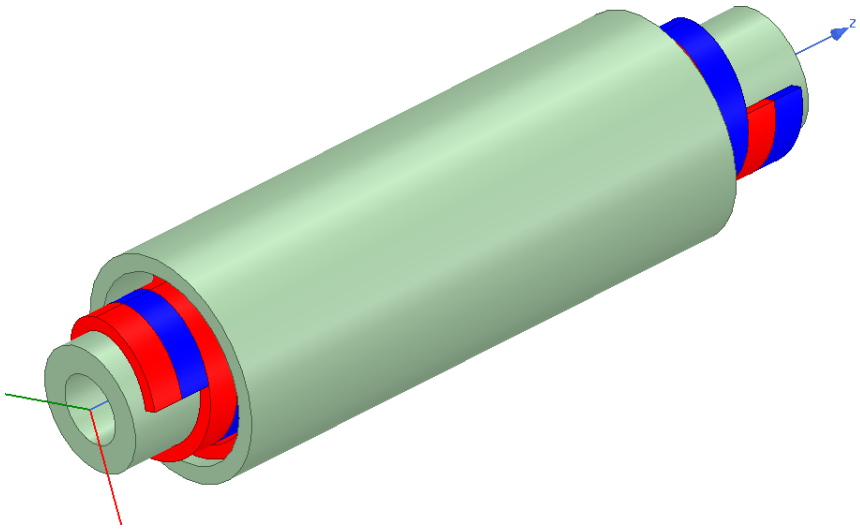

Fig. 5-7 3-D FE mover eccentricity model

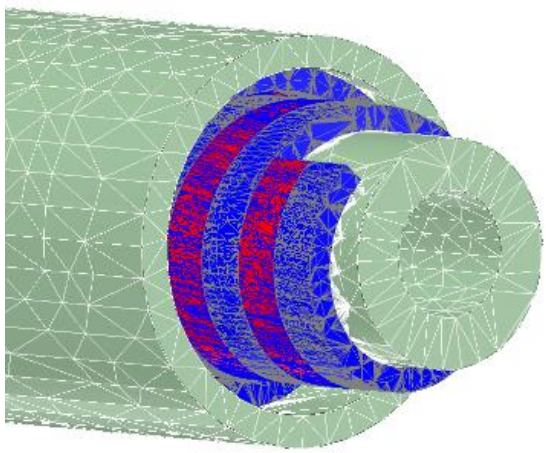

(a)

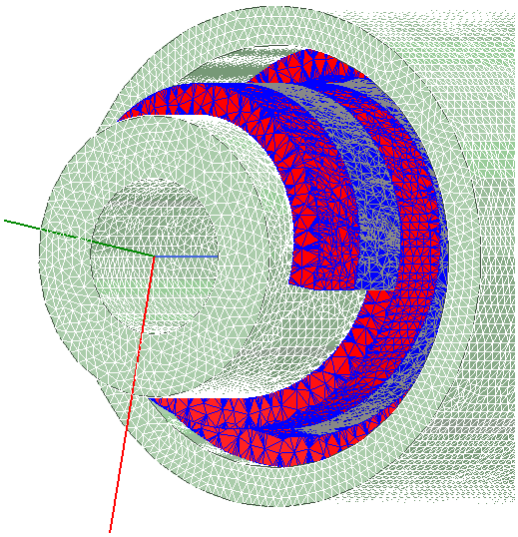

(b)

Fig. 5-8 Meshes of the 3D magnetic model. (a) Automatic generated meshes. (b) Active refined meshes.

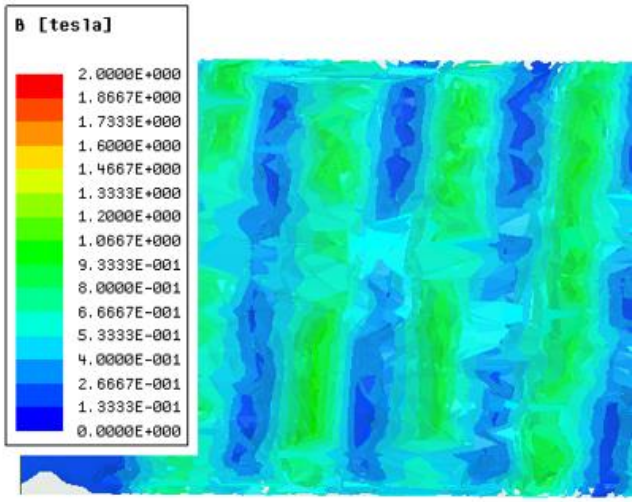

(a)

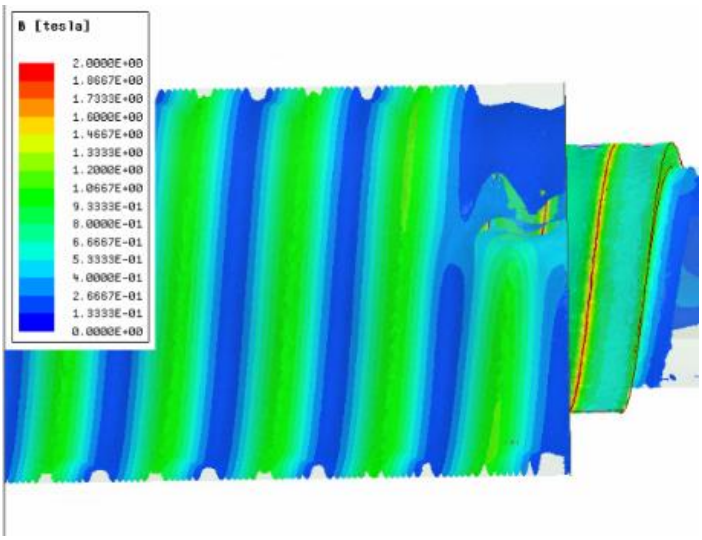

(b)

Fig. 5-9 Nut flux density distribution. (a) Automatic mesh. (b) Active fine mesh.

5.3.2 3-D FE Predicted UMF and Comparison

Fig. 5-10 (a) shows the variations of unbalance magnetic pull in the y-direction with linear displacement of the mover in electrical degree when the eccentricity along the y-axis e varies from 0 to 0.15mm in a step of 0.05mm. Similar to the analytical predicted trend, when the mover linear displacement (angle) is 0 °, the resultant UMF value with 0.15mm eccentricity is the largest and reaches 245N in magnitude. This is because at this position, the axial component of the flux density at the current sheet locations is the largest and hence the device is more sensitive to the eccentricity. On the other hand, when the mover is displaced by a quarter of the pole-pitch, i.e., the electrical angular displacement is 90 °, the UMF value for the same eccentricity is the lowest (50N). This is due to the fact that the axial component of flux density is greatly reduced at this mover position. Fig. 5-10 (b) shows the maximum and minimum UMF changes with eccentric length. The trend of the 3-D FE result is slightly different from the analytical calculation result. As the eccentric length increases, the 3-D FE predicted maximum UMF curve becomes slightly larger than the linear trending. When the eccentricity is 0.15mm, the maximum UMF is 4.6% of the maximum thrust force of the magnetic screw.

Fig. 5-11 shows the comparison between 3-D FE and analytically predicted results. The trend of variations between the two is similar, but there is a clear offset in the two predictions. Different from the analytical results where the UMF is 0 at 90 °, the UMF predicted by 3-D FE at this position is not zero albeit being realtively small. This may be attributed to three factor factors. (1) The analytical prediction assumes 2D field distribution while it will be 3D under mover eccentricity, (2) the analytical prediction neglected helical magnetisation pattern and (3) the end effect is not accounted in the analytical model. Table 5-2 lists the maximum deviations of the UMFs predicted by the two methods for three mover eccentricities. If the FE predicted UMF at 90^0 is added to the analytical prediction for a given eccentricity, the agreement of the two preditions becomes very good.

Fig. 5-12 shows the 3-D predicted output thrust force of the magnetic screw under 0.15mm eccentricity and no eccentricity. It can be seen that while the UMF is not small, the eccentricity has little effect on the thrust force.

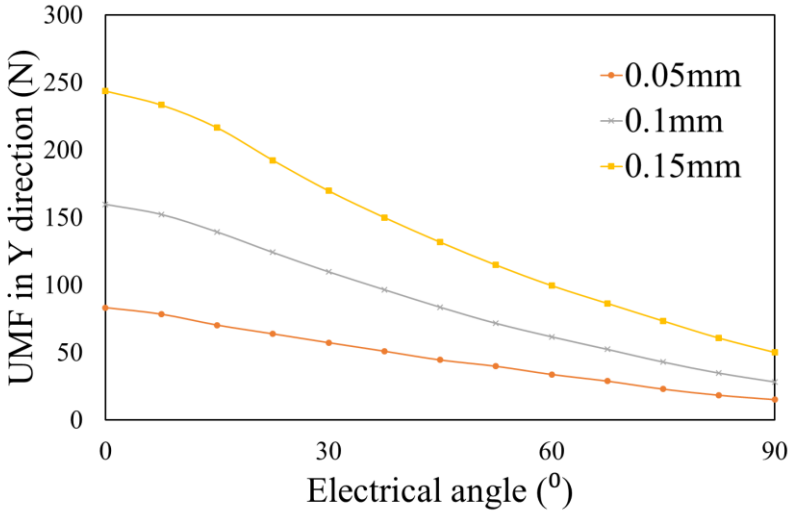

(a)

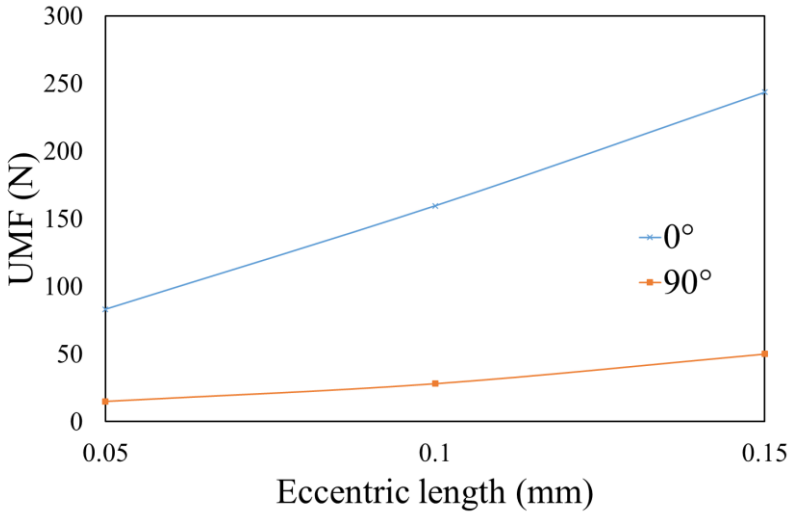

(b)

Fig. 5-10 3-D FE UMF variations with linear displacement (a) Under different eccentricity (b) Maximum and minimum UMF

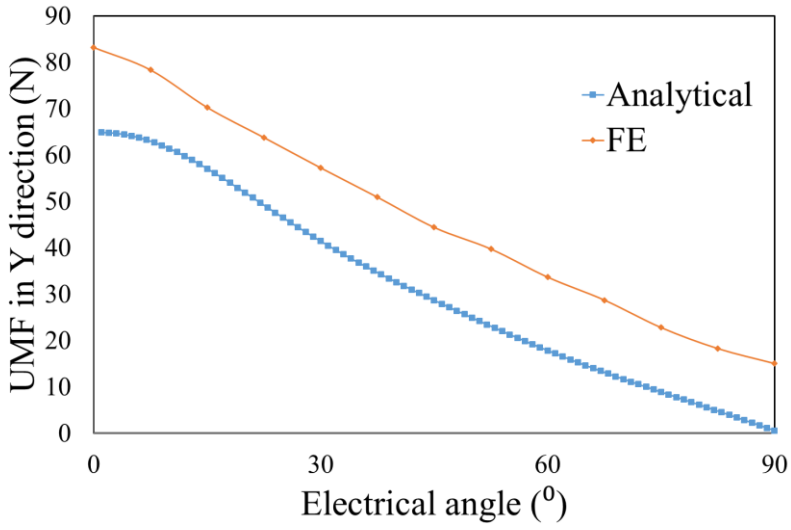

(a)

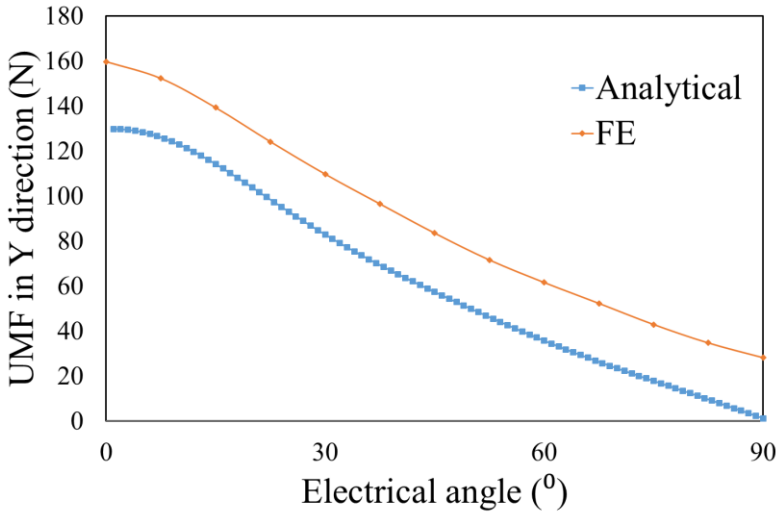

(b)

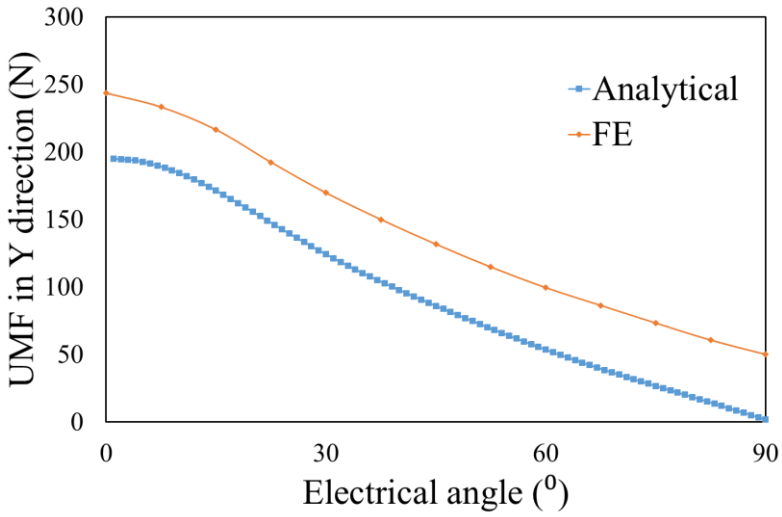

(c)

Fig. 5-11 Comparison of 3-D FE and analytical result (a) 0.05mm eccentricity (b) 0.1mm eccentricity (c) 0.15mm eccentricity

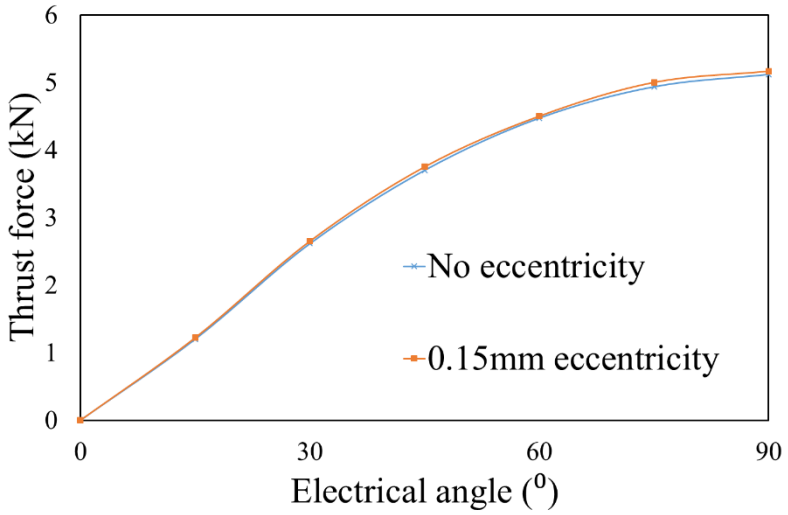

Fig. 5-12 Magnetic screw thrust force under 0.15mm and 0mm eccentricity

Table 5-2 Comparison of 3-D FE and analytical result at 0 °

Eccentricity	Analytical	3-D FE	Percentage difference
0.05mm	64N	83N	22.9%
0.1mm	129N	159N	18.8%
0.15mm	194N	243N	20.1%

5.4 Simplified 3-D Model for UMF prediction

Since the magnetic field distribution in the magnetic screw is 3-D while the eccentricity and air gap are relatively small, the mesh size and density have to be carefully controlled in order to ensure accuracy. However, in order to achieve accurate results, the model with the active refined meshes greatly increases simulation time and computational burden.

Therefore, it is of great value to find a simplified model to reduce the burden of simulation with adequate accuracy.

5.4.1 Radially Magnetised Magnet Arrays

To simplify the 3D simulation of the magnetic screw model, the 9 pole-pairs of helically magnetised magnet arrays are replaced by radially magnetised tubular rings of the same number of pole-pairs, as shown in Fig. 5-13. By exploiting the periodic condition of the tubular PM magnet rings, simulations only need to be performed with one pole-pair and, consequently, the workload is greatly reduced.

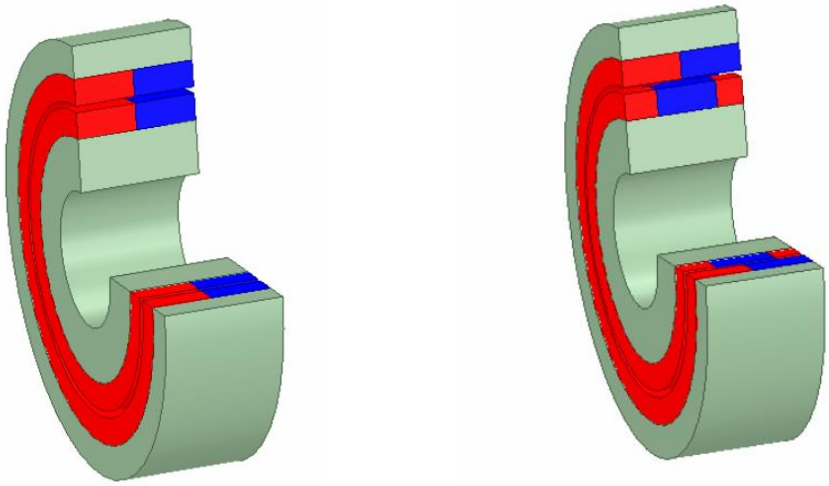

(a) (b)

Fig. 5-13 Tubular PM rings (a) 0 °angle 3D view of tubular PM rings (b) 90 °angle 3D view of tubular PM rings

5.4.2 Comparison of UMF predictions with Magnet Array Model and Magnetic Screw Model

Fig. 5-14 compares the predicted UMFs with the simplified magnet array model and the full 3D FE model of the device shown in Fig. 5-10 (a) as a function of axial displacement in electrical degree under 0.15mm eccentricity. With 9 pole-pair, the minimum and maximum forces in magnitude predicted by the simplified model are 252N and 53N, respectively, being very close to those predicted by the full model. The computation time of the simplified model is 84 times lower than that of the full model. This result indicates that the helical magnetisation and the end effect may be neglected in the UMF prediction of the magnetic screw. In order to reduce the simulation time, the simplified 3D model or the analytical model may be used for assessing the UMF of the magnetic screw.

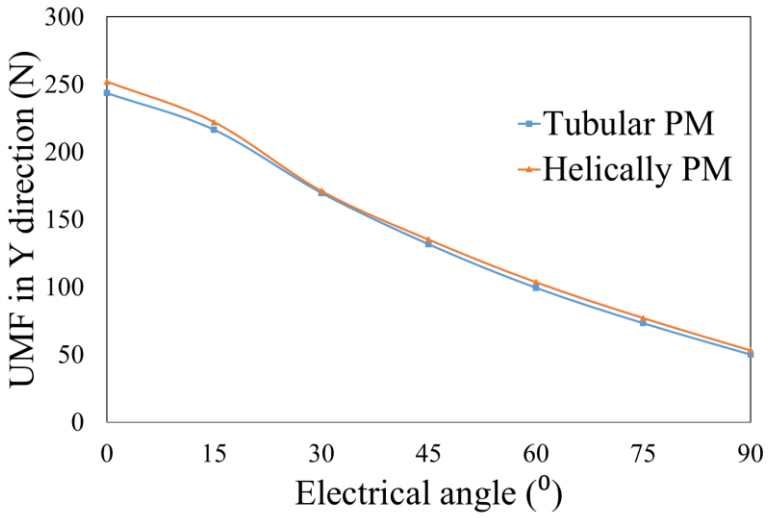

Fig. 5-14 UMF of Tubular PM magnet rings compared magnetic screw under 0.15mm eccentricity

5.5 Summary

In this Chapter, the characteristics of UMF in a magnetic screw under static eccentricity have been studied and an analytical formula for UMF prediction has been derived. The UMFs have also been predicted by a full 3-D FE model of the magnetic screw and the results are compared with the analytical predictions. It has been shown that the maximum UMF in a magnetic screw occurs when the axial displacement of the mover is at 0 electrical degree, and the resultant thrust force is also 0. The maximum UMF even under eccentricity of 0.15mm is 243N, being a few percent of the peak thrust force only. This is quite small and its effect on mechanical design and resultant increase in bearing friction force is less significant. The small UMF results from the fact that with the magnetic gearing the active volume of the magnetic screw to produce the required force capability is much small.

Compared with the UMFs predicted by the 3-D FE model, the analytical calculation incurs a constant offset for a given mover eccentricity, which may be caused by neglecting 3D field distribution in the device. The deviation between the two is about 20%. Finally, the eccentric forces predicted by the helically magnetized PM model and the simpler tubular PM model are compared. The two results are very close; the error may be caused by the irregular edge of the magnetic screw. It has been shown that the eccentric force of the helically magnetized PM structure can be estimated by simulation of the simplified tubular PM structure, thus greatly reducing the time required for 3D simulation.

CHAPTER 6
Mechanical Design of Magnetic Screw Motor Actuator and Prototype Testing

This chapter describes the mechanical design, testing and result analysis of the linear actuator. The mechanical design includes the linear actuator itself as well as the motor housing design and testing rig design. The testing part is divided into the motor testing and the linear actuator overall testing, which mainly verifies the torque characteristics of the motor and the static thrust force characteristics of the linear actuator.

6.1 Introduction

In order to validate whether the performance of the magnetic screw based linear actuator is consistent with the design specifications and simulation results, it is necessary to carry out prototype construction and experimental tests. However, compared with the traditional motor, the magnetic screw based linear actuator has the characteristics of long effective length, multi-layer air gap, etc., so that it's mechanical design and construction are much more complex than a traditional rotary or linear motor. In this Chapter, a high force density linear actuator integrated with the 18-slot 8-pole motor and magnetic screw is built according to the outcomes of the design optimization described in Chapter 4. And as discussed in Chapter 5, due to the progressive tolerance of the linear bearings on both sides and the deformation during the assembly process, the magnetic screw part may have a larger eccentricity. The long effective length of the linear mover would increase friction when the mover and two supporting bearings are not concentric and aligned perfectly. In addition the multi-layer air gap makes the actuator more prone to eccentricity. If the prototype is subjected to extreme friction during testing, it will be difficult to achieve the expected results.

Therefore, the high force density linear actuator must be specially designed to control its eccentricity and friction, and due to the special form of the PMs of the magnetic screw, there is a trade-off between the electromagnetic performance and the difficulty of mechanical processing and assembly. Section 6.2 discusses the mechanical design process of each part in detail, including the motor housing, and list the bearings and sensors selected in the prototype.

Section 6.3 presents the test verification of the prototype. Due to time constraints, this experiment only verified the motor performance and the static characteristics of the magnetic screw. As mentioned above, since the magnetic screw motor actuator is not a conventional motor structure, a conventional test rig cannot be used for measuring the performance of the magnetic screw. Hence, the test rig for the magnetic screw test was first designed. Next is to test the motor part, including the no-load back EMF and the torque characteristics. The static test part of the magnetic screw-motor includes no-load displacement test and static thrust force test. Finally, the experimental results are obtained and analysed, and Section 6.4 summarises the findings.

6.2 Mechanical Design of Magnetic Screw Based Linear Actuator

Fig. 6-1 shows the assembly drawing of the magnetic screw based linear actuator. As illustrated in the Chapter of introduction, the mechanical design of the magnetic screw based linear actuator needs to control the tolerance progressively to ensure that the magnetic screw will not experience excessive friction during operation. The entire motor is supported by 5 structural components from left to right, namely the Support base left and right, End cap left and right, and Motor housing, in which a pair of linear bearings and a pair of rotary bearings are nested. The tolerances of these components are controlled in the design and manufacture according to the matching standard, and the unmarked parts are processed according to the GB-1804.

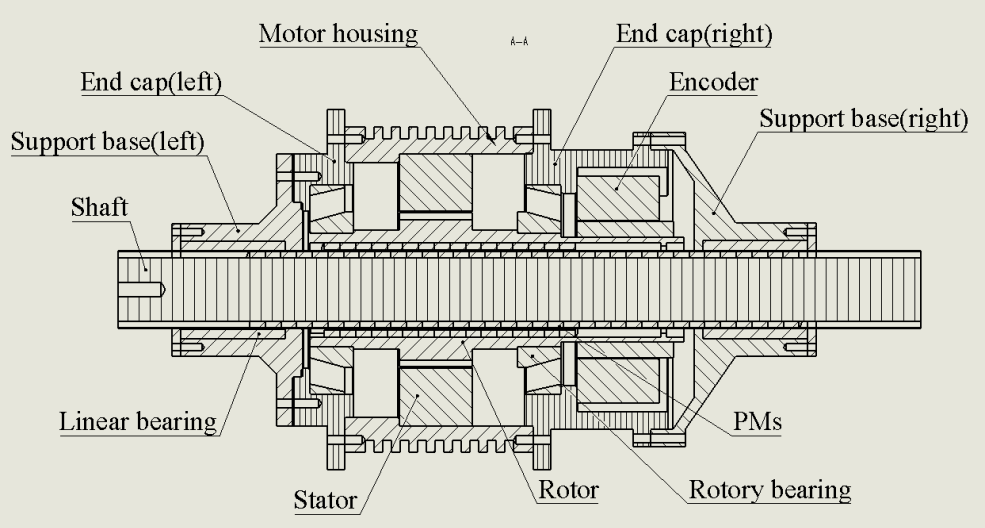

(a)

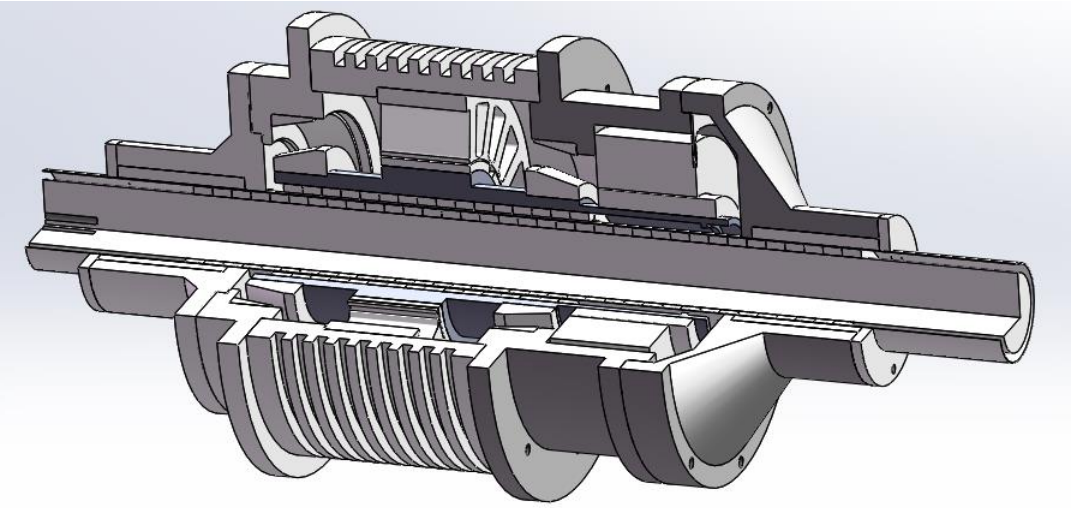

(b)

Fig. 6-1 Assembly drawing of magnetic screw motor (a) Mechanical drawing (b) 3D model

6.2.1 Motor Supporting Structure Design

As shown in the design requirements in Chapter 4, the rated thrust force of the magnetic screw motor is 2000N and the rated speed is 1m/s, so the design of the motor supporting structure must meet the following requirements:

(1) The mechanical strength is sufficient, and the motor housing will not crack or be damaged when the magnetic screw is subjected to a large load force;

(2) The stiffness is sufficient, the magnetic screw, stator and rotor assembly will not be damaged or cannot work normally due to the excessive deformation of the housing under different use conditions of the actuator;

(3) The number of structural components should be as small as possible to reduce the progressive tolerance of the linear bearings at both ends of the magnetic screw, thereby reducing the friction suffered by the magnetic screw in motion.

(4) Under the condition that the performance requirements can be met, a reasonable layout is convenient for the installation of each assembly, reducing its weight to minimise the overall weight of the actuator, saving materials and reducing manufacturing costs.

Fig. 6-2 shows the drawing of the stator housing, a heat sink design is used on the exterior, and through a hole to lead out the wires. A stepped structure on the inside is used for positioning the motor stator axially, and an interference fit is used to fix the stator with the housing. Since there is no special requirement on the circumferential position of the

stator, there is no positioning feature on the inner bore of the housing. To balance mechanical strength and lightness, the entire motor housing is made of aluminium alloy.

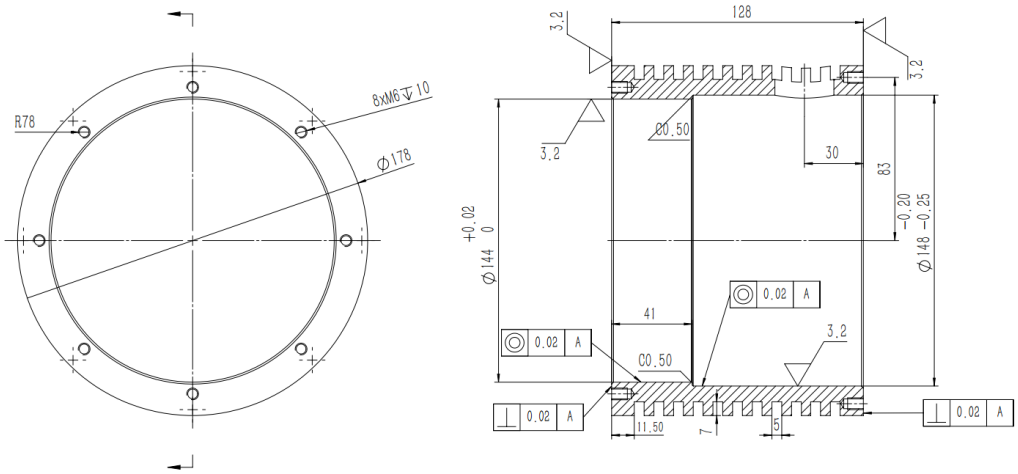

Fig. 6-2 Drawing of stator housing

Connected to the left and right of the stator housing are the end cap left Fig. 6-3 (a) and the end cap right Fig. 6-3 (b), its main functions are (1) supporting the rotor assemply by two rotary bearings nested in them, (2) providing structure support and connection to the linear bearings supporting components, and (3) axial positioning of the two linear bearings. They also provide a seal to the end winding region of the stator, and prevent contamination from dust during operation. As the right end cap needs to accommodate a resolve, its axial is extended. In order to reduce the total length, the end cap is connected to the stator housing externally. Due to the relatively large radius of the rotor part and the high axial load, tapered rotary bearings are used to support the rotor and counter-balancing axial load force of the actuator. Fig. 6-4 shows the large-diameter resolver installed in the motor end cap. The resolver housing is fixed in position by the positioning slots and pressed with 6 M5 screws, and the resolver rotor is fixed on the motor rotor through the pin hole and the pressure ring. The motor rotor speed is converted into an analogue signal by the transmitter and received by a controller or can be displayed on an oscilloscope. Table 6-1 and Table 6-2 show the datasheet of the tapered roller bearings and resolver used in the actuator.

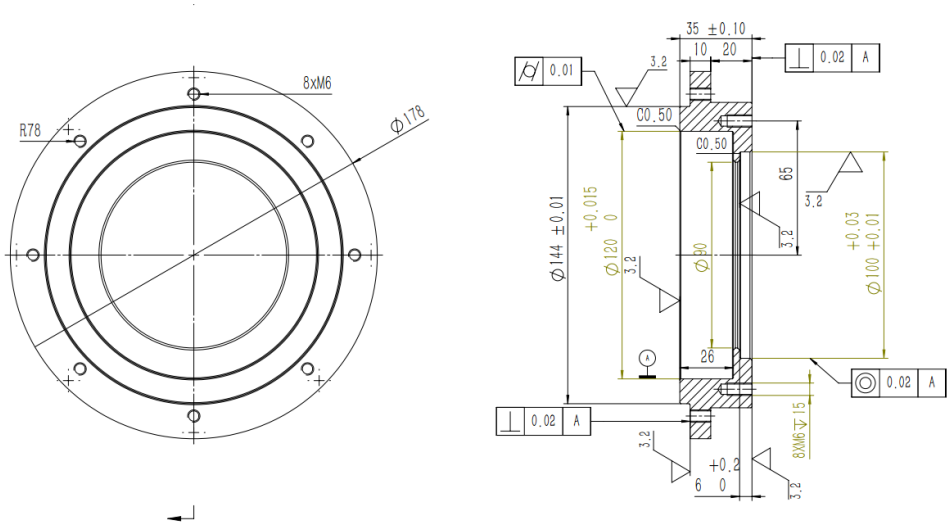

(a)

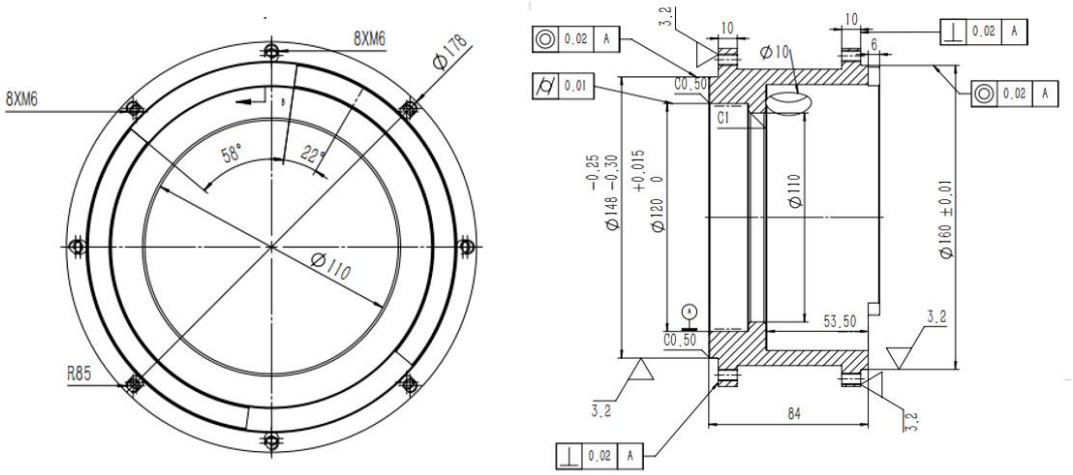

(b)

Fig. 6-3 Drawing of end cap (a) left part (b) right part

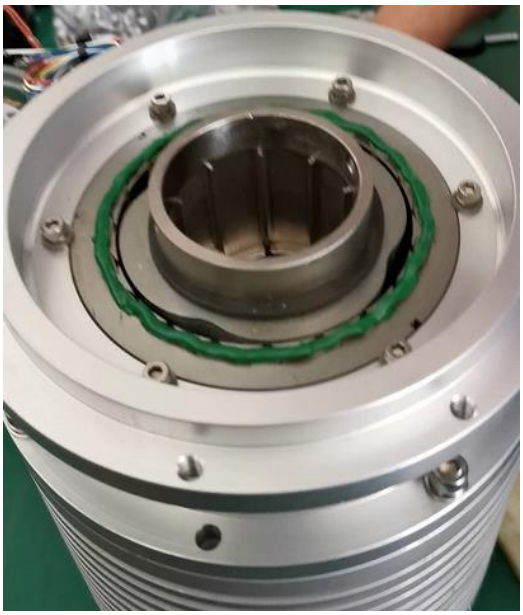

Fig. 6-4 large-diameter resolver

Table 6-1Tapered roller bearing datasheet

Parameters	Value	Unit
Outer diameter	120	mm
Inner diameter	65	mm
Rated load	141	kN
Speed limit	5600	rpm
Bearing quality	1.12	kg

Table 6-2 Magnetoresistive resolver datasheet

Parameters	Value	Unit
Number of pole pairs	4	
Excitation voltage	7	V
Excitation frequency	10	kHz
Outer diameter	114	mm
Inner diameter	64	mm
Speed limit	20000	rpm
Output voltage	2	V

The two end caps of the motor housing are connected to the support base left Fig. 6-5(a) and the support base right Fig. 6-5(b), which support the magnetic screw mover through the two linear bearings. Since the linear bearing directly contacts with the magnetic screw and the PMs on the screw surface has a low strength, the linear bearing design uses a graphite copper sleeve instead of a ball bearing in order to avoid damage to the PMs and reduce friction. The dimensions and frictional coefficient are listed in Table 6-3. The maximum speed is limited to 2 m/s, which coincides with the maximum speed of the linear mover.

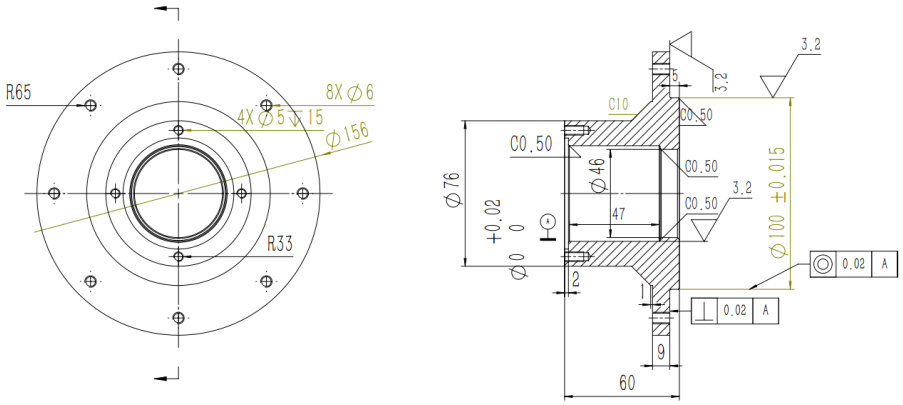

(a)

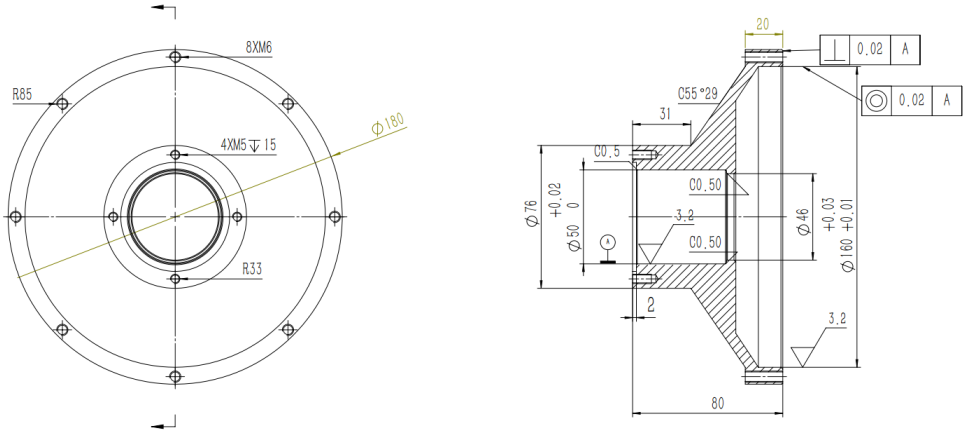

(b)

Fig. 6-5 Drawing of support base (a) left part (b) right part

Table 6-3 Graphite copper sleeve data

Parameters	Value	Unit
Outer diameter	55	mm
Inner diameter	45	mm
Speed limit	2	m/s
Coefficient of friction	<0.16	

6.2.2 Motor Stator and Rotor Design

The motor stator stack adopts M270, 0.35mm stator lamination, laser cutting and high-quality bonding are used in the lamination process, and 2mm non-magnetic glass material is used at both ends of the stator as shown in Fig. 6-6. Each turn consists of 5 strands of 0.62mm diameter magnet wire. The winding leads to A B C three-phase terminals and a neutral point. Epoxy resin is injected into the winding gap to improve the overall strength of the winding and enhance the heat dissipation capacity.

Fig. 6-6 Motor stator with winding

Fig. 6-7 shows the rotor assembly of the magnetic screw based linear actuator for illustration purpose. Since this part needs to incorporate both the rotor magnets of the rotary motor on its outer surface and the magnets of the magnetic screw nut on its inner surface, its structure is very different from that of the conventional linear mover or rotor. Structure features, namely the eight ribs, are used to position the rotor PMs on the outer surface. In order to ensure the strength of the PMs during rotation, the outer PMs are encapsulated in 0.25mm non-magnetic stainless steel sleeve. The magnets are N35UH whose remanence is 1.05T, and it is insensitive to temperature variation. The two left and right steps are used to fix the tapered roller bearings position. And the part extending from the right side is used to connect the resolver with the rotor through a pin hole and pressure ring. On the inner side is assembled with magnets of the magnetic screw nut. 160 tile-shaped PMs approximately constitute a staggered helix PM pattern. Since the magnetic screw rotor has both axial and radial flux paths, the laminated structure cannot be used. The entire rotor hub uses soft iron material to ensure both the magnetic permeability and the mechanical strength.

(a)

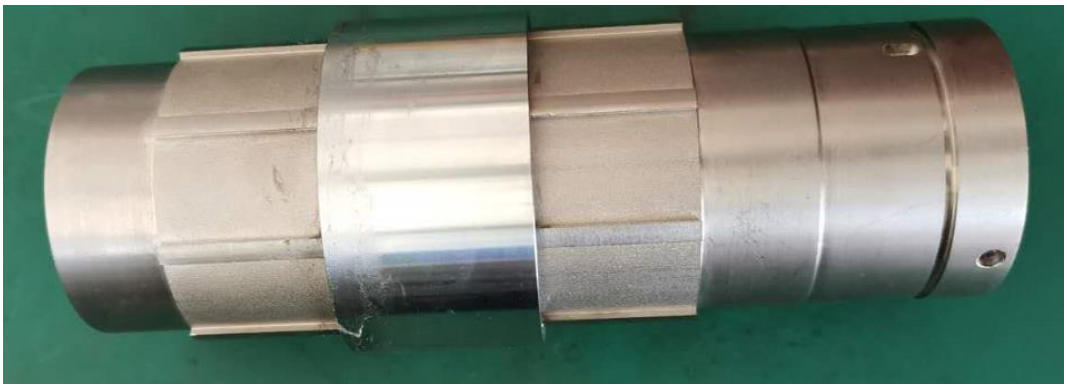

(b)

Fig. 6-7 Motor rotor (a) Front view (b) Side view

6.2.3 Magnetic screw PM Design

According to the previous design, the PMs of the magnetic screw should be composed of two helix PM arrays with magnetization directions that are diametrically opposite, but in fact such PMs can neither be processed nor magnetized in reality. Therefore, it is necessary to design a manufactural structure to approximately replace the helix magnetisation pattern used in the magnetic screw.

Fig. 6-8 shows a tile-shaped PM used to replace the helix PM. From the top view, it is a parallelogram, which makes the PM easy to cut and can be closely fitted in assembly. The side view is similar to the arc shape of the traditional magnets in a surface-mounted PM machine. The magnet material is N42UH. The magnets are magnetized after sintering. The magnetization direction of the tile-shaped PM is selected to be parallel to the centre radial direction. Fig. 6-9 shows the variations of magnetic screw thrust force with radial

and parallel magnetizing directions. The peak force with radial magnetized PMs is 10% higher than that with parallel magnetized PMs. Therefore, after considering the processing cost and difficulty, the PMs of the magnetic screw adopts the parallel magnetization method.

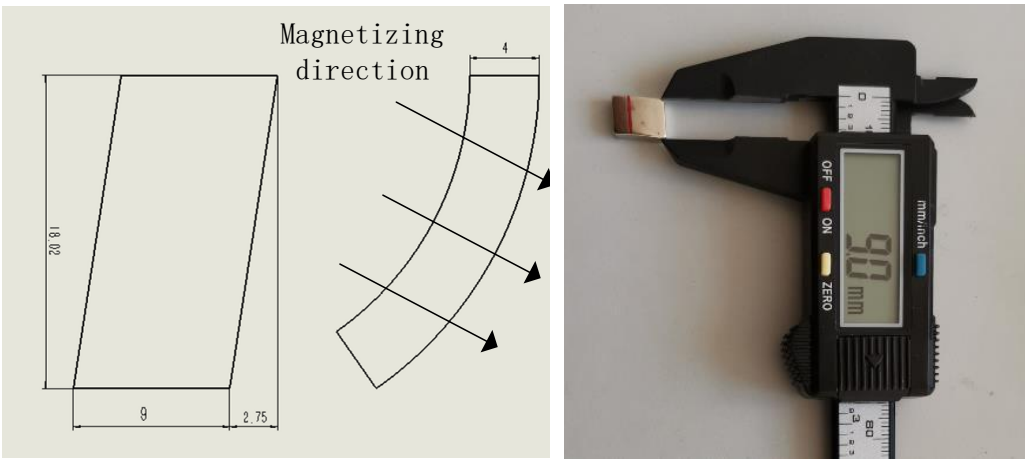

(a) (b)

Fig. 6-8 Magnetic screw PM (a) Mechanical drawing and magnetising direction (b) Physical map

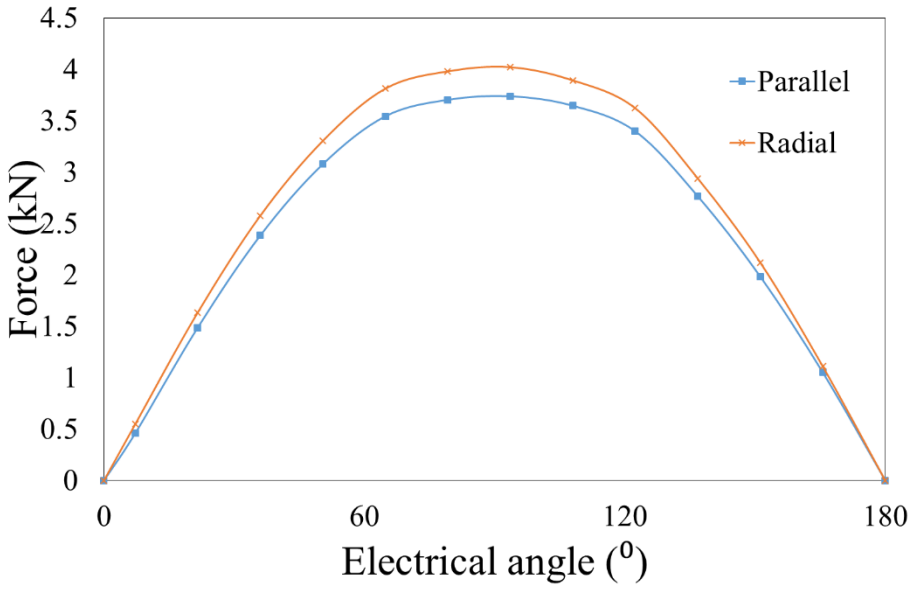

Fig. 6-9 Variations of magnetic screw thrust force with magnetizing direction

6.2.4 Magnetic Screw Mover Design

The mover assembly is shown in Fig. 6-10. The whole mover is composed of a layer of ultra-low carbon steel with a 40cr shaft jacket. There is an M10 screw hole at one end of the mover to connect with the testing rig. Although the ultra-low carbon steel has low magnetic permeability, the mover magnetic circuit will not be too saturated due to the

thicker iron back. This not only ensures the mechanical strength of the screw mover, but also ensures the electromagnetic performance of the mover.

Fig. 6-10 Variations of magnetic screw thrust force with magnetizing direction

Tile-shaped PMs are glued into grooves on the surface of the mover through epoxy resin. Due to the parallel magnetization of the magnetic screw PMs, too few PM segments over 360^{o} circumference will result in uneven distribution of the radial flux density in the magnetic screw airgap and hence more significant reduction in the thrust force. On the other hand, because the PMs need to be processed and assemble in position, too many segments will cause difficulty in processing and PM volume loss. Fig. 6-11 compares the magnetic screw thrust force with the number of permanent magnet segments per 360 °. After comprehensive consideration, the number of PM segments is selected to be 10.

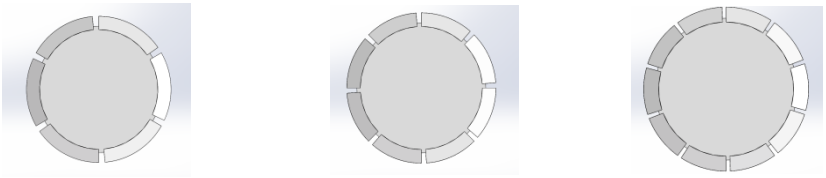

6 Pieces 8 Pieces 10 Pieces

(a)

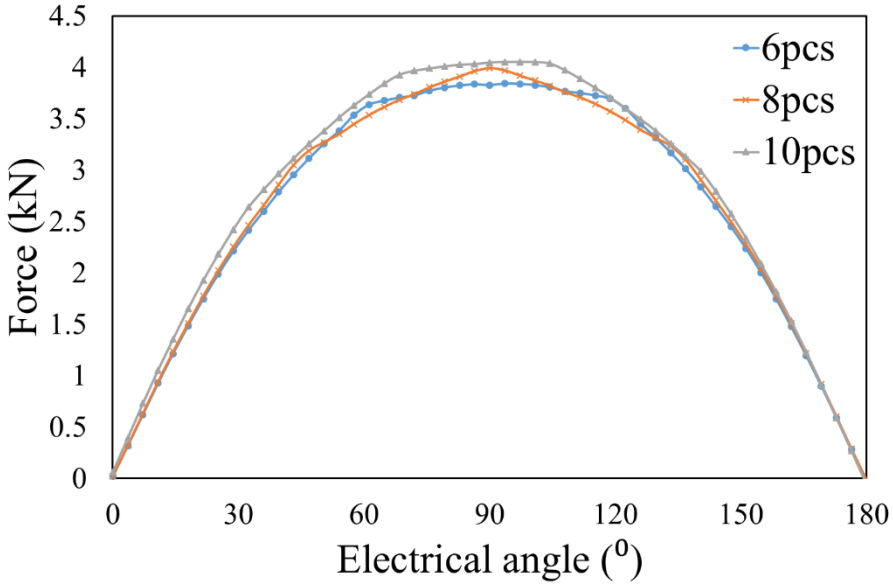

(b)

Fig. 6-11 Variations of magnetic screw thrust force with number of pieces (a) Segmentation in circumenferencial direction (b) resultant force variation with linear displacement in electrical degree

Because the tile-shaped PM is customized, extra care need to be taken during assembly. When the tile-shaped PMs were assembled, the design position were fixed by glue, and then a magnet piece were slowly pushed in from the edge along the slot. Since the two end parts of the mover will directly contact with the linear bearing, a 0.5mm non-magnetic stainless steel sleeve is added on the surface of the mover in order to provide smooth contacts with the bearing and to reduce friction. The assembly process of the mover sleeve is shown in Fig. 6-12. By installing a 2mm thick sleeve and then being processed to 0.5mm by a lathe, the deformation during the assembly of the long sleeve can be avoided.

Fig. 6-12 Assembly process of the mover sleeve

6.3 Testing Rig and Instruments

Test verification of the magnetic screw based linear actuator prototype is divided into two parts, one is the torque characteristic test of the rotating motor part, and another is the static thrust force test of the magnetic screw-rotating-motor part. The two experiments used two test rigs. The rotating motor test rig used an existing test rig and the magnetic screw test rig was designed by the author. Both tests used the same motor part. In rotating motor test an extension shaft is installed in the rotor and the support base on both sides of the motor housing were removed. The static thrust experiment uses the complete actuator structure described in Chapter 4.

6.3.1 Magnetic Screw Test Setup

In order to perform systematic tests on the high force density linear actuator prototype, a static test rig is developed. The test rig should be able to adjust and lock the mover position, measure the actuator output force and record the relevant experimental data. Fig. 6-13 shows the schematic test rig used to measure the thrust force of the magnetic screw motor at different positions. And the data of the motor rotor position and magnetic screw mover position can also be collected while measuring the thrust force.

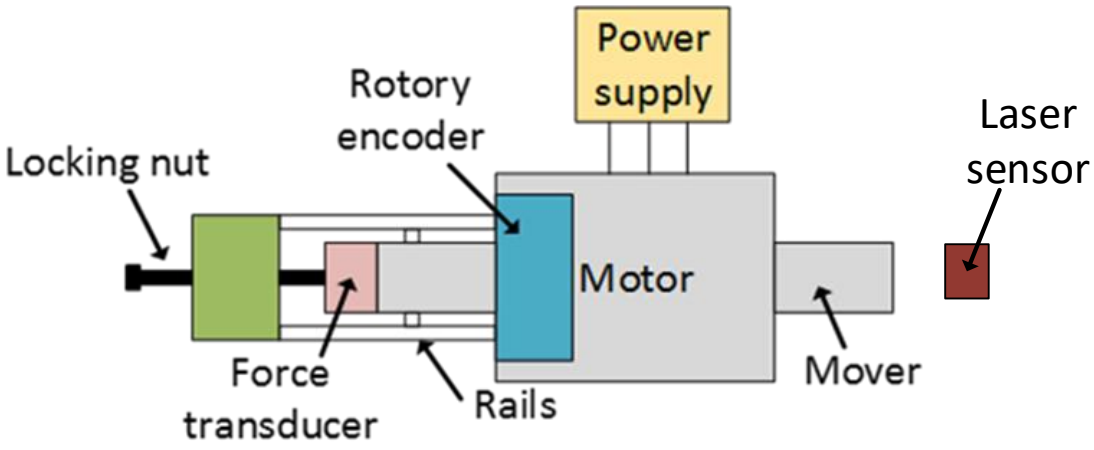

Fig. 6-13 Schematic test rig

As illustrated in Fig. 6-13, the prototype is connected to an adjustable displacement device via couplings with a force transducer, which measures thrust force and moves with the mover when adjusting the mover position with the rocker displacement device. At the same time, the screw mover is connected to the guide rail of the experimental platform through the connecting device, which allows the mover to move freely along the guide rail and prevents the mover from rotating. When the motor is fed and controlled by an

inverter, the motor rotor rotates, and at the same time the mover is locked in a fix position, then the thrust variation with the relative displacement between the magnetic screw nut and the mover can be obtained from the thrust force sensor. To make use of available off-the-shelf components, the mechanism to prevent mover rotation is modified.

Fig. 6-14 shows the modified test rig. The rig consists of a base, two mounting plates, two guide rails, two connecting slides and position adjusting screw. Two mounting plates are placed in front and back of the base to fix the position of the actuator. The back mounting plate is a whole block, and its middle hole matches the left support base of the actuator housing to support the actuator. The front mounting plate consists of two half-block plates, which is convenient for actuator installation and removal. When the actuator is installed, the actuator is fixed in position by two front and rear mounting plates, and the mover is connected with an adjusting screw through a sliding block. A sensor is installed in the slider, and the sliding block is installed on the guide rail and can reciprocate. When the motor is not moving, the position of the mover can be adjusted by loosening and tightening the adjusting screw. The base of the test rig is made of steel, and the other parts are made of aluminium alloy, which not only ensures the strength of the test rig but also reduces the overall weight.

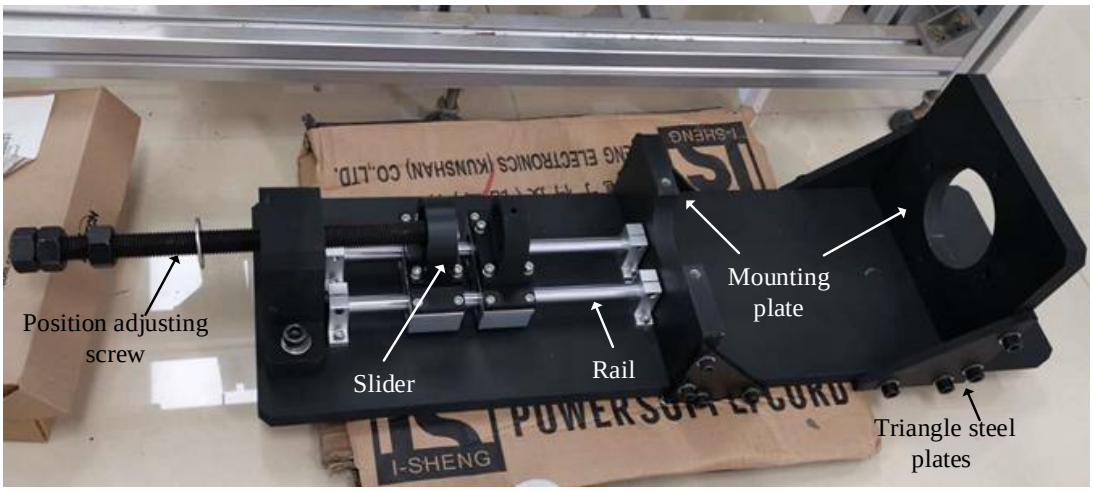

(a)

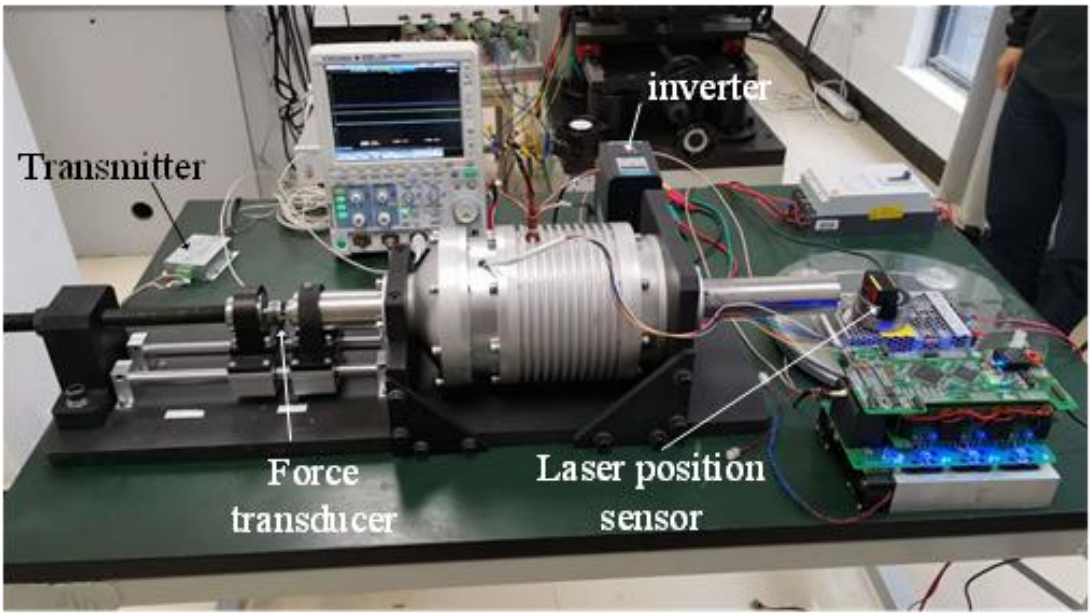

(b)

Fig. 6-14 Real static test rig (a) Test rig without actuator (b) Full test rig (c) dSPACE

In static and dynamic tests, the rotary motor of the actuator is fed and controlled by dSPACE in position control mode, and a commercial 3-phase inverter, MD200ET3.7B, in speed control mode, as shown in Fig. 6-14 (b) and Fig. 6-14(c). In addition, various instruments are in place to monitor and record the machine operation data. The output force is captured by the force transducer Meas-Spec Load Cell, which is installed between the two slides, and its signal is sent to a data storage oscilloscope after being enhanced by the transmitter. The mover position signal is measured by the laser position sensor, which is located at the other end of the test rig, and the position of the mover is obtained by laser reflection. As the laser sensing unit can directly output analogue signal, it can be directly connected to the oscilloscope, so that the thrust force signal, the rotor position signal, and the mover position signal can be displayed and recorded by one oscilloscope. Table 6-4, Table 6-5 and Table 6-6 show the technical data of the inverter, force transducer and the laser sensor. And the required instruments are listed in Table 6-7 with their functions.

Table 6-4 3-phase inverter drive

Parameters	Value	Unit
Supply frequency	50	Hz
Maximum power	5.5	kW
Maximum current	30	A
Speed limit	65535	rpm

Table 6-5 Force transducer

Parameters	Value	Unit
Excitation	10	V
Sensitivity	0.004	mV/N
Maximum force	7.5	kN
Output impedance	359	ohms
Input impedance	376	ohms

Table 6-6 Laser sensor

Parameters	Value	Unit
Measuring center distance	50	mm
Range	+-15	mm
Accuracy	30	um
Reaction time	1.5	ms

Table 6-7 List of instruments used in the test rig

No.	Instruments	Function
1	Prototype	Target actuator
2	3-phase inverter drive	Provide current excitation and speed control
3	Dspace	Provide current excitation and position control
4	Resolver	Measure actuator rotor position
5	Force transducer	Measure actuator mover force
6	Laser sensor	Measure actuator mover position
7	Current sensors	Measure three phase currents
8	Transmitter	Enhanced force transducer signal
9	Resolve decoder	Convert the resolver signal into analogue signal
10	Oscilloscope	Display and record measurement signals

6.3.2 Magnet Material Calibration

The magnets used in the magnetic screw design are N42UH, which have good magnetic properties and heat resistance. The nominal Br of the material is 1.2T. However, since the geometrical shape of the magnets is not conventional and the permanent magnets are made by imperfect sintering and magnetizing, it is likely that the Br of the actual PM

cannot reach the performance data of the material grade. Fig. 6-15 shows the measured B-H curve of magnets used in the mover assembly. After converting to ISO units, the resultant actual Br is 1.05T, which is much smaller than the nominal Br of N42UH, 1.2T, and the reduction is about 12%. However, due to the large margin reserved when designing the magnetic screw, the thrust force with the actual magnets can still meet the performance requirements. The predicted output force of the magnetic screw with measured Br is shown in Fig. 6-16. The design requires a maximum thrust of 4000N, and the predicted maximum thrust of the magnetic screw with the actual PMs is 4500N.

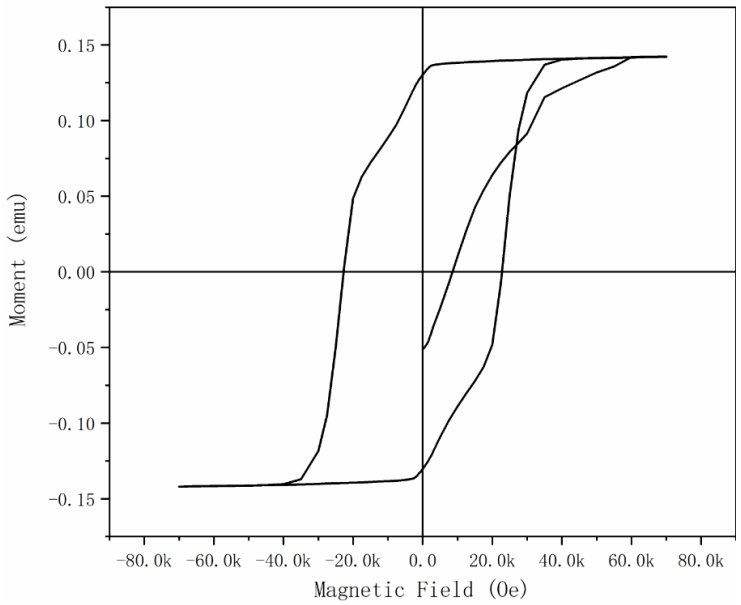

Fig. 6-15 Mover PM performance curve

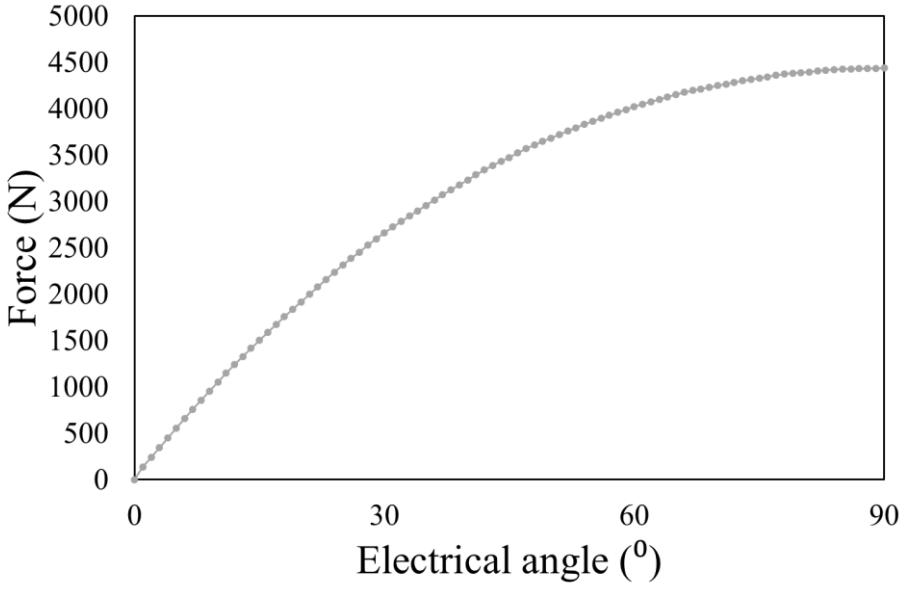

Fig. 6-16 The output force of magnetic screw with actual PMs

6.4 Experimental Validation

Due to the complex structure of the magnetic screw based linear actuator, it is difficult to measure all variables in real time in one experiment. Therefore, the experimental verification of the prototype actuator is carried out in steps.

First, a separate simulation of the rotary motor part is performed to predict motor performance and to obtain the relationship between the motor torque and the current. The predicted torque-current relationship is compared with measurement in a rotary motor testing rig when the magnetic screw mover is removed. Since it is not possible to install a torque sensor in the complete actuator assembly, it is necessary to infer the real-time torque of the rotor through the current from the measured torque-current relationship of the rotary motor.

After that, the entire magnetic screw based linear actuator is assembled for static thrust force experiments to verify the performance of the magnetic screw and calibrate the relative position of the rotor. Theoretically under no-load thrust force condition, the magnetic screw mover displacement with respect to the nut (rotor) should be zero. However, due to the influence of assembly tolerance and friction, the reference zero position of the mover with respect to the rotor helical magnets is not known. The relative initial position of the mover and the rotor is likely to be the balance point of static friction and thrust force, as shown in Fig. 6-17. If it is not calibrated, measurement accuracy may be compromised in subsequent tests.

Finally, a transient load experiment was carried out in which the prototype actuator was subjected to a large sudden load.

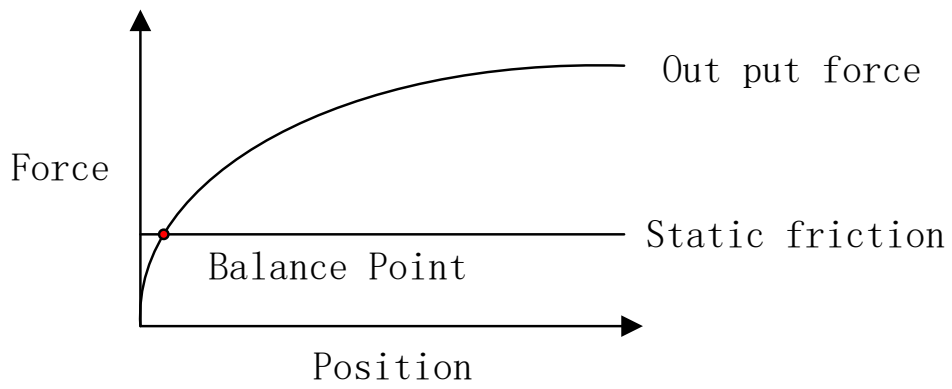

Fig. 6-17 Initial position balance

6.4.1 18-slot, 8-pole Motor Testing

The terminal connections of the motor windings are illustrated in Fig. 6-18. The resistance and inductance of the motor winding are additionally shown in the figure, indicating which branch it belongs to. The resistances and inductance of each phase are measured and compared with the predicted values in Table 6-8 and Table 6-9. From the results, it can be seen that the resistance in testing is higher than the resistance set in the FE simulation. This may be due to the error in estimating the length of the coil for the winding method as well as the additional resistance caused by soldering connection and cables. The actual inductance value fluctuates above and below the predicted value, which may be because the inductance is not only related to the length of the coil but also affected by the tolerance of the stator teeth dimensions.

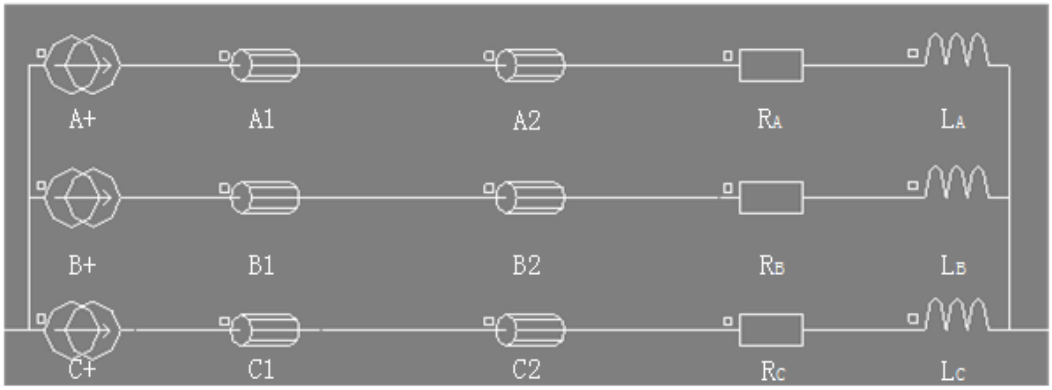

Fig. 6-18 Terminal connection of Motor windings

Table 6-8 Resistance measurement and comparsion

	Measured Resistance/mΩ	Predicted Resistance/mΩ
R_A	26	19
R_B	25.6	19
R_C	24.1	19

Table 6-9 Inductance measurement and comparsion

	Measured Inductance/μH	Predicted Inductance/μH
L_A	1490	1200
L_B	1173	1200
L_C	1532	1200

Fig. 6-19 shows the test rig for the rotary motor sub-assembly of the integrated linear actuator. The actuator is fixed on a movable platform by two clamping plates and the support base at both ends when the mover is removed. Since the rotor of the magnetic

screw actuator is hollow inside, a fennel-shaped extension shaft is fitted to the rotor inner bore and secured through two M5 screws. The extension shaft of the rotor is connected to the dynamometer through a coupling, and the dyno adopts speed control and can operate in a given speed. The test rig has its own torque sensor, and supports no-load operation and on-load operation. The motor load can be increased by adding resistive torque, and its value can also be displayed on the oscilloscope.

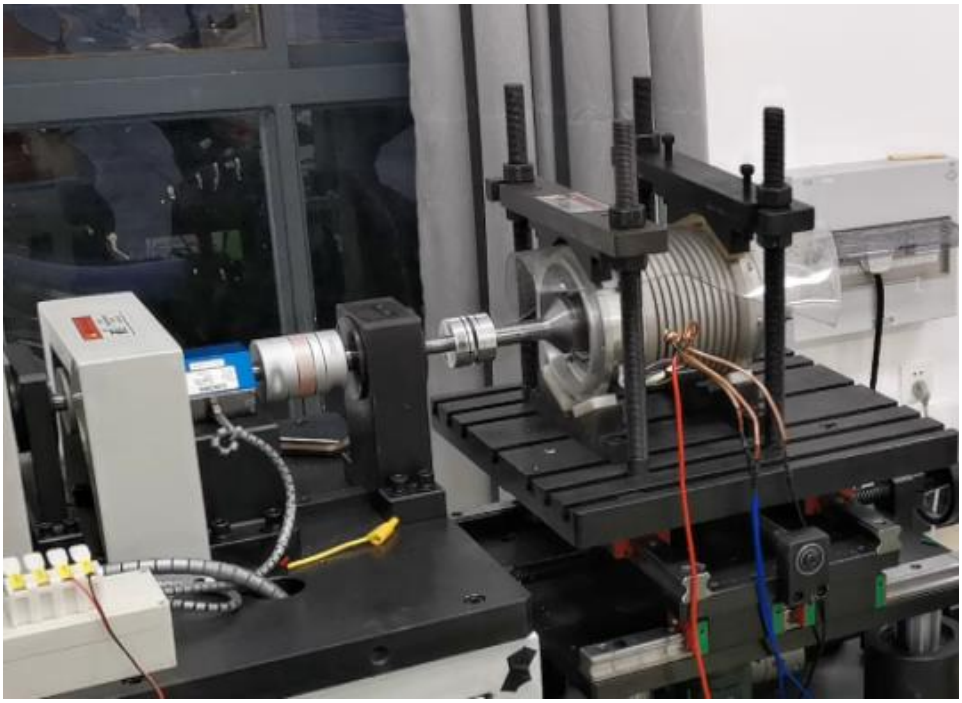

Fig. 6-19 Rotary motor test rig

The first test with the rotary motor is the back EMF measurement. For surface mount PM machines, the back EMF predominantly determines the output torque and machine performance. To achieve the required torque, it is very important that the experimental results are close to the design predictions.

The phase back EMFs of the rotary motor are measured at the room temperature of 28°C from 200rpm to 800rpm in steps of 200rpm. Fig. 6-20 shows the motor phase back-EMF waveforms. The back-EMF of the motor is saddle-shaped. This is because the motor adopts 18-slot 8-pole combination with a significant 3rd harmonic that reduces its peak. The red, green and blue curves represent the back EMFs of phase A, phase B and phase C, respectively. In the figure, each division of the abscissa represents 50ms, and each division of the ordinate in Fig. 6-20 (a) represents 5V while each division of the ordinate in Fig. 6-20 (b), Fig. 6-20 (c) and Fig. 6-20(d) represents 10V. Fig. 6-21 shows the comparison of variations of measured and predicted rms back EMF with speed and the

back EMF measured in 1400 rpm is compared with the predicted value in Fig. 6-22. The predicted back EMF is obtained from the measured Br of the magnets as discussed previously. It can be seen from the results that the back EMF increases proportionally with the speed and is in good agreement with the FE model prediction result.

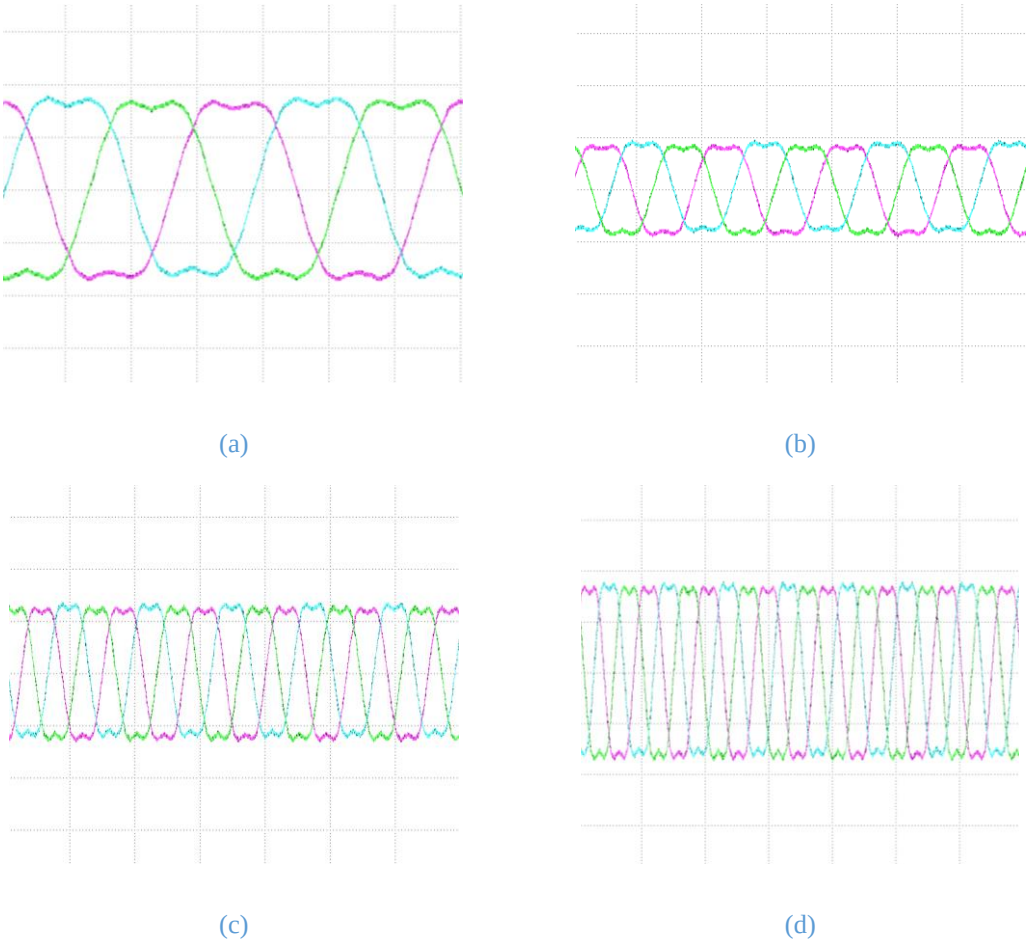

(a) (b)

(c) (d)

Fig. 6-20 Motor Back EMF Oscilloscope Waveform (a) 200 rpm (b) 400 rpm (c) 600 rpm (d) 800 rpm

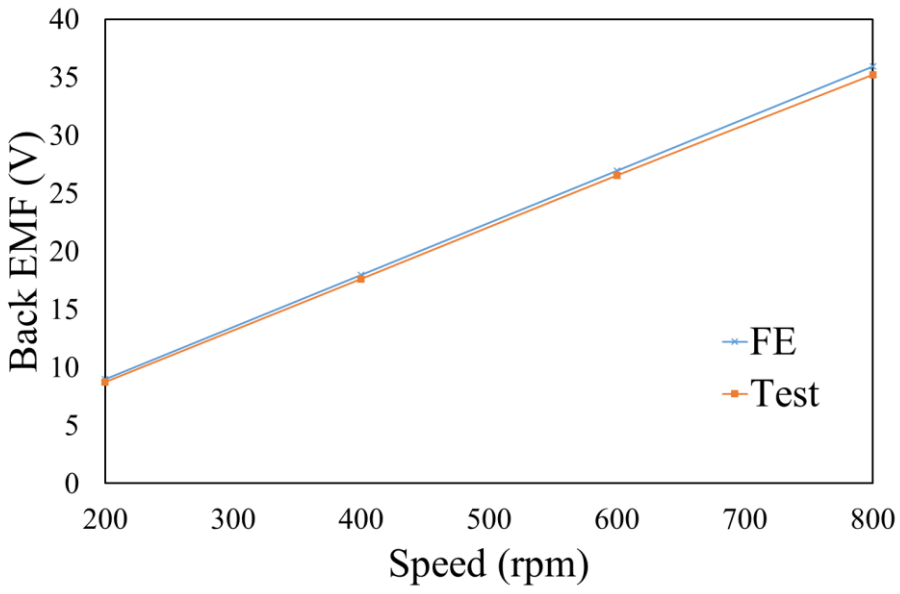

Fig. 6-21 Comparison of variations of measured and predicted back EMF with speed

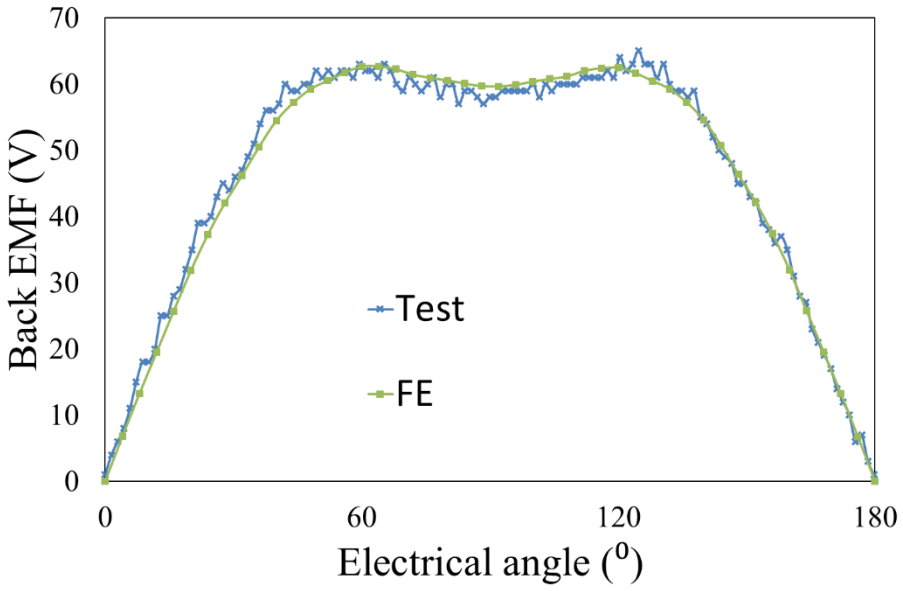

Fig. 6-22 Comparison of back EMF waveforms at 1400 rpm

In order to verify the output performance and estimate the torque through the current, it is necessary to measure the torque characteristics of the rotary motor. Since the rotor has no external shaft in the integrated actuator, it is impossible to connect a torque sensor during actuator operation. Therefore, it is necessary to measure the torque characteristics of the rotary motor, so that the motor torque as a function of phase current can be determined.

The phase current and the output torque of the rotary motor are measured at the 166 rpm from 10A to 16A in steps of 2A. Fig. 6-23 shows the measured motor phase current and torque waveforms on the oscilloscope. In the figure, the red line represents the output torque of the rotary motor, and the purple, blue, and green curves represent the currents in phase A, phase B, and phase C, respectively. Each division of the abscissa represents 50ms, and each division of the ordinate in Fig. 6-23 (a) represents 5A and 1Nm, and each division of the ordinate in Fig. 6-23 (b), Fig. 6-23 (c) and Fig. 6-23 (d) represents 10A and 2Nm. It can be seen from the figure that the measured motor output torque has a small amount of torque ripple and it increases linearly with the current. In addition, the measured and predicted variations of the output torque with current are plotted in Fig. 6-24. It can be seen from the figure that the measured torque and the FE predicted torque do not agree completely. At the rated current of 10A, the measured torque is lower than the FE predicted torque by 2%, and as the current increases, the difference between the

two is about 6% at the peak current. This may be due to the fact that as the current increases in the test, the temperature of the rotor also increases, which reduces the remanence of the rotor magnets, resulting in a larger gap between the measured and predicted torque. In addition, the frictional torque in the tapered bearings also contribute to a small reduction in the measured torque.

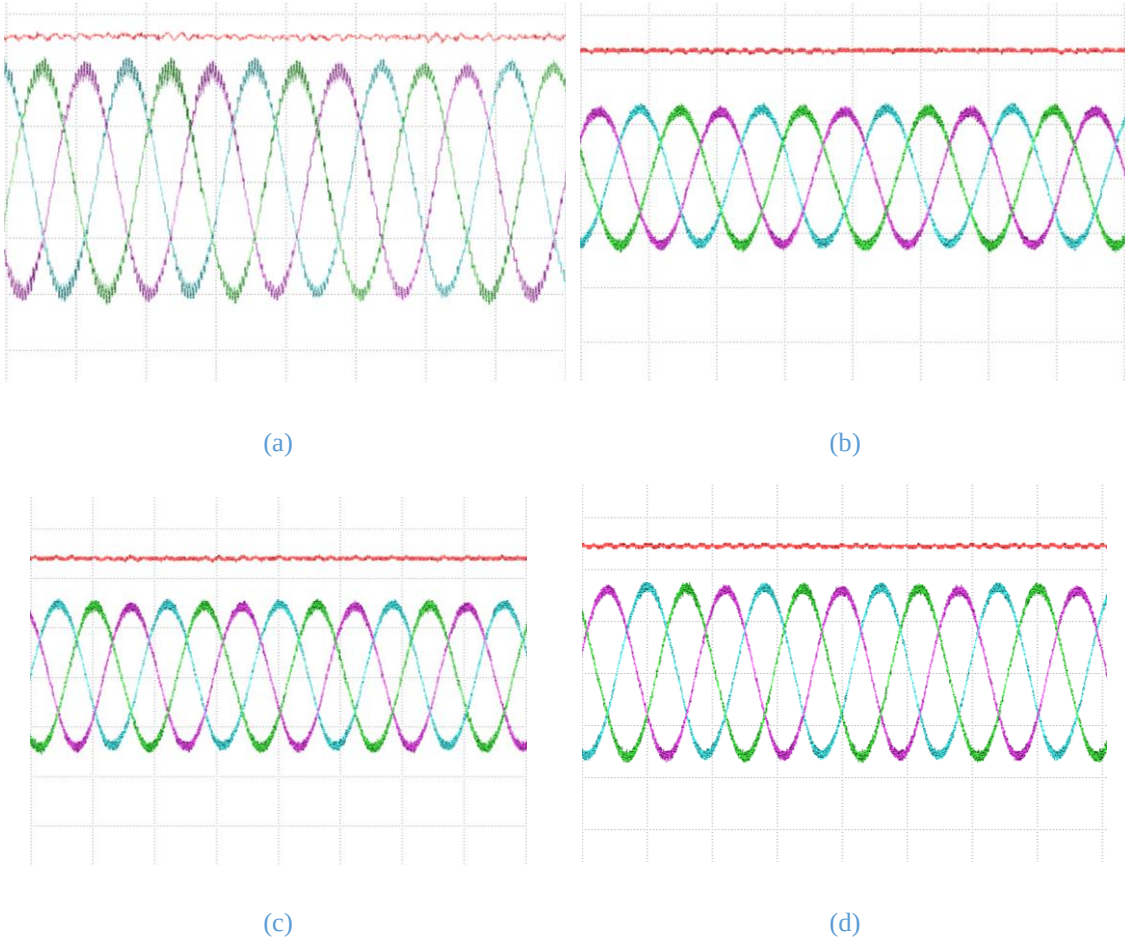

(a) (b)

(c) (d)

Fig. 6-23 Motor current and torque waveforms (a) at 10A (b) at 12A (c) at 14A (d) at 16A

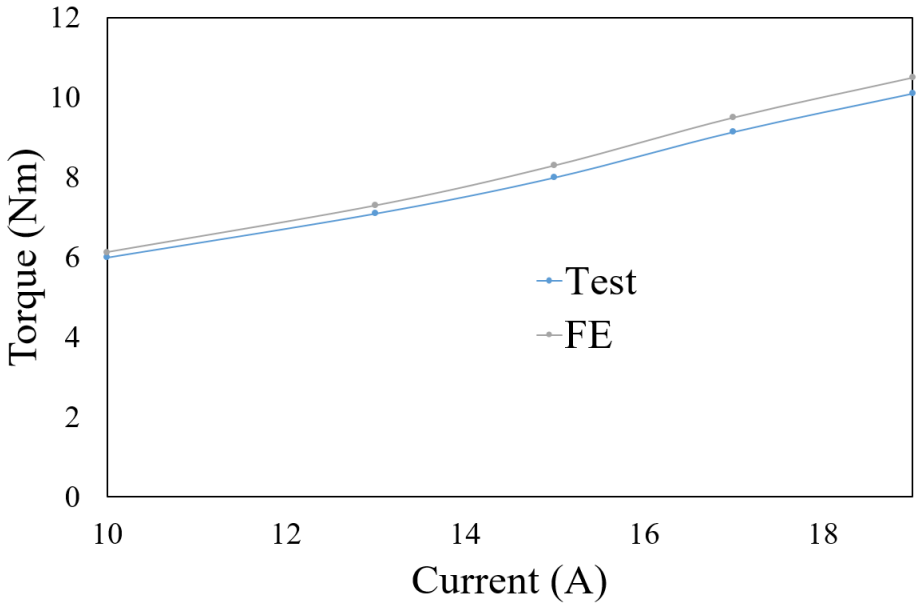

Fig. 6-24 Comparison of variations of measured and predicted output torque with current

6.4.2 Magnetic Screw Mover-Rotor Relationship

Since the magnetic screw generates thrust force only when there is relative displacement between the inner and outer PM arrays, the thrust force will not be generated when the mover moves at a constant speed with the rotor rotation. Fig. 6-25 shows the variations of the rotor torque when the rotor rotates one revolution while the mover is stationary predicted by the 3D FE model. It can be seen that the rotor torque waveform of the actuator is consistent with the mover thrust force waveform. In the 3D FE model the rotor torque and mover thrust force are measured at a given rotor angle as it rotates. When the rotor rotates one revolution, the resultant relative linear displacement between the mover magnet arrays and nut magnet arrays (on the inner surface of the rotor) is two pole-pitches. Thus, the electrical angle of the rotation on the X axis is the electrical angle difference between the two parts of the magnetic screw.

Therefore, neither the rotor position nor the mover position alone can reflect the relative displacement the mover and rotor of the actuator. Due to assembly errors and static friction, the initial positions of the mover and rotor of the prototype actuator cannot be accurately defined at the designed initial position. In the absence of rotor input torque, the relative position of the mover and the rotor will stay at a position that offsets the static friction of the mover. If this position is set to be zero relative position, the results obtained by subsequent tests are not accurate. Therefore, before conducting further experiments on the magnetic screw based linear actuator, it is necessary to calibrate the position of the rotor and mover through a static thrust force test and obtain the relative relationship between the two.

In this case, if the 90-degree electrical angle in the Fig. 6-25 is used as the initial point, the rotor torque T_r and the mover thrust F_m can be written:

$$T_r = T_m \sin(\theta - Gz - \beta) \tag{6-1}$$

$$F_m = GT_r \tag{6-2}$$

where θ and z are the angular and linear displacements of the rotor and mover, respectively, T_m is the maximum torque of the magnetic screw, G is the gear ratio of the magnetic screw, and β is a small offset angle between the mover and rotor due to presence of static friction force. Therefore, when z and θ are known, β was adjusted to make the

test thrust force curve most consistent with the simulated thrust force curve. At this time, β is the initial friction force position.

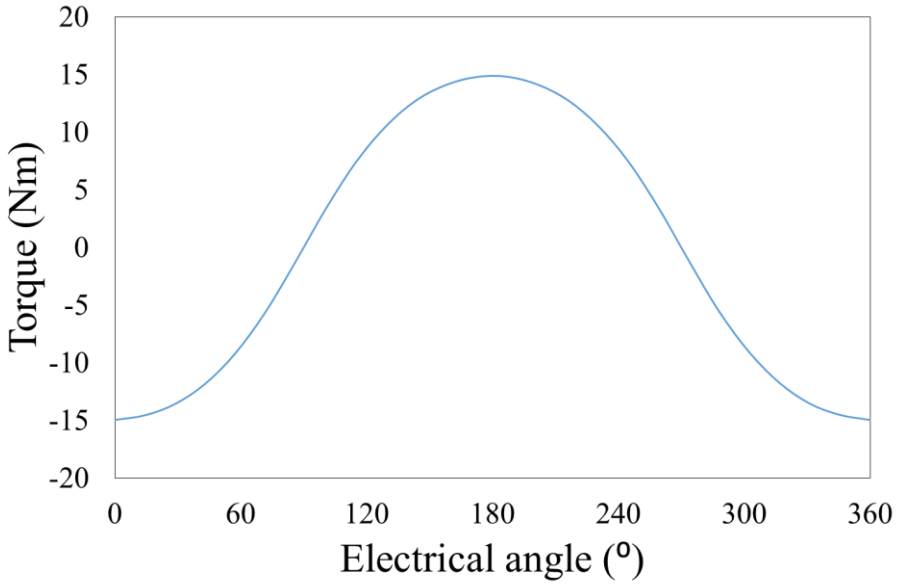

Fig. 6-25 Variations of rotor torque when the rotor rotate one cycle

6.4.3 Magnetic Screw Motor Static Testing

The first test of the magnetic screw based linear actuator is the static thrust force test. The main purpose of this test is to calibrate the position of the mover rotor and verify the thrust force performance of the magnetic screw actuator.

The static test process is as follows. First adjust the position of the screw at the left end of the test rig to secure the mover position of the actuator. Then apply torque (current) which will rotate the rotor to a specific position with the mover fixed, and measure the thrust force and rotor position after the result is stable. Finally, the results are summarized to obtain the thrust force-position curve of the magnetic screw actuator, by adjusting β to obtain the curve that most closely matches the trend of the FE results and compared it with the FE simulation results.

Fig. 6-26 shows the recorded static thrust force and position waveforms. Since this test requires position signal feedback, a PC instead of an oscilloscope is used to display the results. Since the mover of the actuator in this test is fixed, the measured incremental rotor position is the relative position of the mover and rotor. It can be seen from the results that as the position of the rotor changes, the thrust force of the mover also changes, and it remains stable at each position. And due to hysteresis control, small torque ripple is

present. Consequently, its output thrust force also exhibit a small chattering around the average.

Fig. 6-27 compares the measured and predicted variations of the output force with relative mover displacement in electrical angle. The data of each point is selected in the range of thrust increase. It can be seen from the figure that the entire measured thrust force curve is basically in agreement with the FE predictions albeit there are several points that are slightly higher than the FE prediction. It demonstrates that the high force density linear actuator can be realised and the test result is in good agreement with the FE model predictions.

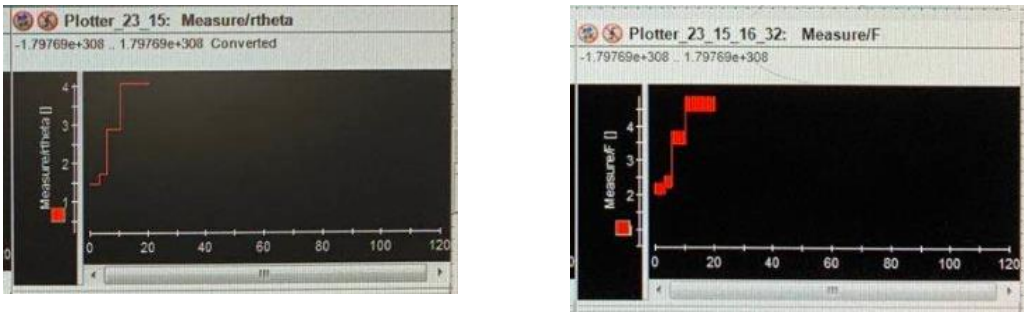

(a) (b)

Fig. 6-26 Static thrust force test waveform (a) Rotor position (b) Thrust force

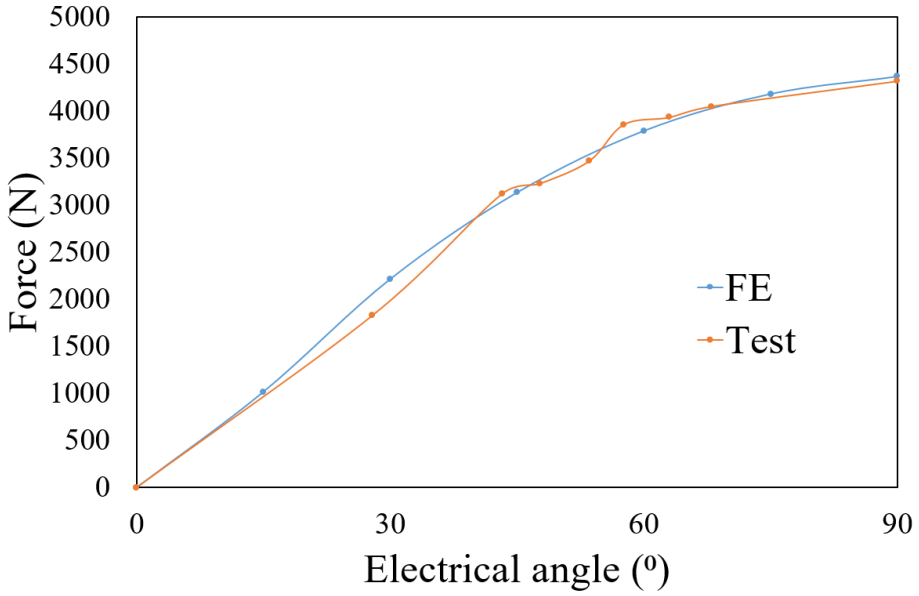

Fig. 6-27 Comparison of variations of output force with electrical angle

6.4.4 Transient Load Testing

The transient load test is performed as follows. First, the actuator start-up and mover is allowed to move until it reaches the fixed position set by the adjusting screw. When the rotor starts to rotate, the actuator mover moves along the guide rail at a constant speed. When the mover reaches the fixed position, it is no longer able to move, but the rotor continues to rotate. The relative position change between the mover (magnetic screw) and the rotor (magnetic nut), generate the thrust force given in (6-1). Because the maximum torque of the motor rotor is limited to be less than the maximum mover torque, the rotor reaches the maximum torque position, and the relative position will no longer change under which the mover generates maximum force. Finally, the motor drive is turned off, the mover bounces back, and the thrust drops to 0.

Fig. 6-28 shows the measured waveforms during the transient load test. The red line in the oscilloscope indicates phase A current of the motor where each division is 20A, the green line indicates the mover thrust force measured by the force transducer, each division is 2000N, the blue line is the rotor position signal measured by the resolver, each repeat is 90 mechanical angle and each division is 30 °mechanical angle, and the purple line is the mover position signal measured by the laser sensor, each division is 15mm.

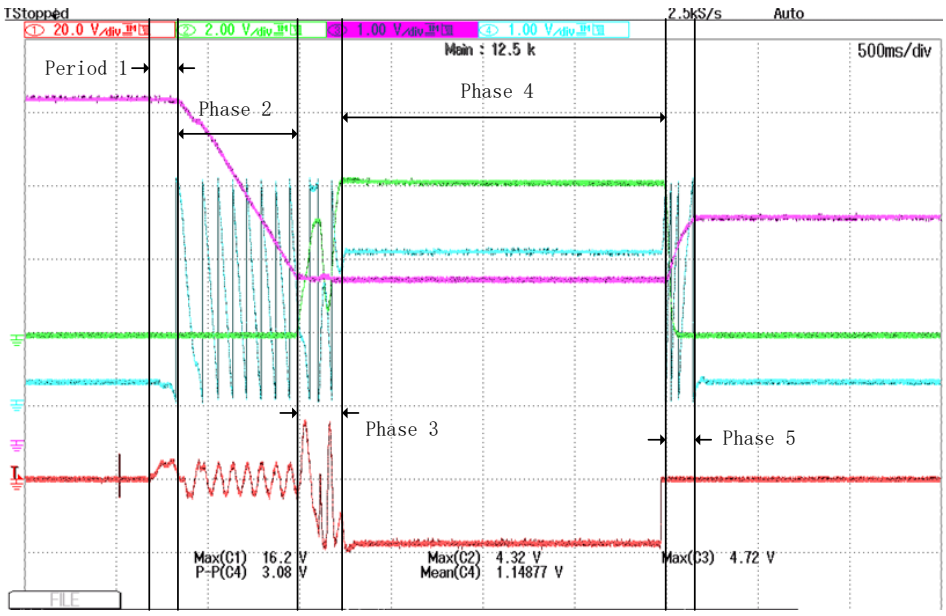

Fig. 6-28 Test waveform of the oscilloscope with different periods

In Fig. 6-28 the whole testing is divided into 5 phases, namely phase 1: start-up, phase 2: no-load forward movement, phase 3: loading, phase 4: force and torque reach an equilibrium when the torque is limited by the magnitude of currents, and phase 5: re-bounce.

The motor is under speed control throughout the testing, and its speed is 180rpm. In the start-up phase, it can be seen that the rotor position changes slightly when the motor is excited by small current, but the mover position remains unchanged because of friction, and there is no thrust force reading on the force transducer. As the relative position between the rotor and the mover changes, the force on the mover gradually increases. When the thrust generated on the mover is greater than the static friction of the mover, the mover moves, and the test enters the next phase.

During the no-load forward phase, there is no load on the mover apart from the friction, and the mover moves forward along with the rotation of the rotor. Since the resolver has 4 pole-pairs, each repeat on its output corresponds to 90^0 mechanical degree of rotor rotation. Hence, for each rotor rotation of mechanical angle of 180 °, according to the principle of magnetic screw operation, the mover advances by a pole pitch of 9mm for every two cycles of the resolver output. However, it can be seen from Fig. 6-28 that the rotor displacement corresponding to the first two resolver cycles result in a mover displacement slightly less than 9mm because of the static friction. The subsequent multiple resolver cycles are consistent with the mover displacement according to the principle. Fig. 6-29 shows the relationship between the measured mover position and the rotor position after the third resolver output cycle. It can be seen that there is a very good agreement between the two. This could be due to the fact that when the mover changes from static friction to sliding friction, the friction force is reduced, so the mover advances a part of the distance to adjust the relative position with the rotor, thereby reducing the thrust force to the sliding friction. After the mover has advanced for several cycles, the mover reaches the position set by the adjustment screw and cannot move forward. At this time, it enters the transient loading phase.

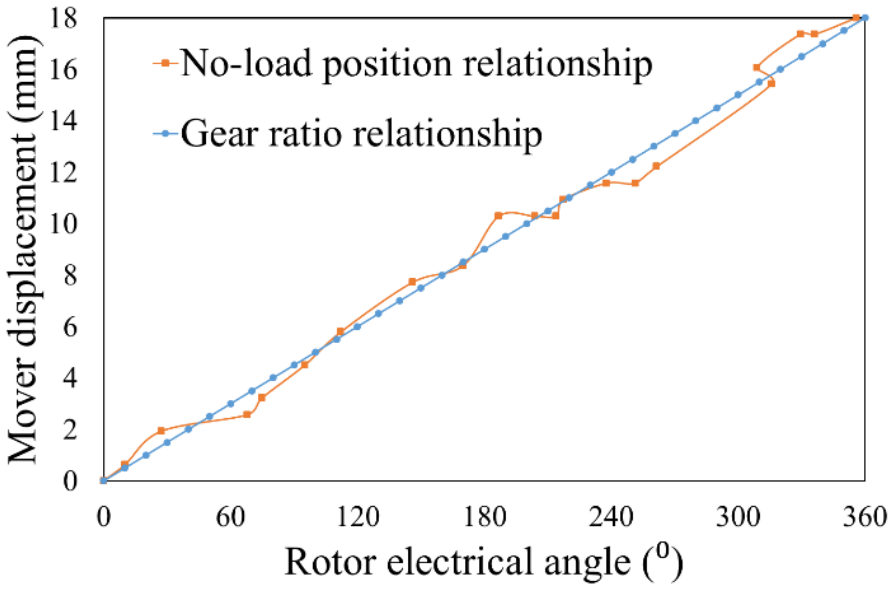

Fig. 6-29 Relationship between the rotor angular position and the mover linear position.

In the loading phase, when the mover of the magnetic screw actuator reaches the position of the adjusting screw, the mover cannot move forward because the screw is locked. At this time, the rotor of the motor is still rotating, the relative displacement between the mover and the rotor increases and the thrust force on the mover continues to increase, which is equivalent to a fast application of loading force on the mover. It can be seen from Fig. 6-28 that the thrust force of the mover does not directly rise to the maximum thrust, and it oscillates before reaching a steady state. This may be caused by lack of damping in the simple motor control as the magnetic screw behaves like a spring-mass system [156]. It can also be seen that when the magnetic screw actuator is suddenly subjected to a load exceeding its capacity, there will be slippage between the mover and the rotor, thereby protecting the magnetic screw actuator from mechanical jamming and damage. Fig. 6-30 shows the instantaneous position of rotor and mover and the relationship between the thrust and position of the magnetic screw actuator during the transient loading phase. It can be seen that, unlike the static test results, the relationship between the thrust force and position when the force increases is more close to linear. This is because when such a large force is exerted on the stopper, it will have a small deformation which allows the mover to have a small displacement. This shows that dynamic effects may impact on the relationship between the thrust and position of the magnetic screw actuator [156], which will be studied in future work.

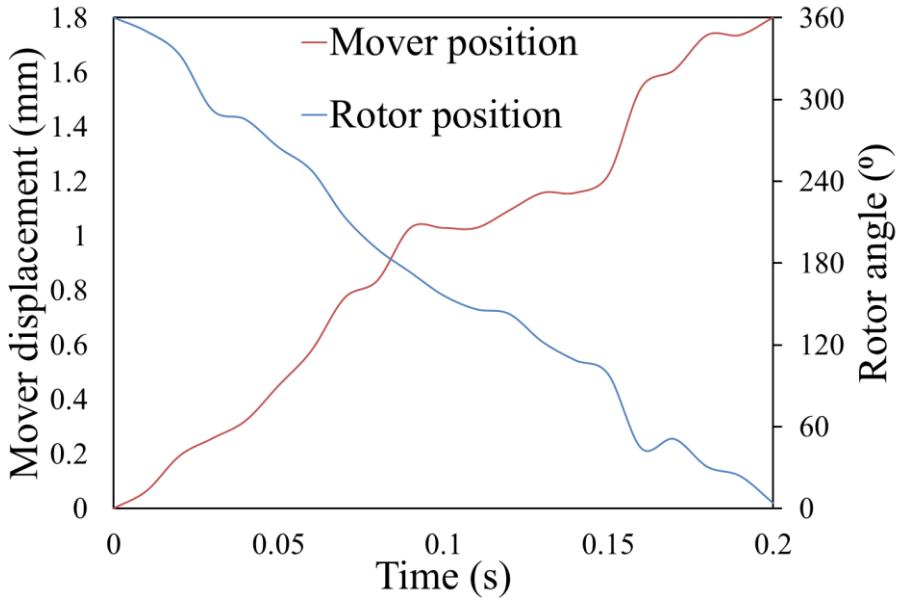

(a)

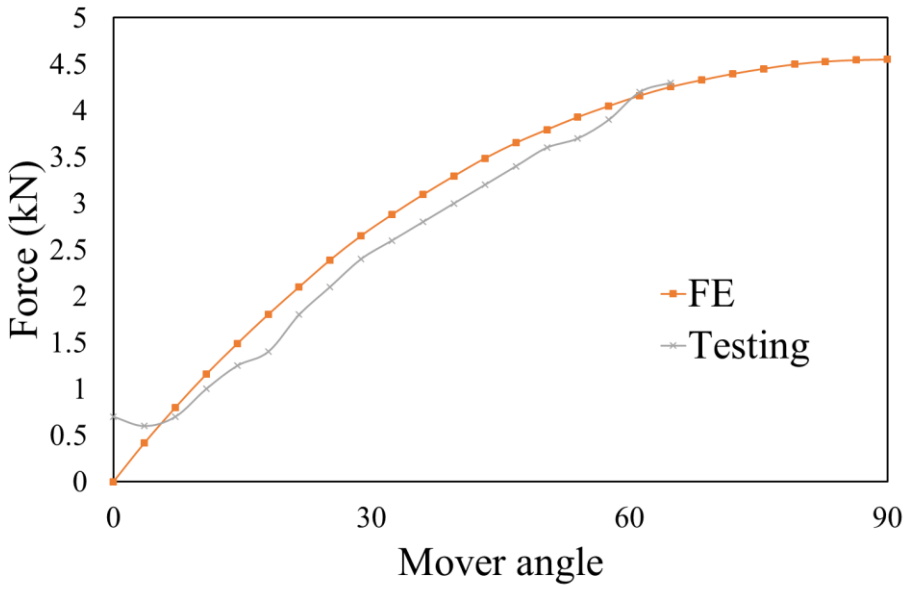

(b)

Fig. 6-30 Comparison of variations of output force with electrical angle in sudden load phase (a) Instantaneous position of rotor and mover (b) Relationship between the rotor angular position and the mover linear position

Since the controller is set to the maximum current, as the motor torque increases, the motor reaches the peak current state which corresponds to the maximum thrust force phase. At this time, the mover and rotor are not moving, and the magnetic screw actuator outputs the maximum thrust. It can be seen from Fig. 6-28 that during the maximum thrust output period, the thrust output of the magnetic screw actuator is stable without obvious fluctuations.

Finally, when the motor current is reduced to zero, the thrust force on the mover is removed and it rebounds. As can be seen from the Fig. 6-28, after the mover rebounds, the rotor rotates about 70^0 mechanical degrees, and backs to its initial position. The mover has also returned to its initial position. This shows that after the magnetic screw actuator is assembled, the relative position between the mover and rotor under no-load is fixed.

It can be seen from the test results of transient loading, the magnetic screw based linear actuator can continuously output a stable thrust force, and when the thrust force is too large, the mover will be protected from jamming. The test results also show that the actuator has a position-dependent thrust force characteristic which need to be taken into account in dynamic control [156].

6.5 Summary

In this chapter, a high force density linear actuator prototype has been built according to the optimised design. All key mechanical components of the actuator including the motor housing are described in detail. The B-H property of the magnets used in the prototype magnetic screw assembly are measured and accounted in the FE model. A test rig is designed and constructed. Motor torque characteristic test and mover static thrust force test have been performed on two different test rigs. The test process and test instruments are explained in detail. Test results are analysed and compared with prediction results.

The test results demonstrate that the linear actuator with the integrated magnetic screw exhibits high torque and high force capability. Although the remanence of the magnets used in the magnetic screw is lower than its datasheet value, the electromagnetic properties of the motor part and magnetic screw part of the actuator are in line with the optimized design results of the FE model. It has been shown that the friction force in the actuator mover is quite small during the test operation and the actuator can output stable maximum thrust force without slipping. And when the magnetic screw actuator is subjected to excessive thrust force, the rotor will produce sliding protection to prevent it from mechanical damage. Thus, the test results validate the machine optimization design, actuator mechanical design and test rig design.

Therefore, the measured force capability of the prototype linear actuator has shown that the thrust force density of the proposed actuator is much higher than that of traditional linear drive. Due to the limited time and the impact of the Covid-19 pandemic, the

dynamic test when the actuator is connected to a passive spring damper unit of a typical vehicle suspension cannot be carried out. In the future, such tests and its application in vehicle active suspension will be studied.

CHAPTER 7
Conclusions and Future Work

7.1 Conclusions

Active suspension has been extensively studied because it improves ride comfort while maintaining good stability of the vehicle under various road conditions. However, Active suspension which employs a rotary electric machine with a rack and pinion will increase instability and loss while those with linear actuators that directly generate thrust force generally have a low force density. In order to meet the high thrust force density requirements for active suspension actuators, this thesis studies, develops and optimises three high force density linear actuators. First, based on the Vernier principle and the tubular SPM topology, high force density tubular linear Vernier motors with two slot-pole number combinations are formed and their performances evaluated. Next is a tubular Vernier motor combining axially magnetised ring magnets sandwiched between ferromagnetic pole pieces with dual stators. This design exhibits high force density and high power factor albeit with a more complex structure. Finally, a high force density linear actuator which integrates a magnetic screw with a rotary PM motor has been developed and tested. The principle of the rotary-to-linear power transmission of the actuator is similar to that of a mechanical feed screw drive. High-density, non-contact electromagnetic power transmission is achieved in the developed actuator. The performances of the candidate high force density actuators are analysed and compared with the existing active suspension actuator defined as the reference. Because its superior force capability, the magnetic screw based linear actuator is mechanically designed, prototyped and tested. The specific contents of the research work are summarised as follows:

An 18-slot 26-pole tubular PM Vernier motor and an 18-slot 28-pole tubular PM Vernier motor have been proposed and globally optimised against the target performance and constraints for an active suspension system in **Chapter 2**. The magnetic field modulation function and basic working principle of the Vernier PM motor, selection of pole slot number combinations, global optimization of leading design parameters, equivalent thermal model, and demagnetization assessment are described and discussed. The performances of the candidate designs are compared with those of the reference motor under the same volumetric and thermal constraints. The results show that the output

thrust force of the tubular PM Vernier motor has certain advantages when the current is below the rated, but their overload capacity is weaker. The amount of magnet materials of the candidate motors is also slightly increased. Overall, the advantage of the PM Vernier motor is not obvious.

To improve force density of linear electromagnetic actuators, a tubular Vernier topology with dual stators is studied in Chapter 3. A tubular mover with axially magnetized ring magnets sandwiched between ferromagnetic pole-piece is placed between the inner and outer stators. The teeth of the outer stator are displaced with respect to those in the inner stator by 90 electrical degrees. This machine topology exploits the Vernier force more effectively while at the same time, achieving high power factor. Three design variants, namely, 9-slot/14-pole, 12-slot/20-pole and 18-slot/32-pole, are analysed and optimally designed. Unlike the single stator topology, the dual stator motor has two air gaps that may affect heat dissipation. A thermal model is subsequently derived and incorporated in the global optimisation. The predicted motor performances are also compared with the reference motor under the same copper loss constraint. The results show that although the dual-stator Vernier motor topology increases the overall structure complexity and manufacturing difficulty, the candidate motor with 12-slots and 20-poles exhibit 50% higher force capability with comparable power factor than that of the reference motor. It could be a potential candidate for active suspension.

Furthermore, a linear actuator with an integrated magnetic screw and rotary motor is investigated Chapter 4. The principle of torque-force transmission by a magnetic screw is described and its thrust force characteristic as a function of linear or angular displacement is derived and discussed. Following structure integration of the magnetic screw with a rotary PM motor, the integrated actuator is optimally designs. Since the magnetic coupling between the magnetic screw and the rotary motor is not significant, their designs can be performed separately with due account of volumetric and structure constraints. When all leading design parameters of the actuator are determined, saturation level in the back iron which supports magnets for the rotary motor on its outer surface and those for the magnetic screw on its inner surface is evaluated. The heat transfer due the losses in the rotary motor to the magnetic screw is also assessed in an equivalent manner. Because the magnetic screw based linear actuator (MSLA) performs rotation and linear motion at the same time, it is necessary to predict its performance by 3D FE analysis. It has been shown from 3D FE analysis that the designed MSLA exhibits extremely high thrust density and high efficiency while meeting the design specifications.

Unbalanced magnetic force (UMF) due to the manufacturing and assembly tolerance is a known problem for linear electromagnetic actuators. Excessive UMF gives rise to large frictional force and compromises efficiency, structural integrity and bearing life. In order to ensure that the MSLA is not subjected to excessive UMF with a degree of eccentricity between the rotor and translator (mover), it is necessary to study the characteristics of the UMF in the magnetic screw under static eccentricity. **Chapter 5** analyses the principle of UMF in the magnetic screw under static eccentricity, and derives the analytical formula for UMF prediction. Further, the UMFs are also obtained through 3D FE simulation. In order to obtain accurate air gap flux density for UMF prediction, high-quality meshes are required for the 3D FE model, which greatly increases memory size and the simulation time. The results show that even at an eccentricity of 0.15mm, which is 15% of air gap, the maximum UMF is 243N, which is about 4.6% of the maximum thrust force. Its impact on the mechanical design and the resultant increase in bearing friction are not significant. The smaller UMF is due to the fact that when a magnetic gear device is used, the effective volume of the magnetic screw that generates the required force is much smaller compared to a tubular actuator which outputs the same thrust force. Compared with the 3D FE prediction, for a given mover eccentricity, the analytical predicted UMF has a certain offset, and this offset increases with the increase of the eccentricity. The deviation between the two predictions is about 20%. This is mainly because the end-effect and helical magnetic field distribution as well as the effect of saturation are neglected in the analytical prediction. Finally, the eccentric force predicted by the helical magnetization PM model and the simpler tubular PM model are compared. It has been shown that the UMF of the helically magnetized PM structure can be estimated by a simplified tubular PM model, thereby greatly reducing the time required for the 3D simulation.

A prototype magnetic screw based high-force-density linear actuator is mechanically designed, constructed, and tested based on the optimised design in **Chapter 6**. All the key mechanical components of the actuator, including the motor housing and bearing supports are described in detail with due consideration of the tolerance progression to minimise its effect on the linear bearings at both ends. To realise the helical magnetisation in a practical manner conducive for manufacturing, the spiral structure of the magnet arrays are approximated by discretised parallel magnetised pieces placed in the helical profile, and the influence of such approximation on thrust force is evaluated by 3D FE. In order to ensure the accuracy of the test results, the B-H characteristics of the magnet used in

the prototype magnetic screw assembly were measured, and represented in the FE model. A test rig is also designed and manufactured. The MSLA test is divided into two parts. The back EMF and torque characteristics of the rotary motor are measured on the motor test rig, and the static thrust force test and transient load test of the mover are performed on the MSLA test rig. And the test process and test equipment are explained in detail. The test results demonstrate that the linear actuator with the integrated magnetic screw exhibits high force capability. Although the remanence of the magnets used in the magnetic screw is lower than its datasheet value, the electromagnetic properties of the motor part and magnetic screw part of the actuator are in line with the optimised design results of the FE model. It has been shown that the friction force in the actuator mover is quite small during the test operation and the actuator can output stable maximum thrust force without slipping. When the magnetic screw actuator is subjected to excessive transient load force, the rotor will slide, which prevents the actuator from mechanical jamming. Thus, the test results validate the machine optimisation design, actuator mechanical design and test rig design. Therefore, the measured force capability of the prototype linear actuator has shown that the thrust force density of the proposed actuator is much higher than that of traditional linear actuators.

7.2 Future work

Although this thesis has described in-depth and systematic research into the development of high force density linear actuators for active suspension, the limited resources and time as well as the impact of the Covid-19 pandemic means that it is not possible to address all technical issues encountered during the PhD study. Hence the following future work is recommended:

1. Prototype construction and test of the dual-stator tubular Vernier motor, as it is one of the potential candidates that exhibits high thrust force density attractive for active suspension. The challenge is to ensure structural integrity and manufacturability and to validate its performance through comprehensive tests.

2. Dynamic performance analysis of the MSLA prototype. As the core component of a high-force-density linear actuator system, the MSLA studied in this thesis must achieve not only high thrust force but also desirable dynamics to meet the requirements of active suspension or other suitable fields of application. The dynamic test when the actuator is connected to a passive spring damper unit of a typical vehicle suspension should be carried out. However, due to limited stiffness of the MSLA, manifested in its force-

displacement characteristics, its response to a step change in load force is insufficient without effective control. It needs further research on modelling and control, and experimental tests.

3. Multi-physics analysis of the MSLA. This thesis mainly focuses on the design and analysis of MSLA from the perspectives of electromagnetic, thermal, and basic mechanical construction. Complex issues such as noise and vibration caused by mover dynamic eccentricity and resultant stress in bearings and mechanical components have not been investigated. In order to realise high-performance operation of the MSLA in active suspension, it is necessary to conduct a comprehensive assessment and global optimization based the multi-physical field analysis of the MSLA.

REFERENCES

[1] Hrovat D., "Survey of advanced suspension developments and related optimal control applications," Automatica, 1997.

[2] Cao D., Song X., Ahmadian M., "Road vehicle suspension design, dynamics, and control," Vehicle System Dynamics, 2011.

[3] Fuller C. R., Elliott S. J., Nelson P. A., "Active control of vibration, l st edition," ActiVe control of vibration, 1996.

[4] Hansen C., Snyder S., Qiu X., "Active control of noise and vibration, Second Edition," Crc Press, 20l2.

[5] Lai C., Liao W., "Vibration controI of a suspension system via a magnetorheological nuid damper," Joumal of Vibration and Control, 2002.

[6] Hrovat D., "Survey of advanced suspension developments and related optimal control applications," Automatica, 1997.

[7] H. Chen, P. -. Sun and K. -. Guo, "Constrained H-infinity control of active suspensions: an lmi approach," The 2002 International Conference on Control and Automation, 2002. ICCA. Final Program and Book of Abstracts., Xiamen, China, 2002, pp. 157-157.

[8] Olley M., "Road manners of the modem car," Automobile Engineers, l946.

[9] Pacejlka H. B., "Tyre and vehicle dynamics(Second Edition)," CRC Press, 2006.

[10] Popp K. Schiehlen W., "Ground Vehicle dynamics," Springer Berlin Heidelberg, 2010.

[11] Gillespie T. D., "Fundamentals of Vehicle dynamics," General Motors Inst, 2000.

[12] M. J. Crosby, D. C. Karnopp, "The Active danlper-A new concept for shock and vibration control," The Shock and Vibration Bull,1973.

[13] C. Kamopp, M. J. Crosby, R. A. Hanvood, "Vibration control using semi-active force generators," Joumal of Engineering forIndustry, l973.

[14] Ieluzzi M., Turco P., Montiglio M, "Development of a heavy truck semi-active suspension control," Control Engineering Practice, 2006.

[15] Bolandhemmat H., Clark C., Golnaraghi F, "Development of a systematic and practical methodology for the design of vehicles semi-active suspension control system," Vehicle System Dynamics, 2009.

[16] M. Zapateiro, F. Pozo, H. R. Karimi and N. Luo, "Semiactive Control Methodologies for Suspension Control With Magnetorheological Dampers," in IEEE/ASME Transactions on Mechatronics, vol. 17, no. 2, pp. 370-380, April 2012.

[17] Eathakota V., Singh A., Krishna K., "Two models of force actuator based active suspension mechanisms for mobility on uneven terrain," Acta Astronautica, 2010.

[18] R. Rajamani, J. K. Hedrick, "Adaptive observers for active automotive suspensions: Theory and experiment", IEEE Trans. Contr. Syst. Technol., vol. 3, no. 1, pp. 86-93, Mar. 1995.

[19] A. Alleyne, J. K. Hedrick, "Nonlinear adaptive control of active suspensions", IEEE Trans. Contr. Syst. Technol., vol. 3, no. 1, pp. 94-101, Jan. 1995.

[20] Y. Huang, J. Na, X. Wu and G. Gao, "Approximation-Free Control for Vehicle Active Suspensions With Hydraulic Actuator," in IEEE Transactions on Industrial Electronics, vol. 65, no. 9, pp. 7258-7267, Sept. 2018.

[21] Q. Zhu, L. Li, C. J. Chen, C. Z. Liu and G. D. Hu, "A Low-Cost Lateral Active Suspension System of the High-Speed Train for Ride Quality Based on the Resonant Control Method," in IEEE Transactions on Industrial Electronics, vol. 65, no. 5, pp. 4187-4196, May 2018.

[22] M. Hirose, S. Matsushige, S. Buma and K. Kamiya, "Toyota electronic modulated air suspension system for the 1986 Soarer," in IEEE Transactions on Industrial Electronics, vol. 35, no. 2, pp. 193-200, May 1988.

[23] T. R. Rao and P. Anusha, "Active suspension system of a 3 DOF quarter car using fuzzy logic control for ride comfort," 2013 International Conference on Control, Automation, Robotics and Embedded Systems (CARE), Jabalpur, India, 2013.

[24] S. Mirzaei, S. M. Saghaiannejad, V. Tahani and M. Moallem, "Electromagnetic shock absorber," IEMDC 2001. IEEE International Electric Machines and Drives Conference (Cat. No.01EX485), Cambridge, MA, USA, 2001.

[25] S. Mirzaei, "A Flexible Electromagnetic Damper," 2007 IEEE International Electric Machines & Drives Conference, Antalya, Turkey, 2007.

[26] Beno J., Hoogterp F. Bresie D., " Electromagnetic suspension for combat vehicles," SAEPaper950775.

[27] Beno J., Bresie DA. Ingram SK., " Electromagnetic suspension System," Final Report to US Army,1995.

[28] Suda, Yoshihiro, Shiiba, Taichi, Hio, Koji, Kawamoto, Yasuhiro, Kondo, Takuhiro, and Yamagata, Hideki. "Study on Electromagnetic Damper for Automobiles with Nonlinear Damping Force Characteristics (Road Test and Theoretical Analysis)." Vehicle System Dynamics, 2004.

[29] Suda, Yoshihiro, Nakadai, Shigeyuki, and Nakano, Kimihiko. "Hybrid Suspension System with Skyhook Control and Energy Regeneration (Development of Self-Powered Active Suspension)." Vehicle System Dynamics, 1998.

[30] Kawamoto Y. Suda Y. Inoue H. and Kondo T., "Electro-mechanical Suspension System considering Energy Consumption and Vehicle Manoeuvre." Vehicle System Dynamics, 2008.

[31] Huang K. Yu F. and Zhang Y., "Active Controller Design for an Electromagnetic Energy-regenerative Suspension." International Journal of Automotive Technology, 2011.

[32] Huang K. Zhang Y. and Yu F., "Predictive Controller Design for Electromagnetic Suspension Based on Mixed Logical Dynamical Model." Journal of Vibration and Control, 2012.

[33] Zhang Y., Huang K., and Yu F., "Experimental Verification of Energy-regenerative Feasibility for an Automotive Electrical Suspension System." 2007 IEEE International Conference on Vehicular Electronics and Safety, 2007.

[34] Zhang Y., Yu F., and Huang K., "Permanent-magnet DC Motor Actuators Application in Automotive Energy-regenerative Active Suspensions." SAE Technical Papers, 2009.

[35] Ebrahimi, Babak, Khamesee, Mir Behrad, and Golnaraghi, Farid., "A Novel Eddy Current Damper: Theory and Experiment." Journal of Physics. D, Applied Physics, 2009.

[36] Ebrahimi, Babak, Khamesee, Mir Behrad, and Golnaraghi, Farid. "Eddy Current Damper Feasibility in Automobile Suspension: Modeling, Simulation and Testing." Smart Materials and Structures, 2009.

[37] Nguyen Duc Ngoc, Deng Zhaoxiang, and Cao Youqiang. "Direct Current Linear Actuator Using in the Active Suspension System of Automobile." 2011 International Conference on Electric Information and Control Engineering, 2011.

[38] J. Lin, K. W. E. Cheng, Z. Zhang, N. C. Cheung, X. Xue and T. W. Ng, "Active Suspension System Based on Linear Switched Reluctance Actuator and Control Schemes," in IEEE Transactions on Vehicular Technology, vol. 62, no. 2, pp. 562-572, Feb. 2013.

[39] J Wang and D. Howe, "Design optimization of radially magnetized, iron-cored, tubular permanent-magnet machines and drive systems," in IEEE Transactions on Magnetics, vol. 40, no. 5, pp. 3262-3277, Sept. 2004.

[40] C. Hwang, P. Li and C. Liu, "Optimal Design of a Permanent Magnet Linear Synchronous Motor With Low Cogging Force," in IEEE Transactions on Magnetics, vol. 48, no. 2, pp. 1039-1042, Feb. 2012.

[41] M. Wang, G. Tian, C. Yang, H. Qiu and J. Wu, "Magnetic Field Calculation of End Region in Permanent Magnet Synchronous Linear Motor," 2018 International Conference on Advanced Mechatronic Systems (ICAMechS), Zhengzhou, China, 2018.

[42] R. E. Clark, D. S. Smith, P. H. Mellor, and D. Howe, “Design optimization of moving-magnet actuators for reciprocating electromechanical systems,” IEEE Trans. Magn., vol. 31, pp. 3746–48, Nov. 1995.

[43] Y. He, Z. Q. Zhu, and D. Howe, “A PWM controlled linear servo system for friction wielding,” in Proc. 2nd Int Conf. Elect. Mach. (CICEM’95), Hangzhou, China, 1995, vol. A 2.3, pp. 51–55.

[44] J Wang, G. W. Jewell and D. Howe, "A general framework for the analysis and design of tubular linear permanent magnet machines," in IEEE Transactions on Magnetics, vol. 35, no. 3, pp. 1986-2000, May 1999.

[45] J. Wang, G. W. Jewell and D. Howe, "Design optimisation and comparison of tubular permanent magnet machine topologies," in IEE Proceedings - Electric Power Applications, vol. 148, no. 5, pp. 456-464, Sep 2001.

[46] J Wang, D. Howe and G. W. Jewell, "Analysis and design optimization of an improved axially magnetized tubular permanent-magnet machine," in IEEE Transactions on Energy Conversion, vol. 19, no. 2, pp. 289-295, June 2004.

[47] J Wang and D. Howe, "Design optimization of radially magnetized, iron-cored, tubular permanent-magnet machines and drive systems," in IEEE Transactions on Magnetics, vol. 40, no. 5, pp. 3262-3277, Sept. 2004

[48] J. Wang et al., “Tubular modular PM machines equipped with quasi- Halbach magnetised magnets—Parts I & II,” IEEE Trans. Magn., vol. 41, no. 9, pp. 2470–2489, Sep. 2005.

[49] J. Wang, W. Wang, K. Atallah and D. Howe, "Demagnetization Assessment for Three-Phase Tubular Brushless Permanent-Magnet Machines," in IEEE Transactions on Magnetics, vol. 44, no. 9, pp. 2195-2203, Sept. 2008.

[50] J. Wang, W. Wang and K. Atallah, "A Linear Permanent-Magnet Motor for Active Vehicle Suspension," in IEEE Transactions on Vehicular Technology, vol. 60, no. 1, pp. 55-63, Jan. 2011.

[51] D. Fu, Y. Xu and J. Gong, "Presentation of E-core transverse-flux permanent magnet linear motor and its no-load magnetic field analysis based on Schwarz-Christoffel transformation," 2016 IEEE Conference on Electromagnetic Field Computation (CEFC), Miami, FL, USA, 2016

[52] D. Fu, Y. Xu, F. Gillon, J. Gong and N. Bracikowski, "Presentation of a Novel Transverse-Flux Permanent Magnet Linear Motor and Its Magnetic Field Analysis Based on Schwarz–Christoffel Mapping Method," in IEEE Transactions on Magnetics, vol. 54, no. 3, pp. 1-4, March 2018.

[53] Junghwan Chang, Dohyun Kang, Jiyoung Lee and Jungpyo Hong, "Development of transverse flux linear motor with permanent-magnet excitation for direct drive applications," in IEEE Transactions on Magnetics, vol. 41, no. 5, pp. 1936-1939, May 2005

[54] Junghwan Chang, Dohyun Kang, Jiyoung Lee and Jungpyo Hong, "Development of transverse flux linear motor with permanent-magnet excitation for direct drive applications," in IEEE Transactions on Magnetics, vol. 41, no. 5, pp. 1936-1939, May 2005

[55] B. Tomczuk, G. Schroder and A. Waindok, "Finite-Element Analysis of the Magnetic Field and Electromechanical Parameters Calculation for a Slotted Permanent-Magnet Tubular Linear Motor," in IEEE Transactions on Magnetics, vol. 43, no. 7, pp. 3229-3236, July 2007.

[56] N. Bianchi, S. Bolognani and F. Tonel, "Design criteria of a tubular linear IPM motor," IEMDC 2001. IEEE International Electric Machines and Drives Conference (Cat. No.01EX485), Cambridge, MA, USA, 2001.

[57] B. H. Smith, "Theory and Performance of a Twin Stator Induction Machine," in IEEE Transactions on Power Apparatus and Systems, vol. PAS-85, no. 2, pp. 123-131, Feb. 1966.

[58] M. Luo and B. Fahimi, "Analytical design methodology for Double Stator Switched Reluctance Machine," 2014 IEEE Transportation Electrification Conference and Expo (ITEC), Dearborn, MI, USA, 2014.

[59] H. Zhou, J. Zhang, Z. Lu, X. Zhu and M. Li, "A Novel Five-Phase Double-Stator Tubular Fault-Tolerant Flux-Modulation Permanent Magnet Motor," in IEEE Transactions on Applied Superconductivity, vol. 28, no. 3, pp. 1-5, April 2018.

[60] Z. Zong, L. Quan and Z. Xiang, "Comparison of double-stator flux-switching permanent magnet machine and double-stator permanent magnet synchronous machine for electric vehicle applications," 2014 17th International Conference on Electrical Machines and Systems (ICEMS), Hangzhou, China, 2014.

[61] S. Yang, F. Zhang, Z. Zhang and H. Liu, "Design of Double Stator Permanent Magnet Synchronous Motor With Low Speed Large Torque," 2018 IEEE Student Conference on Electric Machines and Systems, Huzhou, China, 2018.

[62] J. Yu and C. Liu, "DC-Bias Operation of a Double-Stator Hybrid Flux Switching PM Machine," 2018 Asia-Pacific Magnetic Recording Conference (APMRC), Shanghai, China, 2018.

[63] L. Xu, M. Lin, X. Fu, K. Liu and B. Guo, "Analysis of the end-effects in double stator linear-rotary permanent magnet motor with long mover," 2016 IEEE Conference on Electromagnetic Field Computation (CEFC), Miami, FL, USA, 2016.

[64] L. Xu, M. Lin, X. Fu, X. Zhu, C. Zhang and W. Wu, "Orthogonal Magnetic Field Analysis of a Double-Stator Linear-Rotary Permanent Magnet Motor With Orthogonally Arrayed Permanent Magnets," in IEEE Transactions on Magnetics, vol. 53, no. 11, pp. 1-4, Nov. 2017.

[65] L. Xu, M. Lin, X. Fu and N. Li, "Analysis of a Double Stator Linear Rotary Permanent Magnet Motor With Orthogonally Arrayed Permanent Magnets," in *IEEE Transactions on Magnetics*, vol. 52, no. 7, pp. 1-4, July 2016.

[66] L. Xu, M. Lin, X. Fu and N. Li, "Design and Analysis of a Double-Stator Linear–Rotary Permanent-Magnet Motor," in IEEE Transactions on Applied Superconductivity, vol. 26, no. 4, pp. 1-4, June 2016.

[67] Z. Liu, W. Zhao, J. Ji and Q. Chen, "A Novel Double-Stator Tubular Vernier Permanent-Magnet Motor With High Thrust Density and Low Cogging Force," in IEEE Transactions on Magnetics, vol. 51, no. 7, pp. 1-7, July 2015.

[68] K. Guo and Y. Guo, "Optimization Design of Parallel Double Stator and Outer Mover Linear Rotary Permanent Magnet Machine Used for Drilling Robot," 2020 IEEE International Conference on Applied Superconductivity and Electromagnetic Devices (ASEMD), Tianjin, China, 2020.

[69] E. M. Barhoumi, M. Hajji and B. Ben Salah, "Design of a double stator LSRM with improvements in the mobile structure," 2012 First International Conference on Renewable Energies and Vehicular Technology, Nabeul, Tunisia, 2012.

[70] K. Atallah and D. Howe, "A novel high-performance magnetic gear," in IEEE Transactions on Magnetics, vol. 37, no. 4, pp. 2844-2846, July 2001.

[71] A. Toba and T. A. Lipo, "Novel dual-excitation permanent magnet Vernier machine," Conference Record of the 1999 IEEE Industry Applications Conference. Thirty-Forth IAS Annual Meeting (Cat. No.99CH36370), Phoenix, AZ, USA, 1999, pp. 2539-2544 vol.4.

[72] J. Li, K. T. Chau, J. Z. Jiang, C. Liu and W. Li, "A New Efficient Permanent-Magnet Vernier Machine for Wind Power Generation," in IEEE Transactions on Magnetics, vol. 46, no. 6, pp. 1475-1478, June 2010.

[73] S. Niu, S. L. Ho, W. N. Fu and L. L. Wang, "Quantitative Comparison of Novel Vernier Permanent Magnet Machines," in IEEE Transactions on Magnetics, vol. 46, no. 6, pp. 2032-2035, June 2010.

[74] S. L. Ho, S. Niu and W. N. Fu, "Design and Comparison of Vernier Permanent Magnet Machines," in IEEE Transactions on Magnetics, vol. 47, no. 10, pp. 3280-3283, Oct. 2011.

[75] D. Li, R. Qu and T. A. Lipo, "High-Power-Factor Vernier Permanent-Magnet Machines," in IEEE Transactions on Industry Applications, vol. 50, no. 6, pp. 3664-3674, Nov.-Dec. 2014.

[76] M. Lin, D. Li, X. Ren, K. Xie and R. Qu, "Dual-Stator Line-Start Vernier Permanent Magnet Synchronous Machine," 2019 IEEE International Electric Machines & Drives Conference (IEMDC), San Diego, CA, USA, 2019, pp. 2239-2244.

[77] W. Li and K. T. Chau, "Simulation of a linear permanent magnet vernier machine for direct-drive wave power generation," 2011 International Conference on Electrical Machines and Systems, Beijing, 2011, pp. 1-6.

[78] H. Zhang, Y. Shao, B. Kou, R. Qu and Z. Q. Zhu, "Comparative study of double-sided toroidal-winding linear PM vernier machines with different secondary configurations," 2017 20th International Conference on Electrical Machines and Systems (ICEMS), Sydney, NSW, 2017, pp. 1-5.

[79] J. Wang, K. Atallah, and W. Wang, "Anlysis of a magnetic screw for high force density linear electromagnetic actuators," IEEE Trans. Magn., vol. 47, no. 10, pp. 4477-4480, Oct. 2011.

[80] S. Pakdelian, Y. Deshpande and H. A. Toliyat, "An electric machine integrated with trans-rotary magnetic gear," 2012 IEEE Energy Conversion Congress and Exposition (ECCE), Raleigh, NC, 2012, pp. 3356-3362.

[81] S. Pakdelian and H. A. Toliyat, "Trans-Rotary Magnetic Gear for Wave Energy applicaion," 2012 IEEE Power and Energy Society General Meeting, San Diego, CA, 2012, pp. 1-4.

[82] S. Pakdelian, N. W. Frank and H. A. Toliyat, "Magnetic Design Aspects of the Trans-Rotary Magnetic Gear," in IEEE Transactions on Energy Conversion, vol. 30, no. 1, pp. 41-50, March 2015.

[83] R. K. Holm, N. I. Berg, M. Walkusch, P. O. Rasmussen and R. H. Hansen, "Design of a Magnetic Lead Screw for Wave Energy Conversion," in IEEE Transactions on Industry Applications, vol. 49, no. 6, pp. 2699-2708, Nov.-Dec. 2013.

[84] N. I. Berg, R. K. Holm and P. O. Rasmussen, "Theoretical and Experimental Loss and Efficiency Studies of a Magnetic Lead Screw," in IEEE Transactions on Industry Applications, vol. 51, no. 2, pp. 1438-1445, March-April 2015.

[85] A. Toba and T. A. Lipo, "Generic torque-maximizing design methodology of surface permanent-magnet vernier machine," IEEE Trans. Ind. Appl., vol. 36, no. 6, pp. 1539–1546, Nov./Dec. 2000.

[86] X. Yin, P. Pfister and Y. Fang, "A Novel Magnetic Gear: Toward a Higher Torque Density," in IEEE Transactions on Magnetics, vol. 51, no. 11, pp. 1-4, Nov. 2015.

[87] K. Aiso and K. Akatsu, " A novel reluctance magnetic gear for high speed motor," 2016 IEEE Energy Conversion Congress and Exposition (ECCE), Milwaukee, WI, 2016, pp. 1-7.

[88] F. T. Joergensen, T. O. Andersen and P. O. Rasmussen, "The cycloid permanent magnetic gear," Conference Record of the 2006 IEEE Industry Applications Conference Forty-First IAS Annual Meeting, Tampa, FL, 2006, pp. 373-378.

[89] O. Molokanov, P. Dergachev, S. Osipkin, E. Kuznetsova and P. Kurbatov, "A Novel Double-Rotor Planetary Magnetic Gear," in IEEE Transactions on Magnetics, vol. 54, no. 11, pp. 1-5, Nov. 2018.

[90] L. Jing, J. Gong, Z. Huang, T. Ben and Y. Huang, "A New Structure for the Magnetic Gear," in IEEE Access, vol. 7, pp. 75550-75555, 2019.

[91] K. T. Chau, D. Zhang, J. Z. Jiang, C. Liu and Y. Zhang, "Design of a Magnetic-Geared Outer-Rotor Permanent-Magnet Brushless Motor for Electric Vehicles," in IEEE Transactions on Magnetics, vol. 43, no. 6, pp. 2504-2506, June 2007.

[92] J. Wang, K. Atallah and S. D. Carvley, "A Magnetic Continuously Variable Transmission Device," in IEEE Transactions on Magnetics, vol. 47, no. 10, pp. 2815-2818, Oct. 2011.

[93] Ying Fan, Hehe Jiang, Ming Cheng and Yubin Wang, "An improved magnetic-geared permanent magnet in-wheel motor for electric vehicles," 2010 IEEE Vehicle Power and Propulsion Conference, Lille, 2010, pp. 1-5.

[94] J. Bai, P. Zheng, L. Cheng, S. Zhang, J. Liu and Z. Liu, "A New Magnetic-Field-Modulated Brushless Double-Rotor Machine," in IEEE Transactions on Magnetics, vol. 51, no. 11, pp. 1-4, Nov. 2015.

[95] L. Sun, M. Cheng and H. Jia, "Analysis of a Novel Magnetic-Geared Dual-Rotor Motor With Complementary Structure," in IEEE Transactions on Industrial Electronics, vol. 62, no. 11, pp. 6737-6747, Nov. 2015.

[96] K. Li, Z. Zhu and P. Wu, "A Reluctance Magnetic Gear for High Speed and Vibration Motor Systems," 2018 25th International Conference on Mechatronics and Machine Vision in Practice (M2VIP), Stuttgart, 2018, pp. 1-5.

[97] H. Lee., "Vernier motor and its design," IEEE Transaction on Power Apparams and Systems, 1963.

[98] J. Wang and W. Wang, "Testing and experimental characterization of a linear permanent magnet actuator for active vehicle suspension," 2011 International Conference on Electrical Machines and Systems, 2011

[99] Wang, W. Wang, K. Atallah and D. Howe, "Comparative studies of linear permanent magnet motor topologies for active vehicle suspension," 2008 IEEE Vehicle Power and Propulsion Conference, Harbin, 2008, pp. 1-6.

[100] W. Li, K. T. Chau, C. Liu, S. Gao and D. Wu, "Analysis of Tooth-Tip Flux Leakage in Surface-Mounted Permanent Magnet Linear Vernier Machines," in IEEE Transactions on Magnetics, vol. 49, no. 7, pp. 3949-3952, July 2013

[101] D. Li, R. Qu, J. Li, L. Xiao, L. Wu and W. Xu, "Analysis of Torque Capability and Quality in Vernier Permanent-Magnet Machines," in IEEE Transactions on Industry Applications, vol. 52, no. 1, pp. 125-135, Jan.-Feb. 2016

[102] Zhu Z Q, Howe D., "Influence of design parameters on cogging torque in permanent magnet machines." IEEE Transactions on, Energy Coversion, 2000.

[103] Y. Gao, R. Qu, D. Li and F. Chen, "Force Ripple Minimization of a Linear Vernier Permanent Magnet Machine for Direct-Drive Servo Applications," in IEEE Transactions on Magnetics, vol. 53, no. 6, pp. 1-5, June 2017.

[104] Klimenko, Y.I., Batishchev, D.V., Pavlenko, "Design of a linear electromechanical actuator with an active vehicle suspension system," Russ. Electr. Engin. (2015) 86: 588.

[105] J. Wang, Z. Lin and D. Howe, "Analysis of a short-stroke, single-phase, quasi-Halbach magnetized tubular permanent magnet motor for linear compressor applications", IET Proc. - Electric Power Applications, Vol. 2, No. 3, pp. 193-200, 2008.

[106] J. Wang, M. West, D. Howe, H. Zelaya, and W. Arshad, "Design and experimental verification of a linear permanent magnet generator for a free-piston energy converter", IEEE Trans. on Energy Conversion, Vol. 22., No. 2, pp. 299-306, 2007.

[107] J. Prudell, M. Stoddard, E. Amon, T. K. A. Brekken and A. von Jouanne, "A Permanent-Magnet Tubular Linear Generator for Ocean Wave Energy Conversion," in IEEE Transactions on Industry Applications, vol. 46, no. 6, pp. 2392-2400, Nov.-Dec. 2010.

[108] N. G. Vitale, G. B. Hirschman, and W. A. Smith. Optimization of drive screw pitch in a pulsatileventricle assist device. IEEE Annual Northeast Bioengineering Conference, 2001: 37-38.

[109] J. Wang, K. Atallah and W. Wang, "Analysis of a Magnetic Screw for High Force Density Linear Electromagnetic Actuators," in IEEE Transactions on Magnetics, vol. 47, no. 10, pp. 4477-4480, Oct. 2011.

[110] R. Holm, N. Berg, P. O. Rasmussen, and et al. Design of a magnetic lead screw for wave energyconversion. IEEE Trans. Ind. Appl., 2013.

[111] R. Holm, N. Berg, P. O. Rasmussen. "Theoretical and experimental loss and efficiency studies of amagnetic lead screw". IEEE Trans. Ind. Appl., 2015.

[112] S. Pakdelian, N. Frank, and H. A. Toliyat. "Principles of the trans-rotary magnetic gear". IEEE Trans.Magn., 2013

[113] S. Pakdelian, N. Frank, and H. A. Toliyat. "Magnetic design aspects of the trans-rotary magneticgear". IEEE Trans. Energy. Convers., 2015.

[114] F. Gao, Q. Wang, B. Zou B, and Y. Xu. "Development of equivalent 2-D finite-element models foraccurate prediction of thrust force in permanent magnet lead screws". IEEE Trans. Magn., 2017.

[115] S. Pakdelian, Y. Deshpande, and H. A. Toliyat. "An electric machine integrated with trans-rotarymagnetic gear". IEEE Energy Conversion Congress and Exposition, 2012.

[116] K. Lu and W. Wu. "Electromagnetic lead screw for potential wave energy application". IEEE Trans.Magn., 2014.

[117] F. Gao, Q. Wang, and J. Zou. "Analytical modeling of 3-D magnetic field and performance inmagnetic lead screws accounting for magnetization pattern". IEEE Trans. Ind. Electron., 2019.

[118] S. Pakdelian, Y. Deshpande, and H. A. Toliyat. "Design of an electric machine integrated with tranarotary magnetic gear". IEEE Trans. Energy. Convers., 2015.

[119] Z. Ling, J. Ji, J. Wang and W. Zhao, "Design Optimization and Test of a Radially Magnetized Magnetic Screw With Discretized PMs," in IEEE Transactions on Industrial Electronics, vol. 65, no. 9, pp. 7536-7547, Sept. 2018.

[120] J. Ji, Z. Ling, J. Wang, W. Zhao, G. Liu and T. Zeng, "Design and Analysis of a Halbach Magnetized Magnetic Screw for Artificial Heart," in IEEE Transactions on Magnetics, vol. 51, no. 11, pp. 1-4, Nov. 2015.

[121] J. Wang, V. Patel and W. Wang, “Fractional-slot Per Phase, Per Pole Permanent Magnet Machines with Low Space Harmonic Contents”, IEEE Trans. Magnetics, vol. 50, no. 1, Art. no. 8200209, 2014.

[122] J. Wang, V. I.Patel, andW.Wang, “Fractional-slot permanent magnet brushless machines with low space harmonic contents”. IEEE Transaction on Magnetic, vol. 50, no. 1, Jan. 2014.

[123] Z. Liu and J. Wang, "A High Force Density Linear Actuator for Active Suspension," 2019 12th International Symposium on Linear Drives for Industry Applications (LDIA), Neuchatel, Switzerland, 2019, pp. 1-6.

[124] W. Dai, H. Zhang, D. Halim, J. Yang, Z. Xu and J. Li, "Rotordynamic Analysis of a Permanent Magnet Synchronous Motor Considering Nonlinear Unbalanced Magnetic Pull," 2019 22nd International Conference on Electrical Machines and Systems (ICEMS), Harbin, China, 2019, pp. 1-6.

[125] Y. Calleecharan and J. O. Aidanpää, "On the dynamics of an hydropower generator subjected to unbalanced magnetic pull," IET 8th International Conference on Computation in Electromagnetics (CEM 2011), Wroclaw, 2011, pp. 1-2.

[126] B. M. Ebrahimi, M. Javan Roshtkhari, J. Faiz and S. V. Khatami, "Advanced Eccentricity Fault Recognition in Permanent Magnet Synchronous Motors Using Stator Current Signature Analysis," in IEEE Transactions on Industrial Electronics, vol. 61, no. 4, pp. 2041-2052, April 2014.

[127] D. G. Dorrell, "Calculation of unbalanced magnetic pull in small cage induction motors with skewed rotors and dynamic rotor eccentricity," in IEEE Transactions on Energy Conversion, vol. 11, no. 3, pp. 483-488, Sept. 1996.

[128] A. Burakov and A. Arkkio, "Comparison of the Unbalanced Magnetic Pull Mitigation by the Parallel Paths in the Stator and Rotor Windings," in IEEE Transactions on Magnetics, vol. 43, no. 12, pp. 4083-4088, Dec. 2007.

[129] Xu X P, Han Q K, Chu, F L. "A four degrees-of-freedom model for a misaligned electrical rotor, " in Journal of Sound and Vibration, 2015.

[130] Polat, Y. D. Ertuğrul and L. T. Ergene, "Static, dynamic and mixed eccentricity of induction motor," 2015 IEEE 10th International Symposium on Diagnostics for Electrical Machines, Power Electronics and Drives (SDEMPED), Guarda, 2015, pp. 284-288.

[131] Y. Zhou, X. Bao, C. Di and L. Wang, "Analysis of Dynamic Unbalanced Magnetic Pull in Induction Motor With Dynamic Eccentricity During Starting Period," in IEEE Transactions on Magnetics, vol. 52, no. 7, pp. 1-4, July 2016.

[132] H. N. Koti, H. Chen, Y. Sun and N. A. O. Demerdash, "On Shortening the Numerical Transient in Time-Stepping Finite Element Analysis of Induction Motors Under Static and Dynamic Eccentricity Faults," 2019 IEEE Energy Conversion Congress and Exposition (ECCE), Baltimore, MD, USA, 2019, pp. 3088-3095.

[133] A. Baykov, A. Dar'enkov, A. Plekhov, D. Titov, B. Gordeev and S. Okhulkov, "Analyzing vibration of motors mounted on a single foundation," 2016 IX International Conference on Power Drives Systems (ICPDS), Perm, 2016, pp. 1-5.

[134] M. T. Bin Tarek, S. Das and Y. Sozer, "Comparative Analysis of Static Eccentricity Faults of Double Stator Single Rotor Axial Flux Permanent Magnet Motors," 2019 IEEE Energy Conversion Congress and Exposition (ECCE), Baltimore, MD, USA, 2019, pp. 3223-3228.

[135] R. Moradi, E. Afjei, H. Torkaman and A. Hajihosseinlu, "Investigation of power losses in switched reluctance motors due to rotor eccentricity utilizing FEM," 4th Annual International Power Electronics, Drive Systems and Technologies Conference, Tehran, 2013, pp. 78-82.

[136] E. Rosenberg, "Magnetic Pull in Electric Machines," in Transactions of the American Institute of Electrical Engineers, vol. XXXVII, no. 2, pp. 1425-1469, July 1918.

[137] B. A. Behrend, "On the Mechanical Forces in Dynamos Caused by Magnetic Attraction," in Transactions of the American Institute of Electrical Engineers, vol. XVII, pp. 613-633, 1900.

[138] A. Covo, "Unbalanced Magnetic Pull in Induction Motors with Eccentric Rotors [includes discussion]," in Transactions of the American Institute of Electrical Engineers. Part III: Power Apparatus and Systems, vol. 73, no. 2, pp. 1421-1425, Jan. 1954.

[139] A. Tenhunen, T. P. Holopainen and A. Arkkio, "Effects of saturation on the forces in induction motors with whirling cage rotor," in IEEE Transactions on Magnetics, vol. 40, no. 2, pp. 766-769, March 2004

[140] R. Perers, U. Lundin and M. Leijon, "Saturation Effects on Unbalanced Magnetic Pull in a Hydroelectric Generator With an Eccentric Rotor," in IEEE Transactions on Magnetics, vol. 43, no. 10, pp. 3884-3890, Oct. 2007.

[141] D. G. Dorrell and A. C. Smith, "Calculation of UMP in induction motors with series or parallel winding connections," in IEEE Transactions on Energy Conversion, vol. 9, no. 2, pp. 304-310, June 1994.

[142] K. P. P. Pillai, A. S. Nair and G. R. Bindu, "Unbalanced Magnetic Pull in Train-Lighting Brushless Alternators With Static Eccentricity," in IEEE Transactions on Vehicular Technology, vol. 57, no. 1, pp. 120-126, Jan. 2008.

[143] M. J. DeBortoli, S. J. Salon, D. W. Burow and C. J. Slavik, "Effects of rotor eccentricity and parallel windings on induction machine behavior: a study using finite element analysis," in IEEE Transactions on Magnetics, vol. 29, no. 2, pp. 1676-1682, March 1993.

[144] J. T. Li, Z. J. Liu and L. H. A. Nay, "Effect of Radial Magnetic Forces in Permanent Magnet Motors With Rotor Eccentricity," in IEEE Transactions on Magnetics, vol. 43, no. 6, pp. 2525-2527, June 2007.

[145] N. Lundström, J. Aidanpää. "Dynamic consequences of electromagnetic pull due to deviations in generator shape,".in Journal of Sound and Vibration, 2007.

[146] Tae-Jong Kim, Sang-Moon Hwang and No-Gill Park, "Analysis of vibration for permanent magnet motors considering mechanical and magnetic coupling effects," in IEEE Transactions on Magnetics, vol. 36, no. 4, pp. 1346-1350, July 2000.

[147] M. T. Xuan, J. -. Simond, R. Wetter and S. Keller, "A novel air-gap monitoring system for large low speed hydro-generators," 2006 IEEE Power Engineering Society General Meeting, Montreal, Que., 2006.

[148] D. Ishak, Z. Q. Zhu and D. Howe, "Unbalanced magnetic forces in permanent magnet brushless machines with diametrically asymmetric phase windings," Fourtieth IAS Annual Meeting. Conference Record of the 2005 Industry Applications Conference, 2005., Kowloon, Hong Kong, 2005, pp. 1037-1043.

[149] C. Pompermaier, F. J. H. Kalluf, M. V. Ferreira da Luz, and N. Sadowski, "Analytical and 3D FEM modeling of a tubular linear motor taking into account radial forces due to eccentricity", in proc. of the IEEE International Electric Machines and Drives Conference, Miami, Florida, May 2009.

[150] L. Cappelli, Y. Coia. F. Marignetti. and Z. Q. Zhu, "Analysis of Eccentricity in Permanent-Magnet Tubular Machines" , IEEE Trans. on Industrial Electronics, vol. 61 , no. 5, pp. 2208- 2216,2014.

[151] D. Sarr Lo, H. Lawali Ali, Y. Amara, G. Barakat and F. Chabour, "3D Finite Element Analysis of Eccentricity in a Tubular Linear Permanent Magnet Machine," 2018 XIII International Conference on Electrical Machines (ICEM), Alexandroupoli, 2018, pp. 1996-2001.

[152] L. J. Wu, Z. Q. Zhu, J. T. Chen and Z. P. Xia, "An Analytical Model of Unbalanced Magnetic Force in Fractional-Slot Surface-Mounted Permanent Magnet Machines," in IEEE Transactions on Magnetics, vol. 46, no. 7, pp. 2686-2700, July 2010.

[153] F. Marignetti. P. Cancelli ere, M. Scarano, "Analytical formulation of the no-load magnetic field in IPM tubular machines with translator eccentricity". in proc. of the 32nd Annual Conference on IEEE Industrial Electronics, Paris, France, November 2006.

[154] Q. Wang, H. Chen, and R. Nie, Unbalanced normal force reduction in the eccentric double-sided linear switched reluctance machine, lET Electric Power Applications, Vol. 10, no. 5, pp. 384393, 2016.

[155] M. W. Zouaghi, I. Abdennadher, and A. Masmoudi, "Investigation of the eccentricity effect on the quasi-Halbach magnetized PM T-LSM features," in Proceedings of 2017 Twelfth International Conference on Ecological Vehicles and Renewable Energies (EVER), 11-13 April 2017, Monte Carlo, Monaco.

[156] M. Bouheraoua, J. Wang and K. Atallah, "Slip Recovery and Prevention in Pseudo Direct Drive Permanent-Magnet Machines," in IEEE Transactions on Industry Applications, vol. 51, no. 3, pp. 2291-2299, May-June 2015.

Table of Figure

List of Table

APPENDIX A MATLAB Code for PM Demagnetization Analysis

In order to evaluate the PM demagnetization area, the practical method has been described in Chapter 2. This section lists the detailed MATLAB code of the calculation.

```
clear all;

% Input parameters
%-------------------------------------------------------------

a=78;%Width
b=51;%Hight
e=1;%Stepbegin
c=2;%Stepend
d=0.65;%Br

% Draw the PM matrix
%---------------------------------------

z1 = rand(a,b);
z2 = rand(a,b);
x2 = rand(a,1);
y2 = rand(1,b);
y3 = rand(1,b-1);
for l=1:a
    for k=1:b
        z1(l,k)=1;
    end
end

% Input data table
%---------------------------------------

for i=e:c

filename=['F:\work\excle\2020\2020.5.15\1828\sheet',num2str(i),'.xlsx'
];
    A = xlsread(filename);
    for j=1:a
        for h=1:b
            z2(j,h) = A((j-1)*b+h,1);
            y2(1,h) = (h-1)*0.1;
            if z2(j,h)< d
                z1(j,h)=0;
            end
        end
        x2(j,1)= (j-1)*0.1;
    end
end

% Determine whether to demagnetize
%---------------------------------------
```

```
 for m=1:a
        for n=1:b-1
            z3(m,n) = z1(m,n+1);
        end
 end
for o=1:b-1
    y3(1,o) = y2(1,o+1);
end
surf(y2,x2,z1)
%surf(y3,x2,z3)
view(0,90)
```

APPENDIX B MATLAB Code for Magnetic Screw Eccentric Force Calculation

In order to evaluate the magnetic screw eccentric force, the practical method has been described in Chapter 5. This section lists the detailed MATLAB code of the calculation.

```
%-------------------------------------------------------------------------
% This Matlab function performs design optimisation of surface
mounted,
% slotless tubular linear machines using the analytical magnetic field
% solution model. The current density is kept constant. One parameter
%-------------------------------------------------------------------------

% Input parameters
%-----------------------------------------------------------------
  Brem = 1.05;     % remanence of magnet
  ur   = 1.05;     % relative recoil permeability of magnet
  u0   = 4*pi*1e-7;
  Rb   = 0.007;    % thickness of back iron
  g    = 0.001; % airgap length
  g1   = 0.00005; % airgap ec
  hm   = 4.0e-3;     % thickness of magnets
  Ro   = 28e-3; % radius of inner back iron
  Rm   = Ro+hm; % outer radius of inner magnet ring
  %Rs   = Rm+g+hm;  % outer radius of outer magnet ring
  p    = 8;          % number of pole pairs
  Jc   = Brem/ur/u0;
  K0   = 8*pi*p*Jc;
  Tp   = 9e-3;  % pole pitch
  Tm   = Tp;
  Tpi  = pi/Tp;
  tal  = 1.0;
  %R1   = Rm+g;
  e1   = g1/g;
% Calculation of Field Coefficients
%-----------------------------------------------------------------
  Mra = zeros(40);
  Mrb = zeros(40);
  Ham = zeros(40);
  Hbm = zeros(40);
  g2 = 0.0;
  Np  = 5;
  a1  = 359;
   for n=1:Np
      K2(n)=0.0;
   end
  for s=0:a1
      g2=g-g1*cosd(s);
    for n=1:Np
      Rs   = Rm+g2+hm;
      R1   = Rm+g2;
      mrs  = (2*n-1)*Tpi*Rs;
      mrm  = (2*n-1)*Tpi*Rm;
      mro  = (2*n-1)*Tpi*Ro;
      C1(n)= besseli(0,mrs);
      C2(n)= besselk(0,mrs);
```

```
      C3(n)= besseli(0,mro);
      C4(n)= besselk(0,mro);
      C5(n)= besseli(0,mrm);
      C6(n)= besselk(0,mrm);
      C7(n)= besseli(1,mrm);
      C8(n)= besselk(1,mrm);
      Rspan=[mro mrm];
      options = odeset('RelTol',1e-4);
      [Ma,habm]=ode23('Fam',Rspan,[0;0],options);
      ham = habm(:,1);
      hbm = habm(:,2);
      Mb  = Ma;
      mpi=(2*n-1)*pi;
      Bm(n) = 4*Brem*sin(mpi*tal/2)/mpi;
      ham = ham*Bm(n);
      hbm = hbm*Bm(n);
      c2c5 = C2(n)*C5(n);
      c1c6 = C1(n)*C6(n);
      c1c8 = C1(n)*C8(n);
      c2c7 = C2(n)*C7(n);
      c2c6 = C2(n)*C6(n);
      c2c8 = C2(n)*C8(n);
      Am(1,1) = ur*(c2c5-c1c6);
      Am(1,2) = -(c2c5-C3(n)*c2c6/C4(n));
      Am(2,1) = (c2c7+c1c8);
      Am(2,2) = -(c2c7+C3(n)*c2c8/C4(n));
      jam = length(ham);
      jbm = length(hbm);
      ja(n)=jam;
      jb(n)=jbm;
      Mra(1:jam,n)=Ma;
      Mrb(1:jbm,n)=Mb;
      Ham(1:jam,n)=ham;
      Hbm(1:jbm,n)=hbm;
      Rhm =[ham(jam)*c2c5+hbm(jbm)*c2c6;ham(jam)*c2c7-hbm(jbm)*c2c8];
      det = Am(1,1)*Am(2,2)-Am(1,2)*Am(2,1);
      A1(n)=(Am(2,2)*Rhm(1)-Am(1,2)*Rhm(2))/det;
      A2(n)=(-Am(2,1)*Rhm(1)+Am(1,1)*Rhm(2))/det;
      B1(n)= C1(n)*A1(n)/C2(n);
      B2(n)= C3(n)*A2(n)/C4(n);
      mn  = (2*n-1)*Tpi;
      sn(n)  = quad('ftm',R1,Rs,[],[],mn,A1(n),-B1(n));
      kpn = sin(mn*Tm/2);
      K1(n)= kpn*sn(n)*cosd(s);
      K2(n)= K2(n)+K1(n);
    end;

  end

% Calculate force capability
%----------------------------------------


  for i = 1:181
     zd(i) = (i-1)*Tp/180;
     F(i) = 0.0;
     for n=1:Np
        mn  = (2*n-1)*Tpi;
        F(i)=F(i)+K2(n)*cos(mn*zd(i))/360;
     end
  end;
  F = K0*F;
```

APPENDIX C MATLAB Code for DTVPM Thermal Calculation

In order to evaluate the temperature rise in each area of DTVPM, the practical method has been described in Chapter 3. This section lists the detailed MATLAB code of the calculation.

```
% Input parameters
%-------------------------------------------------------------

pcu1=3;%Outer stator copper loss
pcu2=3;%Inner stator copper loss
pfe1=1.25;%Outer stator iron loss
pfe2=1.25;%Inner stator iron loss
lmove=0.0174;
routbr=0.09;
routsh=0.0833;
routwd=0.0697;
routag=0.056;
tsout=0.01667;
twout=0.008;
swout=0.008;
rinbr=0.0046;
rinsh=0.0113;
rinwd=0.025;
rinag=routag-lmove;
lline=0.001;
kfe=61;%Core Axial thermal conductivity
kline=2;%Copper Radial thermal conductivity
kair=0.031;%Air gap thermal conductivity
kco=377;%Copper thermal conductivity
h=21.7;%Heat dissipation coefficient

% Calculate the thermal conductivity
%---------------------------------------

rc=1/(pi*tsout*h*routbr);
rfe1=log(routbr/routsh)/(pi*tsout*kfe);
rfe2=log(routsh/routwd)/(pi*tsout*kfe);
rfe3=twout/(4*kfe*pi*(routsh*routsh-routag*routag));
rfe4=log(routag/rinag)/(pi*tsout*kfe);
rfe5=twout/(4*kfe*pi*(rinag*rinag-rinsh*rinsh));
rfe6=log(routbr/routsh)/(pi*tsout*kfe);
rs1=lline/(pi*swout*routsh*kline);
rs2=lline/(pi*(routsh*routsh-routag*routag)*kline);
rs3=lline/(pi*tsout*lmove*kair);
rs4=lline/(pi*tsout*lmove*kair);
rs5=lline/(pi*tsout*lmove*kair);
rs6=lline/(pi*tsout*lmove*kair);
rs7=lline/(pi*(rinag*rinag-rinsh*rinsh)*kline);
rs8=lline/(pi*swout*rinsh*kline);
rw1=log(routbr/routsh)/(pi*swout*kco);
rw2=tsout/(4*kco*pi*(routsh*routsh-routag*routag));
rw3=log(routbr/routsh)/(pi*swout*kco);
rw4=tsout/(4*kco*pi*(rinag*rinag-rinsh*rinsh));
```

```
r1=rc+rfe1;
r2=rs1+rw1;
r3=rfe2;
r4=rw2+rs2+rfe3;
r5=rs3;
r6=rs4;
r7=rfe4;
r8=rs6;
r9=rs5;
r10=rfe5+rs7+rw4;
r11=rfe6+rs8+rw3;

% Calculate the temperature rise
%---------------------------------------

g1=1/r1;
g2=1/r2;
g3=1/r3;
g4=1/r4;
g5=1/r5;
g6=1/r6;
g7=1/r7;
g8=1/r8;
g9=1/r9;
g10=1/r10;
g11=1/r11;

b=[g1+g2+g3 -g2 -g3 0 0 0 0;
    -g2 g2+g4+g5 -g4 -g5 0 0 0;
    -g3 -g4 g6+g4+g3 -g6 0 0 0;
    0 -g5 -g6 g5+g6+g7 -g7 0 0;
    0 0 0 -g7 g7+g8+g9 -g8 -g9;
    0 0 0 0 -g8 g8+g10+g11 -g11-g10;
    0 0 0 0 -g9 -g10-g11 g11+g10+g9];
c=[0; pcu1; pfe1; 0; 0; pfe2; pcu2];
a=inv(b);
d= b\c;
```